

Towards increased performance of iron(II)-based
dye sensitized solar cells

Inauguraldissertation

zur

Erlangung der Würde eines Doktors der Philosophie

vorgelegt

der Philosophisch-Naturwissenschaftlichen Fakultät

der Universität Basel

von

Mariia Becker

Basel, 2021

Genehmigt von der Philosophisch-Naturwissenschaftlichen Fakultät

auf Antrag von

Prof. Dr. E. C. Constable

Prof. Dr. K. Tiefenbacher

Prof. Dr. M. K. Nazeeruddin

Basel, 25.05.2021

Prof. Dr. Marcel Mayor

Dekan der Philosophisch-
Naturwissenschaftlichen Fakultät

Моей Семье

Acknowledgments

I would like to express my gratitude to Prof. Dr. Catherine Housecroft and Prof. Dr. Edwin Constable for their trust and the amazing opportunity to join their group. Under your guidance I could enter the solar cells world and was able to uncover my research interests. I always enjoyed our discussions about professional matters and beyond. Regular exchange of ideas and the freedom of trying new things gave an infinite number of research opportunities that I highly appreciate.

I would like to thank Prof. Dr. Konrad Tiefenbacher for being my second supervisor. Our annual meetings were always beneficial and new ideas could be found.

I am grateful to Prof. Dr. Mohammad K. Nazeeruddin, who kindly accepted the role of the external expert and found the time to read this thesis.

I would like to thank Prof. Dr. Christof Sparr for kindly agreeing to be the chair of my defense committee.

I would like to thank the whole Constable/Housecroft group and all members whom I met during these amazing four years. From each of you I could learn something new. Big thanks for being my students go to Sophie, Vanessa and Doro. It was a big pleasure to work with each of you. Special thanks go to Marco, Paola, Sven, Giacomo, Dalila, Isaak and Guglielmo. Without all of you the atmosphere in the labs would never be so easy and friendly. We could share a lot of fun together and despite all difficult times in 20/21, we still managed to keep our Texas-team. Special thanks go to Dalila for being my partner in crime during our shared lunchbreaks. I would like to thank Marco and Sven for their help with EndNote. Without you, I would fight with references till this day. Moreover, I would like to thank my long-term lab mate Guglielmo, who broadened my musical experience.

Furthermore, I would like to thank the whole staff of the Department of Chemistry without whom work would be literally impossible. Additional and special thanks go to Beatrice Erismann and Isa Worni, Dr. Bernhard Jung and the IT team, the team of Prof. Dr. Daniel Häussinger for NMR support, and Markus Hauri for keeping the whole department running.

I really would like to thank Prof. Dr. Catherine Housecroft, Sascha and Matthias for proofreading my thesis and their careful corrections.

Мои дорогие мама, папа, бабушка и Никита. Без вашей любви и поддержки я бы никогда не смогла решиться на подобное приключение. Это невероятное чувство, знать, что тебя

всегда ждут и примут таким, какой ты есть, что есть место, куда я всегда могу вернуться. Просто потому, что я ваша Маша. Спасибо вам за это.

My dear husband Matthias Медведь. Despite all the difficulties we had to face, we still walk our way together, and I am grateful for this. Your enormous support keeps me going, and I would never manage to come to this point without you.

Abstract

Today, because of the current climate situation, renewable energy sources are of high importance. Over the last few decades, solar cells have become a vital technology due to their ability to convert sunlight into electrical energy. Most of the commercially available solar cells are made of crystalline silicon. Silicon-based solar cells are already well known in the market, but their costly and tedious fabrication motivates the examination of alternative systems. Since the pioneering work of O'Regan and Grätzel in 1991, dye-sensitized solar cells (DSCs) have become a promising substitute. The sandwich-type DSC structure is easy to manufacture, and a broad variety of sensitizers offers lower costs of materials. However, the use of metals such as ruthenium with low natural abundances still significantly increases the price and reduces the sustainability of DSCs.

In this work, the focus is set on *n*-type DSCs, which combine the use of Earth abundant iron(II) coordination complexes as dyes and the advantageous effects of using different additives in electrolytes. Tuning of electrolyte composition can also remarkably enhance the photoconversion efficiency (PCE) and, as shown for other dyes, has the potential to make iron-sensitizers a promising alternative to ruthenium-based compounds. It has been demonstrated that both the redox couple and the components of the electrolyte have a critical influence on the PCE, and this effect originates from its role as a charge transfer medium. The effects of lithium salts, ionic liquids with different counter-ions and solvents while retaining an I^-/I_3^- redox shuttle are presented.

Sometimes small changes might lead to significant progress. The design of an alternative iron(II)-based dye is proposed with a corresponding synthetic route. The synthesis towards the target complex is presented.

Moreover, a statistical study of electrochemical impedance (EIS) measurements was performed. EIS offers a possibility to study complex electronic systems and is commonly used for solar cells, but there is a general tendency in the literature to present impedance data only for one device. At the same time, the current density–voltage plots can illustrate that measurements may vary within one set of DSCs with identical components. The multiple DSCs impedance measurements are presented on the example of two dyes and provide the statistical analysis for their reproducibility between the cells.

The work in the First, Second and Third Chapters has been published in open access journals.^{1,2} Some parts in the introduction in the First Chapter have been taken from the publications as well as a part of the discussion in the Second and Third Chapters.

¹ M. Becker, M.-S. Bertrams, E. C. Constable, C. E. Housecroft, *Materials*, 2020, 13, 1547.

² M. Karpacheva, V. Wyss, C. E. Housecroft, E. C. Constable, *Materials*, 2019, 12, 4181.

Abbreviations

| | |
|--|---|
| % | percent |
| [BDMI] ⁺ | 1-butyl-2,3-dimethylimidazolium cation |
| [BF ₄] ⁻ | tetrafluoroborate |
| [CF ₃ SO ₃] ⁻ | trifluoromethanesulfonate |
| [Im] ⁺ | imidazolium cation |
| [N(CF ₃ SO ₂) ₂] ⁻ | bis(trifluoromethylsulfonyl)imide |
| [PF ₆] ⁻ | hexafluorophosphate |
| [PMI] ⁺ | 1-propyl-3-methylimidazolium cation |
| °C | degree Celsius |
| µm | micrometre |
| AC | alternating current |
| AcOEt | ethyl acetate |
| AcOH | acetic acid |
| AM | air mass |
| API | after pre-irradiation |
| aq. | aqueous |
| Ar | aryl |
| BDMIBF | 1-butyl-2,3-dimethylimidazolium tetrafluoroborate |
| BDMICFSO | 1-butyl-2,3-dimethylimidazolium trifluoromethanesulfonate |
| BDMII | 1-butyl-2,3-dimethylimidazolium iodide |
| BDMIPF | 1-butyl-2,3-dimethylimidazolium hexafluorophosphate |
| BMIFeCl | 1-butyl-3-methylimidazolium tetrachloroferrate |
| BMII | 1-butyl-3-methylimidazolium iodide |
| BMIPF | 1-butyl-3-methylimidazolium hexafluorophosphate |
| Boc | <i>tert</i> -butoxycarbonyl |
| Boc ₂ O | di- <i>tert</i> -butyl dicarbonate |
| bpy | 2,2' bipyridine |
| br. | broad peak |
| BrettPhos | 2-(dicyclohexylphosphino)-3,6-dimethoxy-2',4',6'-triisopropyl-1,1'- biphenyl |
| calc. | calculated |
| CB | conduction band |

| | |
|--------------------|---|
| cheno | chenodeoxycholic acid |
| cm | centimetre |
| CO ₂ | carbon dioxide |
| COOH | carboxylic acid |
| CPE _{Pt} | constant phase element |
| C _{Pt} | capacitance of a counter electrode |
| c-Si | crystalline silicon |
| OAc | acetate |
| C _μ | chemical capacitance |
| D | deuterium |
| <i>d</i> | thickness of a semiconductor |
| dc bpy | 2,2'-bipyridyl-5,5'-dicarboxylic acid |
| DCM | dichloromethane |
| DSC | dye sensitized solar cell |
| dd | doublet of doublets (NMR) |
| ddd | doublet of doublets of doublets (NMR) |
| DMF | <i>N,N</i> -dimethylformamide |
| DMII | 1,3-dimethylimidazolium iodide |
| DMSO | dimethyl sulfoxide |
| DodMII | 1-dodecyl-3-methylimidazolium iodide |
| dt | doublet of triplets |
| DX1 | extended distributed element |
| EDA | ethylenediamine |
| e^-_{inj} | electron injected into the semiconductor |
| EIS | electrochemical impedance spectroscopy |
| EMIBCN | 1-ethyl-3-methylimidazolium tetracyanoborate |
| EMII | 1-ethyl-3-methylimidazolium iodide |
| EMIMPF | 1-ethyl-3-methylimidazolium hexafluorophosphate |
| EQE | external quantum efficiency |
| EQE _{max} | maximum external quantum efficiency |
| equiv | equivalent |
| ESI-MS | electron spray ionisation mass spectrometry |
| Et | ethyl |
| EtOH | ethanol |

| | |
|---------------------|---|
| eV | electronvolt |
| f | frequency |
| ff | fill factor |
| FIB | focused ion beam |
| f_{\max} | maximum frequency |
| FTO | fluorine doped tin oxide |
| g | gram |
| G | global |
| h | hour |
| HDMII | 1-hexyl-2,3-dimethylimidazolium iodide |
| HETPHEN | heteroleptic bisphenanthroline complexes |
| HMII | 1-hexyl-3-methylimidazolium iodide |
| HOMO | highest occupied molecular orbital |
| HPLC | high performance liquid chromatography |
| Hz | hertz |
| I | current |
| IL | ionic liquid |
| cP | centipoise |
| IPCE | incident photon to electrical conversion efficiency |
| IQE | internal quantum efficiency |
| IR | infrared |
| I - V | current versus potential |
| J | current density; coupling constant (NMR, experimental part) |
| J_{MPP} | maximum power point current density |
| J_{SC} | short circuit current density |
| J - V | current density versus potential |
| K | degree Kelvin |
| kHz | kilohertz |
| O ^t Bu | <i>tert</i> -butoxide |
| L_{anchor} | anchoring ligand |
| L_{ancill} | ancillary ligand |
| L_{d} | diffusion length |
| LHE | light harvesting efficiency |
| LiX | lithium salt |

| | |
|----------|-------------------------------------|
| LUMO | lowest unoccupied molecular orbital |
| m | multiplet (NMR) |
| M | molarity |
| mmol | millimol |
| m/z | mass to charge ratio |
| mA | milliampere |
| MBI | 1-methylimidazole |
| MC | metal centred |
| MeCN | acetonitrile |
| MeI | methyl iodide |
| MeOH | methanol |
| mg | milligram |
| MHz | megahertz |
| min | minute |
| mL | millilitre |
| MLCT | metal-to-ligand charge transfer |
| mM | millimolar |
| MO | molecular orbital |
| mPa | millipascal |
| MPN | 3-methoxypropionitrile |
| MPP | Maximum power point |
| ms | millisecond |
| MTBE | methyl <i>tert</i> -butyl ether |
| mV | millivolt |
| mW | milliwatt |
| MW | microwave |
| NHC | <i>N</i> -heterocyclic carbene |
| nm | nanometre |
| NMR | nuclear magnetic resonance |
| ON | overnight |
| <i>P</i> | theoretical power |
| PCE | photoconversion efficiency |
| PCS | perovskite solar cells |
| Pd | palladium |

| | |
|-----------|--|
| dba | dibenzylideneacetone |
| dppf | 1,1'-bis(diphenylphosphino)ferrocene |
| PDMII | 1,2-dimethyl-3-propylimidazolium iodide |
| PEDOT | poly(3,4-ethylenedioxythiophene) |
| Ph | phenyl |
| phen | 1,10-phenanthroline |
| Phth | phthalimide |
| Phtpy | 4'-phenyl-2,2':6',2''-terpyridine |
| P_{IN} | total incident solar power of the cell |
| PMIBF | 1-propyl-3-methylimidazolium tetrafluoroborate |
| PMII | 1-propyl-3-methylimidazolium iodide |
| PMINCFSO | 1-propyl-3-methylimidazolium bis(trifluoromethylsulfonyl)imide |
| PPh_3 | triphenylphosphine |
| ppm | parts per million |
| PPSE | polyphosphoric acid trimethylsilyl ester |
| ps | picoseconds |
| PSS | polystyrenesulfonate |
| Q | pre-factor of CPE |
| QE | quantum efficiency |
| rac-BINAP | racemic 2,2'-bis(diphenylphosphino)-1,1'-binaphthyl |
| R_d | diffusion resistance of charge carriers in an electrolyte |
| R_{Pt} | resistance of a counter electrode |
| R_{rec} | recombination resistance |
| R_s | series resistance |
| RSD | relative standard deviation |
| R_{SH} | shunt resistance |
| rt | room temperature |
| R_{tr} | transport resistance |
| s | second; singlet (NMR, experimental part) |
| SALSAC | surface-as-ligand, surface-as-complex |
| sat. | saturated |
| SD | standard deviation |
| ssUV-Vis | solid state UV-Vis spectroscopy |
| t | triplet (NMR) |

| | |
|-----------------|--|
| TBP | 4- <i>tert</i> -butylpyridine |
| td | triplet of doublet |
| TD-DFT | time-dependent density functional theory |
| TFA | trifluoroacetic acid |
| THF | tetrahydrofuran |
| TLC | thin layer chromatography |
| TMP | 2,2,6,6-tetramethylpiperidiny1 |
| TMS | trimethylsilyl |
| tpy | 2,2':6',2''-terpyridine |
| UV | Ultra Violet |
| UV-Vis | Ultra Violet Visible |
| v | volume |
| V_{MPP} | maximum power point voltage |
| V_{OC} | open circuit voltage |
| WOPI | without pre-irradiation |
| W_s | Warburg element |
| wt% | wight percent |
| Z_G | Gerischer impedance |
| α | empirical constant |
| δ | chemical shift |
| η | solar-to-electrical energy conversion efficiency |
| λ | wavelength |
| λ_{max} | wavelength of absorbance maximum |
| μF | microfarad |
| τ | electron lifetime |
| τ_t | transport time |
| Φ_{in} | incident photon flux |
| Ω | ohm |

Table of Contents

| | |
|---|-----------|
| First Chapter | 1 |
| 1. Introduction | 2 |
| 1.1 Energy usage and consequences | 2 |
| 1.2 Solutions | 5 |
| 1.3 Photovoltaic technologies | 6 |
| 1.4 Dye-sensitized solar cells | 6 |
| <i>1.4.1 Working principle</i> | <i>7</i> |
| <i>1.4.2 Photoanode</i> | <i>8</i> |
| <i>1.4.3 Sensitizer</i> | <i>10</i> |
| <i>1.4.4 Electrolyte</i> | <i>16</i> |
| <i>1.4.5 Counter electrode</i> | <i>18</i> |
| <i>1.4.6 Challenging aspects of iron(II)-complexes</i> | <i>19</i> |
| 2. Materials and Methods | 24 |
| 2.1 DSC manufacturing | 24 |
| 2.2 J-V plots and solar simulator | 25 |
| 2.3 External quantum efficiency | 29 |
| 2.4 Solid state UV-Vis spectroscopy | 30 |
| 2.5 Electrochemical impedance spectroscopy | 31 |
| Second Chapter | 35 |
| 1. Motivation | 36 |
| 2. Introduction | 36 |
| 3. Results | 37 |
| <i>3.1 Effect of the pre-irradiation of DSCs</i> | <i>37</i> |
| <i>3.2 General reproducibility of DSCs in terms of EIS measurements</i> | <i>41</i> |
| 4. Conclusions | 54 |

| | |
|---|------------|
| Third Chapter | 55 |
| 1. Motivation | 56 |
| 2. Optimisation of DSC sensitized with bis(2,2':6',2''-terpyridine)iron(II) complexes..... | 56 |
| 3. Electrolyte tuning for DSCs sensitized with Fe-NHC complexes | 64 |
| 3.1 Electrolyte optimisation based on effects of solvent and additives..... | 66 |
| 3.1.1 <i>The effect of solvent and ionic liquid</i> | 66 |
| 3.1.2 <i>The effect of nitrogen-containing heterocyclic additives.....</i> | 68 |
| 3.1.3 <i>Analysing the effect of MBI additive via electrochemical impedance spectroscopy</i> | 72 |
| 3.1.4 <i>Effect of additives towards different ionic liquids</i> | 75 |
| 3.1.5 <i>External quantum efficiency measurements for DSCs with electrolytes E2b, E2c, E2e and E4</i> | 77 |
| 3.1.6 <i>DSC stability test for electrolytes E2b and E2e.....</i> | 78 |
| 3.1.7 <i>Summary: Solvents and additives</i> | 81 |
| 3.2 Investigations of the effect of lithium salts and ionic liquid concentration | 82 |
| 3.2.1 <i>The effect of lithium salts in electrolyte</i> | 82 |
| 3.2.2 <i>The EQE and EIS study of Li⁺ ion influence on DSCs</i> | 89 |
| 3.2.3 <i>The effect of increased IL concentration in electrolyte.....</i> | 95 |
| 3.2.4 <i>Summary: Li⁺ salts and IL concentration.....</i> | 99 |
| 3.3 Influence of structure of IL on a DSC operation | 100 |
| 3.3.1 <i>The change in an alkyl chain length of 1-alkyl-3-methylimidazolium iodide</i> | 100 |
| 3.3.2 <i>The influence of a methyl group in the 2-position in imidazolium-based IL</i> | 106 |
| 3.3.3 <i>The influence of IL counterion on DSC performance</i> | 109 |
| 3.3.4 <i>The influence of mixed counterions of 1-alkyl-3-methylimidazolium ILs</i> | 111 |
| 3.3.5 <i>Summary: The influence of n-alkyl substituents and counterions of ILs</i> | 115 |
| 3.4 Influence of iodine concentration on DSCs performance..... | 116 |
| 3.4.1 <i>Motivation.....</i> | 116 |
| 3.4.2 <i>Comparison of electrolytes with 0.05 M and 0.10 M I₂.....</i> | 117 |

| | |
|--|------------|
| 3.4.3 EIS measurements of DSCs with 0.10 M I ₂ | 121 |
| 3.4.4 Further iodine concentration study for electrolytes with DMII, EMII and PDMII ionic liquids..... | 126 |
| 3.4.5 EQE measurements of DSCs with 0.02 M, 0.20 M and no iodine in electrolytes.. | 131 |
| 3.4.6 EIS measurements of DSCs with 0.02 M, 0.20 M and no iodine in electrolytes.... | 133 |
| 3.4.7 Summary: Electrolytes with different iodine concentration..... | 138 |
| 4. Conclusion..... | 139 |
| Fourth Chapter | 143 |
| 1. Motivation | 144 |
| 2. Discussion..... | 145 |
| 3. Summary and Outlook..... | 166 |
| Fifth Chapter | 171 |
| Experimental part | 172 |
| 1. General considerations | 172 |
| 2. Synthesis of ligands and complexes | 173 |
| 2.1 Synthesis of terpyridine compounds..... | 173 |
| 2.2 Synthesis towards N-heterocyclic carbene compounds | 179 |
| Sixth Chapter..... | 185 |
| Summary and Outlook | 186 |
| References | 189 |

First Chapter

*Annushka has already spilled the oil.
The Master and Margarita,
Mikhail Bulgakov*

1. Introduction

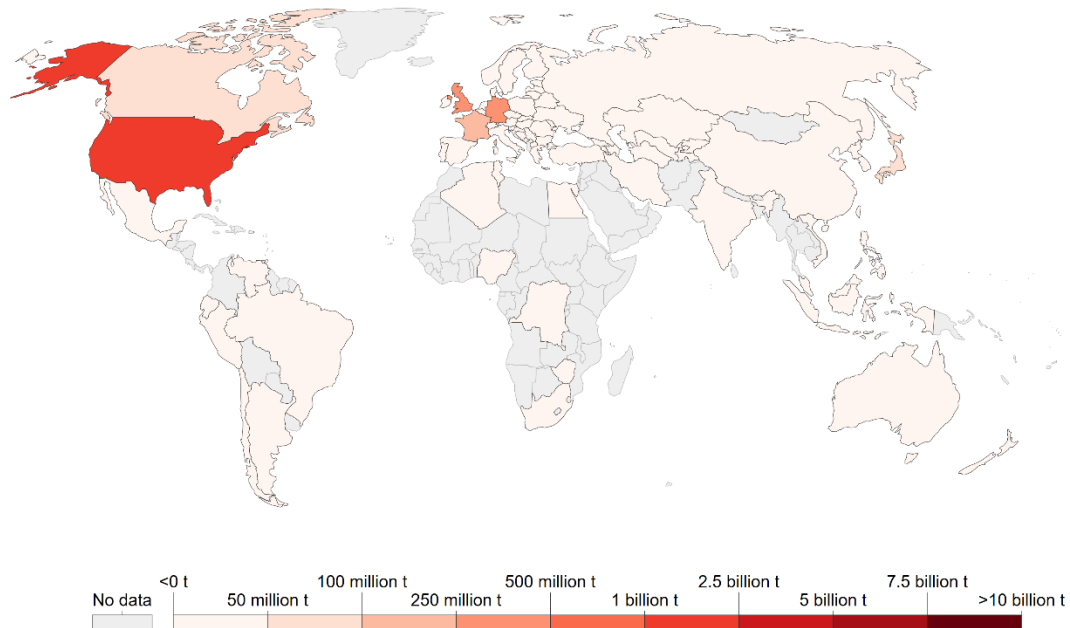
1.1 Energy usage and consequences

Energy has a great impact on our everyday life. When we turn on the light in the evening, heat up the stove to cook dinner or start the machine for morning coffee – we depend on a regular and efficient energy source. Moreover, we expect the source to be not only reliable but also safe for the environment and our personal health as well as inexpensive.

Today, fossil fuels still supply most of the world's energy. While burning of fuels is used to produce electricity, refined qualities like kerosene or gasoline are also used for heating or transportation.¹ 70 years ago, coal was already one of the main energy sources, which has a great pollution potential due to impure combustion and release of ash.² Nowadays, coal supplies a third of the world's energy demands, and is the source of 44% released carbon dioxide (CO₂).¹ Oil fuels generate 40% of the world's energy and serve as a source for about one third of global CO₂ emission. Natural gases are considered as the cleanest fossil choice in terms of CO₂ production, but still account for a fifth of the world's emissions.¹ In Figure 1.1 the dramatic increase of the annual CO₂ emissions over the last 100 years is presented.

Annual CO₂ emissions, 1919

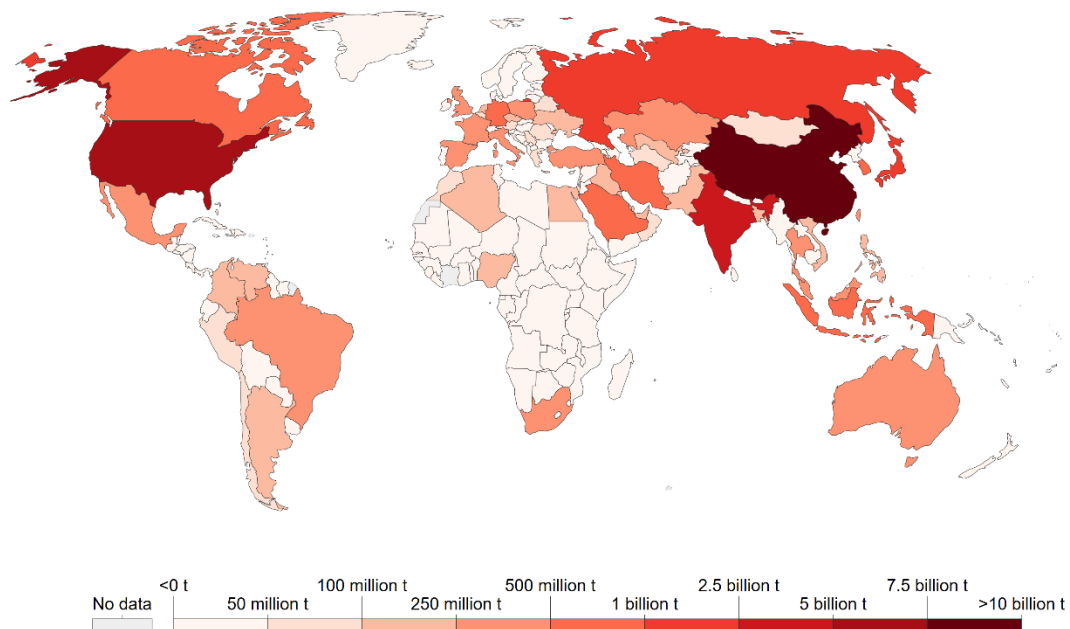
Carbon dioxide (CO₂) emissions from the burning of fossil fuels for energy and cement production. Land use change is not included.



Source: Global Carbon Project; Carbon Dioxide Information Analysis Centre (CDIAC) [OurWorldInData.org/co2-and-other-greenhouse-gas-emissions/](https://ourworldindata.org/co2-and-other-greenhouse-gas-emissions/) • CC BY
Note: CO₂ emissions are measured on a production basis, meaning they do not correct for emissions embedded in traded goods.

Annual CO₂ emissions, 2019

Carbon dioxide (CO₂) emissions from the burning of fossil fuels for energy and cement production. Land use change is not included.



Source: Global Carbon Project; Carbon Dioxide Information Analysis Centre (CDIAC) [OurWorldInData.org/co2-and-other-greenhouse-gas-emissions/](https://ourworldindata.org/co2-and-other-greenhouse-gas-emissions/) • CC BY
Note: CO₂ emissions are measured on a production basis, meaning they do not correct for emissions embedded in traded goods.

Figure 1.1. Annual CO₂ emissions in 1919 and 2019. [<https://ourworldindata.org/fossil-fuels>, CC BY 4.0 licence, https://creativecommons.org/licenses/by/4.0/deed.en_US].

First Chapter

The emissions enhance the greenhouse effect and accelerate the changes in climate. As a result of CO₂ accumulation in the atmosphere, a large portion of it gets absorbed by the oceans. This leads to the acidification of water, which becomes corrosive for thousands of marine shell species.³ Once water gets sufficiently acidic, the extinction of these species may take place with a domino effect on the food chains for fish, birds, and mammals.³ Moreover, the mining of fossil fuels leads to land degradation and water pollution.³ Considering human health, oil and gas refining and consumption result in air pollution, which has amongst others an impact on human's respiratory system. In 2016 it was shown that the air pollution directly harms the health of the general public, which is living near oil and gas production facilities (the study was done in the United States).⁴ A study of 2017 has shown that air pollution from fossil fuels is one of the top ten risk factors for death in the world.^{5,6} Additionally, the enhanced greenhouse effect promotes the global warming, which affect all parts of our planet. Nowadays, we can witness the irreversible changes which include the melting of glaciers, the rise of global sea levels and warming of the oceans. This has a direct effect on the plant and animal life.⁷



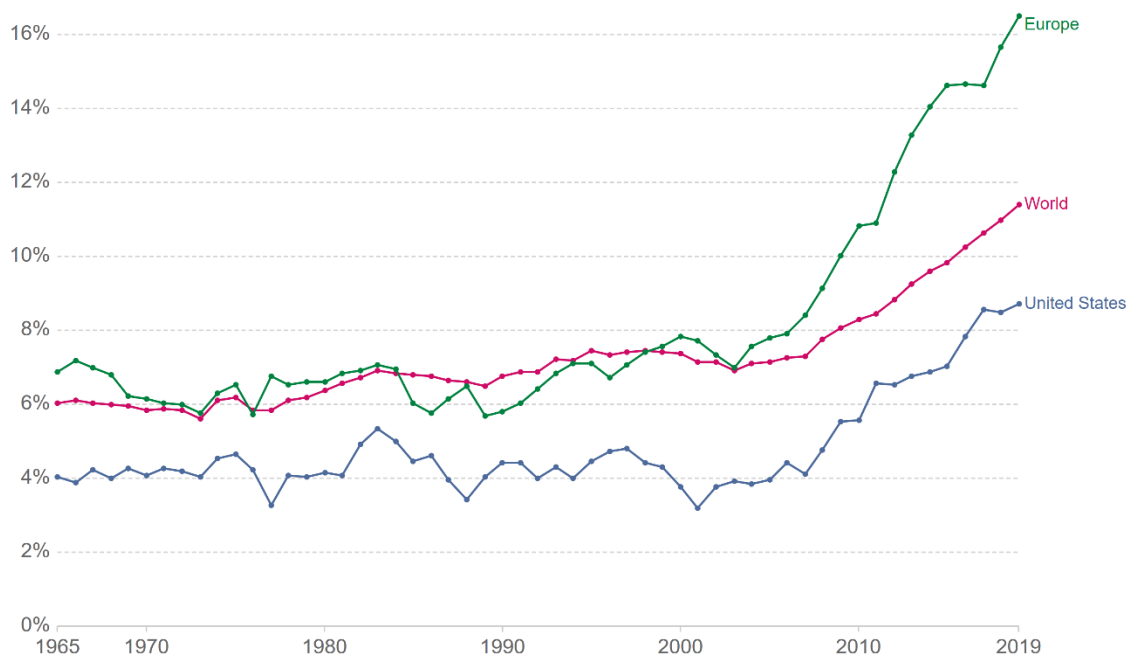
Figure 1.2 Polar bear whose home is literally melting under his paws. [Credit: "Polar Bear seen Ice Cruising in the Arctic" by Tips For Travellers, CC BY 2.0 license, <https://creativecommons.org/licenses/by/2.0/>].

1.2 Solutions

Modern world cannot live without energy. However, the current climate situation demands the actions and renewable energy sources are a promising alternative for fossil fuels. Nowadays up to 14% of the total world energy is provided by renewable sources.⁸ This includes particularly the use of wind, hydropower, sunlight, and biomasses, which are considered to be inexhaustible.^{9, 10} In Figure 1.3 the development of renewable energy sources is presented. Over the last ten years, a significant increase of green energy (especially for Europe) can be seen. In 2019, 66% of Switzerland's energy came from water sources and 8.4% was generated from photovoltaics, wind, small hydroplants (production <50 MW) and biomasses.¹¹ Hydropower has the highest impact on the world's energy production, compared to other renewable sources. Hydropower plants are emissions-free and require only one natural source – (flowing) water. However, big dams change original river courses, disturb surrounding inhabitants, harm the wildlife and the overall ecosystems.¹² Thus, the usage of hydropower is unlikely to be the ultimate solution.

Share of primary energy from renewable sources

Renewable energy sources includes hydropower, solar, wind, geothermal, bioenergy, wave and tidal. It does not include traditional biofuels, which can be a key energy source especially in lower-income settings.



Source: Our World in Data based on BP Statistical Review of World Energy (2020)

OurWorldInData.org/energy • CC BY

Note: Primary energy is calculated using the 'substitution method' which takes account of the inefficiencies energy production from fossil fuels.

Figure 1.3. Percentage of energy, which comes from renewable sources, used from 1965 till 2019. [<https://ourworldindata.org/renewable-energy#how-much-of-our-primary-energy-comes-from-renewables>, CC BY 4.0 licence, https://creativecommons.org/licenses/by/4.0/deed.en_US].

The Sun is sustainable, near-infinite and most importantly, harmless to the ecosystem as its use does not directly affect it. The total amount of solar energy delivered from the Sun to Earth vastly

exceeds the world's current as well as foreseeable future needs.¹³ Thus, the necessity of light-harvesting technologies resulted in the field of photovoltaics.

1.3 Photovoltaic technologies

Today, most of commercially available solar cells are made of crystalline silicon (c-Si)¹⁴ and can reach an efficiency close to its theoretical maximum.¹⁴ The cells are composed of a silicon wafer, glass, junction box, silver and aluminium electrodes and wires.¹⁵ Mono- and polycrystalline silicon wafers both can be used for solar panels, but polycrystalline cells perform slightly lower. Nevertheless, their tedious, costly fabrication and the necessity of using environmentally non-benign metals such as gallium or cadmium as alternative semiconductors are major drawbacks for their use as a green energy source.¹⁶ Complicated and expensive recycling of silicon wafers reduces the sustainability of c-Si cells as well.

Dye-sensitized solar cells (DSCs) offer a low-cost alternative. They are single junction solar cells that are based on a semiconductor sensitized with a dye. Their efficiency is lower than c-Si cells, but over the last couple of decades, they have become of high research interest. Another type of solar cell is the perovskite solar cell (PSCs). PSCs developed from DSCs into a separate class of solid-state sensitized solar cells. PSCs are based on a perovskite material, which serves as a hole-transport material and induces a heterojunction.¹⁷ They offer a high efficiency over 20% but suffer from low-device stability and the usage of lead. The use of multi-dimensional junction with 2D/3D interface helps to overcome the sensitivity towards moisture.¹⁸ However, the usage of this architecture is combined with reduced efficiency ($\approx 13\%$).

1.4 Dye-sensitized solar cells

The pioneering development of dye-sensitized solar cells by O'Regan and Grätzel in 1991 gave an alternative to overcome the limitations of c-Si solar cells.^{19, 20} Lower material costs and less sophisticated manufacturing processes combined with the avoidance of toxic materials offer considerable advantages²¹, and the demonstrated upscaling from a research laboratory to commercial DSCs makes their introduction to the market viable.²¹⁻²³

1.4.1 Working principle

A DSC consists of a photoanode, an electrolyte containing a redox shuttle, and a counter electrode (Figure 1.4). The dye is adsorbed on the semiconductor surface (for detail see section 1.4.2). Photoexcitation of the dye ($S \rightarrow S^*$) results in electron injection into the conduction band (CB). The electron travels through the electrical load and reduces a redox couple, that is typically consisting of iodide/triiodide (I^-/I_3^-), at the platinum-coated counter electrode. The reduced form of the redox couple regenerates the dye in the ground state, which completes the circuit. The difference between the Fermi level of a semiconductor and a redox potential of redox couple is the open circuit voltage that is the maximum potential a DSC can provide (in section 2.2 V_{oc} will be discussed in detail).

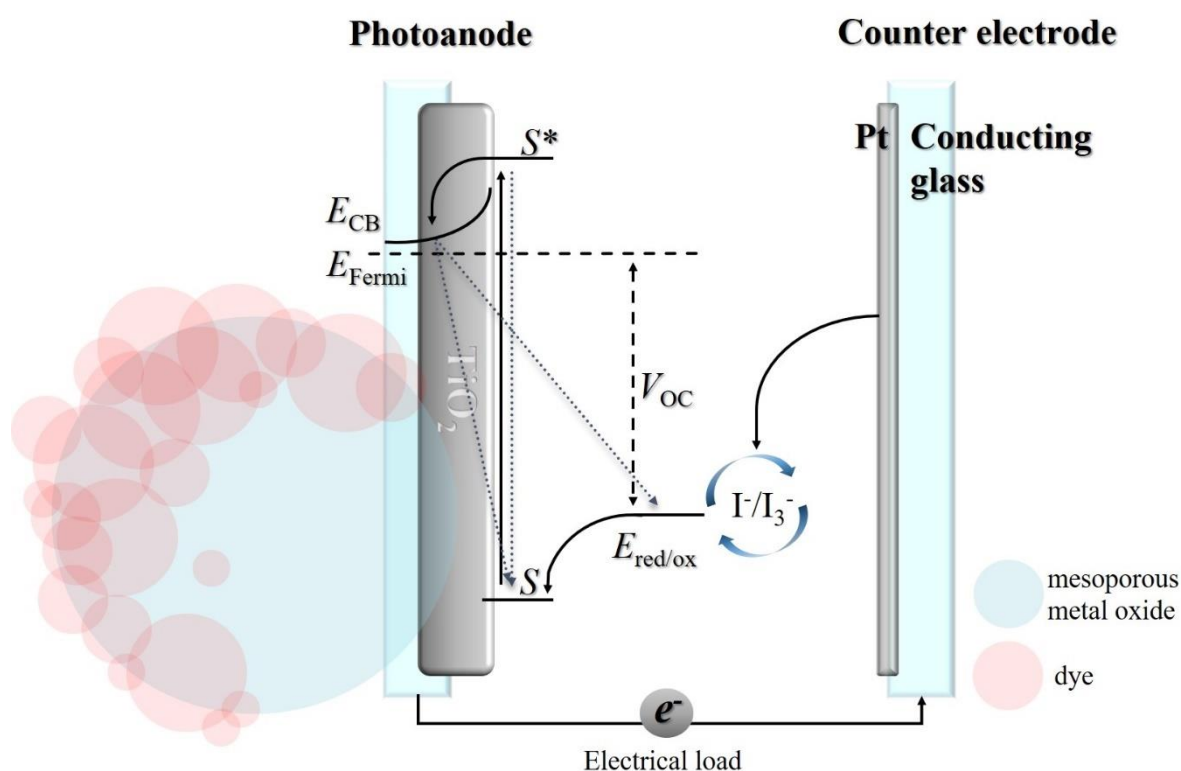


Figure 1.4. The schematic structure of an n-type DSC. Arrows show the direction of electron movement; CB – conduction band, V_{oc} – open circuit voltage, red/ox – electrolyte redox couple. Dotted lines show the recombination processes in DSC.

Various recombination processes can occur during the operation of a DSC. One of them is the recombination of the electron injected into the semiconductor (e^-_{inj}) with the oxidized dye. For the efficient electron transport, this recombination process has to be slower than dye reduction by the redox shuttle.²⁴ The recombination kinetics are strongly affected by the electrolyte composition

and electron occupation in CB and trap states. It also depends on the metal oxide, the dye structure, and the binding model to the surface.²⁴ Another dark current (recombination) process is the reaction of e^-_{inj} with the oxidized redox specie (Equation 1.1).²⁵



Moreover, the decay of the excited state of the dye (S^*) to the ground state (S) can occur, instead of the electron injection, resulting in the deactivation of the sensitizer.²⁵

1.4.2 Photoanode

The schematic representation of the working electrode is shown in Figure 1.5. The photoanode is made of glass, which is coated on one side with a transparent conducting metal oxide, usually fluorine-doped tin oxide (FTO). On the top of FTO, the nanostructured metal oxide layer is deposited. The semiconductor sensitized with a dye by immersing the electrode in the dye solution.



Figure 1.5. The schematic representation of working electrode.

Various metal oxides show n-type semiconductor properties and are used for DSC applications. The most common ones are TiO_2 , ZnO , and SnO_2 .²⁶⁻²⁸

Typically, titanium dioxide (TiO_2) is used as a semiconductor in an n-type DSC. TiO_2 is a non-toxic compound, which is commonly used in cosmetics and paints due to its ability to absorb UV radiation and its light scattering properties, and for drug tablet coating.²⁹ Moreover, it is an abundant, low cost and biocompatible material.³⁰ In nature, the oxide is sourced from minerals. Mostly it is found in ilmenite, a titanium-iron oxide mineral ($FeTiO_3$).³¹ The most abundant natural form of TiO_2 is rutile mineral, but it also can be found as other polymorphs, for example anatase or brookite.³²

For DSC applications, anatase is widely used due to the photocatalytic activity. The photons in the visible light are in the energy range from ≈ 2 to ≈ 3 eV.³³ Anatase has a wide bandgap of 3.2 eV³⁴, which matches the photon energy in violet light. Rutile has a similar band gap of 3.0 eV, but it was shown that rutile-based DSC had lower photocurrent compared to anatase. The dye adsorption properties are lower for rutile, which plays an important role in DSC functioning. Due to the bigger size of its nanoparticles, a smaller surface area for rutile was observed than that of anatase.³⁵ Brookite is rare compared to anatase and synthetic brookite is challenging to prepare. Thus, it is not considered for DSC applications.³⁶

The efficiency of DSC depends on the dye load on the semiconductor. Porous titanium dioxide crystals offer a high surface area, which maximizes the dye amount.³⁷ The TiO₂ layer is transparent and has a low light harvesting capability (Figure 1.6a).³⁷ To increase the light scattering, an opaque layer is usually added on the top of the TiO₂ surface and nowadays commonly used for commercial electrodes (Figure 1.6b). The light scattering layer is uneven compared to the TiO₂ without opaque layer and increases the semiconductor thickness (Figure 1.7).

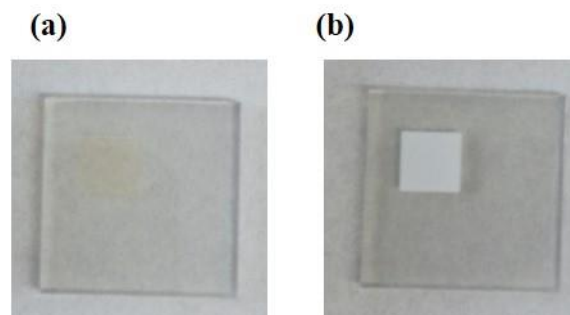


Figure 1.6. (a) TiO₂ electrode (due to its transparency, the metal oxide is barely visible); (b) TiO₂ electrodes with opaque layer.

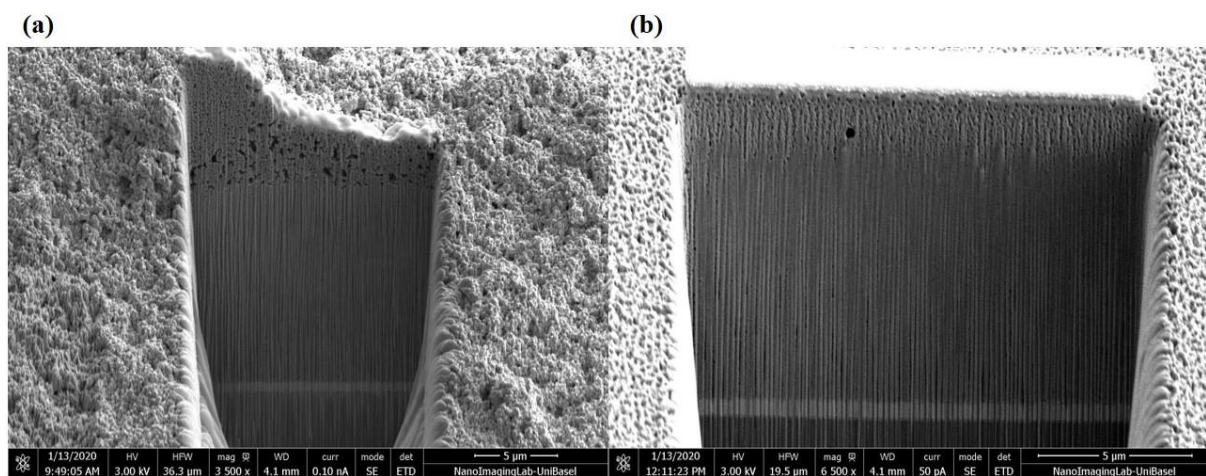


Figure 1.7. FIB images of TiO₂ electrodes; (a) opaque electrode; (b) transparent electrode. The images were provided by Sven Freimann, the operator of the instrument was Daniel Mathys from NanoImagingLab-UniBasel.

First Chapter

Zinc oxide has similar physical properties as well as band gap, but a higher electron mobility compared to TiO₂. However, the efficiencies of DSCs with ZnO as the semiconductor are still lower than those for TiO₂. ZnO-based DSCs suffer from fast recombination. There is a strong electrostatic interaction between the injected electrons (e^-_{inj}) and oxidized form of the dye (S^+) on the ZnO surface, which leads to the formation of a complex $[S^+e^-_{inj}]$.³⁸ This complex can recombine or dissociate into S^+ and a mobile electron in the semiconductor.³⁹ Formation of the $[S^+e^-_{inj}]$ complex causes fast charge recombination and decreases the electron mobility.^{24, 38} Moreover, DSCs based on ZnO suffer from electron trapping and optical reflection.⁴⁰

Tin(IV) oxide has a larger band gap of 3.6-3.8 eV compared to TiO₂. It is a promising alternative to titanium dioxide but suffers from weak adsorption of dyes with acidic anchoring groups.²⁸ Moreover, the recombination of electrons from CB with the oxidized dye result in a loss in current.²⁸

1.4.3 Sensitizer

As it derives from the name dye-sensitized solar cell, the sensitizer (or dye) is of key importance in the cell. The dye is responsible for the light absorbance and the electron injection into the semiconductor (see Working principle of DSC, section 1.4.1). Thus, a dye needs to have a broad absorption range with a high extinction coefficient. Ideally, it should cover the whole UV-Vis part of the solar spectrum and even the near IR region as it will make the absorbance of photon flux most effective. As shown in Figure 1.1 (DSC structure), the energy level of the excited state of the dye must be higher than the conduction band energy for the efficient electron injection. On the other hand, the oxidized-state energy level needs to be more positive than the redox potential of the electrolyte for a successful dye regeneration.⁴¹ Another requirement is the general photo- and thermal stability of the sensitizer.

In addition to these aspects, the dye needs to be anchored to the semiconductor. Dye molecules can be adsorbed (chemisorption and physisorption) on the semiconductor surface *via* several mechanisms including covalent bonding, hydrogen bonding, electrostatic interaction or van der Waals forces.⁴² Covalent bonding is the preferred way of attachment for DSC on the surface, since chemical bonding reduces the mobility of molecules.⁴³ Other types of interactions are reversible and lead to molecules being de-attached from the metal oxide. Various anchoring groups can be

implemented in dye structures for covalent bonding onto the semiconductor like carboxylic, phosphonic, and cyanoacrylic acids and their various derivatives (Figure 1.8).^{44, 45}

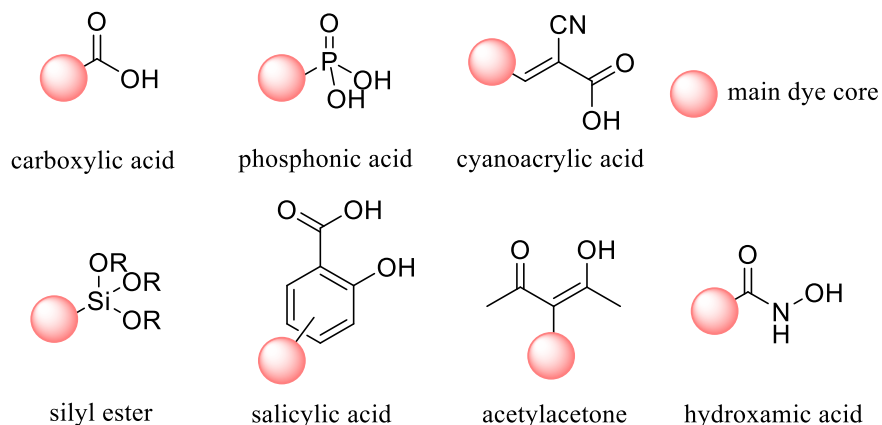


Figure 1.8. The several examples of anchoring groups for DSCs.

Anchoring groups like silyl ester, salicylic or hydroxamic acids are more rarely employed.^{44, 46, 47, 48} These groups show promising performances in individual cases, but not as commonly used as those shown at the top of Figure 1.8.

Several types of carboxylic acid chemisorption models at TiO_2 were identified, which are presented in Figure 1.9, and they depend on dye structure, pH, and metal oxide pretreatment.⁴⁴ The binding can be formed between Ti and O atoms directly as a monodentate ester, bidentate chelating, or bidentate bridging. Anchoring also can be created with a help of hydrogen bonds between the acid and the metal oxide. Despite the covalent bonding, dye molecules still can be desorbed from the metal oxide under basic conditions.

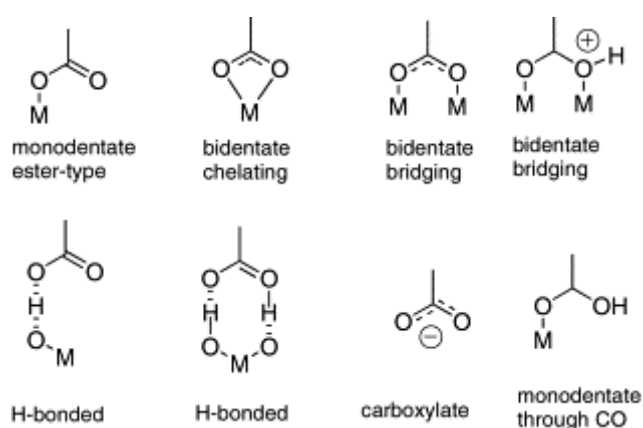


Figure 1.9. Possible binding models of carboxylic acid anchoring group to metal oxide semiconductor ($M = \text{Ti}$). Reproduced with permission from reference ⁴⁴.

Dyes can be separated in two groups – organic dyes and metal complexes. Organic or metal-free dyes offer a broad absorption range which goes to near IR region.⁴⁹⁻⁵⁴ Typically, these dyes have a push-pull structure, which means [donor]-[π -bridge]-[acceptor] architecture.⁵⁵ This design considers (for an n-type DSC), electron transfer from a donor group through a π -bridge (spacer) to an acceptor moiety, which is the anchor.⁵⁶ The donor groups often contain an arylamine or carbazole group, the spacer includes one or more thiophene rings.⁵⁶ Often the spacer bears alkyl groups, which prevent the dye aggregation on the surface and electron recombination. The common anchoring groups for organic dyes are cyanoacrylic acids.^{56, 57} Nevertheless, silyl esters and carboxylic acids are also actively used for organic dyes.^{46, 52, 58, 59} Some organic dyes are presented in Figure 1.10. Using the example of the LEG4 dye, the push-pull strategy for the dye design is illustrated. Among the others, porphyrin-based dyes show particularly remarkable light absorbance due to strong π - π^* electronic transitions.⁵⁴

Organic dyes show a photoconversion efficiency (PCE) up to 13% (PCE of 13% was achieved for porphyrin-based dye).⁵⁹⁻⁶¹ To increase the absorption range and, therefore, efficiency of a solar device, the co-sensitization of several dyes is commonly used, which allows the adsorption of more than one dye on the semiconductor. A successful example is the co-sensitization of the two organic dyes ADEKA-1 and LEG-4 (Figure 1.10), which led to a remarkable efficiency of 14% in the presence of the $[\text{Co}(\text{phen})_3]^{2+/3+}$ (phen = 1,10-phenanthroline) redox shuttle.⁵⁸ Another co-sensitization of the blue AP25 dye with the orange dye D35 (Figure 1.10) resulted in a photocurrent $<21 \text{ mA cm}^{-2}$ and a photoconversion efficiency of 8.0%, while AP25 alone affords 19.9 mA cm^{-2} and 6.8%, respectively. However, organic dyes can be co-sensitized not only with each other, but also with metal complexes. In 2017 it was shown that the combination of the organic dye SQ2 (Figure 1.10) with a heteroleptic copper(I)-based dye resulted in the panchromatic EQE spectra (for EQE see section 2.3) and a significant increase in the efficiency compared to single dye performance.⁶² Despite high and promising efficiencies, organic dyes still suffer from complicated and time-consuming synthesis, which increases their costs for potential commercial applications.

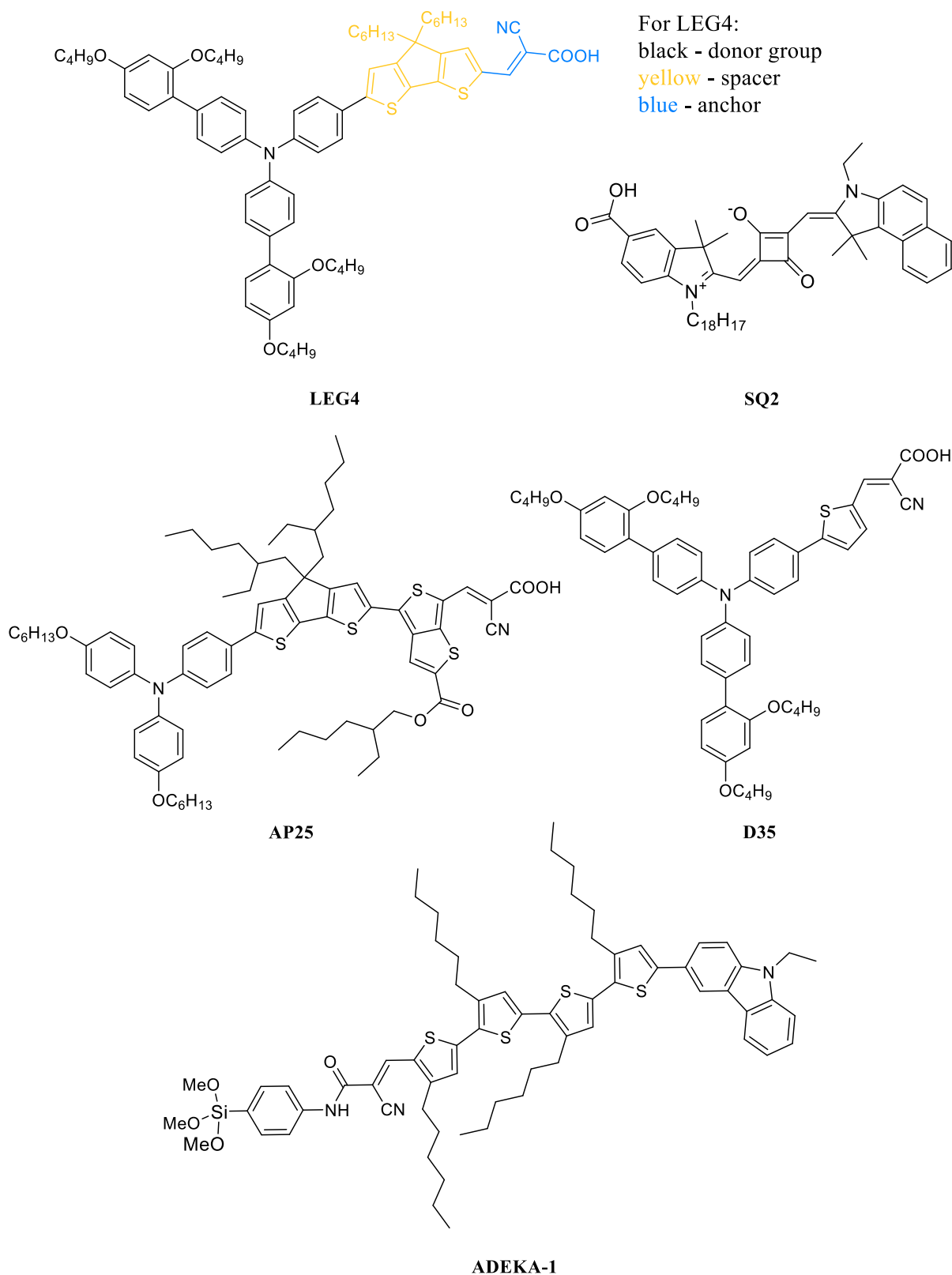


Figure 1.10. Examples of organic dyes. The LEG4 dye illustrates the push-pull strategy for the dye design.

Inorganic dyes or metal complexes were introduced by O'Regan and Grätzel in 1991 and since then, they have been widely used for DSC applications. The most common sensitizers with photoconversion efficiencies (PCE) of up to 11% are ruthenium-oligopyridine complexes

(Figure 1.11).⁶³⁻⁶⁷ Upon absorption of light, these dyes can provide an efficient metal-to-ligand charge transfer (MLCT) with a long lifetime and a low-energy excited state.⁶³ This results in efficient electron injection into the semiconductor. For example, the N3 dye published by Nazeeruddin *et al.* in 1993 reached a PCE of 10% and showed a broad range of absorption in combination with relatively long excited state lifetime.⁶⁸ The dye N719, which is the deprotonated version of N3, had shown a remarkable efficiency up to 11.18%.⁶⁹ In 2001, the black dye exceeded the performance of the N3 dye because of the panchromatic light absorption and nearly quantitative electron injection from the dye in the excited state into the semiconductor.⁶⁶ In 2017 it was shown that a derivative of the black dye exhibited the broad absorption to near IR region.⁷⁰

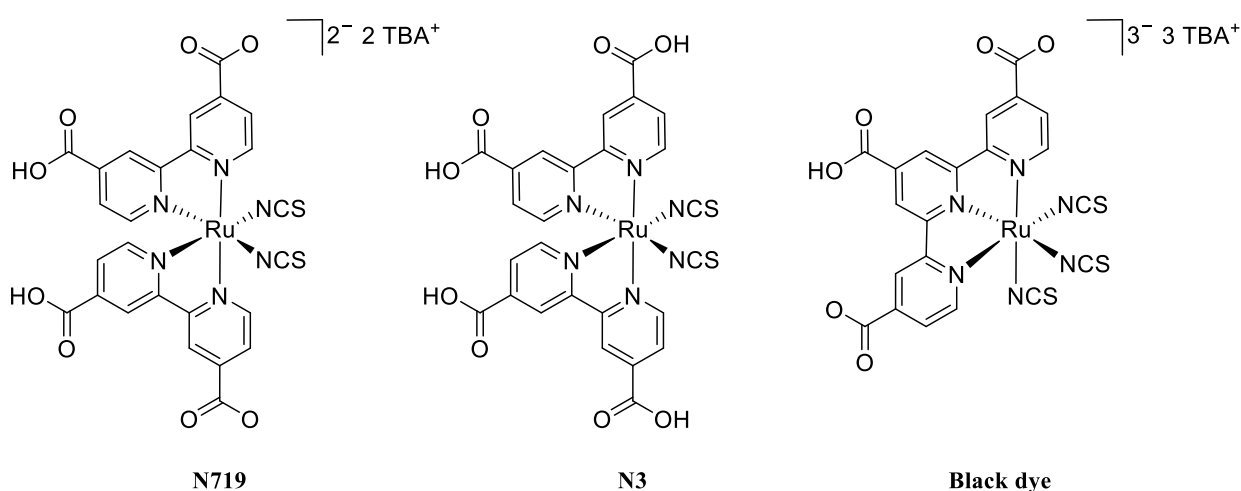


Figure 1.11. Common Ru-based dyes with PCE up to 11.18 %.

However, the use of metals with low natural abundancies like ruthenium significantly increases the cost and sustainability of DSCs.⁷¹ Therefore, the development of complexes with Earth abundant metals for DSC applications became of greater importance. One alternative are copper(I) complexes, which show promising photophysical characteristics similar to Ru(II) dyes.⁷² Copper(I)-complexes have a long lifetime of the MLCT excited state and show high absorption in the visible region of the solar spectrum. For the first time a copper(I) complex was employed in a DSC by J.-P. Sauvage *et al.* in 1994.⁷³ A bis(2,9-diphenyl-1,10-phenanthroline)copper(I) complex with carboxylate anchor on phenyl rings at *para* position, which was used in this work, had shown a broad absorption spectrum in the visible region, but low performance. However, it was shown that Cu(I)-complexes with a 6,6'-dimethyl-2,2'-bipyridine ligand core prove to be a promising alternative to ruthenium dyes.^{74, 75} These Cu(I)-dyes exhibited rather high potential (up to 566 mV for dye [Cu(I-1)₂]⁺, Figure 1.12) and remarkably high EQE (up to 50% for dye [Cu(I-2)₂]⁺).⁷⁶

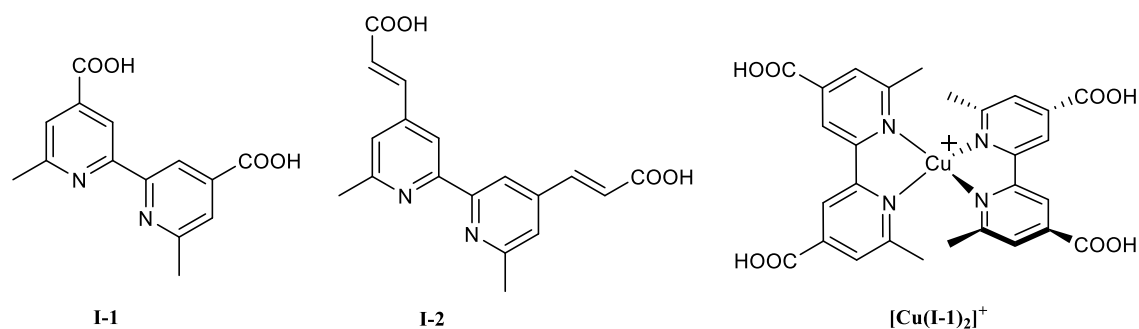


Figure 1.12. The structures of the 6,6'-dimethyl-2,2'-bipyridine ligands and the copper(I)-complex [Cu(I)₂]⁺.

The change from homoleptic to heteroleptic copper(I)-complexes offered an approach to push-pull design, which is commonly used for organic dyes. Typically, an ancillary ligand contains donor moiety, and an anchoring ligand contains carboxylic or phosphonic acid groups. The isolation of heteroleptic Cu(I)-complexes is not trivial since homo- and heteroleptic complexes are in equilibrium in the solution. Two synthetic strategies were developed for heteroleptic Cu(I)-complexes. The HETPHEN (heteroleptic bisphenanthroline complexes) requires the usage of sterically demanding ligands. These complexes have a broad absorption in the UV-Vis spectrum, but limited light harvesting efficiencies.⁷⁷ Another approach was designed by the Constable/Housecroft research group and includes the stepwise dye assembly on the surface (SALSAC - surface-as-ligand, surface-as-complex).^{78, 79} This approach will be discussed in detail in the Third Chapter, section 2. This strategy offers an unlimited number of combinations of ancillary and anchoring ligands for copper(I)-dyes.

The exploration of Earth abundant and low-cost metals brought iron complexes into the solar cell application. In 1998, the first DCSs based on a tris(2,2'-bipyridine)iron(II) complex were reported with a short-circuit current density (J_{SC}) of $290 \mu\text{A cm}^{-2}$.⁸⁰ The use of iron(II) complexes for DSC applications is challenging due to their fast deactivation from an MLCT to metal-centred (MC) state⁸¹, which results in inefficient electron injection and low J_{SC} values. In 2013, Wärnmark and co-workers⁸² published the first iron(II) *N*-heterocyclic carbene (NHC) complex I-3 (Figure 1.13) with an extended ³MLCT lifetime of 9 ps. Following from this, Gros and co-workers⁸³ fabricated the first series of iron-sensitized DSCs (complex I-4, Figure 1.13) with the best efficiency (0.13%) known at that time. Iron(II) NHC complexes will be discussed in detail in section 1.4.6.

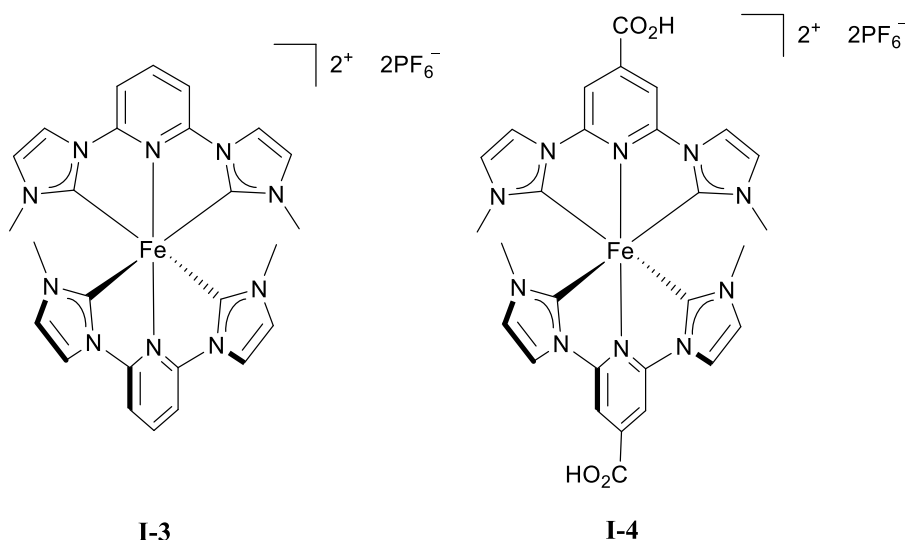
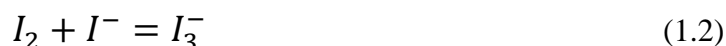


Figure 1.13. The structures of iron(II) NHC complexes I-3 and I-4.

1.4.4 Electrolyte

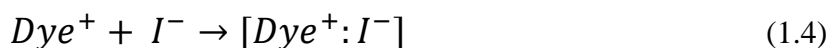
A conventional liquid electrolyte consists of a redox couple, a solvent and additives. The term 'additives' is used to encompass species such as ionic liquids (ILs), lithium salts (LiX) and various Lewis bases. The redox couple is one of the key constituents of a DSC and it ensures effective dye regeneration. One of the most common redox couple is the iodide/triiodide (Equation 1.2). In solution, triiodide is formed from iodine and iodide. It is also known that polyiodide species can be formed in case of high iodine concentration, but they are not of importance for dye regeneration.⁸⁴



The operation of a DSC is based on the effective dye regeneration after electron injection into the conduction band (CB, Equation 1.3) of the semiconductor, which is a multistep process.

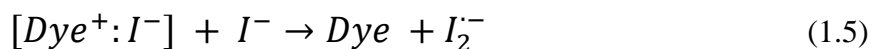


After the formation of oxidized species D^+ , the dye needs to be reduced by iodide *via* a dye-iodide complex (Equation 1.4).



The formation of this complex was studied for the example of the dye $Ru(dcbpy)_2X_2$ and considered to be crucial for the dye regeneration.^{85, 86} The addition of a second iodide ion results

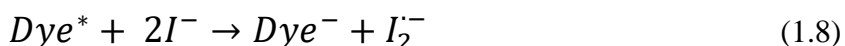
in complex dissociation and formation of the diiodide radical $I_2^{\cdot-}$ and a dye D in a ground state (Equation 1.5). Further, two radicals undergo disproportionation into iodide and triiodide (Equation 1.6).⁸⁴



The oxidized triiodide specie diffuses to the counter electrode, where it gets reduced to iodide (Equation 1.7).



According to Equation 1.5, dye regeneration depends upon the presence of iodide anions in the electrolyte solution. It is known that an increase in iodide concentration can be beneficial for DSC performance.⁸⁷ Wang *et al.* have shown that for solvent free electrolytes with ILs as media high iodide concentration is essential for the efficient dye regeneration.⁸⁸ On the other hand, it leads to undesired quenching of dye in the excited state (Equation 1.8).⁸⁸



Moreover, too high I^- concentration provokes the formation of ion-pairs, which have reduced mobility and, thus, less conductivity. This effect is especially present in gel electrolytes.⁸⁹ In addition, the iodide/triiodide redox couple has several drawbacks like absorption in the visible light and metal corrosion.^{90, 91}

The change of redox shuttle has a direct influence on the maximum possible potential of a DSC.⁹⁰ Thus, alternative redox shuttles based on metal complexes were developed. One of these newly developed systems is Co^{2+}/Co^{3+} . Cobalt-based electrolytes are commonly used for DSCs in combination with organic dyes.^{58, 92-94} Moreover, they had demonstrated a great potential with copper(I) dyes. It was shown that the more positive potential of Co^{2+}/Co^{3+} redox couples, compared to iodide/triiodide, exhibited higher PCE of copper(I)-sensitized DSCs.⁹⁵ Over the last years Cu^+/Cu^{2+} redox couples are intensively investigated. Their potential is also shifted more positive than I^-/I_3^- . Copper-based redox mediators have a broad use in combination with organic dyes, ruthenium, and copper sensitizers.⁹⁶⁻¹⁰¹

The oxidized form of the redox couple must subsequently diffuse to the counter electrode for reduction.¹⁰² The solvent must allow a fast diffusion of both components of the redox couple, needs to solubilize charged species, and should have a low vapour pressure for the long-term stability of cells. It has been shown by Han *et al.*¹⁰³ that the donor abilities of solvents scale with good performances of DSCs by enhancing the open circuit voltage (V_{OC}). Additives are mainly used to

tune the semiconductor conduction band energy¹⁰⁴ and for suppressing the rate of recombination of injected electrons from the semiconductor with the electrolyte. The most common additives used in electrolytes are based on guanidine or nitrogen-containing heterocycles, which can move the CB of a semiconductor towards negative potentials. This leads to a significant increase in V_{OC} .¹⁰⁴⁻¹⁰⁶ The presence of Li^+ ions also influences the CB due to their adsorption on the surface. This effect moves the CB towards more positive potentials, leading to efficient electron injection into the semiconductor, but also resulting in a decrease in V_{OC} .¹⁰⁷ It is generally recognized that addition of Li^+ ions improves the photocurrent with ruthenium dyes.¹⁰⁸ At the same time, it was shown that for copper(I)-based DSCs the presence of LiI is not beneficial.¹⁰⁹ Other common additives to electrolytes are ionic liquids, which could, potentially, substitute the organic solvent. Advantages of ILs are their thermal stability, high boiling point and ionic conductivity, which contribute to long DSC lifetimes. On the other hand, high viscosities or the fact that some ILs are solid at 298 K, are disadvantages. IL-based and solvent-free electrolytes have been thoroughly studied by many research groups. The work of Grätzel and co-workers¹¹⁰ demonstrates that high performing solar cells can be achieved with pure IL electrolytes. In 2008, they reported¹¹¹ promising device lifetimes indicating the future potential of ILs. The current challenge of using ILs as electrolyte media is their high viscosity, which results in less effective mass transport. The addition of a co-solvent helps to overcome these limitations and allows the use of ILs with high melting points. The most commonly employed ILs in electrolytes are imidazolium salts. ILs with an iodide counterion in combination with iodine lead to polyiodide structures. In 2015, it was reported that $C-H \cdots I-I-I$ and $\pi \cdots I-I$ interactions between these polyiodide anions and imidazolium cations cause a weakening of the I-I bonds resulting in a higher conductivity of ILs.¹¹² This effect can greatly contribute to the performance of the I^-/I_3^- redox shuttle and result in more efficient performance of a DSC.

1.4.5 Counter electrode

The counter electrode plays an important role in an n-type DSC operation as it reduces the oxidized redox mediator species. The counter electrode has a similar composition as the photoanode. It is made of glass covered with a FTO layer (Figure 1.14). On top of the FTO layer the catalyst is placed. Typically, the electrode is platinum-coated, and these electrodes are commercially available.

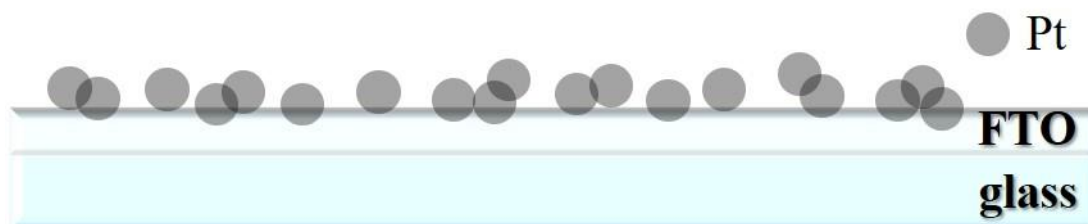


Figure 1.14. The composition of counter electrode.

However, Pt can be corroded over time in the presence of I^-/I_3^- .¹¹³ Furthermore, Pt increases the price of the device. These disadvantages created the need of Pt replacement and various substitutes were investigated in recent years. DSCs with carbon counter electrodes have shown a good stability over the period of twenty days.¹¹⁴ At the same time, the carbon particles can get detached from the electrode, thus generating dark current in the DSC.¹¹³ Conductive polymers such as poly(3,4-ethylenedioxythiophene) (PEDOT) also could be used.¹¹⁵⁻¹¹⁷ Usually, these electrodes are additionally doped with polystyrenesulfonate (PSS) or/and with cobalt sulfide.^{117, 118} Doping on the electrodes increases the conductivity, but the large size of PSS provokes low fill factor values (the fill factor will be discussed in section 2.2).¹¹⁸

1.4.6 Challenging aspects of iron(II)-complexes

As it was mentioned above, the efficient electron injection from the dye in the excited state into the semiconductor is of key importance for a well-performing DSC. The electron injection is strongly depended on the long-lived excited state of the dye. The fulfilment of this criterion among the others, which have already been discussed in the previous chapters, makes Ru-bipyridine complexes promising and high performing sensitizers. The ³MLCT state is the lowest excited state for most Ru(II) polypyridine complexes and exhibits a relatively long lifetime.¹¹⁹ A schematic representation of a ruthenium polypyridine complex in the excited state is shown in Figure 1.15a. The $[Ru(bpy)_3]^{2+}$ ($bpy = 2,2'$ -bipyridine) complex will be taken as an example for the following discussion. Despite the fact that $[Ru(bpy)_3]^{2+}$ has D_3 symmetry, the nitrogen lone electron pairs create an almost octahedral environment with the exception that N-Ru-N angles for *cis*-nitrogens are not equal to 90° .⁶³ Consequently, the octahedral symmetry will be considered for the discussion.

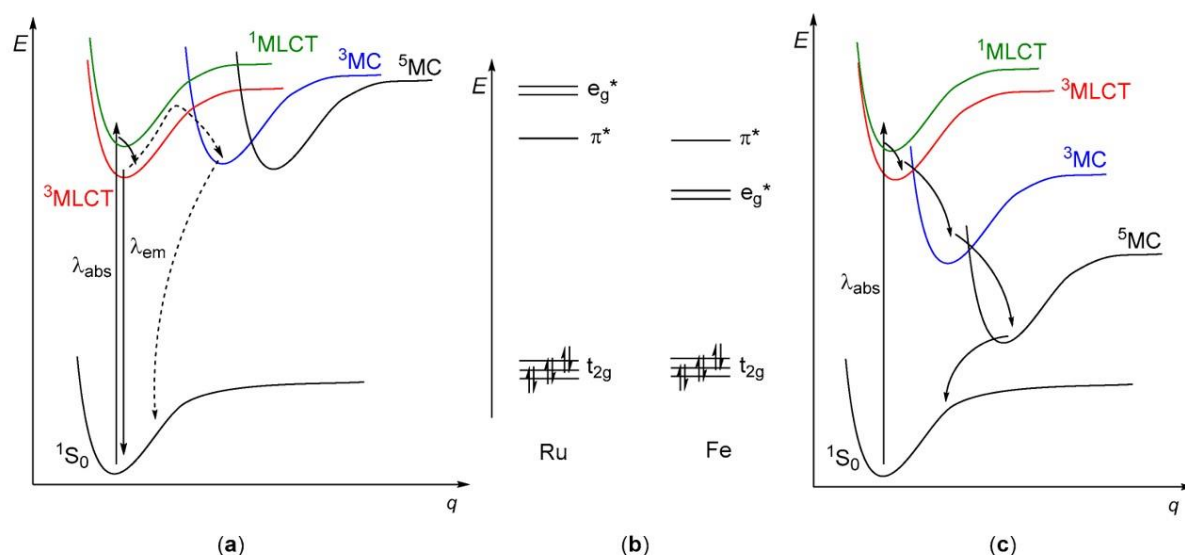


Figure 1.15 (a) Schematic illustration of the excited state for Ru polypyridine complexes (b) corresponding illustration of MO scheme for Ru and Fe polypyridine complexes (c) schematic illustration of the excited state for Fe polypyridine complexes. Solid lines represent electron movement, dashed lines represent the depopulation of MLCT states via MC states (the activation barrier must be overcome). Reprint from reference ¹²⁰. [CC BY 4.0 license, <https://creativecommons.org/licenses/by/4.0/>].

In the O_h environment the d -orbitals of $[\text{Ru}(\text{bpy})_3]^{2+}$ (as a 4d metal complex) will energetically split into t_{2g} and e_g^* orbitals that will be well separated from each other.¹²¹ Thus, the π^* orbitals of bpy ligands will be of lower energy than the e_g^* orbitals. This results in the lowest unoccupied molecular orbital (LUMO) having ligand character and the highest occupied molecular orbital (HOMO) having metal character (Figure 1.15b).⁶³ At the same time, metal centered (MC) states have similar or higher energy compared to the MLCT state. Therefore, the long-lived $^3\text{MLCT}$ state is a consequence of the activation barrier, which has to be overcome to populate MC states.¹²⁰

Compared to $[\text{Ru}(\text{bpy})_3]^{2+}$, the $[\text{Fe}(\text{bpy})_3]^{2+}$ complex has a weaker ligand field although it is strong enough to afford a low-spin complex.¹²¹ Thus, the π^* ligand orbitals are of higher energy than the e_g^* orbitals. This results in low-lying MC states, which provide rapid and nonradiative deactivation of the excited state.¹²¹ For the application in the photovoltaic field, a long-lived MLCT excited state has to be achieved for iron(II)-complexes. This can be done by increasing the energy of MC states or by lowering the MLCT states.¹²⁰

The complex design with near octahedral symmetry will lead to a stronger ligand field.⁸¹ The N-Fe-N *trans*-angles of 180° will maximize the overlap between the metal and the ligand, thus increasing the t_{2g} and e_g^* orbitals splitting. As it was shown by McCusker and co-workers, the combination of a polypyridyl ligand with strong π -acceptor properties and N-Fe-N *trans*-angles of 178.3° resulted in a stabilization of t_{2g} orbitals.¹²² Furthermore, Jakubikova and co-workers have shown in a computational study that the ligand field strength could be increased on going from

$[\text{Fe}(\text{tpy})_2]^{2+}$ to cyclometalated iron(II) complexes with donor abilities of the ligand (Figure 1.16).¹²³

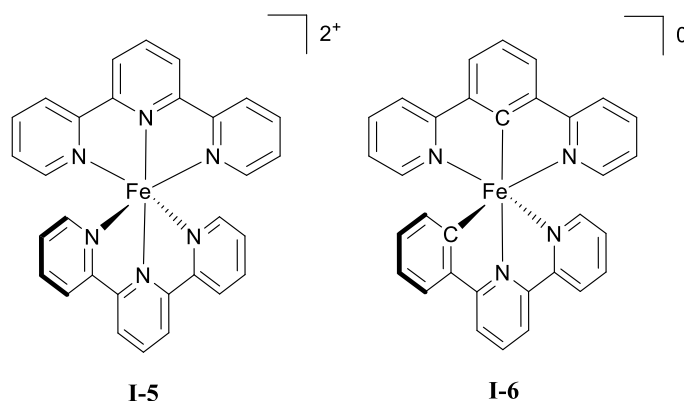


Figure 1.16. The structures of $[\text{Fe}(\text{tpy})_2]^{2+}$ and cyclometalated iron(II) complex.

The MC states could be destabilized by the ligands with strong σ -donor abilities. For example, *N*-heterocyclic carbene ligands offer this property. However, NHC compounds have limited π -acceptor possibilities.⁸¹ To compensate this shortage, Wärnmark and co-workers implemented a pyridine ring in the ligand I-7 design (Figure 1.17) for an iron(II) NHC complex.¹²⁴

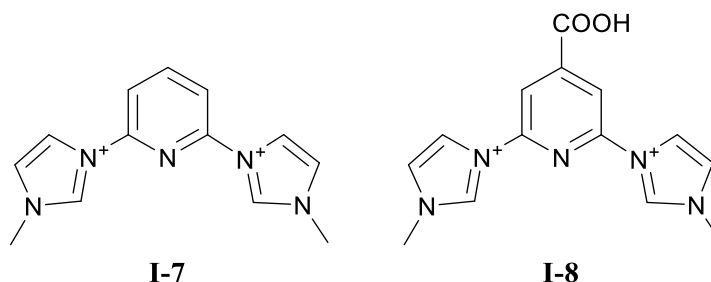


Figure 1.17. The structure of NHC ligand I-7 employed by Wärnmark and co-workers and of NHC ligand I-8 employed by Gros and co-workers for DSC manufacturing. The structures of corresponding iron(II) complexes are shown in Figure 1.13.

The iron(II) NHC complex I-3 (Figure 1.13) achieved a remarkable excited state lifetime of 9 ps (in MeCN at room temperature) compared to previously known iron(II)-complexes. Nevertheless, the complex must be connected on the semiconductor surface for DSC application. In 2015 two groups^{83, 125} independently published that the ligand with carboxylic acid functionality (Figure 1.17, structure I-8) contributed not only to the binding on the surface, but also significantly increased the excited state lifetime of the corresponding iron(II) NHC complex I-4 (Figure 1.13) to 18 ps.¹²⁵ It was shown by Wärnmark *et al.* that the LUMO level of complex I-4 lies above the CB of the TiO_2 , which is of importance for electron injection.¹²⁵ In the same work, the quantum yield of 92% for injection into TiO_2 was found. However, some of the injected electrons were rapidly recombined with the oxidized dye. The work from Duchanois *et al.*⁸³, which was reported in the same year, revealed by the use of time-dependent density functional theory (TD-DFT)

calculations that the electron-withdrawing abilities of carboxylic acid displaced the excited state electron density to the periphery of the ligand. Moreover, Persson and co-workers have shown in a computational study the rapid electron injection on ~ 100 fs time scale.¹²⁶

The absorption spectra of complexes I-3 and I-4 revealed two MLCT transitions in the visible region (in MeCN).⁸³ The one at higher energies ($\lambda_{\text{max}} = 380$ nm) includes the carbene unit and is the same for both complexes. For the complex I-3 the second transition which involves the pyridine ring is ≈ 450 nm. The complex I-4 which contains the COOH group has a red shift to $\lambda_{\text{max}} = 520$ nm. This shift is correlated to stabilization of the π -energy level of the ligand and was confirmed by the decrease of the HOMO-LUMO gap compared to I-3 which was found by quantum chemical calculations.¹²⁵

The DSCs sensitized with complex I-4 exhibited photoconversion efficiency of 0.13% and short-circuit current density of 0.41 mA cm^{-2} (the short-circuit current density will be explained in section 2.2).⁸³ It is important to note that the deprotonation of the non-anchored carboxylic group promoted the faster electron injection into the semiconductor.¹²⁷ The published PCE of the iron(II) dye I-4 was significantly lower compared to the N719 dye. However, these results have shown the potential of Fe(II) NHC dyes.

Further structural optimizations of Fe(II) NHC complex were published (Figure 1.18).¹²⁷ Interestingly, the absorption spectrum of complex I-9 with an extended π -system on the imidazole unit had only one MLCT transition, which was blue-shifted ($\lambda_{\text{max}} = 501$ nm) with lower extinction coefficient, compared to complex I-4. In terms of photovoltaic performance, dye I-9 revealed PCE of 0.03%. The poor performance was associated with fast recombination processes and inefficient interfacial charge separation.¹²⁷

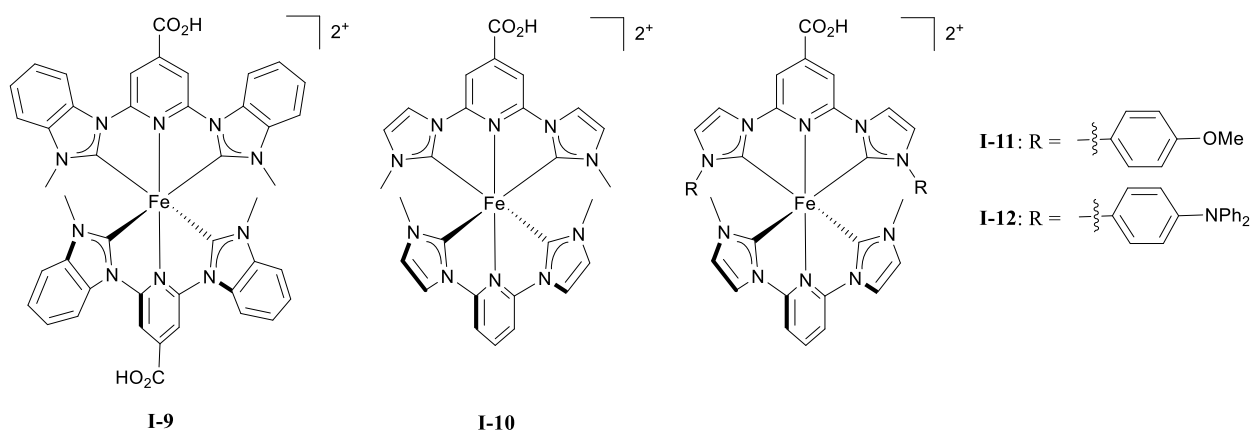


Figure 1.18. The structures of iron(II) NHC complexes; I-9 has an extended π -system; I-10 – I-12 are heteroleptic complexes with different substituents.

First Chapter

The heteroleptic complexes I-10 – I-12 all exhibited absorption spectra with three MLCT transitions (in MeCN). Two transitions are equal to those of complex I-4 ($\lambda_{\text{max}} = 380 \text{ nm}$ and $\lambda_{\text{max}} = 520 \text{ nm}$) and the third one ($\lambda_{\text{max}} = 430 \text{ nm}$) corresponded to a ligand without carboxylic acid. The dye I-12 displayed the characteristic $\pi-\pi^*$ transition in the triphenylamine group.¹²⁷ All three complexes revealed an improved charge separation. Despite different substituents on the imidazole moiety, a similar PCE of 0.10-0.11% was observed for all complexes. The poor performance of heteroleptic complexes was associated with low electron injection rates.¹²⁷

2. Materials and Methods

2.1 DSC manufacturing

The DSC manufacturing for cells described in this thesis consisted of four steps (Figure 1.19).

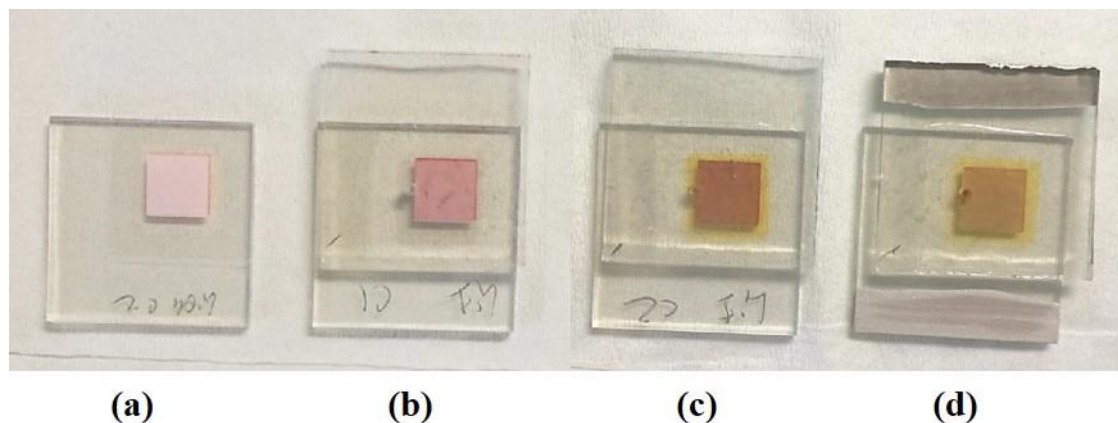


Figure 1.19. Four steps of DSC manufacturing. (a) the working electrode was sensitized with dye; (b) the working electrode was combined with the platinum counter electrode using hot-melt sealing foil; (c) the electrolyte was added via a pre-drilled hole in the counter electrode by vacuum back-filling. The hole was closed with a glass cap using sealing foil; (d) silver paste was applied on the edges of each electrode from the FTO side.

In the first step, the commercial working TiO_2 electrode (photoanode) was rinsed with water, EtOH and dried on a heating plate at $450\text{ }^\circ\text{C}$ for 30 min. Afterwards, the electrode was cooled to $60\text{ }^\circ\text{C}$ and immersed in the ligand or dye solution (dye bath). Further details of dye baths used in this study are shown in Table 1.1. After sensitizing with dye, the electrode was rinsed with a solvent used in the dye bath and dried with nitrogen flow (Figure 1.19a).

Table 1.1. The composition of dye baths used in this study.

| Dye bath composition | Section in the thesis ¹ | Solvent | Concentration | Dipping time |
|--|-------------------------------------|---------|-------------------|-------------------------------------|
| N719 | Reference dye throughout the thesis | EtOH | 0.30 mM | overnight ($\approx 16\text{ h}$) |
| Iron(II) NHC (I-4) / cheno | 3.1 – 3.4 | MeCN | 0.50 mM / 0.10 mM | overnight ($\approx 16\text{ h}$) |
| 4-([2,2':6',2''-terpyridin]-4'-yl)phenyl)phosphonic acid | 2 | DMSO | 1.0 mM | overnight ($\approx 16\text{ h}$) |
| FeCl_2 | 2 | EtOH | 0.5 mM | overnight ($\approx 16\text{ h}$) |

| | | | | |
|---|---|---------|--------|------------|
| 4'-phenyl-2,2':6',2''-terpyridine (Phtpy) | 2 | Acetone | 0.1 mM | three days |
| [Fe(Phtpy) ₂] ²⁺ | 2 | Acetone | 0.1 mM | three days |

[†] Only in Third Chapter; cheno – chenodeoxycholic acid.

The commercial platinum counter electrode (photocathode) was washed and dried like the photoanode. Then anode and cathode were assembled together using thermoplast hot-melt sealing foil by pressing them together while heating (Figure 1.19b). Afterwards, the electrolyte was introduced into the DSC through a pre-drilled hole in the counter electrode *via* vacuum backfilling. The hole was sealed with hot-melt sealing foil and a cover glass (Figure 1.19c). Finally silver paint was applied on the edges of each electrode from the FTO side as a last step (Figure 1.19d).

2.2 *J-V* plots and solar simulator

The key characteristic of all solar cells is their photoconversion efficiency (PCE) or the solar-to-electrical energy conversion efficiency (η). This parameter can be extracted from the so-called *J-V* plot, which is recorded with a solar simulator. The solar simulator is an instrument which mimics the solar irradiation including intensity and spectral composition and allows testing solar cells in research laboratories under representative conditions. The international standard used for DSC measurements is 1 sun (1 sun = 100 mW cm⁻²) at 25°C under the air mass (AM) of 1.5G (G = global). AM is an important factor, which refers to the air mass coefficient. It describes the path length that the sunlight passes through the atmosphere between the Sun and global surface.¹²⁸ It is necessary to consider the AM coefficient, since the atmosphere may remarkably modify the solar spectrum that reaches the global surface (Figure 1.20).¹²⁸

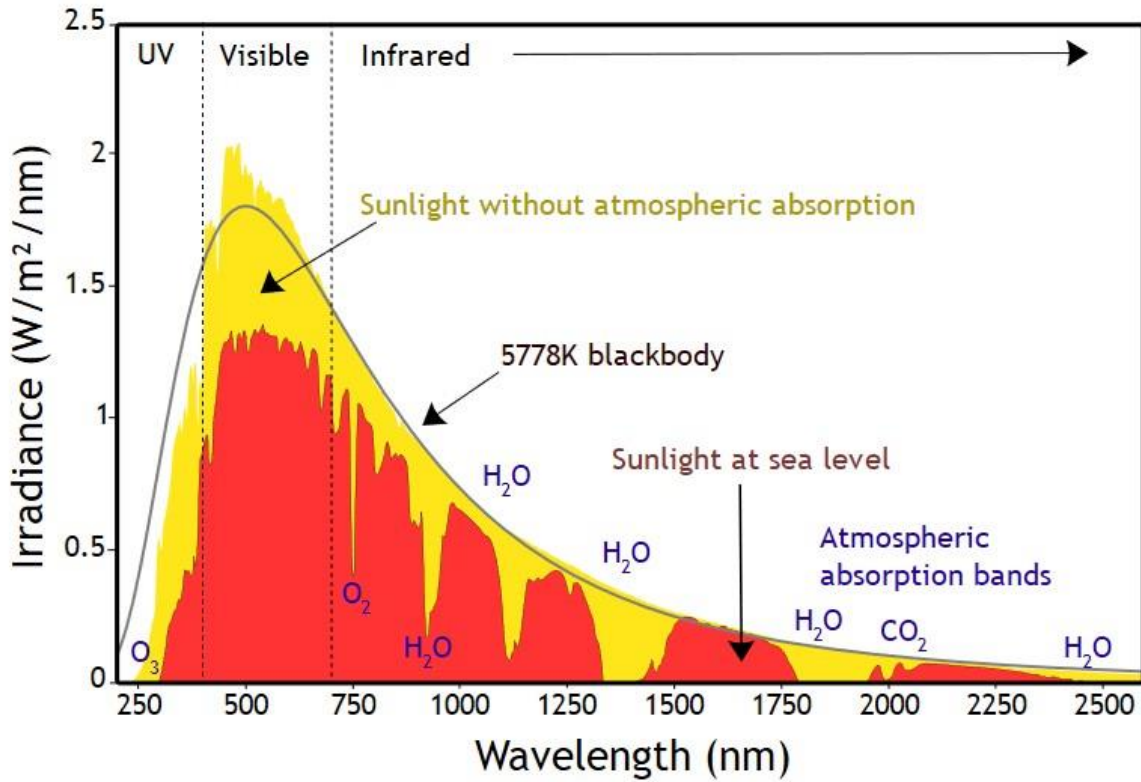


Figure 1.20. Solar irradiation spectrum [Credit: Nick84, CC BY-SA 3.0 license, <https://creativecommons.org/licenses/by-sa/3.0>].

In case that AM is zero, the Sun is in zenith and the sunlight does not have any interactions with the atmosphere. If light scattering and absorption are considered and the Sun is directly over sea level, the AM is defined as 1 (Figure 1.21). The international standard implies AM1.5G, where 1.5 equals the 1.5 longer sunlight path than the direct sun at the sea level and represents the zenith angle of 48.2° (Figure 1.22). G corresponds to global spectrum and includes light scattering and diffusion.

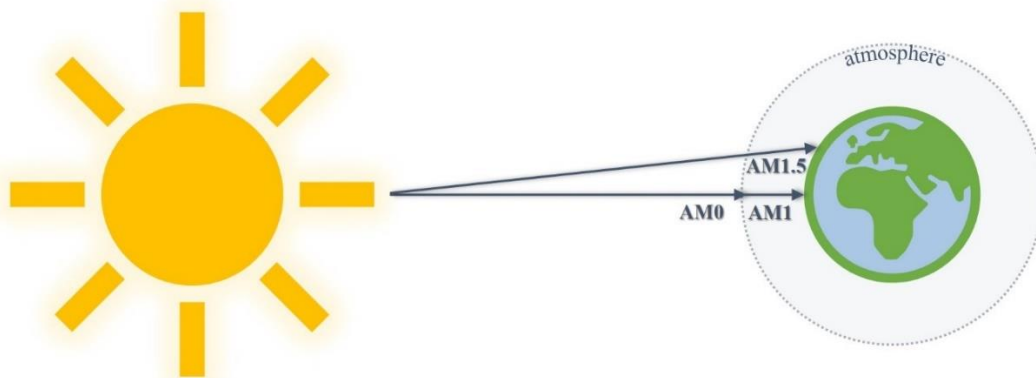


Figure 1.21. Schematic representation of AM coefficient [Redrawn from <https://g2voptics.com/solar-simulation/>].

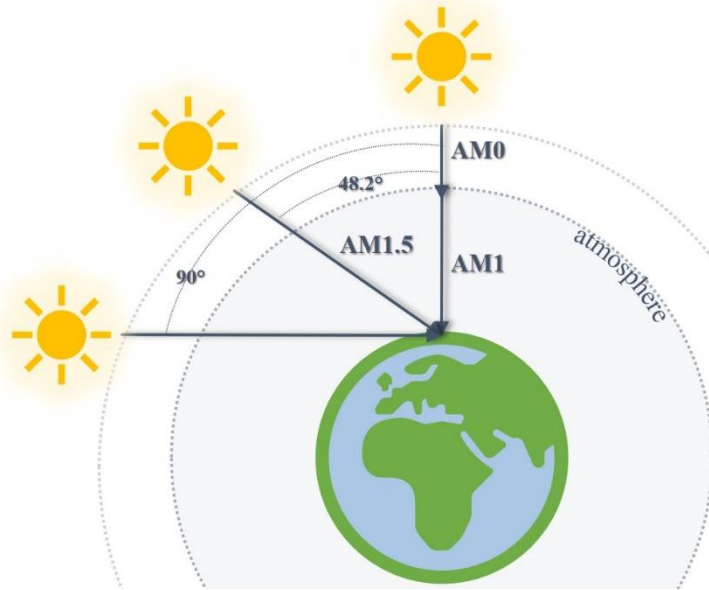


Figure 1.22. Schematic representation of AM dependency on zenith angle [Redrawn from <https://g2voptics.com/solar-simulation/>].

Therefore, the irradiance of the solar simulator was calibrated before each measurement sequence according to the discussed standard with a silicon reference cell. Afterwards, the DSC was preirradiated under the light for 20 min. Then, the cell was placed on the measuring table and connected to the potentiostat. The cell was covered with a black copper sheet mask, which was placed on top of the cell. The mask area was smaller than the solar cell surface. The remaining cell was covered with a black plastic cap to protect it from the light. Application of the full masking was necessary to avoid the performance overestimation.^{129, 130} It is important to note that not all DSCs measurements, which are reported in literature, were performed with mask application, since it significantly decreases the cell efficiency.¹³¹ In this case, a comparison between the reported performances is not accurate.

The cell measurement resulted in the so-called J - V plot. The J - V curve was obtained by applying the voltage range on the cell under the solar simulator. The current (I) output was measured and then converted into current density (J) according to Equation 1.9, where irradiated active area is the area of the cell, which is exposed under irradiance and is smaller than the actual surface of the cell as was discussed above.

$$J = \frac{I}{\text{irradiated active area}} \quad (1.9)$$

The typical J - V curve is shown in Figure 1.23. The plot is based on current density and potential axes and it includes several important parameters that are used for the analysis of DSC performance.

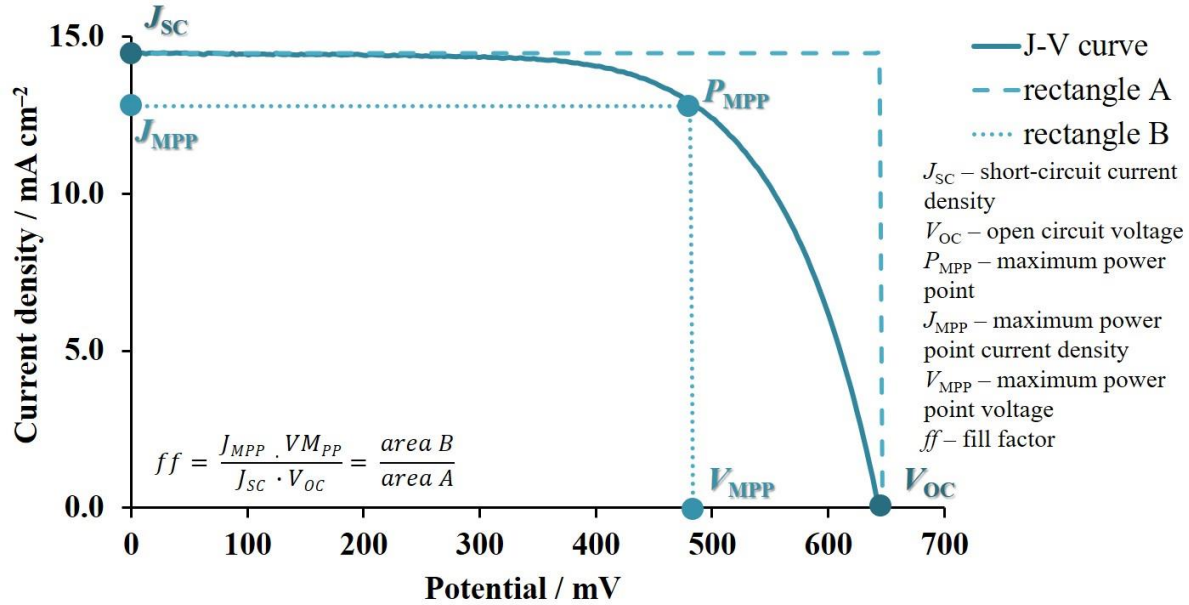


Figure 1.23. Typical J - V curve obtained under solar irradiation with the key parameters used for DSC analysis.

The short-circuit current density (J_{SC}) is the highest current that a DSC can generate when voltage is zero. In case no current passes through the cell, the highest possible voltage that can be obtained is called open circuit voltage (V_{OC}). These parameters define the area of the rectangle A (Figure 1.23) which gives the maximum theoretical power (P) of the cell. P can be achieved only if no losses occur during the cell operation. Rectangle B defines the area of maximum power point (P_{MPP}) of the cell. P_{MPP} can be obtained from maximum power point current density (J_{MPP}) and maximum power point voltage (V_{MPP}). Together, these parameters result in definition of the fill factor (ff), which is described in Equation 1.10.

$$ff = \frac{J_{MPP} \cdot V_{MPP}}{J_{SC} \cdot V_{OC}} = \frac{\text{area B}}{\text{area A}} \quad (1.10)$$

The fill factor is responsible for the shape of the J - V curve. In ideal case $ff = 100\%$ and the curve will repeat the shape of rectangular A. The value of ff is reduced by internal resistances like the shunt resistance (R_{SH}) and the series resistance (R_s) that occur in the DSC. The R_{SH} is defined as a slope of dark current versus applied voltage and should be infinite for an ideal cell.^{132, 133} The R_s includes the resistance in conducting electrodes, applied wires and connections, and results in a voltage drop. In an ideal DSC R_s should be zero.¹³³

Finally, all the parameters are used to determine the solar-to-electrical energy conversion efficiency (η) according to Equation 1.11:

$$\eta = \frac{J_{SC} \cdot V_{OC} \cdot ff}{P_{IN}} = \frac{P_{OUT}}{P_{IN}}, \quad (1.11)$$

where P_{IN} is the total incident solar power of the cell (1 sun at AM1.5G). Thus, J_{SC} , V_{OC} , ff and η are the parameters that will be broadly discussed in this thesis for comparison of DSCs performances between each other.

2.3 External quantum efficiency

The photocurrent of a DSC is determined by the quantum efficiency of light harvesting, electron injection and electron collection efficiencies.¹³⁴ The quantum efficiency (QE) of a cell involves two types of efficiencies – external quantum efficiency (EQE) and internal quantum efficiency (IQE).¹³⁵ EQE (or IPCE) is defined as the ratio between the number of electrons harvested by the solar cell and the number of incident photons (Equation 1.12).¹³⁶⁻¹³⁸

$$IPCE = \frac{\text{number of collected electrons}}{\text{number of collected photons}} \quad (1.12)$$

Monochromatic light of a predefined range of wavelengths is applied on the cell during the EQE measurement and the current output is detected at each wavelength. The current produced during the measurement is the product of the light harvesting efficiency (LHE), the charge collection efficiency and electron injection. Therefore, the spectral response will be different depending on the side (working or counter electrode) of cell, which was illuminated, since it will affect the light harvesting efficiency.¹³⁸ At the same time the usage of scattering layers can increase the LHE for DSCs.¹³⁹

The EQE spectra can be used for short-circuit current estimation. If the incident light is calibrated to 1 sun, the EQE current can be integrated according to Equation 1.13 to give J_{EQE} :

$$J_{EQE} = \int_{near\ UV}^{near\ IR} EQE(\lambda) \cdot e \cdot \Phi_{in} d\lambda, \quad (1.13)$$

where Φ_{in} is the incident photon flux and e is the electron elementary charge.¹³⁸

The typical EQE curves is shown in Figure 1.24. The maximum EQE value is found at the particular wavelength in the defined region and specified as percentage.

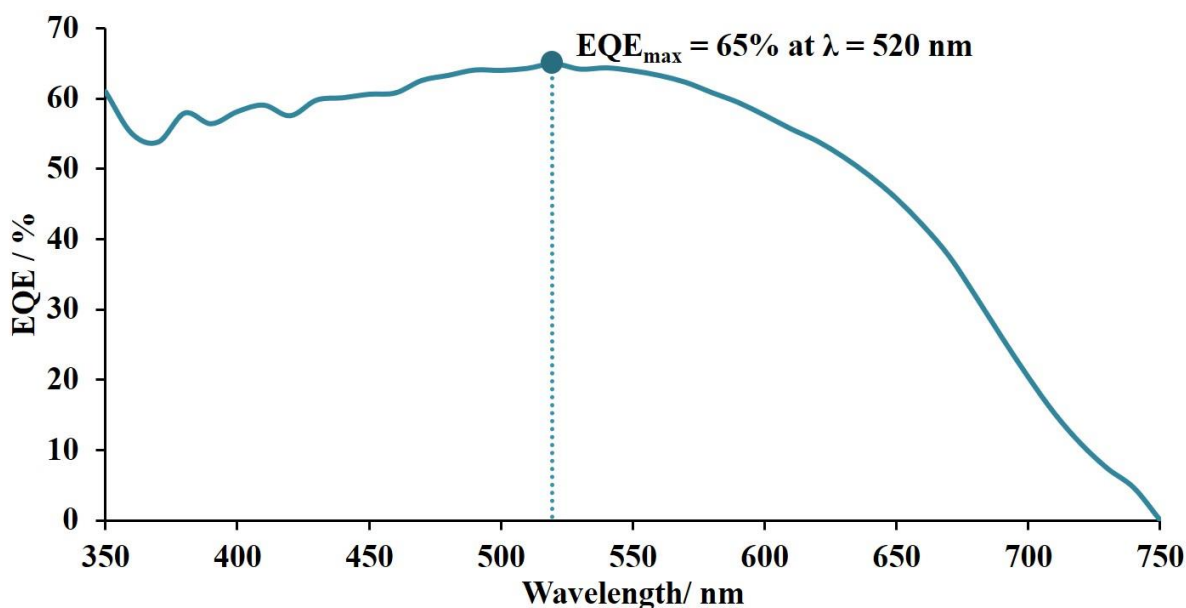


Figure 1.24. The typical EQE curve with EQE_{max} value.

In our study EQE was measured in the working range of DSCs between 350-740 nm.¹³⁷

2.4 Solid state UV-Vis spectroscopy

Solid state UV-Vis spectroscopy (ssUV-Vis) is a measurement technique that provides an absorption characteristics of the dye, which was sensitized on the semiconductor surface. Transparent working electrodes without scattering layer are used for the measurements, since the light has to pass through the sample to the detector. Partially the light is absorbed by the glass electrode and therefore the baseline measurements are required for the correct data interpretation. The baseline measurement is done with the transparent working electrode, which was not functionalized with a dye.

The typical UV-Vis measurements in solution are concentration-dependent and the Beer-Lambert law is used to calculate the extinction coefficient which is a characteristic property of the compound. In case of ssUV-Vis the amount of dye adsorbed on the surface depends on the dye bath concentration and the sensitization time. Thus, concentration is no longer meaningful for a solid-state sample and arbitrary units of absorbance are used accordingly. Moreover, ruthenium dyes are commonly used as standards for spectra comparison as their performance is known in the literature. In this study, N719 dye was used as a standard for ssUV-Vis with 0.3 mM dye bath concentration and overnight sensitization.

2.5 Electrochemical impedance spectroscopy

Electrochemical impedance spectroscopy (EIS) is a well-known technique used for studying electrical properties of different materials.^{140, 141} A DSC has a complicated structure involving multiple interfaces at which many electronic processes take place simultaneously. In contrast to resistance, impedance is not limited to one circuit element and can therefore be used to describe the system as a more complex and general circuit. EIS is based on the application of a small alternating current (AC) perturbation (\tilde{V}) at a fixed frequency (f) over a sample in equilibrium at stationary bias.¹⁴² The impedance at a specific frequency is denoted $Z(f)$ and can be presented as the product of \tilde{V} and \tilde{I} , where \tilde{I} is an AC modulation (Equation 1.14):

$$Z(f) = \frac{\tilde{V}}{\tilde{I}} \quad (1.14)$$

The impedance can be seen as a frequency dependent differential resistance of the I - V curve, because of the small amplitude of the AC voltage modulation (Figure 1.25).¹³⁴ For the full impedance spectrum, a measurement is made in a frequency range from Hz to kHz.

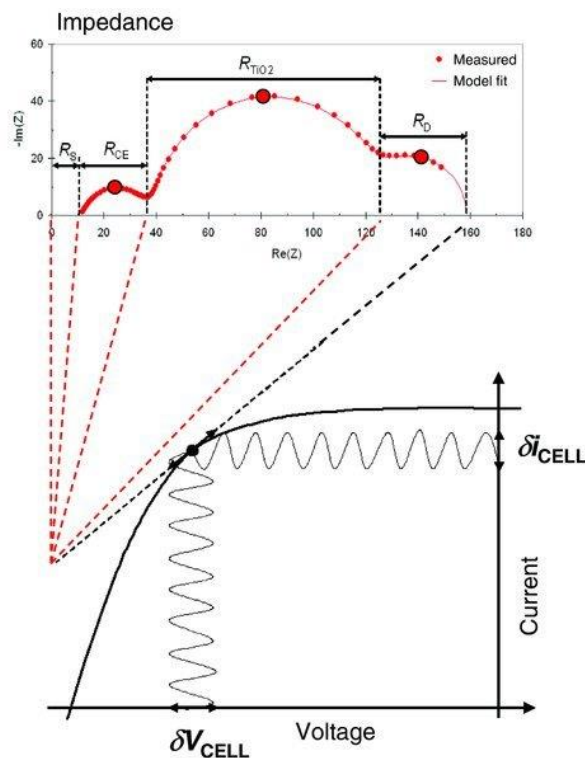


Figure 1.25. Schematic representation of the relationship between a I - V plot and its differential resistances measured by EIS. Individual differential resistance components of the I - V curve appear as separate impedance arcs due to their different characteristic frequencies. Reproduced with permission from reference ¹³⁴.

EIS results are typically presented in Nyquist and Bode plots, fitting of which results in parameters including a series resistance (R_s), a resistance (R_{Pt}) and capacitance (C_{Pt}) of a counter electrode, recombination resistance (R_{rec}), chemical capacitance (C_{μ}) and diffusion resistance of charge carriers in an electrolyte (R_d). Impedance plots include the real (Z') and imaginary (Z'') parts. Classically, a Nyquist plot consists of three semicircles at open circuit potential (Figure 1.26a). The high frequency region before the beginning of the curve depicts the series resistance. The first semicircle at high f is associated with the counter electrode, the second semicircle with the semiconductor-electrolyte interface, and the last semicircle at low f with the diffusion of the electrolyte. The resistance value can be estimated by the width of the arc along the abscissa.¹⁴³ The Bode plot provides an important representation of resistances from the plateaus (Figure 1.26b). The electron lifetime (τ) is a critical parameter, which is inversely proportional to the maximum frequency (f_{max}), and can be extracted from the Bode plot.¹⁴⁴

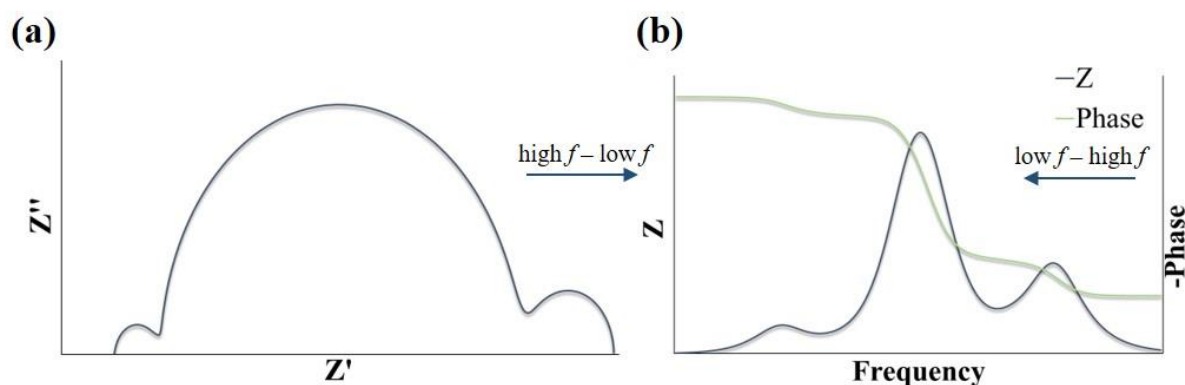


Figure 1.26. (a) Nyquist plot representation; (b) Bode plots representation.

EIS spectra can be recorded with different irradiation intensities, circuit conditions and frequency ranges. Under carefully chosen conditions a significant number of essential processes can be distinguished according to the spectral shapes of an impedance response, including electron transport in the TiO_2 , electron recombination at the TiO_2 -electrolyte interface and charge transfer at a counter electrode.¹⁴⁵ Data extracted from J - V curves can be explained in more detail with the help of EIS. For example, EIS parameters including the recombination resistance, chemical capacitance, transport resistance and diffusion length contribute to the value of J_{SC} for a DSC. This allows for a more precise explanation about the limiting factors of the DSC performance. Many studies have been reported in order to investigate the correct interpretation of EIS results.¹⁴⁶⁻¹⁵¹

For the fitting of the experimental EIS data, the equivalent circuit model 1 was used (Figure 1.27). This circuit model 1 consists of five elements and includes a series resistance (R_s), a resistance (R_{Pt}) and a constant phase element (CPE_{Pt}) to model a counter electrode, an extended distributed

element (DX1) to represent the mesoporous TiO₂/electrolyte interface as a transmission line model, and a Warburg short element (Ws), which represents the diffusion of the electrolyte. The transmission line model is broadly used for the fitting of DSCs impedance plots. The constant phase element is employed because of the roughness of the surface.^{140, 152}

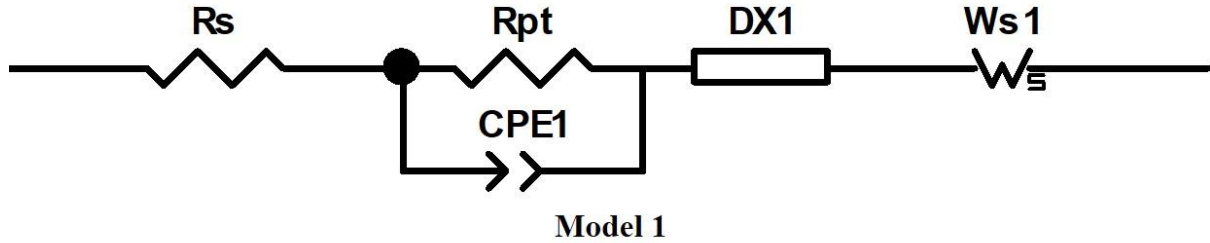


Figure 1.27. The equivalent circuit model used in this study.

The chemical capacitance was calculated according to Equation 1.15, where Q is a pre-factor of CPE and α is an empirical constant.

$$C_{\mu} = (R_{rec}^{1-\alpha} Q)^{1/\alpha} \quad (1.15)$$

The diffusion length (L_d) was calculated according to Equation 1.16, where d is the thickness of the semiconductor.

$$L_d = d \sqrt{\frac{R_{rec}}{R_{tr}}} \quad (1.16)$$

The electron lifetime (τ) was calculated according to Equation 1.17.

$$\tau = R_{rec} C_{\mu} \quad (1.17)$$

Second Chapter

The content in this chapter has been published.³ Part of this study was performed with the help of Wahlpraktikum student Maria-Sophie Bertrams.

1. Motivation

The sandwich-type structure of the DSC makes the manufacturing process undemanding under laboratory conditions but results in the need for reproducible measurements for acceptable DSC characterization. This is a challenge when cells are made by different members of the research group. Electrochemical impedance spectroscopy offers the possibility to study complex electronic systems and is commonly used for investigating the interfacial processes in solar cells. There is a tendency in the literature for researchers to present impedance data only for one representative device, that leads to discussions of the data without confirmation that the data are reproducible. At the same time, as current density-voltage plots illustrate, measurements can vary within one set of DSCs with identical components. In this chapter, multiple DSC impedance measurements are presented on “identical” devices prepared using two commercial dyes (one metal-free dye and one ruthenium(II) dye). A statistical analysis regarding the reproducibility of the DSCs is presented.

2. Introduction

To the best of our knowledge, there is no discussion in the literature of how reproducible EIS results for DSCs are. Usually, published data refer only to one measured cell. It is a common, but by no means universal, practice for current density-voltage measurements to be presented in the literature for two or more cells. A reproducibility study of DSCs with the standard dye N719 showed only a small deviation in η of $5.76 \pm 0.14\%$.¹⁵³ In order to broaden this investigation to gain insight into the reproducibility of EIS measurements for DSCs, we performed impedance analysis of DSCs functionalized with the two commercially available dyes, N719 and SQ2. The Nyquist profiles are considerably different for N719 and SQ2 (Figure 2.1)^{62, 154, 155} and in this paper we examine the impedance reproducibility for DSCs sensitized with a metal complex and an organic dye.

³ M. Becker, M.-S. Bertrams, E. C. Constable, C. E. Housecroft, *Materials* **2020**, *13*, 1547.

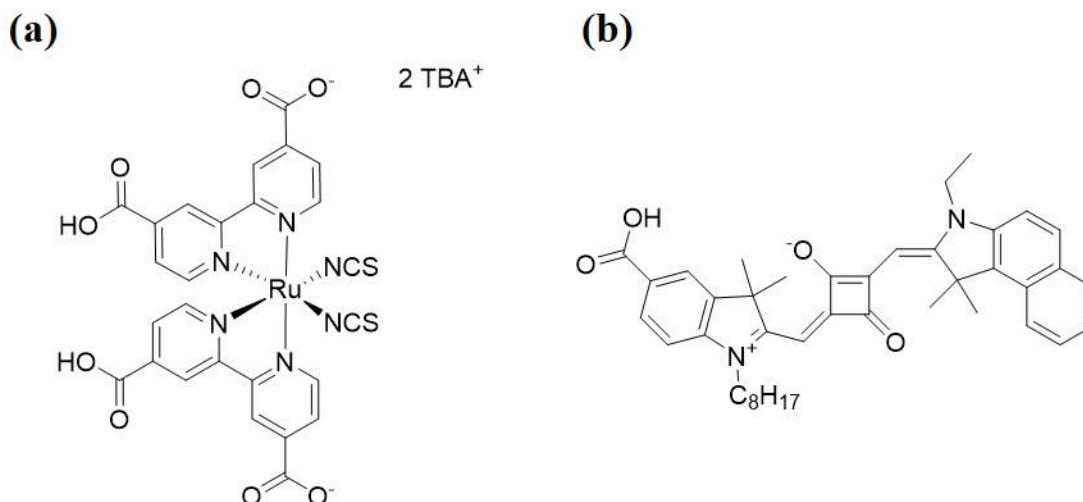


Figure 2.1. (a) Structure of N719, where TBA – tetra-n-butylammonium; (b) structure of SQ2.

3. Results

DSC fabrication is described in the First Chapter, Part 2. The dipping time of the working electrodes for N719 in the dye bath containing the dye (0.3 mM in EtOH) was 16 h and for SQ2 (0.1 mM in CH₂Cl₂) was 1 h.¹⁵³ The electrolyte contained the I₃⁻/I⁻ redox shuttle and had a composition of 0.1 M LiI, 0.05 M I₂, 0.5 M 1-methylimidazole and 0.6 M 1-butyl-3-methylimidazolium iodide in 3-methoxypropionitrile for both N719 and SQ2.

3.1 Effect of the pre-irradiation of DSCs

In order to study the reproducibility of the EIS experiments, we measured two sets of DSCs with dyes N719 and SQ2. For the fitting of the N719 set, we used the equivalent circuit model 1 (Figure 2.2a). This circuit model 1 consists of five elements and was described in detail in First Chapter. Unfortunately, model 1 is not always suitable. In the case of the SQ2 set, a simplified equivalent circuit model is needed (model 2), which does not have a DX1 element (Figure 2.2b). Instead, elements R1 and CPE1 model a recombination charge transfer resistance and chemical capacitance. The usage of model 1 will result in extremely high transport resistance values, which will be greater than recombination resistance. This effect shows that transmission line model cannot be used. For realistic comparison between N719 and SQ2-based DSCs, we also used model 2 for fitting the DSCs with N719 dye. Thus, we can compare the reproducibility of sets with

two different dyes and the reproducibility of EIS experiments in terms of two models – circuit model 1 and circuit model 2 in the case of the N719-based DSCs.

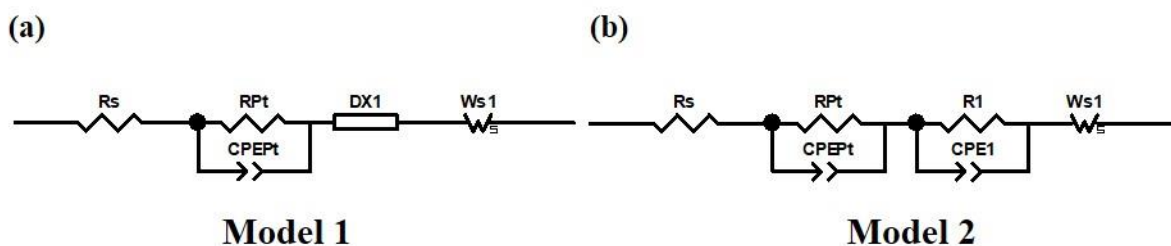


Figure 2.2. The two different equivalent circuit models used in this study: (a) The equivalent circuit model 1 used for fitting N719 sensitized DSCs; (b) the equivalent circuit model 2 used for fitting DSCs with N719 or SQ2 as sensitizer.

Our first goal was comparing and understanding the reproducibility of the DSCs during EIS measurements. It is known that the J - V performance and PCE are dependent on the pre-irradiation of DSCs before measurements.¹⁵⁶ In 2013, Nguyen *et al.* published a work where they performed light stress EIS measurements within a period of 6 to 175 hours.¹⁵⁷ It was shown that impedance spectra significantly changed depending on the time under irradiation. Thus, we decided to test if a pre-irradiation of cells is also beneficial for EIS. We measured two DSCs with N719 and two with SQ2. The experiments were performed directly after fabrication of the DSCs without pre-irradiation (WOPI) and each DSC was measured 5 times with a break of 15 minutes between measurements. Then, in the same manner, we measured the same DSC after pre-irradiation (API) of 15 minutes with the light intensity of 1 sun at 1.5 AM (100 mW cm^{-2}). The J - V parameters with and without pre-irradiation are shown in Table 2.1, Figure 2.3. Between the EIS experiments, the DSCs were kept under ambient light.

Table 2.1. J - V parameters for DSCs with N719 and SQ2 dyes WOPI and API. All DSCs were masked.

| DSC | $J_{sc} / \text{mA cm}^{-2}$ | V_{oc} / mV | $ff / \%$ | $\eta / \%$ |
|------------------|------------------------------|----------------------|-----------|-------------|
| N719 WOPI cell 1 | 14.64 | 622 | 68 | 6.17 |
| N719 WOPI cell 2 | 12.84 | 603 | 69 | 5.33 |
| N719 API cell 1 | 14.62 | 621 | 66 | 6.04 |
| N719 API cell 2 | 12.70 | 613 | 67 | 5.24 |
| SQ2 WOPI cell 1 | 1.07 | 465 | 70 | 0.35 |
| SQ2 WOPI cell 2 | 1.67 | 480 | 71 | 0.57 |
| SQ2 API cell 1 | 1.74 | 477 | 71 | 0.58 |
| SQ2 API cell 2 | 2.17 | 489 | 72 | 0.77 |

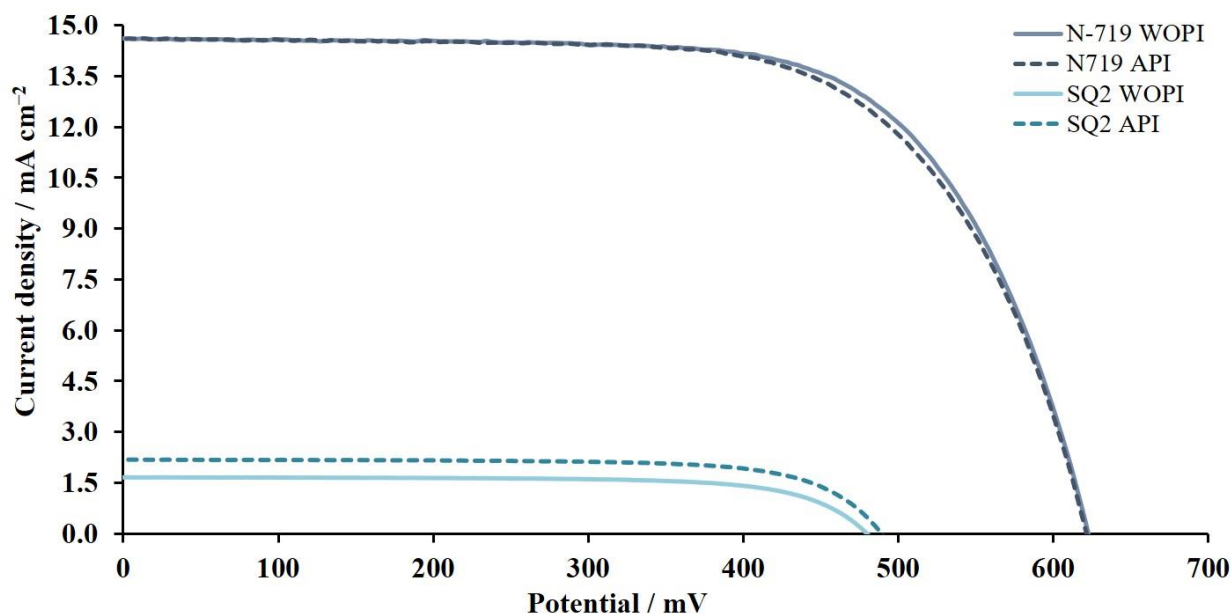


Figure 2.3. *J-V* curves for dyes N719 (blue) and SQ2 (green) measured without pre-irradiation (WOPI) and after pre-irradiation of 15 minutes (API).

According to the data in Table 2.2, the time at which the EIS measurements are made after building the DSC has an impact on the impedance measurements. We observed that DSCs with SQ2 were more affected by the waiting time before the measurement than N719-based cells.

Table 2.2. The EIS parameters for DSCs with N719 and SQ2 dyes. The DSCs were measured without pre-irradiation.

| DSC ¹ | R_{rec} / Ω | $C_{\mu} / \mu\text{F}$ | τ / ms | R_d / Ω | R_s / Ω | R_{Pt} / Ω | $C_{Pt} / \mu\text{F}$ |
|------------------|--------------------|-------------------------|--------------------|----------------|----------------|-------------------|------------------------|
| N719 WOPI 0 min | 26 | 845 | 22 | 11 | 15 | 7 | 4 |
| N719 WOPI 15 min | 22 | 905 | 20 | 11 | 13 | 8 | 4 |
| N719 WOPI 30 min | 19 | 955 | 18 | 10 | 13 | 8 | 4 |
| N719 WOPI 45 min | 22 | 981 | 22 | 10 | 12 | 8 | 5 |
| N719 WOPI 60 min | 22 | 970 | 21 | 10 | 12 | 8 | 5 |
| SQ2 WOPI 15 min | 185 | 18 | 3 | 15 | 12 | 32 | 9 |
| SQ2 WOPI 30 min | 136 | 20 | 3 | 11 | 12 | 23 | 6 |
| SQ2 WOPI 45 min | 107 | 22 | 2 | 11 | 11 | 20 | 6 |
| SQ2 WOPI 60 min | 94 | 23 | 2 | 10 | 11 | 19 | 5 |

¹ The DSC SQ2 WOPI 0 min was not fitted due to high resistance values, which resulted in a high error of the fitting.

For N719, R_{rec} was only slightly affected by standing for four periods of 15 minutes (hereafter, referred to as 60 minutes) after cell fabrication and the values changed only from 26 to 22 Ω . On the other hand, the values of C_{μ} changed from 845 to 970 μF , τ values were only slightly variable and are in the range of 22 to 18 ms. The diffusion resistance in electrolyte (R_d) and parameters for

the counter electrode stay constant. In the case of SQ2-based DSCs, we could clearly observe a trend that after each 15 minutes period of allowing the DSC to stand in ambient light, R_{rec} significantly decreased. The R_{rec} values reduced from 185 to 94 Ω , which is reflected in the values of C_{μ} and R_d . At the same time, the counter electrode was affected with R_{Pt} changing from 32 to 19 Ω after 60 minutes of standing after DSC fabrication.

For both DSC sets, the main difference between 0 minutes and 60 minutes under ambient light after cell building lies in recombination resistance and capacitance values. For both sensitizers, the recombination resistance decreases with the standing time. The value of C_{μ} depends on the values of R_{rec} , Q and α according to equation (2.4). The values of α stay constant over 60 minutes, and values of Q have only a small variation (Table 2.3). Thus, R_{rec} has the highest impact on C_{μ} and its lower values result in a higher chemical capacitance.

Table 2.3. Experimental parameters α and Q needed for the correction of CPE and the final capacitance for DSCs with N719 and SQ2 dyes WOPI and API.

| DSC | $C_{\mu} / \mu\text{F}$ | α | Q |
|------------------|-------------------------|----------|--------|
| N719 WOPI 0 min | 845 | 0.92 | 1.2E-3 |
| N719 WOPI 15 min | 905 | 0.92 | 1.3E-3 |
| N719 WOPI 30 min | 955 | 0.91 | 1.3E-3 |
| N719 WOPI 45 min | 981 | 0.91 | 1.4E-3 |
| N719 WOPI 60 min | 970 | 0.91 | 1.4E-3 |
| SQ2 WOPI 15 min | 18 | 0.88 | 3.6E-5 |
| SQ2 WOPI 30 min | 20 | 0.87 | 4.2E-5 |
| SQ2 WOPI 45 min | 22 | 0.87 | 4.8E-5 |
| SQ2 WOPI 60 min | 23 | 0.87 | 5.1E-5 |

It is known ¹⁴⁶ that R_{rec} values are lower under irradiation than in the dark. Our next step was to measure DSCs after pre-irradiation. According to the data in Figure 2.3 and Table 2.1, the J - V curves for N719-based DSCs were not affected by the pre-irradiation in contrast to the SQ2-based cells. For N719, R_{rec} changed from 19 to 22 Ω from 0 minutes to 60 minutes API (Table 2.4). These resistance values are very similar to the values obtained between 15 and 60 minutes after DSCs building WOPI. The C_{μ} values between 0 and 60 minutes API have only a small variation (976 to 990 μF) compared to those WOPI. For the SQ2 dye, we observed the opposite trend. The increase in J_{SC} results in a higher overall performance, which is reflected in the impedance of the cells. For 0 minutes and 60 minutes API, C_{μ} values change little (37 to 42 μF), while the difference

in R_{rec} values is greater than 10Ω . Other parameters including τ , R_d and counter electrode parameters, stay constant.

Table 2.4. The EIS parameters for DSCs with N719 and SQ2 dyes. The DSCs were measured with 15 minutes pre-irradiation under 1 sun at 1.5 AM (100 mW cm^{-2}). Between the measurements, DSCs were kept under ambient light.

| DSC | R_{rec} / Ω | $C_{\mu} / \mu\text{F}$ | τ / ms | R_d / Ω | R_s / Ω | R_{Pt} / Ω | $C_{Pt} / \mu\text{F}$ |
|-----------------|--------------------------------------|---|--------------------------------------|----------------------------------|----------------------------------|-------------------------------------|--|
| N719 API 0 min | 19 | 976 | 19 | 11 | 11 | 9 | 5 |
| N719 API 15 min | 23 | 948 | 22 | 10 | 11 | 9 | 5 |
| N719 API 30 min | 20 | 991 | 20 | 10 | 11 | 9 | 5 |
| N719 API 45 min | 20 | 1007 | 20 | 10 | 11 | 9 | 5 |
| N719 API 60 min | 22 | 990 | 21 | 10 | 13 | 9 | 5 |
| SQ2 API 0 min | 65 | 37 | 2 | 10 | 10 | 17 | 5 |
| SQ2 API 15 min | 62 | 37 | 2 | 9 | 10 | 18 | 5 |
| SQ2 API 30 min | 56 | 39 | 2 | 9 | 10 | 17 | 5 |
| SQ2 API 45 min | 48 | 42 | 2 | 9 | 10 | 16 | 5 |
| SQ2 API 60 min | 52 | 42 | 2 | 9 | 10 | 17 | 5 |

3.2 General reproducibility of DSCs in terms of EIS measurements

To check the impedance reproducibility of DSCs and to confirm how many cells should be measured in order to obtain an overview of representative cell impedance for a target system, we measured 15 DSCs containing N719 and 15 cells with SQ2 API in the range of 45 - 60 minutes. The experimental data are presented in Figure 2.4. For N719, three semi-circles in each Nyquist plot could be clearly separated from each other. In the case of SQ2, the first two semi-circles overlap, which makes electron transport resistance indistinguishable from R_{rec} . Thus, the model 2 (Figure 2.2b) was used for fitting the experimental data.

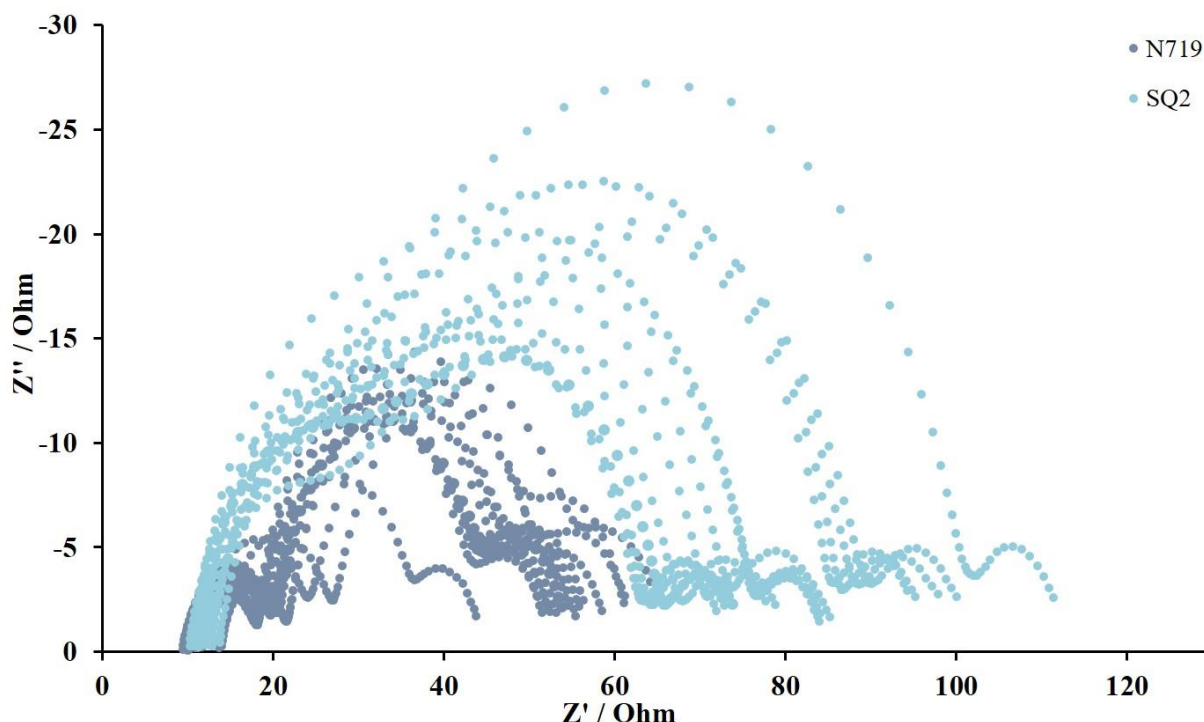


Figure 2.4. Nyquist plots of the DSCs with N719 (dark) and SQ2 (bright) sensitizers. Plots represent experimental data.

As mentioned above, in the case of N719, we fitted the EIS curves using both models 1 and 2. Since model 1 is commonly used, we have shown, that the data in Tables 2.5 and 2.6 reveal that the fitting with model 1 compared to that using model 2 does not result in significant differences in recombination resistance, chemical capacitance, empirical constant, electron lifetime and diffusion resistance. The platinum counter electrode fitting is also comparable for both models. Thus, our further statistical analysis can be suitable for model 1 as well. The fitted data are shown in Figures 2.5-2.7. Data for J - V measurements are presented in Table 2.7.

Table 2.5. The EIS parameters for DSCs with N719 dye with fitting model 1.

| DSC | R_{rec} / Ω | $C_{\mu} / \mu F$ | α | τ / ms | R_d / Ω | R_s / Ω | R_{Pt} / Ω | $C_{Pt} / \mu F$ |
|--------------|--------------------|-------------------|----------|-------------|----------------|----------------|-------------------|------------------|
| N719 cell 1 | 25 | 759 | 0.93 | 19 | 12 | 11 | 11 | 4 |
| N719 cell 2 | 22 | 724 | 0.95 | 16 | 11 | 11 | 8 | 4 |
| N719 cell 3 | 24 | 902 | 0.94 | 22 | 9 | 14 | 7 | 4 |
| N719 cell 4 | 22 | 853 | 0.94 | 19 | 10 | 11 | 8 | 5 |
| N719 cell 5 | 25 | 850 | 0.93 | 22 | 11 | 10 | 8 | 5 |
| N719 cell 6 | 24 | 972 | 0.94 | 24 | 9 | 11 | 6 | 5 |
| N719 cell 7 | 25 | 957 | 0.95 | 24 | 14 | 14 | 7 | 4 |
| N719 cell 8 | 23 | 934 | 0.94 | 21 | 11 | 10 | 9 | 4 |
| N719 cell 9 | 28 | 955 | 0.94 | 26 | 11 | 9 | 7 | 5 |
| N719 cell 10 | 27 | 828 | 0.93 | 22 | 11 | 14 | 12 | 4 |

| | | | | | | | | |
|--------------|----|-----|------|----|----|----|---|---|
| N719 cell 11 | 22 | 756 | 0.94 | 17 | 10 | 11 | 8 | 4 |
| N719 cell 12 | 17 | 810 | 0.96 | 14 | 9 | 12 | 6 | 4 |
| N719 cell 13 | 23 | 670 | 0.95 | 16 | 10 | 10 | 7 | 5 |
| N719 cell 14 | 25 | 718 | 0.94 | 18 | 10 | 10 | 8 | 4 |
| N719 cell 15 | 29 | 615 | 0.95 | 18 | 9 | 11 | 7 | 4 |

Table 2.6. The EIS parameters for DSCs with N719 dye API (45-60 min), which were fitted with model 2. The Nyquist and Bode plots are presented in Figures 2.5-2.7.

| DSC | R_{rec} / Ω | $C_{\mu} / \mu F$ | α | τ / ms | R_d / Ω | R_s / Ω | R_{Pt} / Ω | $C_{Pt} / \mu F$ |
|--------------|--------------------|-------------------|----------|-------------|----------------|----------------|-------------------|------------------|
| N719 cell 1 | 25 | 756 | 0.92 | 19 | 12 | 12 | 13 | 4 |
| N719 cell 2 | 22 | 724 | 0.95 | 16 | 11 | 11 | 9 | 4 |
| N719 cell 3 | 24 | 902 | 0.94 | 22 | 9 | 14 | 8 | 4 |
| N719 cell 4 | 22 | 852 | 0.94 | 19 | 10 | 11 | 9 | 4 |
| N719 cell 5 | 26 | 847 | 0.92 | 22 | 11 | 10 | 9 | 4 |
| N719 cell 6 | 24 | 971 | 0.94 | 24 | 9 | 11 | 7 | 5 |
| N719 cell 7 | 25 | 955 | 0.94 | 24 | 14 | 14 | 8 | 4 |
| N719 cell 8 | 23 | 927 | 0.93 | 21 | 11 | 10 | 10 | 4 |
| N719 cell 9 | 28 | 951 | 0.94 | 26 | 11 | 9 | 8 | 5 |
| N719 cell 10 | 27 | 826 | 0.93 | 22 | 11 | 14 | 13 | 4 |
| N719 cell 11 | 22 | 753 | 0.94 | 17 | 10 | 11 | 9 | 4 |
| N719 cell 12 | 17 | 801 | 0.95 | 14 | 9 | 12 | 6 | 4 |
| N719 cell 13 | 24 | 660 | 0.94 | 16 | 10 | 10 | 9 | 4 |
| N719 cell 14 | 26 | 711 | 0.93 | 18 | 10 | 10 | 10 | 4 |
| N719 cell 15 | 30 | 604 | 0.93 | 18 | 9 | 11 | 9 | 4 |

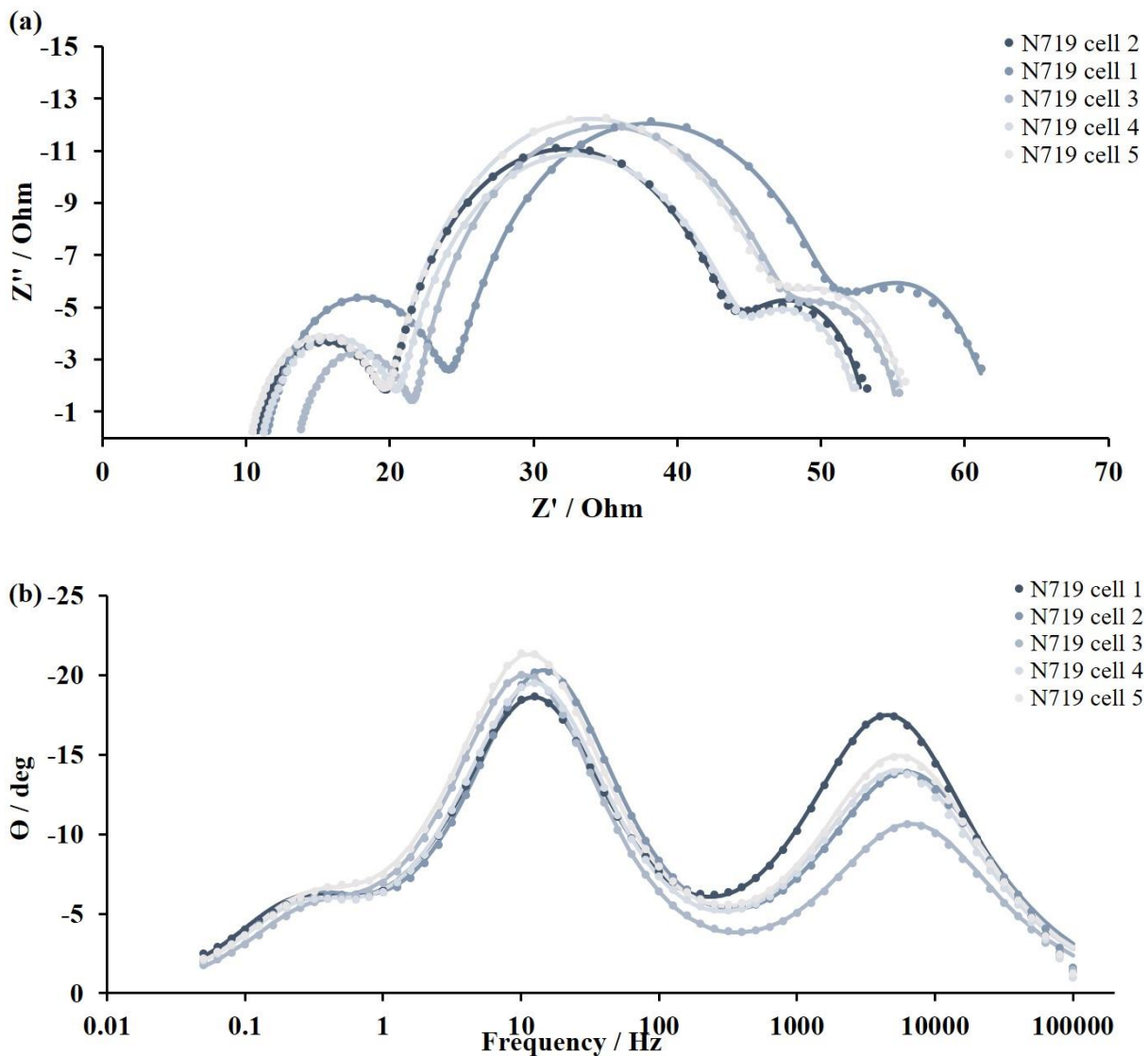
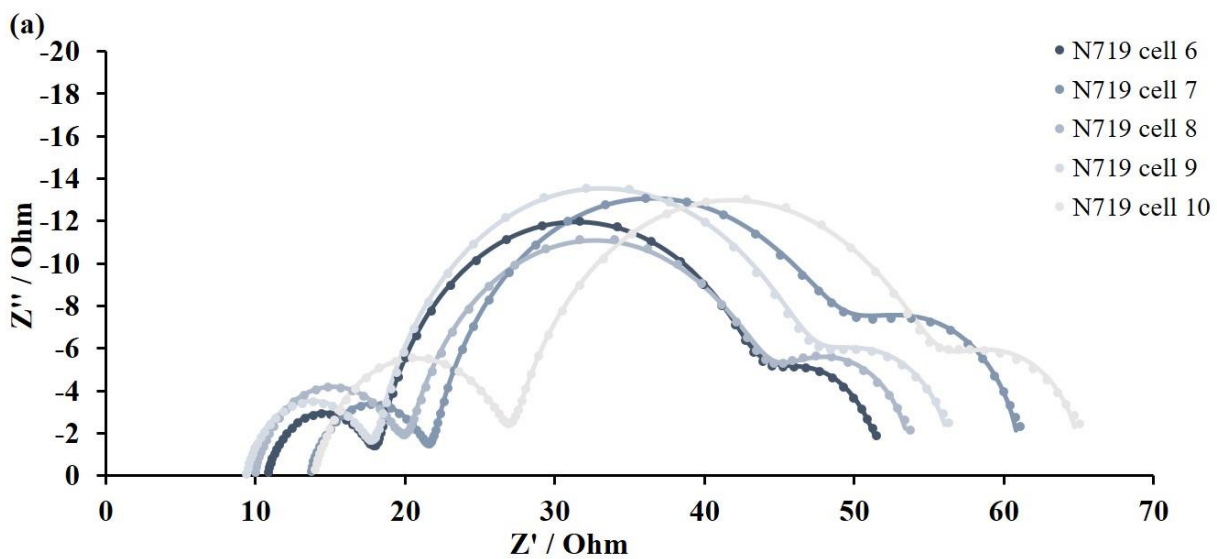


Figure 2.5. EIS data for DSCs with N719 dye (cells 1-5). (a) Nyquist plots, the expansion shows the high frequency region. (b) Bode plot. Solid lines represent fitted curves, dotted lines represent experimental data.



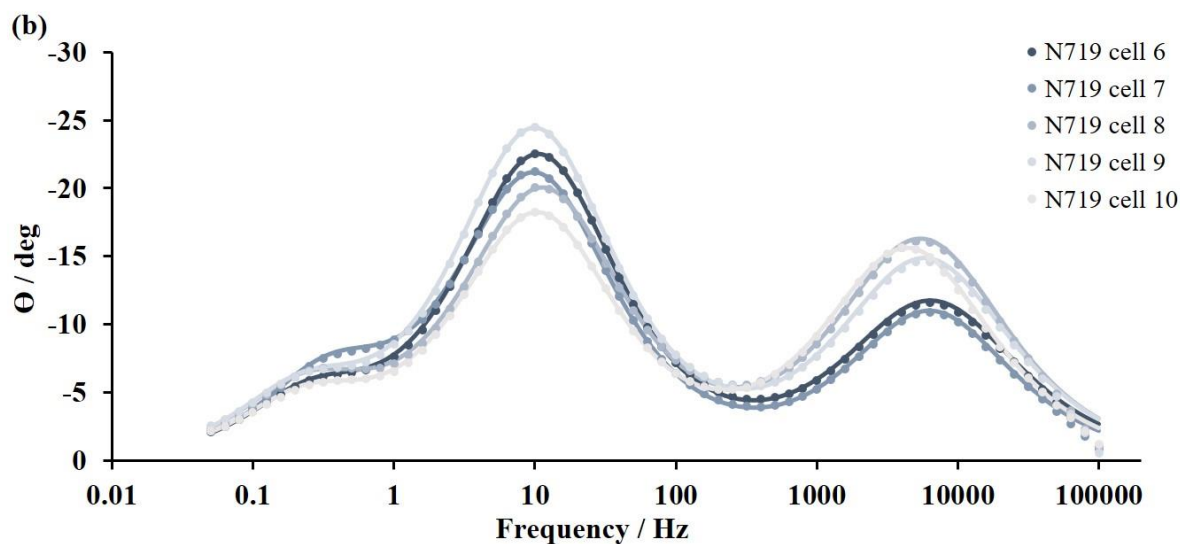


Figure 2.6. EIS data for DSCs with N719 dye (cells 6-10). (a) Nyquist plots, the expansion shows the high frequency region. (b) Bode plot. Solid lines represent fitted curves, dotted lines represent experimental data.

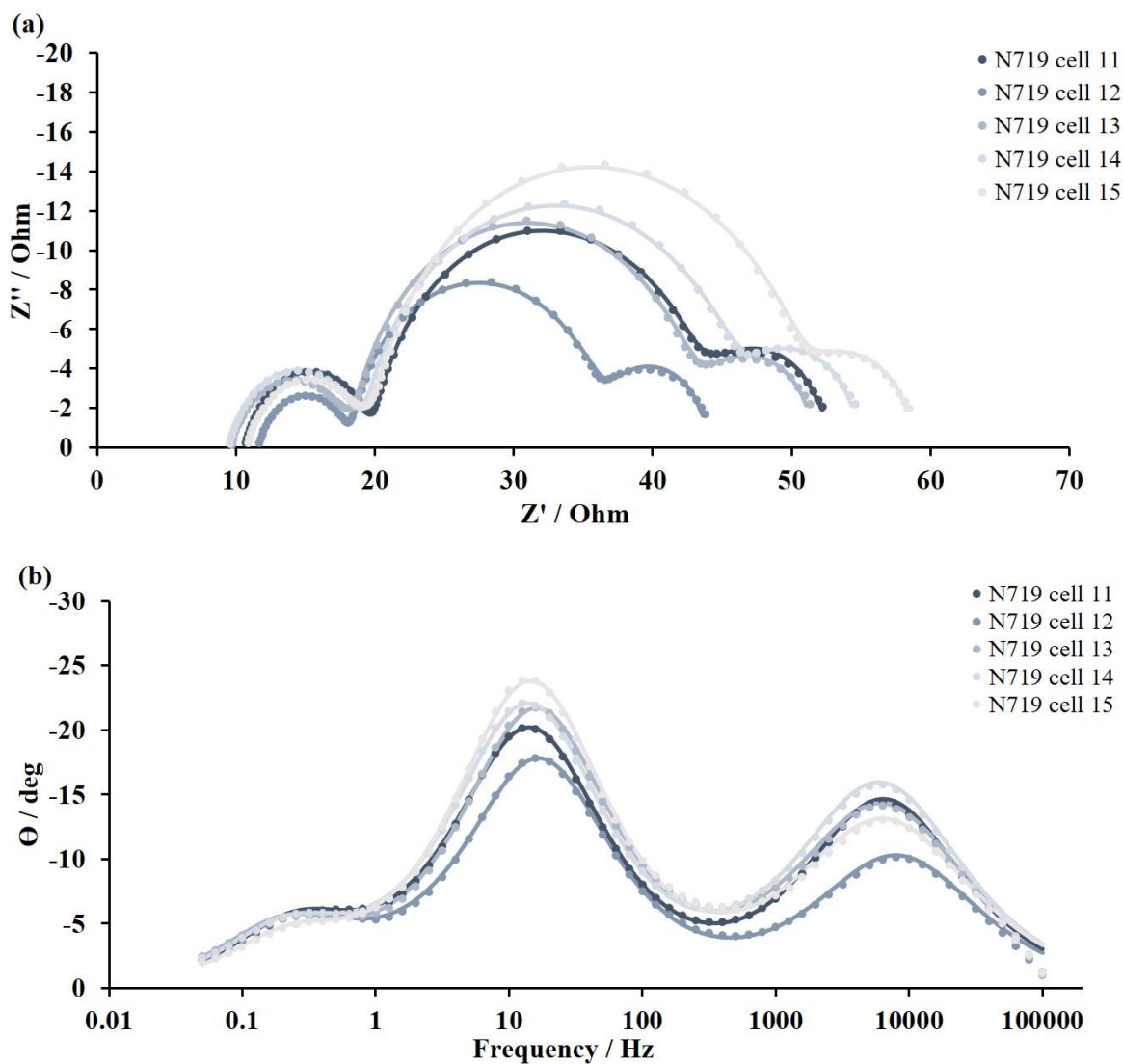


Figure 2.7. EIS data for DSCs with N719 dye (cells 11-15). (a) Nyquist plots, the expansion shows the high frequency region. (b) Bode plot. Solid lines represent fitted curves, dotted lines represent experimental data.

Table 2.7. *J-V* parameters for DSCs with N719 dye. All DSCs were masked.

| DSC | $J_{sc} / \text{mA cm}^{-2}$ | V_{oc} / mV | $ff / \%$ | $\eta / \%$ |
|--------------|--|--|-----------------------------|-------------------------------|
| N719 cell 1 | 13.37 | 604 | 69 | 5.59 |
| N719 cell 2 | 13.33 | 588 | 69 | 5.41 |
| N719 cell 3 | 14.19 | 611 | 67 | 5.85 |
| N719 cell 4 | 13.94 | 602 | 63 | 5.25 |
| N719 cell 5 | 14.12 | 606 | 66 | 5.67 |
| N719 cell 6 | 13.49 | 602 | 69 | 5.59 |
| N719 cell 7 | 13.15 | 595 | 66 | 5.13 |
| N719 cell 8 | 13.65 | 597 | 66 | 5.41 |
| N719 cell 9 | 13.70 | 606 | 68 | 5.64 |
| N719 cell 10 | 13.14 | 603 | 67 | 5.31 |
| N719 cell 11 | 13.46 | 581 | 68 | 5.28 |
| N719 cell 12 | 13.18 | 578 | 69 | 5.27 |
| N719 cell 13 | 13.30 | 592 | 70 | 5.54 |
| N719 cell 14 | 13.83 | 597 | 69 | 5.67 |
| N719 cell 15 | 13.13 | 579 | 68 | 5.20 |

In Table 2.8, statistical data for N719-based DSCs are presented. These include maximum (max) and minimum (min) values, average, standard deviation (SD) and relative standard deviation (RSD). Statistical data were extracted from the fitted EIS parameters. The average value is a sum of all the values for a given parameter divided by 15 (Equation 2.1). SD is a statistical value, which gives information about the dispersion of a data set values (Equation 2.2). RSD is a ratio of the SD to the average and expressed as a percentage (Equation 2.3).

$$average = \frac{x_1 + x_2 + \dots + x_n}{n} \quad (2.1)$$

$$SD = \sqrt{\frac{1}{n} \sum_{i=1}^n (n_i - n_{average})^2} \quad (2.2)$$

$$RSD = \frac{SD}{average} \cdot 100 \quad (2.3)$$

Table 2.8. Statistical data for N719-based DSCs extracted from the fitted EIS parameters.

| Parameter | R_{rec} / Ω | $C_{\mu} / \mu\text{F}$ | τ / ms | R_d / Ω | R_{Pt} / Ω | $C_{Pt} / \mu\text{F}$ |
|------------------|--------------------------------------|---|--------------------------------------|----------------------------------|-------------------------------------|--|
| max | 30 | 971 | 26 | 14 | 13 | 5 |
| min | 17 | 604 | 14 | 9 | 6 | 4 |

| | | | | | | |
|---------|----|-----|----|----|----|-----|
| Average | 24 | 816 | 20 | 11 | 9 | 4 |
| SD | 3 | 113 | 4 | 1 | 2 | 0.3 |
| RSD / % | 12 | 14 | 18 | 13 | 19 | 6 |

Analysis of the N719-based DSCs allows us to assess the statistical difference between 15 cells. RSD values for R_{rec} , C_{μ} , τ , R_{d} , R_{Pt} and C_{Pt} are in the range of 14% to 19% (Figure 2.8). The maximum value in the case of R_{rec} is 30 Ω , while the minimum value is 17 Ω , giving an average value of 24 Ω . Within the set of DSCs with N719, only 3 cells differ from the average value by more than 3 Ω . This shows that the RSD value of 12% is mainly due to a few outlying cells and most of the DSCs have good reproducibility in terms of recombination resistance. The values of C_{μ} are not as reproducible as R_{rec} and range from 604 to 971 μF . Thus, the SD of the chemical capacitance is ± 113 μF and the average is 816 μF , giving an RSD of 14%. The average value of R_{d} is 11 Ω and the SD is ± 1 Ω . Most of the cells have R_{d} values between 9 Ω and 12 Ω with one DSC having $R_{\text{d}} = 14$ Ω . This results in an RSD value of 13%. The highest RSDs are observed for τ and R_{Pt} with 18% and 19%, respectively. Since values of τ depend on R_{rec} and C_{μ} ¹⁵⁸, the range of τ values is rather broad (14 to 26 ms). The counter electrode values are usually considered as constant and should have minimal deviation from cell to cell. Despite this, the DSCs in this investigation exhibit an RSD of R_{Pt} of 19%. Most of the cells have R_{Pt} in the range of 9 ± 2 Ω but two cells with $R_{\text{Pt}} = 13$ Ω . The values of C_{Pt} have the smallest RSD of 6% and lie between 5 and 6 μF . Nonetheless, the fact that there are outlying cells underlines the importance of acquiring EIS data for a series of cells and not for a single device.

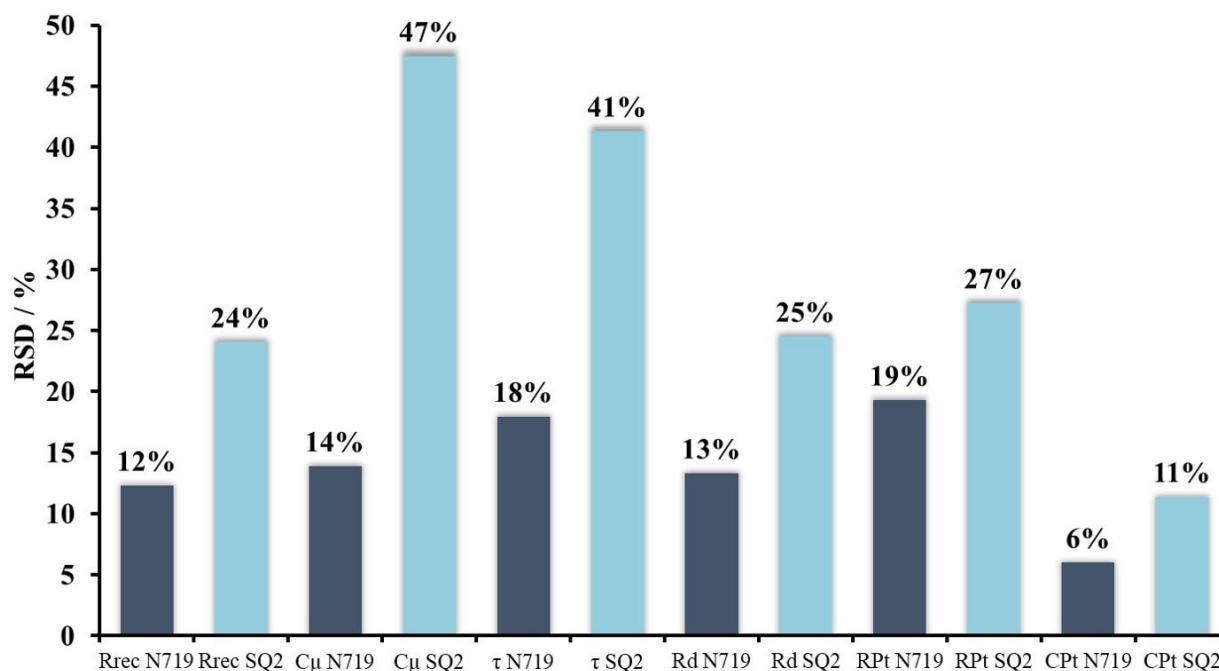


Figure 2.8. The overview of RSD for N719 and SQ2 dyes. Dark blue bars refer to N719, bright blue bars to SQ2.

In order to understand whether SD values for N719 could be considered as rather high or low, we performed same study for SQ2 dye. Compared to DSCs containing N719, SQ2-based DSCs exhibit a lower reproducibility in terms of overall performance because of the significant differences in values of J_{SC} (Table 2.9). The same trend is observed in the EIS measurements. In Table 2.10, EIS parameters for 15 DSCs with SQ2 as the sensitizer are presented. The fitted data are shown in Figures 2.9-2.11.

Table 2.9. J - V parameters for DSCs with SQ2 dye. All DSCs were masked.

| DSC | $J_{SC} / \text{mA cm}^{-2}$ | V_{OC} / mV | $ff / \%$ | $\eta / \%$ |
|-------------|------------------------------|----------------------|-----------|-------------|
| SQ2 cell 1 | 2.85 | 458 | 69 | 0.9 |
| SQ2 cell 2 | 2.59 | 471 | 70 | 0.86 |
| SQ2 cell 3 | 2.52 | 466 | 71 | 0.83 |
| SQ2 cell 4 | 3.29 | 470 | 69 | 1.06 |
| SQ2 cell 5 | 2.88 | 463 | 69 | 0.92 |
| SQ2 cell 6 | 3.97 | 486 | 70 | 1.35 |
| SQ2 cell 7 | 2.84 | 466 | 68 | 0.91 |
| SQ2 cell 8 | 3.31 | 479 | 70 | 1.1 |
| SQ2 cell 9 | 3.65 | 484 | 68 | 1.2 |
| SQ2 cell 10 | 2.94 | 473 | 70 | 0.98 |
| SQ2 cell 11 | 3.77 | 479 | 69 | 1.24 |
| SQ2 cell 12 | 3.23 | 502 | 72 | 1.17 |

Second Chapter

| | | | | |
|-------------|------|-----|----|------|
| SQ2 cell 13 | 2.27 | 484 | 72 | 0.79 |
| SQ2 cell 14 | 2.14 | 487 | 72 | 0.75 |
| SQ2 cell 15 | 3.83 | 496 | 72 | 1.36 |

Table 2.10. The EIS parameters for DSCs with SQ2 dye API (45-60 min), which were fitted with model 2. The Nyquist and Bode plots are presented in Figures 2.9-2.11.

| DSC | R_{rec} / Ω | $C_{\mu} / \mu F$ | α | τ / ms | R_d / Ω | R_s / Ω | R_{Pt} / Ω | $C_{Pt} / \mu F$ |
|-------------|--------------------|-------------------|----------|-------------|----------------|----------------|-------------------|------------------|
| SQ2 cell 1 | 45 | 39 | 0.81 | 2 | 8 | 11 | 20 | 4 |
| SQ2 cell 2 | 53 | 30 | 0.80 | 2 | 2 | 12 | 12 | 5 |
| SQ2 cell 3 | 54 | 26 | 0.79 | 1 | 8 | 10 | 12 | 5 |
| SQ2 cell 4 | 37 | 32 | 0.82 | 1 | 11 | 11 | 19 | 5 |
| SQ2 cell 5 | 52 | 27 | 0.81 | 1 | 11 | 11 | 26 | 5 |
| SQ2 cell 6 | 37 | 36 | 0.82 | 1 | 9 | 10 | 16 | 4 |
| SQ2 cell 7 | 72 | 23 | 0.80 | 2 | 11 | 13 | 17 | 5 |
| SQ2 cell 8 | 38 | 35 | 0.82 | 1 | 10 | 11 | 14 | 5 |
| SQ2 cell 9 | 33 | 66 | 0.83 | 2 | 9 | 11 | 21 | 4 |
| SQ2 cell 10 | 57 | 35 | 0.81 | 2 | 10 | 10 | 20 | 5 |
| SQ2 cell 11 | 41 | 45 | 0.82 | 2 | 11 | 12 | 19 | 5 |
| SQ2 cell 12 | 34 | 93 | 0.86 | 3 | 9 | 13 | 24 | 4 |
| SQ2 cell 13 | 45 | 59 | 0.88 | 3 | 10 | 11 | 30 | 4 |
| SQ2 cell 14 | 44 | 77 | 0.89 | 3 | 11 | 14 | 27 | 4 |
| SQ2 cell 15 | 34 | 78 | 0.85 | 3 | 10 | 12 | 17 | 4 |

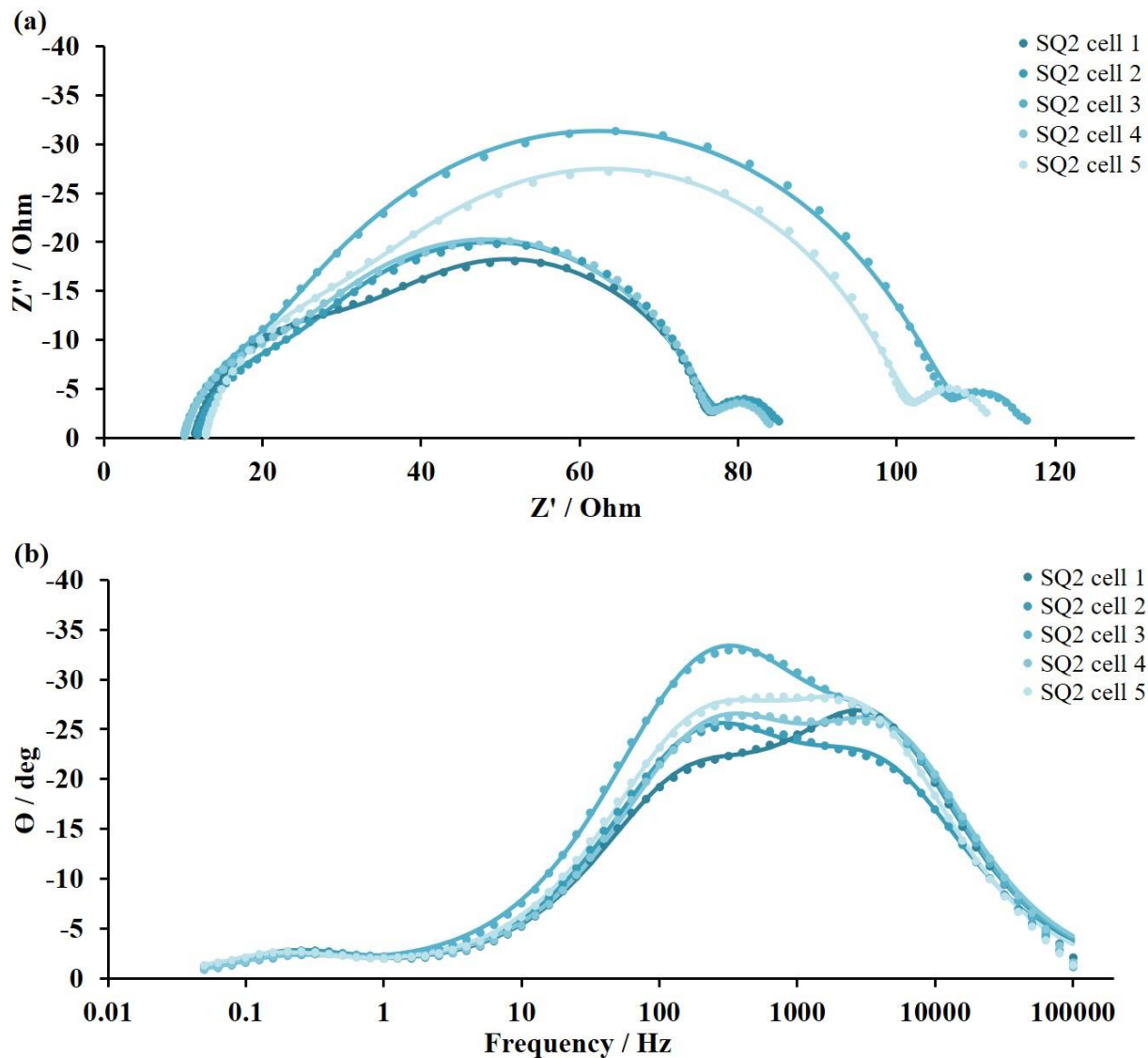
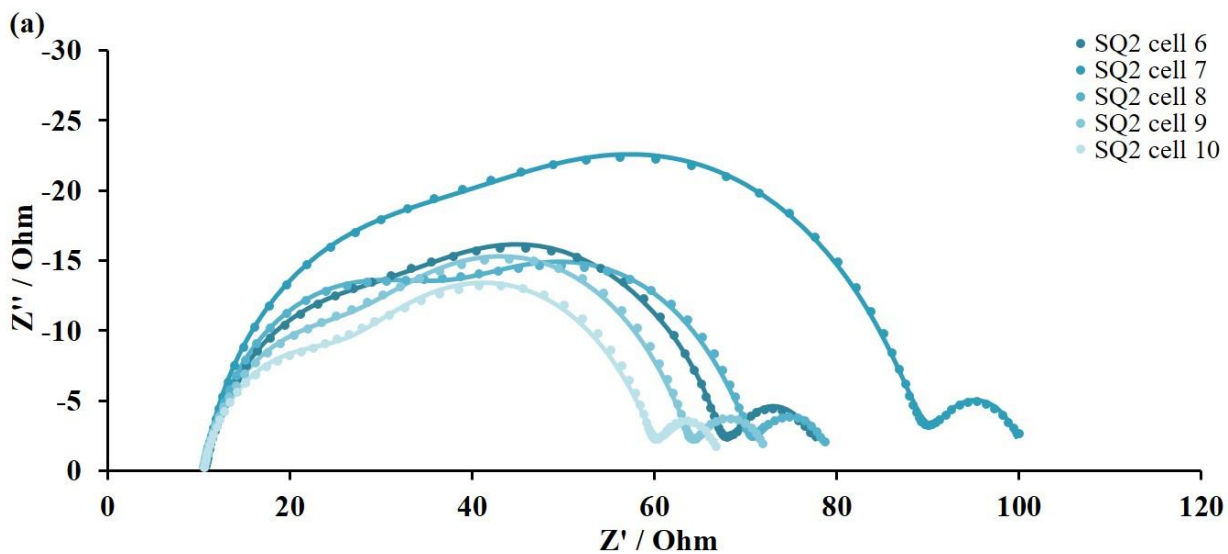


Figure 2.9. EIS data for DSCs with SQ2 dye (cells 1-5). (a) Nyquist plots, the expansion shows the high frequency region. (b) Bode plot. Solid lines represent fitted curves, dotted lines represent experimental data.



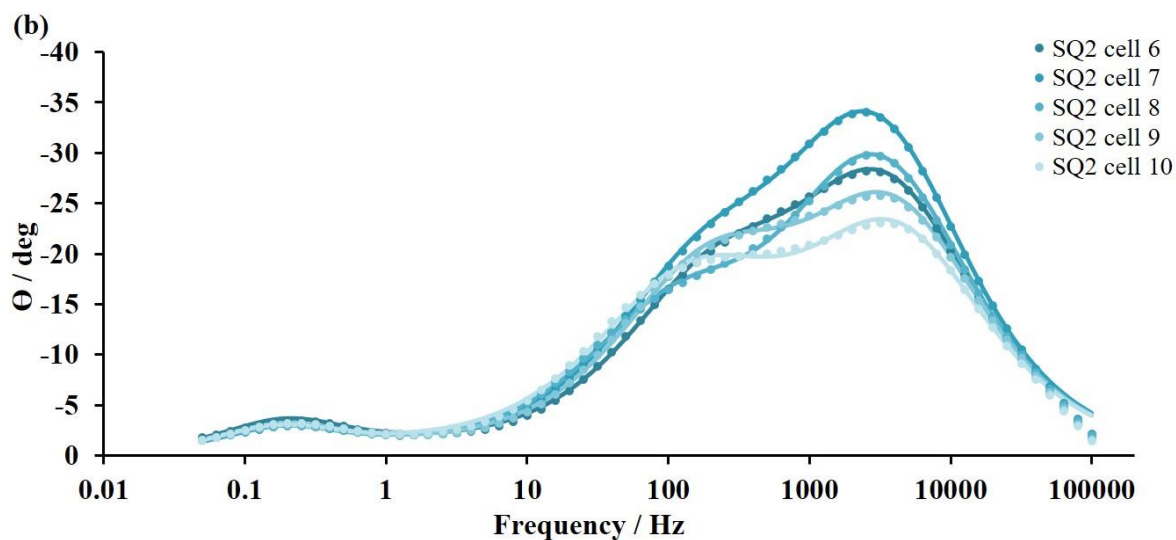


Figure 2.10. EIS data for DSCs with SQ2 dye (cells 6-10). (a) Nyquist plots, the expansion shows the high frequency region. (b) Bode plot. Solid lines represent fitted curves, dotted lines represent experimental data.

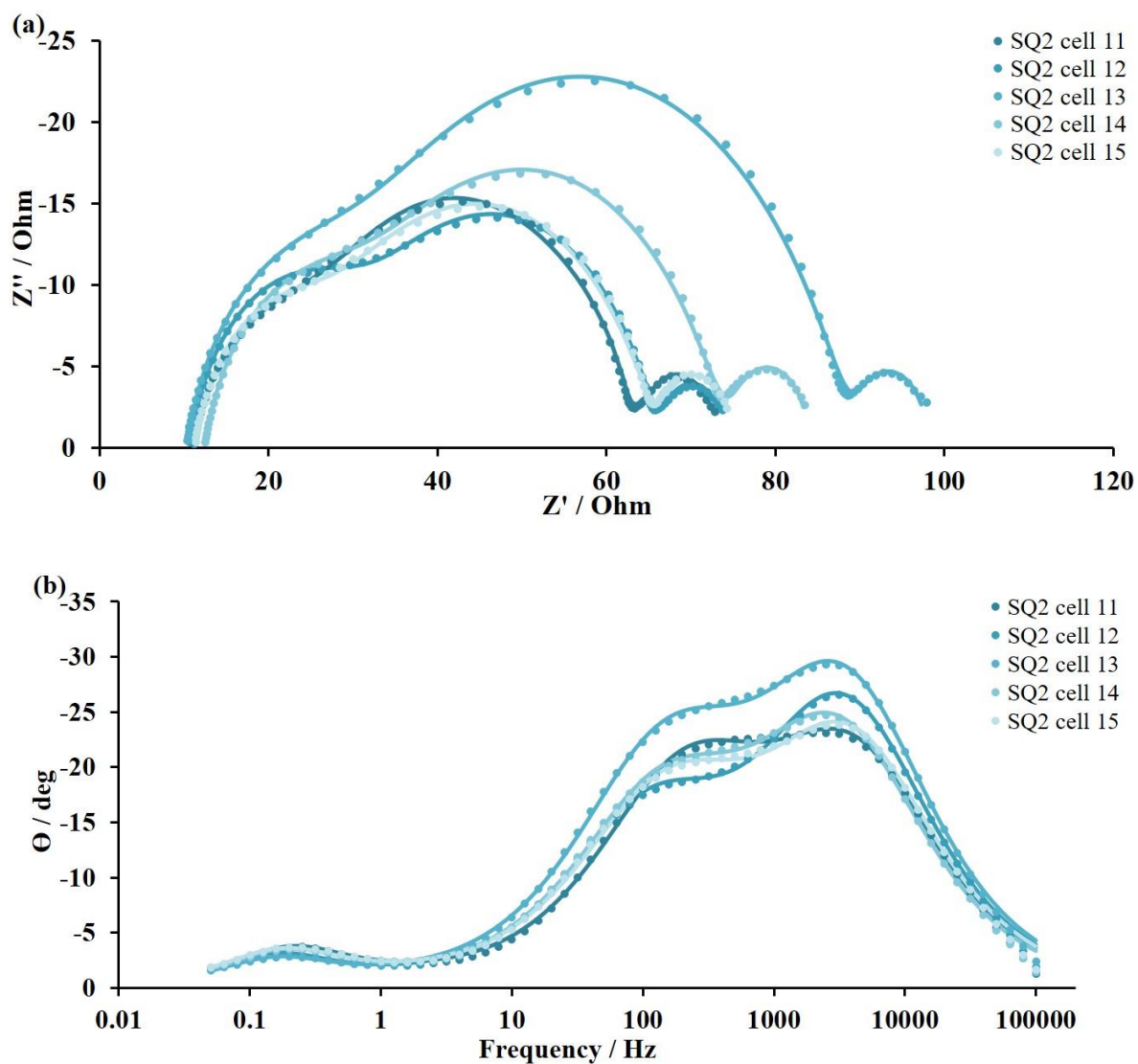


Figure 2.11. EIS data for DSCs with SQ2 dye (cells 11-15). (a) Nyquist plots, the expansion shows the high frequency region. (b) Bode plot. Solid lines represent fitted curves, dotted lines represent experimental data.

The statistical analysis of the EIS parameters confirms the lower reproducibility for SQ2 compared to N719-containing devices (Table 2.11, Figure 2.8). The R_{rec} values range between 72 and 33 Ω with an average value of 45 Ω . The SD and RSD values are ± 11 Ω and 24% compared to 3 Ω and 12% for N719, respectively. The C_{μ} values vary widely (93 to 23 μF) with an average value of 47 μF leading to an RSD = 47%. Since R_{rec} and C_{μ} are related to J_{SC} , their high RSD values could explain the low reproducibility of J_{SC} , which varies from 3.94 to 2.14 mA cm^{-2} . The electron lifetime maximum and minimum values are 3 and 1 ms, respectively ($\tau_{\text{average}} = 2$ ms). This leads to an SD of ± 1 ms and RSD of 41%. The R_{d} has only one outlying cell with a value of 2 Ω which leads to an RSD value of 25% for the set of 15 DSCs. The rest of the DSCs have R_{d} values within the range of 8 to 11 Ω . The R_{Pt} values of the counter electrodes vary significantly (12 to 30 Ω), more so than for the N719-based DSCs. The SD is ± 5 Ω and RSD is 27%. At the same time, C_{Pt} stays more or less constant and has a standard deviation of ± 1 μF with an average value of 5 μF , resulting in an RSD of 11%.

Table 2.11. Statistical data for SQ2-based DSCs extracted from the fitted EIS parameters.

| Parameter | R_{rec} / Ω | $C_{\mu} / \mu\text{F}$ | τ / ms | R_{d} / Ω | R_{Pt} / Ω | $C_{\text{Pt}} / \mu\text{F}$ |
|-----------|---------------------------|-------------------------|--------------------|-------------------------|--------------------------|-------------------------------|
| max | 72 | 93 | 3 | 11 | 30 | 5 |
| min | 33 | 23 | 1 | 2 | 12 | 4 |
| average | 45 | 47 | 2 | 9 | 20 | 5 |
| SD | 11 | 22 | 1 | 2 | 5 | 1 |
| RSD / % | 24 | 47 | 41 | 25 | 27 | 11 |

C_{μ} and R_{rec} represent the shift of the conduction band and electron injection rate, which affect the J_{SC} values. In Figure 2.12, values of C_{μ} and R_{rec} are presented as a function of J_{SC} for both the N719 and SQ2 dyes, since all three parameters are related to one other. The data for the two dyes form separate groups on the graph and can be easily distinguished between each other, despite the rather high RSD values for C_{μ} and R_{rec} for SQ2.

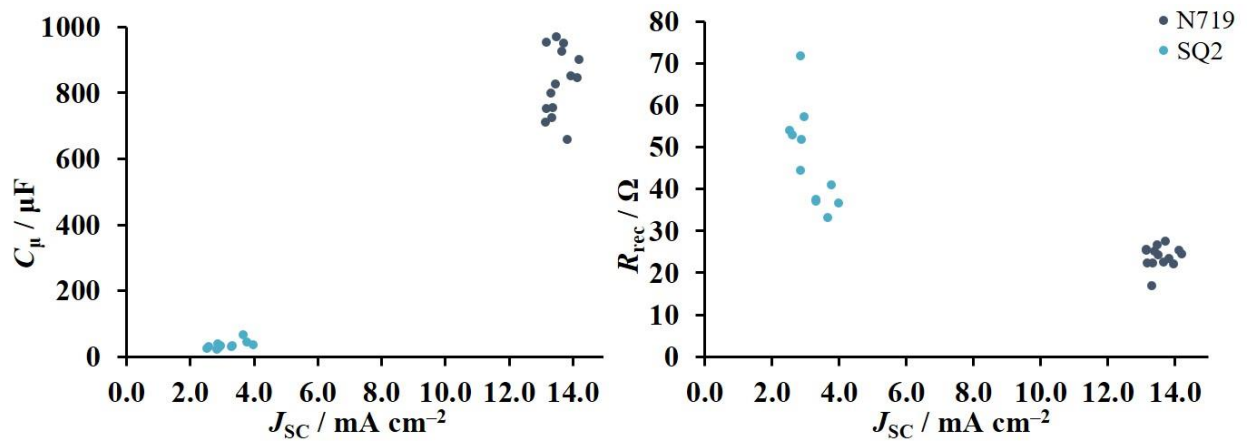


Figure 2.12. C_{μ} and R_{rec} presented as a function of J_{SC} for DSCs with N719 and SQ2 dyes.

4. Conclusions

The results in this chapter confirm that it is important to perform EIS measurements on multiple cells to ensure representative data are collected about the electronic processes in DSCs. SQ2 is a good example of a dye which has a wide variability and illustrates how diverse the parameters can be within one set of devices with identical components and fabricated in the same manner. There is a strong tendency in the DSC literature to present EIS data for only one device for a given dye and conclusions based on these data may be erroneous. Best practice would be to perform EIS measurements on at least four cells in order to determine reasonable average values.

Third Chapter

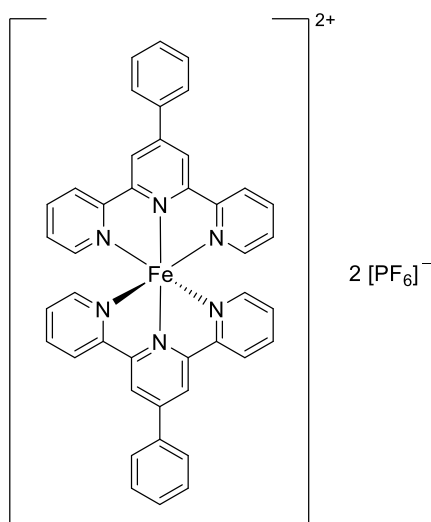
1. Motivation

Iron(II)-sensitizers are a promising alternative to ruthenium(II) complexes as well as organic (so-called 'metal-free') dyes due to the higher abundance and lower cost of iron versus ruthenium. It has been demonstrated in ruthenium(II) and copper(I) sensitizers that a carefully chosen electrolyte composition can remarkably enhance the DSC performance.^{63, 79, 108, 159, 160} Classically, an electrolyte consists of a redox couple and various additives. The most common redox couple (shuttle) in the electrolyte is iodide/triiodide (I^-/I_3^-) couple.

In this work, we investigated more closely the effects of additives in the electrolyte and their impact on the performances of iron(II)-sensitized solar cells while retaining the I^-/I_3^- redox shuttle. This chapter starts with a discussion of DSCs based on bis(2,2':6',2''-terpyridine)iron(II) complexes used as sensitizers and their optimisation. Then, a detailed electrolyte composition study will be presented for DSCs sensitized with heteroleptic *N*-heterocyclic carbene (NHC) iron(II) complexes.

2. Optimisation of DSC sensitized with bis(2,2':6',2''-terpyridine)iron(II) complexes

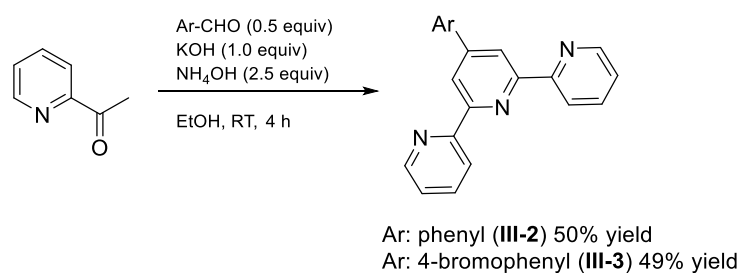
The study started with the literature-known bis(4'-phenyl-2,2':6',2''-terpyridine)iron(II) complex $[Fe(Phtpy)_2]^{2+}$ III-1 (Figure 3.1). $[Fe(Phtpy)_2][PF_6]_2$ was prepared by complexation of Phtpy with iron(II) chloride followed by anion exchange. $[Fe(Phtpy)_2]^{2+}$ is a homoleptic complex, which cannot be adsorbed on TiO_2 surface because of the absence of an anchoring moiety.

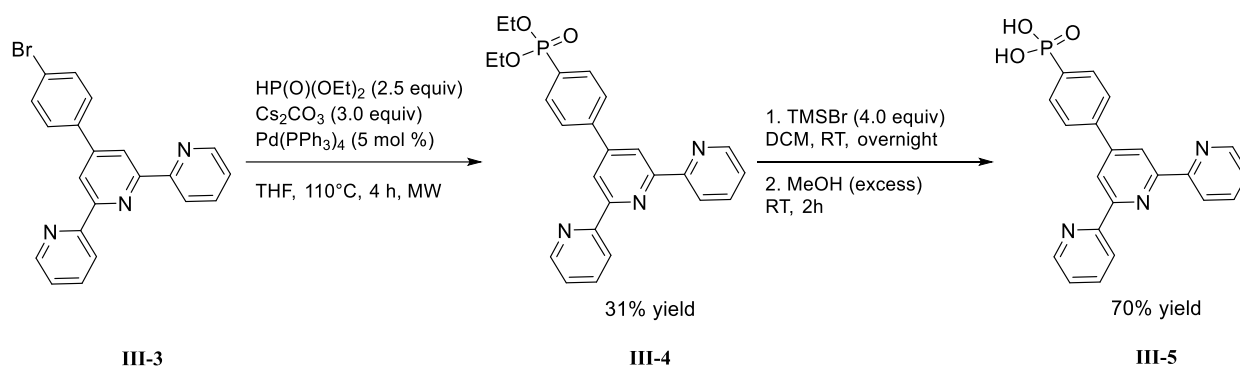


III-1

Figure 3.1. Structure of $[\text{Fe}(\text{Phtpy})_2]^{2+}$ (III-1) complex.

To overcome this limitation, a phosphonic acid was introduced to the tpy-ligand as an anchoring group in order to adsorb the complex on the semiconductor surface. The scaffold of the tpy-ligands was synthesized *via* the Kröhnke reaction (Scheme 3.1). In the first step, 4'-(4-bromophenyl)-2,2':6',2''-terpyridine III-3 was prepared by Michael adduct formation following reaction with ammonia. Then, the phosphonic ester group was introduced by a cross-coupling reaction with diethyl phosphite (Scheme 3.2). The obtained ester III-4 was hydrolysed to afford the target terpyridine phosphonic acid III-5.

Scheme 3.1. Preparation of tpy-ligands *via* the Kröhnke synthesis.



Scheme 3.2. Synthesis of terpyridine phosphonic acid 5.

Compound III-2 was used for preparing a heteroleptic tpy-complex using FeCl_2 . The isolation of a heteroleptic tpy complex $[\text{FeL}_{\text{anchor}}\text{L}_{\text{ancill}}]^{2+}$ is not trivial, because the equilibrium is shifted in solution towards a stoichiometric mixture of the target complex $[\text{FeL}_{\text{anchor}}\text{L}_{\text{ancill}}]^{2+}$ and the two homoleptic complexes $[\text{FeL}_{\text{ancill}}\text{L}_{\text{ancill}}]^{2+}$, $[\text{FeL}_{\text{anchor}}\text{L}_{\text{anchor}}]^{2+}$ (Scheme 3.3).

Scheme 3.3. Synthesis of heteroleptic complex $[\text{Fe(III-5)(Phtpy)}]^{2+}$, where L_{anchor} is III-5 and L_{ancill} is III-2 (Phtpy).

In order to avoid such limitations, we decided to assemble the complex directly on the semiconductor surface. The commonly used strategy ‘surface-as-ligand, surface-as-complex’ (SALSAC)¹⁶¹ was developed for the assembly of heteroleptic copper(I) complexes on nanoparticulate TiO_2 surfaces and has a broad application in the field of DSCs. The strategy consists of a stepwise approach, the so called two or three step dye assembly (Figure 3.2). The three step path describes the adsorption of the anchoring ligand on the semiconductor surface by dipping the TiO_2 electrode in a solution of L_{anchor} III-5 (in DMSO). Then, the electrode is dipped in the FeCl_2 solution (in EtOH) and afterwards in an Phtpy (an ancillary ligand III-2) solution in MeCN (Figure 3.3a-c). The second two-step approach (from now on called the ligand exchange approach) includes a ligand exchange step with the $[\text{Fe(Phtpy)}_2]^{2+}$ complex instead of the FeCl_2 - L_{ancill} dipping following the immersion of an electrode in a L_{anchor} solution (Figure 3.3a,d). The dipping conditions for all steps are shown in Table 1.1 (First Chapter).

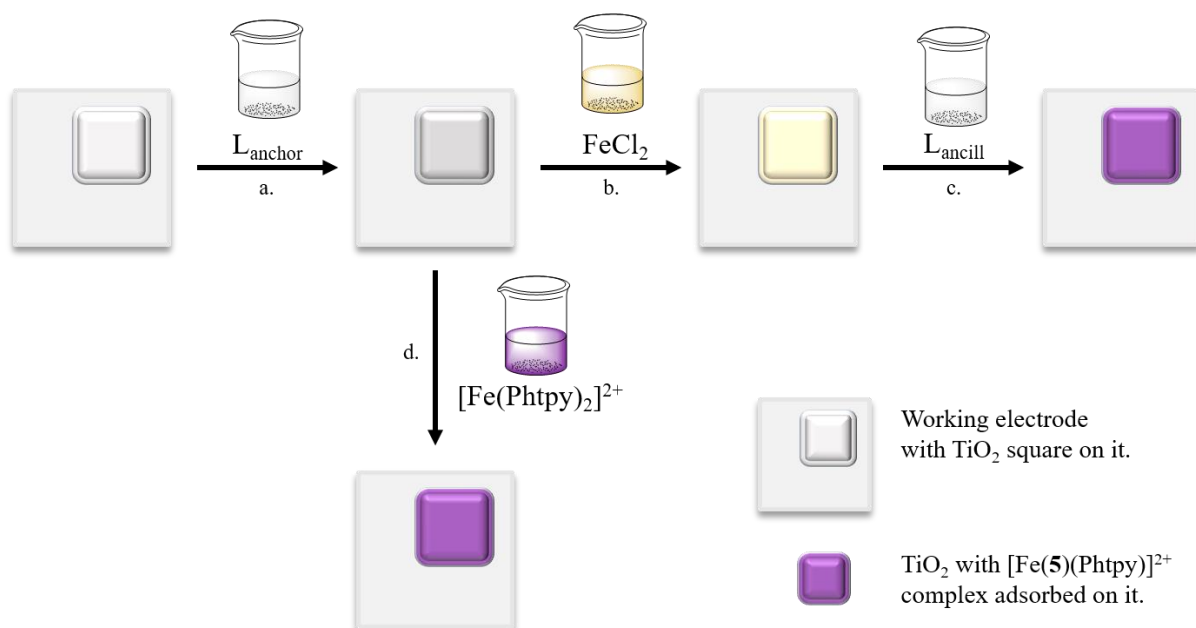


Figure 3.2. Stepwise approach (a-b-c) and ligand exchange (a-d) strategy for $[\text{Fe}(\text{III-5})(\text{Phtpy})]^{2+}$ dye assembling on the semiconductor surface.

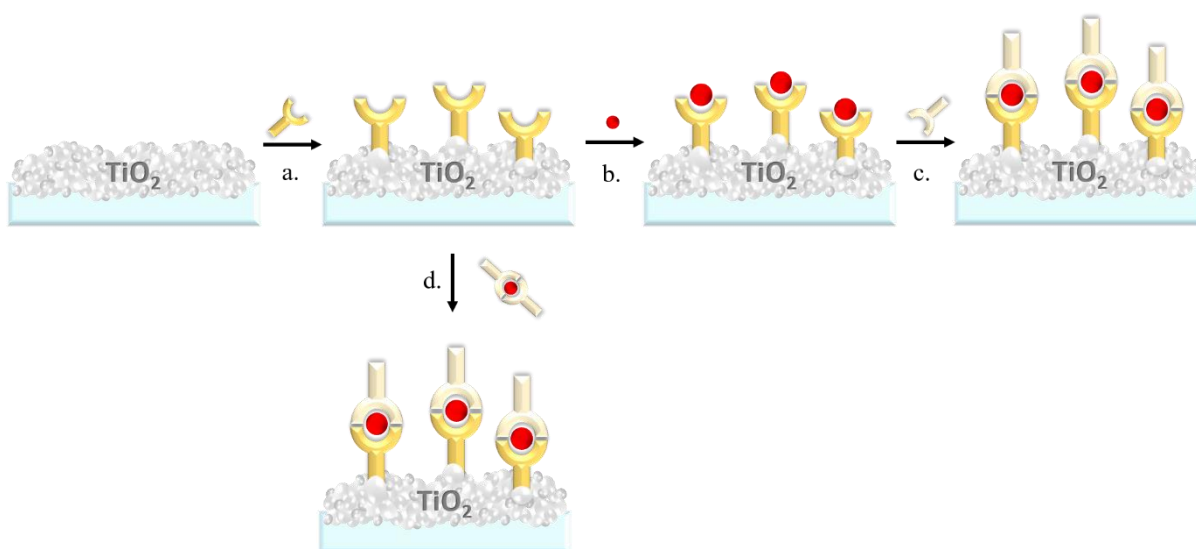


Figure 3.3. Stepwise approach (a-b-c) and ligand exchange (a-d) strategy for dye assembling on the semiconductor surface: a. an anchoring group on the ligand $\mathbf{5}$ covalently attaches to the TiO_2 ; b. metal ion is coordinated to the ligand binding site; c. an ancillary ligand $\mathbf{2}$ binds to the metal ion and forms the final heteroleptic complex $[\text{Fe}(\text{III-5})(\text{Phtpy})]^{2+}$; d. ligand exchange between a homoleptic metal complex $[\text{Fe}(\text{Phtpy})_2]^{2+}$ and an anchoring ligand results in the final heteroleptic complex $[\text{Fe}(\text{III-5})(\text{Phtpy})]^{2+}$.

We performed solid state UV-Vis spectroscopy ($ss\text{UV-Vis}$) to find out if there are any absorption differences between the product of the two dye assembling approaches. Two electrodes were measured for each approach to confirm the reproducibility. As shown in Figure 3.4, the maximum absorbance is observed at $\lambda_{\text{max}} \approx 573 \text{ nm}$, which is characteristic for the MLCT band of $[\text{Fe}(\text{Phtpy})_2]^{2+}$ complexes. Despite the high energy band at λ_{max} , the complex does not have a broad absorption in the visible region and shows limitations in the range of 470-620 nm. Comparing the two dye assembling approaches, the absorbance is slightly higher for the stepwise pathway than for the ligand exchange one.

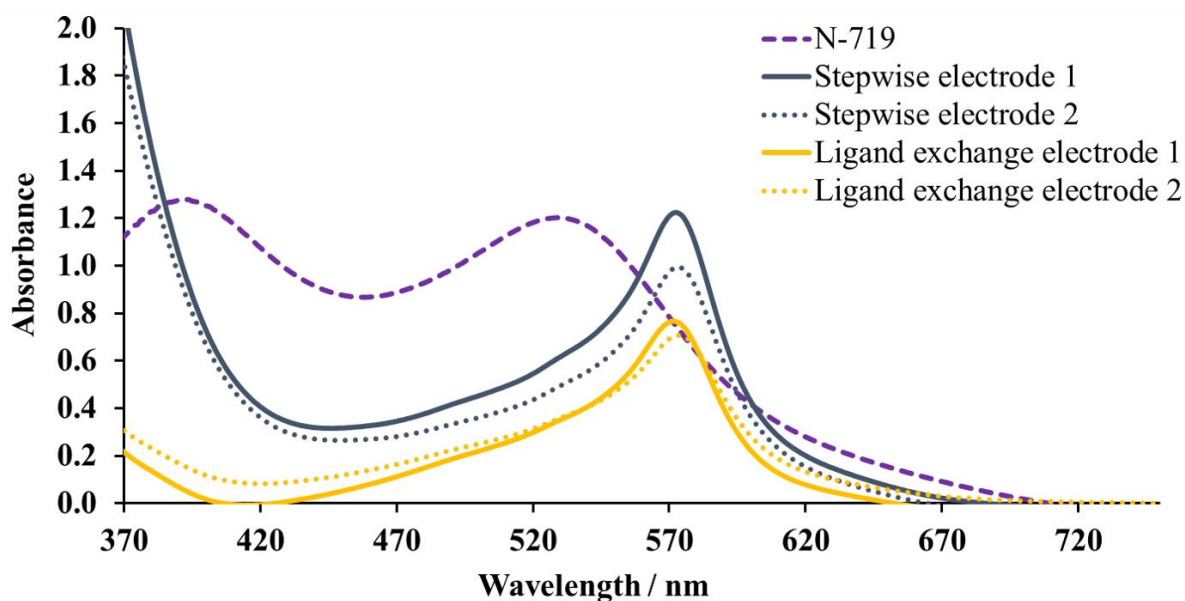


Figure 3.4. Solid state UV-Vis absorption spectra of Fe(II) complexes on a TiO₂ surface using stepwise (blue) and ligand exchange (yellow) approaches. Violet line refers to ruthenium complex N719 used as a standard.

Not only the dye is responsible for the DSC performance. The electrolyte has a great influence on PCE as well. Our starting point for measuring the overall performance of iron-based DSCs was the electrolyte Stnd II PF. It consists of LiI, I₂, 1-butyl-3-methylimidazolium hexafluorophosphate (BMIPF) and 1-methylbenzimidazole (MBI) in 3-methoxypropionitrile (MPN) as solvent (Figure 3.5, Table 3.1, electrolyte composition Stnd II PF). The first DSCs devices with [Fe(III-5)(Phtpy)]²⁺ complex had shown no performance. As a consequence, we had to change our electrolyte composition. In iodide/triiodide redox couple iodine binds with iodide for formation of triiodide (Equation 3.1).⁸⁴



Thus, iodine concentration influences the redox shuttle formation. Since iodide/triiodide redox couple was used in our case, the concentration of iodine was changed from 0.05 to 0.1 M (Table 3.1, electrolyte composition Stnd II A).

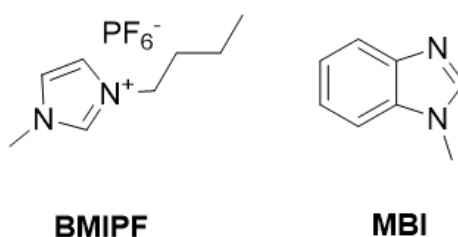


Figure 3.5. Structures of BMIPF and MBI.

Table 3.1. Electrolyte compositions used for the $[\text{Fe}(\text{III}-5)(\text{Phtpy})]^{2+}$ -based DSCs with MPN as a solvent.

| Electrolyte | LiI / M | I ₂ / M | BMIPF / M | MBI / M |
|-------------|---------|--------------------|-----------|---------|
| Std II PF | 0.10 | 0.05 | 0.60 | 0.50 |
| Std II A | 0.10 | 0.10 | 0.60 | 0.50 |
| Std II B | 0.20 | 0.10 | 0.60 | 0.50 |

The performances of both DSC sets were low compared to the commonly used reference dye N719 (Table 3.2). However, to our knowledge it was the first performing DSC based on an $[\text{Fe}(\text{III}-5)(\text{Phtpy})]^{2+}$ complex. The open-circuit voltage is pleasingly high when compared to N719, but low values of J_{SC} lead to PCE values of 0.02-0.05% (Table 3.2). Despite the fact that the $_{\text{ss}}\text{UV-Vis}$ absorption is higher for the stepwise approach, the performance of DSCs based on this dye assembly strategy is lower compared to the ligand exchange on the surface (Table 3.2). This can be explained with two times higher J_{SC} values for DSCs KAM013. The unmasking of KAM014 DSCs did not improve the overall efficiency (the effect of masking is described in the First Chapter, Section 2.2). Despite a higher V_{OC} value, J_{SC} was not affected by mask removal (Figure 3.6). This observation is not so different from the trends seen on masking DSCs with a bis(diimine)copper(I) sensitizer.¹⁶² The electrolyte Std II A caused for N719 a low efficiency of 0.82% compared to values (PCE of $\approx 6.0\%$) obtained with an electrolyte, which is commonly employed for this dye (LiI 0.10 M, I₂ 0.05 M, BMII 0.60 M and MBI 0.50 M in MPN). These results demonstrate that an increased amount of iodine in the electrolyte system is beneficial only for $[\text{Fe}(\text{III}-5)(\text{Phtpy})]^{2+}$ dye and not for N719. Further changes in the electrolyte did not lead to additional positive effects. Increasing the LiI concentration from 0.10 to 0.20 M (Table 3.1, electrolyte Std II B) resulted in no current going through the cell. Another electrolyte with I^-/I_3^- redox shuttle (LiI 0.10 M, I₂ 0.05 M and TBP 0.50 M) in MeCN had a negative influence on PCE. Changing the redox couple to $\text{Co}^{2+}/\text{Co}^{3+}$ (electrolyte composition $[\text{Co}(\text{bpy})_3][\text{PF}_6]_2$ 0.20 M, $[\text{Co}(\text{bpy})_3][\text{PF}_6]_3$ 0.05 M, 4-*tert*-butylpyridine 0.20 M, LiClO₄ 0.10 M in MeCN) resulted in no current going through cells.

Table 3.2 Parameters for DSCs with $[\text{Fe}(\text{III}-5)(\text{Phtpy})]^{2+}$ as sensitizers using different dye assembly approaches. The tested electrolyte was Std II A. All DSCs were fully masked if not mentioned different.

| DSC | Dye assembly | $J_{\text{sc}} / \text{mA cm}^{-2}$ | $V_{\text{oc}} / \text{mV}$ | $ff / \%$ | $\eta / \%$ |
|---------------|-----------------|-------------------------------------|-----------------------------|-----------|-------------|
| N719 | – | 2.11 | 602 | 64 | 0.82 |
| KAM013 cell 1 | Ligand exchange | 0.14 | 445 | 71 | 0.05 |
| KAM013 cell 2 | Ligand exchange | 0.15 | 437 | 59 | 0.04 |
| KAM014 cell 1 | Stepwise | 0.07 | 407 | 65 | 0.02 |

Third Chapter

| | | | | | |
|-------------------------------------|----------|------|-----|----|------|
| KAM014 cell 1 unmasked | Stepwise | 0.07 | 469 | 69 | 0.02 |
| KAM014 cell 2 unmasked ¹ | Stepwise | 0.06 | 520 | 65 | 0.02 |

¹ Due to the low performance, KAM014 cell 2 is presented only unmasked. No current was detected with mask.

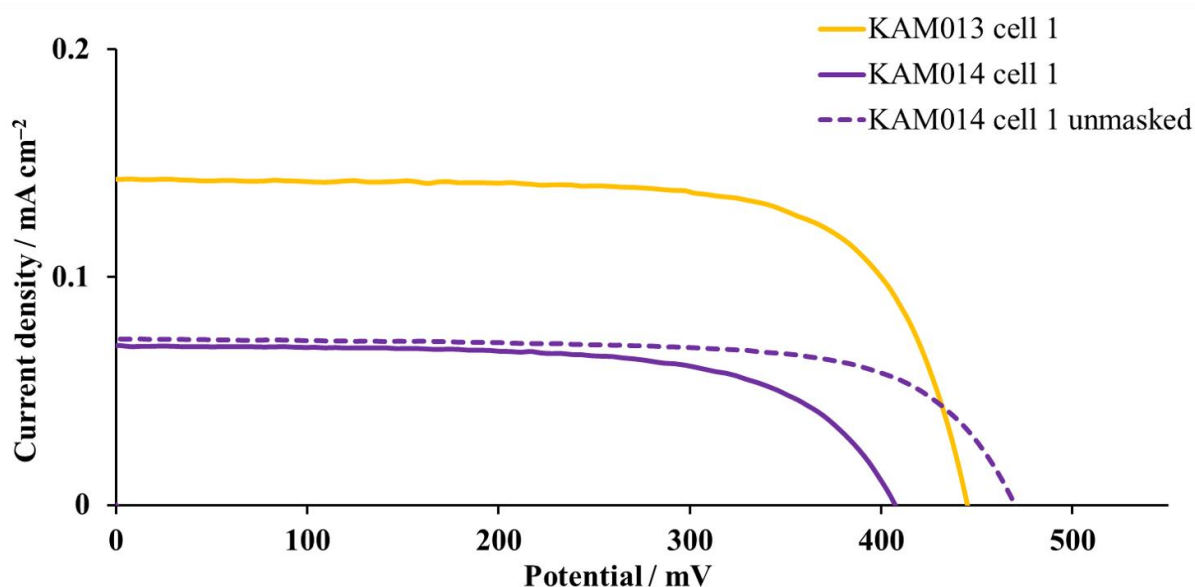
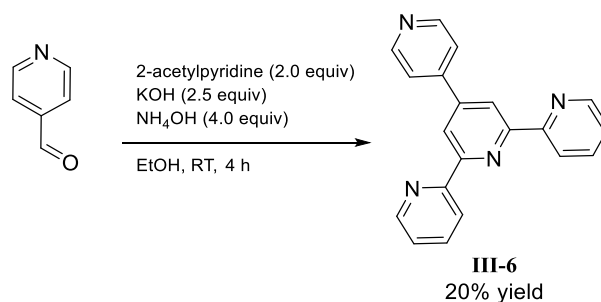


Figure 3.6. *J-V* curves for DSCs KAM013 and KAM014 with electrolyte Sntd II A.

Different derivatives of tpy-ligands (III-6 – III-10, Figure 3.7) were prepared by the Kröhnke pyridine synthesis starting from substituted benzaldehyde or isonicotinaldehyde and 2-acetylpyridine (Scheme 3.4). The ligands III-7 – III-10 were chosen to create a push-pull complex design. The ancillary ligand III-6 has a negative mesomeric effect and it was of our interest to compare its performance with donative systems. All ancillary ligands were used in dye assembly with phosphonic acid III-5 as the anchoring ligand *via* the stepwise approach. However, DSCs based on these dyes had only low short-circuit current densities ($J_{SC} \leq 0.01 \text{ mA cm}^{-2}$) looking at the cells with the electrolytes mentioned above (Tables 3.1 and 3.2).



Scheme 3.4. Preparation of 4'-(pyridin-4-yl)-2,2':6,2''-terpyridine ligand III-6 *via* the Kröhnke synthesis.

Third Chapter

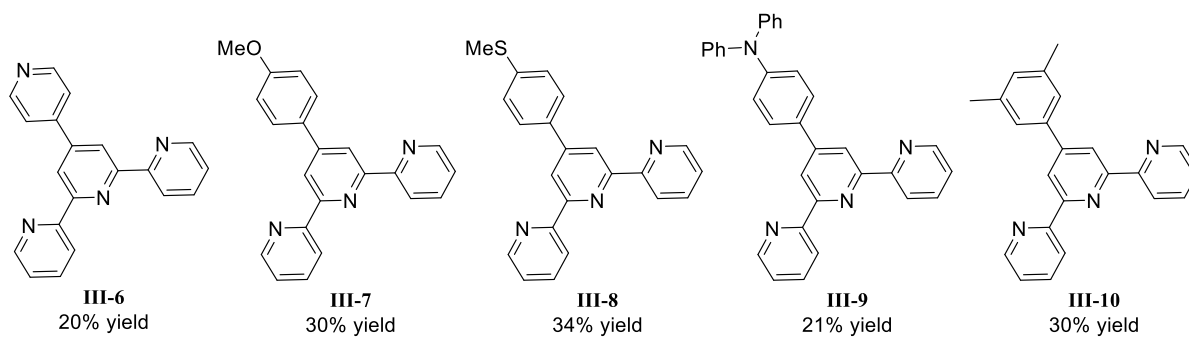


Figure 3.7. Structures of tpy derivatives used as ancillary ligands for various dyes $[\text{Fe}(\text{III-5})(\text{L}_{\text{ancill}})]^{2+}$ assembled with the stepwise approach.

3. Electrolyte tuning for DSCs sensitized with Fe-NHC complexes ⁴

The part of this study was performed with a help of Wahlpraktikum student Vanessa Wyss.

As discussed in the Introduction (First Chapter), iron(II)-complexes suffer from electron recombination from an MLCT state to a low-lying MC state. A short electron lifetime results in an inefficient electron injection and low values of J_{SC} . In 2013, the first iron(II) NHC complex with an extended ³MLCT lifetime was published by the group of Wärnmark (Figure 3.8, complex I-3).⁸² In 2015, Gros and co-workers reported an Fe-NHC based DSC with an I^-/I_3^- redox shuttle and PCE of 0.13% (PCE of 6.1% with a respect to N719 reference, Figure 3.8, complex I-4).⁸³ However, this report does not mention the use of a mask for the DSCs during $J-V$ measurements, and it is therefore assumed that the cells were not masked. As noted above, this could lead to an over-estimation of cell performance.

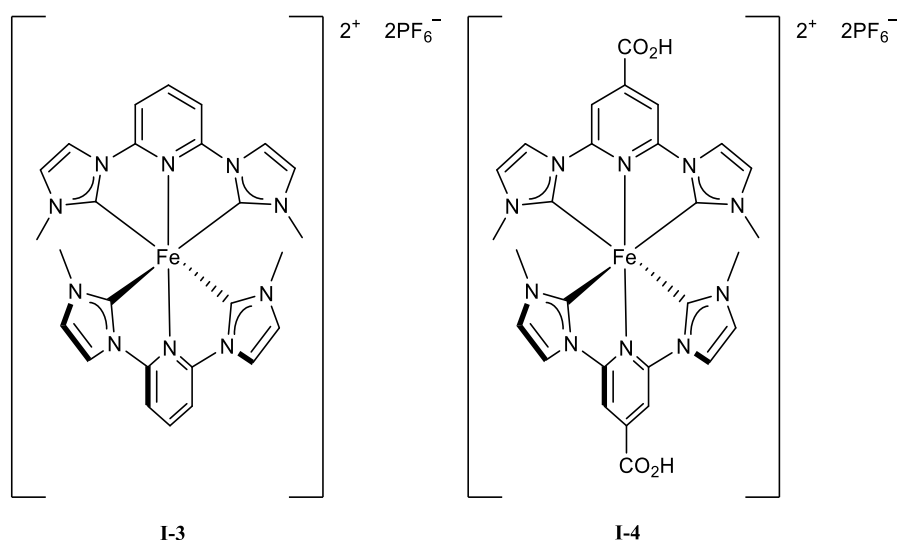


Figure 3.8. The structures of iron(II) NHC complexes I-3 and I-4.

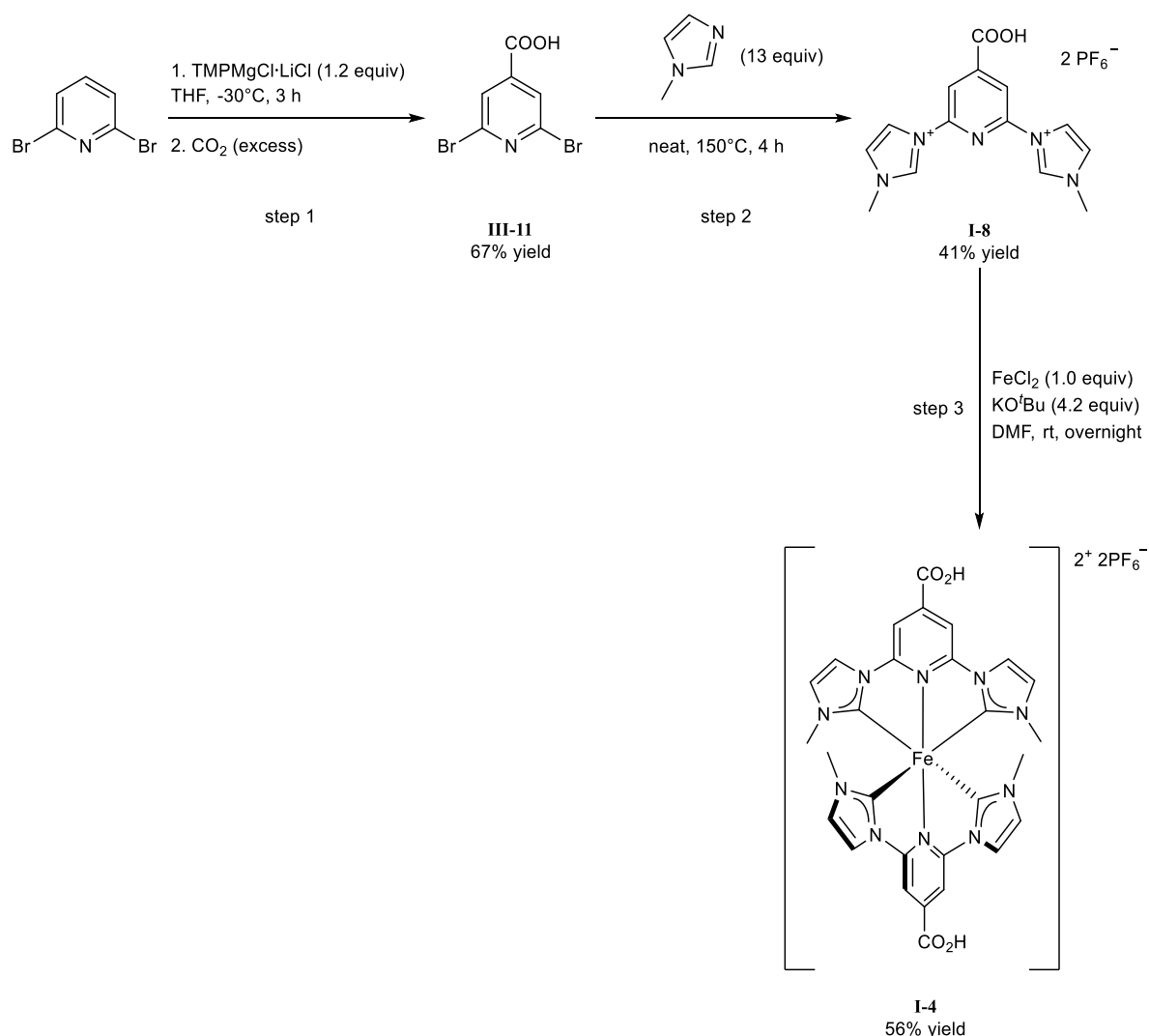
Having decided to move from the $[Fe(tpy)_2]^{2+}$ -based dyes to iron(II) NHC dyes, we chose to focus on electrolyte-tuning as a first exploration, rather than develop the dye structure. Both compounds I-3 and I-4 have previously been reported.^{83, 125} The synthesis of I-4 is shown in Scheme 3.5. In the first step, the 2,6-dibromoisonicotinic acid (III-11) was synthesized *via* metalation of 2,6-dibromopyridine and sequential quench with dry ice. The product was isolated with 67% yield. This reaction will be discussed in detail in the Fourth Chapter. In the next step ligand I-8 was synthesized in 41% yield from 2,6-dibromoisonicotinic acid *via* substitution

⁴ Parts of this study have been published:

- M. Karpacheva, C. E. Housecroft, E. C. Constable, *Beilstein J. Nanotechnol.* **2018**, *9*, 3069.
- M. Karpacheva, V. Wyss, C. E. Housecroft, E. C. Constable, *Materials*, **2019**, *12*, 4181.

Third Chapter

reaction with 1-methylimidazole. The last step includes the complexation reaction of the ligand with iron(II) chloride in the presence of KO^tBu as the base. The reaction afforded the target complex I-4 in 56% yield.



Scheme 3.5. The synthesis of dye I-4.

The previously reported study has focused on the structural modification of Fe(NHC)-complexes. Our investigations of [Fe(Phtpy)₂]²⁺ as a sensitizer have shown that changes in an electrolyte composition have a noticeable effect on the PCE of an iron-based DSC. Here, we demonstrated the influence of varying electrolyte composition on the DSC performance sensitized by the NHC iron(II) dye I-4 shown in Figure 3.8. From here on until the end of the third chapter we will exclusively focus on electrolyte optimisation and the working electrode is sensitized with dye III-4 and chenodeoxycholic acid (0.5 mM and 0.1 mM, respectively) constantly for all experiments.

3.1 Electrolyte optimisation based on effects of solvent and additives

3.1.1 The effect of solvent and ionic liquid

The Stnd II A electrolyte was first investigated for iron(II) NHC-based DSCs, since it was the only one performing for a DSC sensitized with $[\text{Fe}(\text{III}-5)(\text{Phtpy})_2]^{2+}$. The reference was the commercially available (Solaronix) electrolyte AN-50 (Table 3.3) employed by Gros⁸³ combined with an I^-/I_3^- redox shuttle, 1,2-dimethyl-3-propylimidazolium iodide (PDMII, Figure 3.9) and various N-containing heterocyclic additives in MeCN (Table 3.3).

Table 3.3. Parameters for DSCs with NHC Fe(II)-complex as sensitizer with Stnd II A electrolyte. For the electrolyte compositions see Table 3.1. All DSCs were fully masked.

| DSC | $J_{\text{sc}} / \text{mA cm}^{-2}$ | $V_{\text{oc}} / \text{mV}$ | $ff / \%$ | $\eta / \%$ |
|--------------------|-------------------------------------|-----------------------------|-----------|-------------|
| Stnd II A cell 1 | 0.03 | 35 | 28 | 0.0003 |
| Stnd II A cell 2 | 0.02 | 42 | 29 | 0.0003 |
| AN-50 ¹ | 0.41 | 457 | 68 | 0.13 |

¹ Previously published data by Gros.⁸³

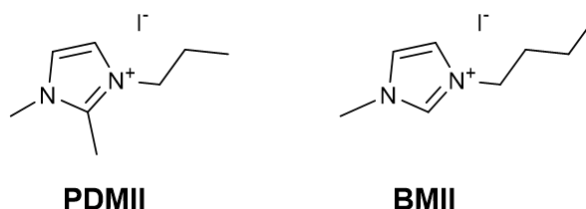


Figure 3.9. Structures of 1-propyl-2,3-dimethylimidazolium iodide (PDMII) and 1-butyl-3-methylimidazolium iodide (BMII).

The performances of NHC iron(II)-based DSCs with electrolyte Stnd II A were lower than previously reported for AN-50 due to low values of J_{sc} , V_{oc} and ff . As known in the literature, the usage of BMII is common for bis(diamine)copper(I) sensitizers instead of BMIPF as ionic liquid alongside lower iodine concentrations (Figure 3.9). Therefore, we decided to apply this knowledge to our system. The IL was changed from BMIPF to BMII (Figure 3.9) and the I_2 concentration was reduced from 0.10 M to 0.05 M while keeping the rest of the electrolyte composition unmodified (electrolyte composition E1, Table 3.4). The change of the counter-ion from $[\text{PF}_6]^-$ to I^- positively affected the overall performance of DSCs and resulted in values close to the DSC with commercial AN-50 electrolyte (Table 3.5). The example of BMIPF and BMII demonstrates how crucial the influence of IL counter-ion is. Further change of ionic liquid from BMII to PDMII (electrolyte

composition E2, Table 3.5) enhanced the PCE from 0.11 to 0.17%, due to the higher J_{SC} values of 0.54 mA cm^{-2} compared to 0.34 mA cm^{-2} for E1.

Table 3.4. Electrolyte compositions used for the NHC iron(II)-based DSCs with MPN as a solvent.

| Electrolyte | LiI / M | I ₂ / M | IL / M | MBI / M | Solvent |
|-------------|---------|--------------------|------------|---------|---------|
| E1 | 0.10 | 0.05 | BMII 0.60 | 0.50 | MPN |
| E2 | 0.10 | 0.05 | PDMII 0.60 | 0.50 | MPN |
| E1a | 0.10 | 0.05 | BMII 0.60 | 0.50 | MeCN |
| E2a | 0.10 | 0.05 | PDMII 0.60 | 0.50 | MeCN |

Table 3.5. Parameters for DSCs with NHC Fe(II)-complexes as sensitizers using different electrolytes. For the electrolyte compositions see Table 3.4. All DSCs were fully masked.

| Electrolyte | $J_{SC} / \text{mA cm}^{-2}$ | V_{OC} / mV | $ff / \%$ | $\eta / \%$ | Rel. $\eta / \%$ ¹ |
|-------------|------------------------------|----------------------|-----------|-------------|-------------------------------|
| E1 cell 1 | 0.32 | 429 | 72 | 0.10 | 1.7 |
| E1 cell 2 | 0.34 | 451 | 73 | 0.11 | 1.8 |
| E2 cell 1 | 0.54 | 427 | 71 | 0.17 | 2.8 |
| E2 cell 2 | 0.54 | 426 | 71 | 0.16 | 2.6 |
| N719 | 13.87 | 705 | 62 | 6.02 | 100 |

¹ Relative to a value of η for N719 set at 100%.

Electrolytes E1 and E2 are based on 3-methoxypropionitrile as solvent. Another solvent, which is often employed in electrolytes, is MeCN (the electrolyte composition is shown in Table 3.4). Comparing E1 to E1a and E2 to E2a, we changed the solvent from MPN to MeCN with the retained compositions. The solvent change did not have beneficial effects and PCE values decreased to 0.07% for both E1a and E2a electrolytes (Table 3.6). Remarkably, a change from MPN to MeCN affected V_{OC} and ff only slightly and the main decrease in PCE is observed by lower J_{SC} values of 0.24 and 0.25 mA cm^{-2} for E1a and E2a, respectively. Figure 3.10 illustrates the effect of solvent for electrolytes E1, E2, E1a and E2a. Interestingly, the use of MeCN as solvent resulted in no significant differences in DSC performance between electrolytes E1a and E2a (Table 3.6) what is not the case for the similar electrolyte compositions E1 and E2 with MPN as a solvent.

Table 3.6. Parameters for DSCs with NHC Fe(II)-complexes as sensitizers using MeCN as solvent in electrolytes. For the electrolyte compositions, see Table 3.4. All DSCs were fully masked.

| Electrolyte | $J_{SC} / \text{mA cm}^{-2}$ | V_{OC} / mV | $ff / \%$ | $\eta / \%$ | Rel. $\eta / \%$ ¹ |
|-------------------------|------------------------------|----------------------|-----------|-------------|-------------------------------|
| E1a cell 1 | 0.19 | 419 | 68 | 0.05 | 0.8 |
| E1a cell 2 | 0.24 | 418 | 68 | 0.07 | 1.2 |
| E2a cell 1 | 0.25 | 432 | 69 | 0.07 | 1.2 |
| E2a cell 2 ² | – | – | – | – | – |

| | | | | | |
|------|-------|-----|----|------|-----|
| N719 | 13.87 | 705 | 62 | 6.02 | 100 |
|------|-------|-----|----|------|-----|

¹ Relative to a value of η for N719 set at 100%; ² No current was detected going through the DSC.

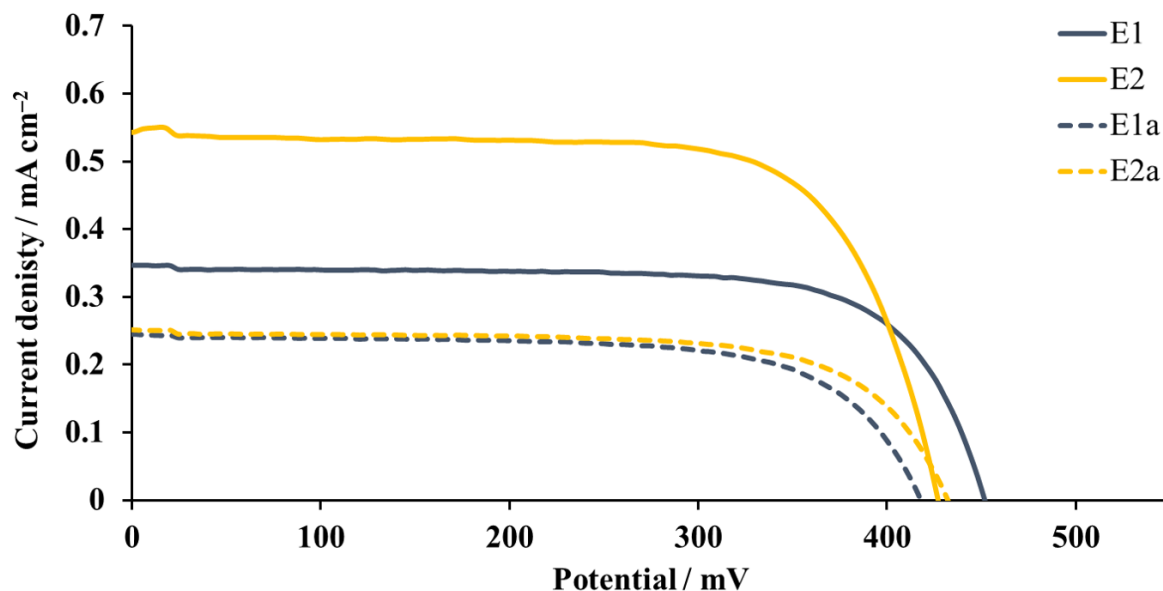


Figure 3.10. The effect of solvent change from MPN to MeCN.

3.1.2 The effect of nitrogen-containing heterocyclic additives

Each component of an electrolyte contributes to the performance of a DSC. Nitrogen-containing heterocycles such as 1-methylbenzimidazole or 4-*tert*-butylpyridine (Figure 3.11) are commonly used as additives because of their ability to move the conduction band of a semiconductor towards negative potentials.¹⁶³ This effect leads to an increase in open-circuit potential which depends on the Fermi level of the semiconductor.¹⁶⁴

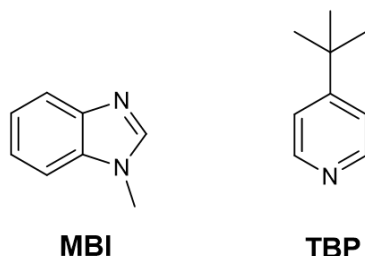


Figure 3.11. Structures of 1-methylbenzimidazole (MBI) and 4-*tert*-butylpyridine (TBP).

As DSCs with E2 have a better performance than with E1, the further optimisation of the components of the electrolyte containing PDMII was performed. Electrolyte compositions with

different concentrations of MBI and TBP are presented in Table 3.7. The electrolyte compositions include LiI 0.10 M, I₂ 0.05 M, PDMII 0.60 M and variable additives with MPN as a solvent. The dependency of J_{SC} values on the additive concentration is obvious. Upon decrease the concentration of MBI from 0.50 M to 0.01 M, the J_{SC} value was enhanced from 0.54 mA cm⁻² to 2.78 mA cm⁻² (Tables 3.5 and 3.7). The values of V_{OC} were expectedly decreased from 395 to 307 mV for E2 and E2e, respectively, with lower MBI concentrations. Despite the significant drop in V_{OC} , the overall efficiency increased from 0.17 to 0.53% because of higher J_{SC} values, which are result of more favourable electron injection into the CB of the semiconductor.

Table 3.7. Parameters for DSCs with NHC Fe(II)-complexes as sensitizers. Electrolyte compositions include LiI 0.1 M, I₂ 0.05 M, PDMII 0.6 M and variable additives with MPN as a solvent. All DSCs were fully masked.

| Electrolyte | Additive / M | J_{SC} / mA cm ⁻² | V_{OC} / mV | ff / % | η / % | Rel. η / % ¹ |
|-------------|--------------|--------------------------------|---------------|----------|------------|------------------------------|
| E2b cell 1 | – | 2.31 | 339 | 65 | 0.51 | 8.5 |
| E2b cell 2 | | 2.34 | 374 | 65 | 0.57 | 9.3 |
| E2c cell 1 | MBI 0.10 M | 0.69 | 395 | 65 | 0.18 | 2.9 |
| E2c cell 2 | | 0.54 | 393 | 64 | 0.14 | 2.3 |
| E2d cell 1 | MBI 0.05 M | 1.31 | 395 | 60 | 0.31 | 5.1 |
| E2d cell 2 | | 1.22 | 358 | 58 | 0.25 | 4.2 |
| E2e cell 1 | MBI 0.01 M | 2.78 | 307 | 62 | 0.53 | 8.8 |
| E2e cell 2 | | 2.51 | 315 | 62 | 0.51 | 8.5 |
| E2f cell 1 | TBP 0.10 M | 0.39 | 368 | 66 | 0.09 | 2.6 |
| E2f cell 2 | | 0.69 | 387 | 67 | 0.18 | 2.9 |
| E2g cell 1 | TBP 0.05 M | 1.16 | 380 | 65 | 0.29 | 4.8 |
| E2g cell 2 | | 1.09 | 372 | 66 | 0.27 | 4.5 |
| E2h cell 1 | TBP 0.50 M | 0.76 | 541 | 62 | 0.26 | 4.3 |
| E2h cell 2 | | 0.73 | 518 | 64 | 0.24 | 4.0 |
| N719 | – | 13.87 | 705 | 62 | 6.02 | 100 |

¹ Relative to a value of η for N719 set at 100%.

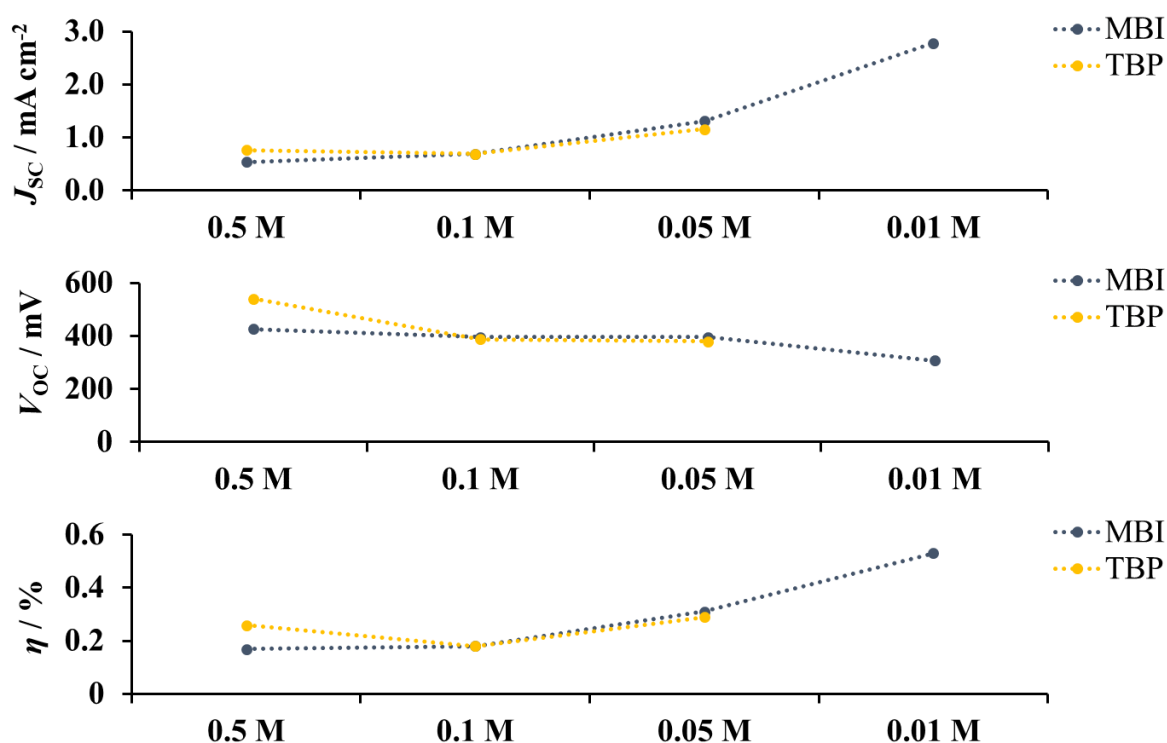


Figure 3.12. The trends of J_{sc} , V_{oc} and η depending on the concentration of additives. Blue lines correspond to MBI additive, yellow lines correspond to TBP.

It is well established in the literature that the presence of TBP in an electrolyte remarkably improves the open-circuit voltage.^{165, 166} Therefore, we considered investigating a change from MBI to TBP, while retaining the rest of the electrolyte composition.

At the maximum concentration of 0.50 M TBP (E2h), the overall efficiency as well as J_{sc} and V_{oc} is slightly higher than for MBI with the same concentration (Figure 3.12). From 0.10 M TBP concentration the trend in J - V curves becomes similar to electrolyte with MBI in it. A decrease of the TBP concentration to 0.05 M results in a significant decrease in open-circuit voltage, while J_{sc} values are slightly improved. Overall, this resulted in a small increase of η from 0.26 (0.5 M TBP) to 0.29% (0.05 M TBP). Since the TBP concentration trends look remarkably similar to MBI a further reduction of the TBP concentration was not considered and as a next step, the electrolyte without any additives was tested.

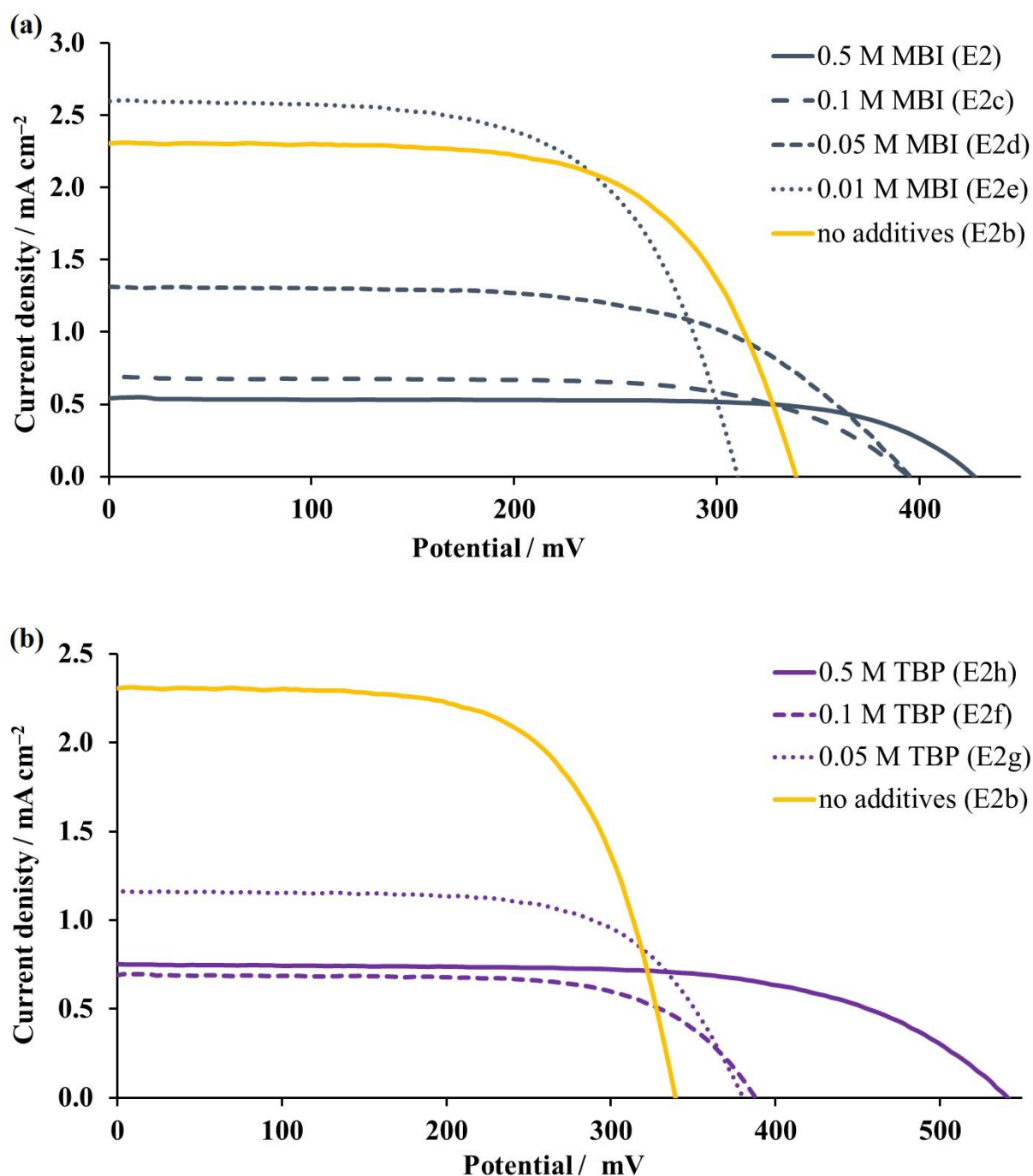


Figure 3.13. J - V curves illustrate the effects of removing additives (in both figures yellow line refers to DSC with no additives): (a) DSCs with MBI additive; (b) DSCs with TBP additive.

Interestingly, the removal of additives resulted in a minor decrease in J_{SC} from 2.78 to 2.34 mA cm^{-2} and in a gain in V_{OC} from 307 mV to 374 mV going from E2e to E2b, respectively (Figure 3.13a). This improvement in V_{OC} caused a remarkable overall efficiency for iron(II)-sensitizers of 0.57%, which is representing 9.3% relative to N719 set as 100%. The comparison between electrolytes E2 and E2h (each using 0.5 M of additive) to E2b, which has no additive, clearly shows the trend on improving J_{SC} at the expense of V_{OC} , which can be clearly

seen in Figure 3.13 (yellow line represents J - V curve for E2b electrolyte). High V_{OC} values of 427-426 mV for electrolyte E2 and 541-518 mV for electrolyte E2h are followed with low J_{SC} . More than twice higher short-circuit density is combined with V_{OC} of 374-339 mV for electrolyte E2b. However, the gain in short-circuit density overtakes the loss in open-circuit voltage and results in higher η values.

3.1.3 Analysing the effect of MBI additive via electrochemical impedance spectroscopy

For a more thorough understanding of the role of the MBI additive in the NHC iron(II)-system, EIS measurements were conducted for electrolytes E2b, E2c and E2e with no MBI, 0.10 M and 0.01 M, respectively. Experiments and curve fittings were made for multiple DSCs of each electrolyte for obtaining a representative outcome and to confirm the observed trends. J - V curves were measured to confirm that the devices were fully operational and reproducible (Table 3.8, parameters for electrolyte E2c are presented in Table 3.7).

The equivalent circuit model 1 used in this study is shown in Figure 3.14 and consists out of five elements. The first element R_s represents series resistance, resistance R_{Pt} and constant phase element CPE model a platinum counter electrode, an extended distributed element represents TiO_2 /electrolyte interface. The last element in the circuit is the Warburg element, which is associated with diffusion of the electrolyte. The elements of the model are discussed in detail in First Chapter.

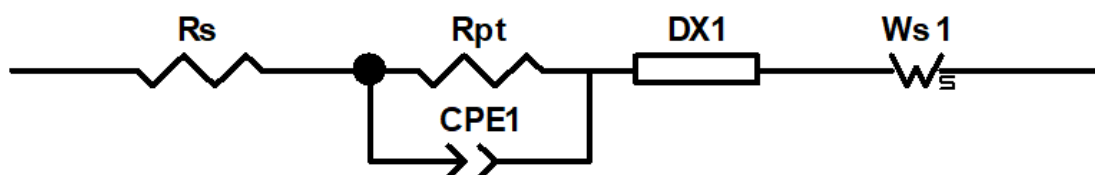


Figure 3.14. The equivalent circuit model 1. R_s is series resistance; R_{Pt} – platinum resistance and CPE1 – constant phase element to model platinum counter electrode; $DX1$ – distributed element to represent TiO_2 /electrolyte interface; W_s – Warburg element associated with diffusion of the electrolyte.

Table 3.8. Parameters for multiple DSCs with electrolytes E2b and E2e. All DSCs were fully masked.

| Electrolyte | DSC | $J_{SC} / \text{mA cm}^{-2}$ | V_{OC} / mV | $ff / \%$ | $\eta / \%$ | Rel. $\eta / \%$ ¹ |
|-------------|-----|------------------------------|----------------------|-----------|-------------|-------------------------------|
| E2b | 1 | 2.58 | 292 | 63 | 0.47 | 7.8 |
| | 2 | 2.38 | 326 | 65 | 0.51 | 8.5 |
| | 3 | 2.31 | 339 | 65 | 0.51 | 8.5 |
| | 4 | 2.34 | 374 | 65 | 0.57 | 9.3 |
| E2e | 1 | 2.60 | 310 | 62 | 0.50 | 8.3 |
| | 2 | 2.51 | 308 | 63 | 0.49 | 8.1 |
| | 3 | 2.78 | 307 | 62 | 0.53 | 8.8 |
| | 4 | 2.61 | 315 | 62 | 0.51 | 8.5 |
| N719 | - | 13.87 | 705 | 62 | 6.02 | 100 |

¹ Relative to a value of η for N719 set at 100%.

Parameters and their average values extracted from fitting experimental EIS curves with circuit model 1 are given in Table 3.9. The Nyquist plots are shown in Figure 3.15. The values of the counter electrode remain constant, setting R_s is $\approx 10 \Omega$, R_{Pt} is $\approx 10 \Omega$ and C_{Pt} is $\approx 8 \mu\text{F}$. DSCs based on electrolytes E2b and E2e, either with no additive or 0.01 M MBI, have similar photoconversion efficiencies as well as close J_{SC} values (Table 3.8). A ten-fold increase of MBI to 0.1 M significantly lowered J_{SC} values from 2.38 to 0.69 mA cm^{-2} and, as a result, PCE. This effect has a response in the EIS data as well. The recombination resistance values greatly increased starting from low concentrations (0.01 M) of MBI to 0.1 M. This results in an overlap of the second semicircle with the third one corresponding to charge carrier diffusion resistance in the electrolyte (Figure 3.15). High values of R_{rec} for E2c electrolyte correspond to a low rate of electron injection into a CB of semiconductor and consequently explain low J_{SC} . The changes in MBI concentration did not fundamentally affect transport resistance (R_{tr}), electron lifetime and diffusion length as shown in Table 3.9. Thus, high values of R_{rec} for E2c electrolyte is the only parameter, which is mainly depended on MBI concentration and has a dramatic effect on the overall performance of the cell. For each electrolyte, diffusion length (L_d) is greater than semiconductor thickness, and transport time (τ_t) is smaller than electron lifetime (τ). The combination of these factors results in an efficient electron transport through the semiconductor and collection of electrons on the back of the working electrode. These elements contribute to the value of J_{SC} in combination with recombination and transport resistances. L_d , τ and τ_t increase in the order E2c \rightarrow E2b \rightarrow E2e and the trend is consistent with V_{OC} values (Table 3.8). EIS measurements were also performed for electrolyte E2 containing 0.5 M of MBI. Despite similar DSC performance to E2c, no separation

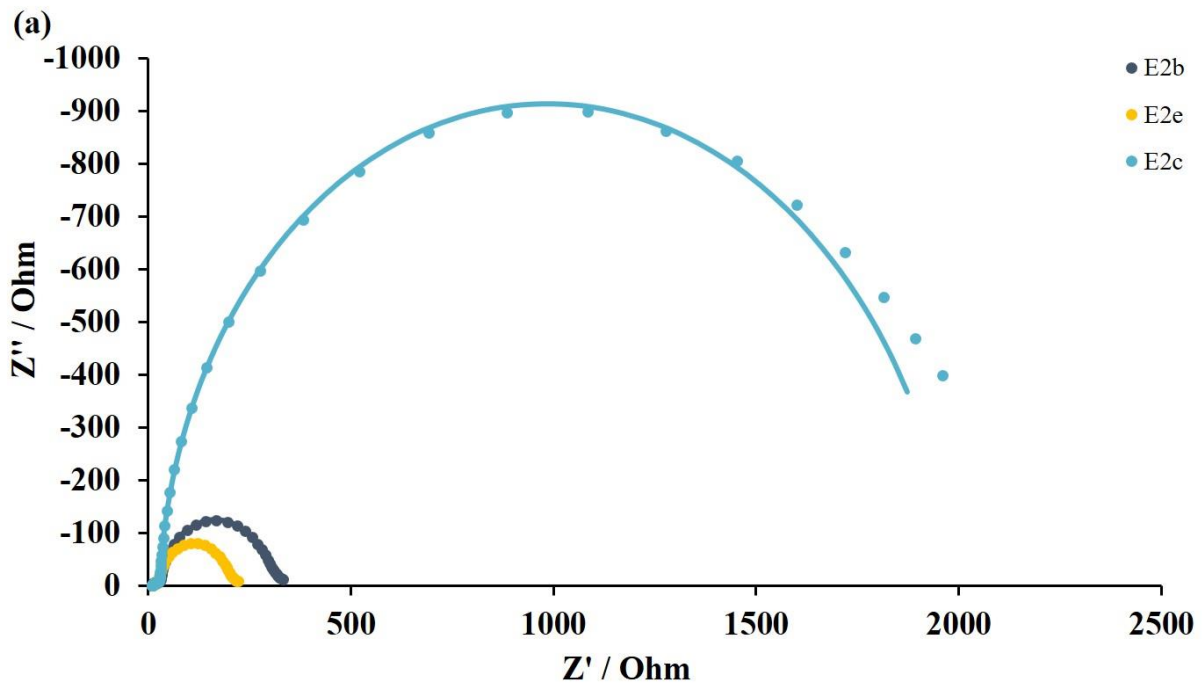
Third Chapter

between three semicircles in Nyquist plot was observed. Therefore, we were unable to fit the results due to the extremely high resistance dominating the second semicircle.

Table 3.9. EIS parameters for DSCs using electrolytes with different concentration of MBI.

| Electrolyte ¹ | R_{rec} / Ω | $C_{\mu} / \mu F$ | R_{tr} / Ω | τ / ms | τ_t / ms | $L_d / \mu m$ | R_s / Ω | R_{Pt} / Ω | $C_{Pt} / \mu F$ |
|--------------------------|--------------------|-------------------|-------------------|-------------|---------------|---------------|----------------|-------------------|------------------|
| E2b cell 1 | 124 | 360 | 28 | 45 | 10 | 25 | 10 | 13 | 7 |
| E2b cell 2 | 198 | 257 | 54 | 51 | 14 | 23 | 10 | 8 | 8 |
| E2b cell 3 | 255 | 233 | 30 | 59 | 7 | 35 | 9 | 9 | 7 |
| E2b cell 4 | 259 | 400 | 14 | 103 | 6 | 52 | 9 | 6 | 8 |
| E2e cell 1 | 138 | 322 | 26 | 45 | 8 | 28 | 9 | 6 | 9 |
| E2e cell 2 | 158 | 365 | 32 | 58 | 12 | 27 | 11 | 9 | 9 |
| E2c cell 1 | 1830 | 307 | 25 | 561 | 8 | 102 | 10 | 8 | 8 |
| E2c cell 2 | 1889 | 328 | 18 | 620 | 6 | 122 | 11 | 15 | 7 |
| E2b _{average} | 209 | 312 | 31 | 65 | 9 | 34 | 10 | 9 | 8 |
| E2e _{average} | 148 | 344 | 29 | 52 | 10 | 28 | 10 | 8 | 9 |
| E2c _{average} | 1860 | 317 | 22 | 591 | 7 | 112 | 10 | 11 | 7 |

¹ average – the sum of all values for a given parameter divided by number of cells.



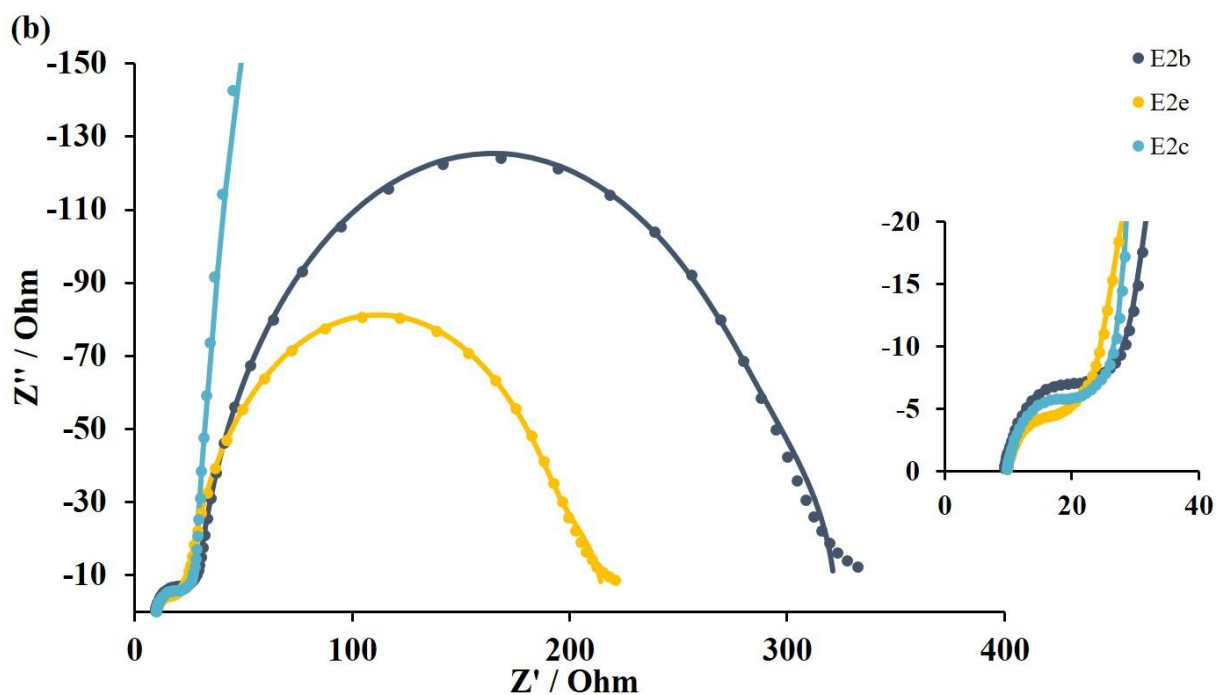


Figure 3.15. Nyquist plot of DSCs with electrolytes E2b, E2e and E2c; a. Full Nyquist plot; b. Expansion of Nyquist plot region. Dotted lines represent experimental data, solid lines represent fitted data.

3.1.4 Effect of additives towards different ionic liquids

It was discussed in section 3.1.2 that heterocyclic additives are not beneficial in the presence of PDMII ionic liquid. Thus, we decided to investigate if the same tendency is observed for other ionic liquids of the imidazolium family with different counterions (Figure 3.16). The electrolyte compositions are shown in Table 3.10.

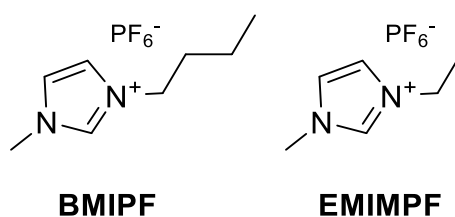


Figure 3.16. Structures of ionic liquids 1-butyl-3-methylimidazolium hexafluorophosphate (BMIPF) and 1-ethyl-3-methylimidazolium hexafluorophosphate (EMIMPF).

Table 3.10. Electrolyte compositions with and without additives. MPN was used as a solvent.

| Electrolyte | LiI / M | I ₂ / M | IL / M | MBI / M |
|-------------|---------|--------------------|-------------|---------|
| E3 | 0.10 | 0.05 | BMIPF 0.60 | 0.50 |
| E4 | 0.10 | 0.05 | EMIMPF 0.60 | 0.50 |
| E1b | 0.10 | 0.05 | BMII 0.60 | – |
| E3b | 0.10 | 0.05 | BMIPF 0.60 | – |
| E4b | 0.10 | 0.05 | EMIMPF 0.60 | – |

The effects of eliminating MBI from other ionic liquids such as BMII and BMIPF were positive (Table 3.11, with the electrolyte compositions given in Table 3.10). Despite a loss in V_{OC} from 451 to 304 mV, the significant gain in J_{SC} led to an increase in PCE from 0.11 to 0.38% on going from E1 to E1b, respectively. This corresponds to a relative efficiency of 6.3% with N719 set as 100% for E1b electrolyte. The same trend is observed for BMIPF based electrolytes E3 and E3b. The combination of lower V_{OC} and higher J_{SC} resulted in greater overall efficiency of 0.37% (6.1% with a respect to N179).

At the same time, the absence of the additive in E4b caused bleaching of the working electrode. When the electrolyte came into contact with the dye-sensitized surface, the original red colour of dye-functionalized TiO₂ turned almost white. This had a dramatic effect on the DSC performance. The fall in V_{OC} from 538 to 50 mV caused the overall efficiency of 0.01% for E4b (Figure 3.17). Interestingly, despite the bleaching of the electrode, the values of J_{SC} were not affected and stayed in the same range of 0.74-0.83 mA cm⁻².

Table 3.11. Parameters for DSCs with and without MBI and different ILs. All DSCs were fully masked.

| Electrolyte | J_{SC} / mA cm ⁻² | V_{OC} / mV | ff / % | η / % | Rel. η / % ² |
|------------------------|--------------------------------|---------------|----------|------------|------------------------------|
| E1 cell 1 ¹ | 0.32 | 429 | 72 | 0.10 | 1.7 |
| E1 cell 2 | 0.34 | 451 | 73 | 0.11 | 1.8 |
| E3 cell 1 | 0.24 | 477 | 69 | 0.08 | 1.3 |
| E3 cell 2 | 0.29 | 480 | 73 | 0.10 | 1.6 |
| E4 cell 1 | 0.74 | 519 | 69 | 0.26 | 4.3 |
| E4 cell 2 | 0.70 | 529 | 70 | 0.26 | 4.3 |
| E4 cell 3 | 0.90 | 538 | 69 | 0.33 | 5.5 |
| E4 cell 4 | 0.82 | 542 | 69 | 0.31 | 5.1 |
| E1b cell 1 | 1.94 | 304 | 64 | 0.38 | 6.3 |
| E1b cell 2 | 2.90 | 261 | 47 | 0.36 | 6.0 |
| E3b cell 1 | 2.13 | 308 | 56 | 0.37 | 6.1 |

| | | | | | |
|------------|-------|-----|----|------|-----|
| E3b cell 2 | 1.64 | 343 | 62 | 0.35 | 5.8 |
| E4b cell 1 | 0.74 | 43 | 26 | 0.01 | 0.2 |
| E4b cell 2 | 0.83 | 50 | 27 | 0.01 | 0.2 |
| N719 | 13.87 | 705 | 62 | 6.02 | 100 |

¹ Data for electrolyte E1 are taken from Table 3.5 and included for convenience. ² Relative to a value of η for N719 set at 100%.

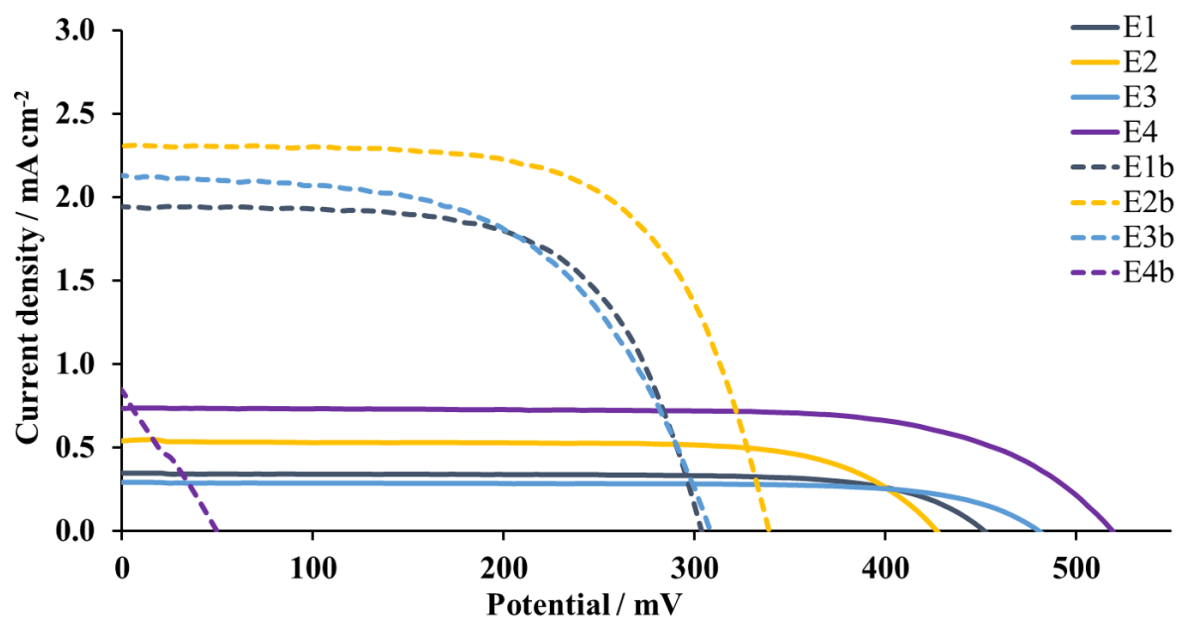


Figure 3.17. The effect of removal of MBI as additive from electrolytes E1, E2, E3 and E4.

3.1.5 External quantum efficiency measurements for DSCs with electrolytes E2b, E2c, E2e and E4

External quantum efficiency measurements reveal the number of photons that are converted into the electrons in the operating device under irradiance. DSCs based on PDMII ionic liquid exhibited broad external quantum efficiency spectra in the range of 420-570 nm (Figure 3.18). EQE was performed for duplicate cells to show the reproducibility of the measurement. The values of EQE_{max} were between $\approx 6\text{-}15\%$ at λ_{max} 470-530 nm and they were consistent with trends in J_{SC} for electrolytes $\text{E2e} > \text{E2b} \gg \text{E2c}$. Small difference in J_{SC} values for E2b and E2e resulted in close EQE_{max} values. The highest EQE_{max} of $\approx 15\%$ was observed for E2e electrolyte and $\approx 12\%$ for E2b. The electrolyte E2c with 0.1 M MBI had lower EQE_{max} of $\approx 8\%$. This decrease in EQE_{max} was consistent with a drop in J_{SC} . The use of EMIMPF (electrolyte E4) instead of PDMII further decreased the value of EQE_{max} to $\approx 6\%$.

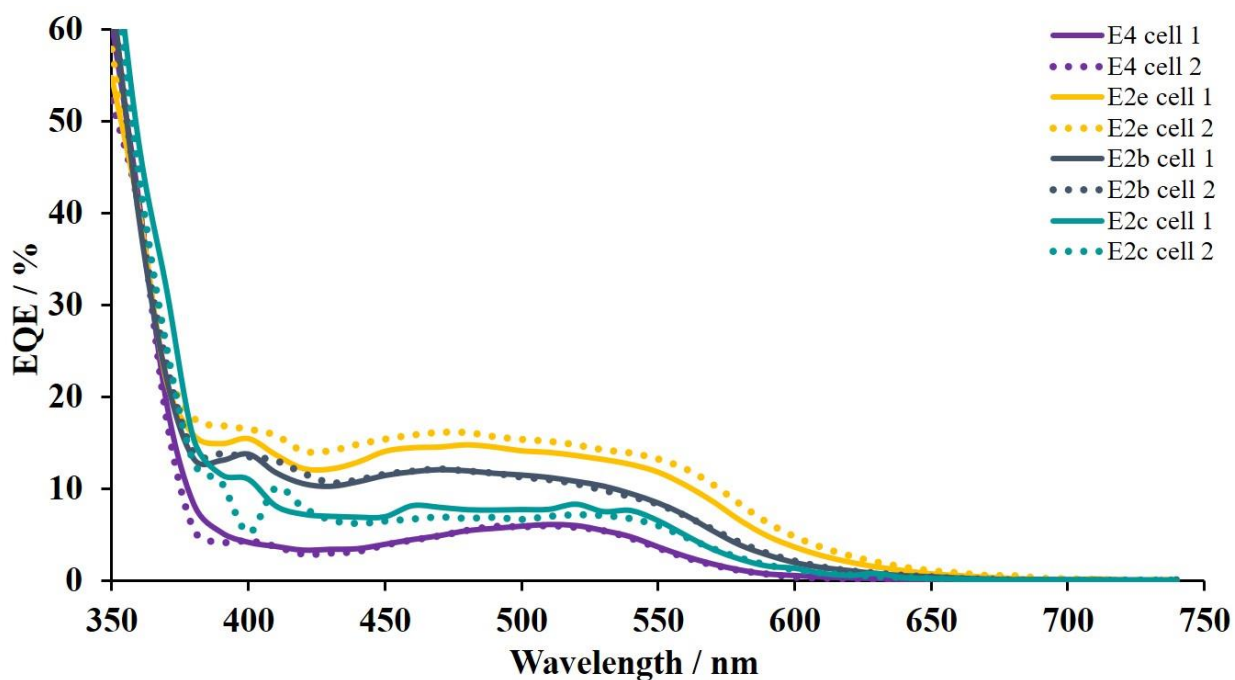


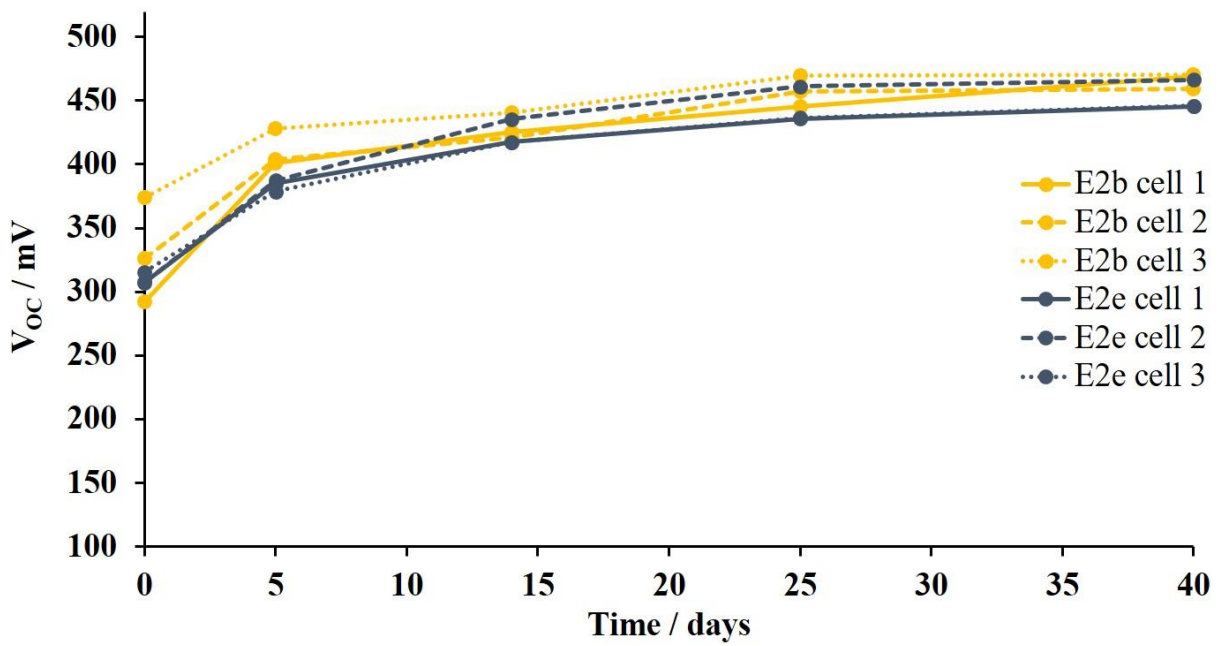
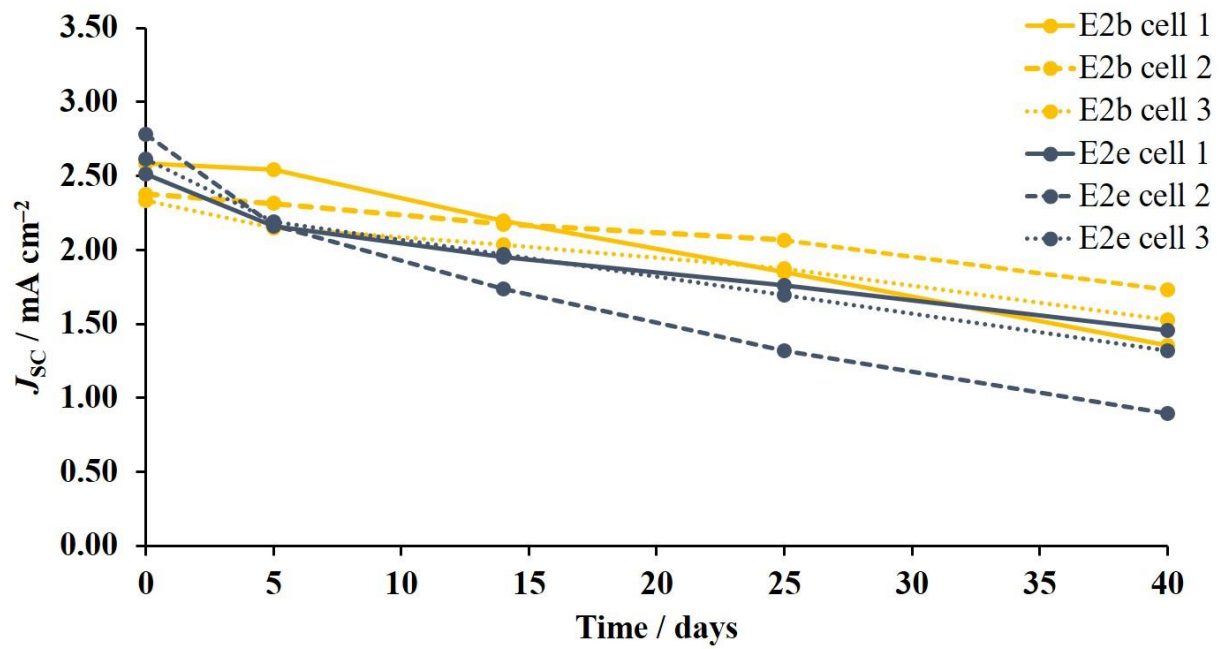
Figure 3.18. EQE curves for DSCs with electrolytes E4, E2e, E2c and E2b.

3.1.6 DSC stability test for electrolytes E2b and E2e

DSC performances were measured over a period of 40 days for electrolytes E2b and E2e on the example of three devices for each electrolyte. The DSC stabilities have been successfully demonstrated for both electrolytes over this period (Table 3.12). In average, PCE of the electrolyte decreased from 0.52 to 0.47% for E2b. In the case of E2e, the average PCE decreased from 0.51 to 0.37%. The changes in overall efficiencies for electrolyte E2b are less than 10% and for E2e $\approx 28\%$ and in the acceptable range for both electrolytes. Figure 3.19 shows the changes in short-circuit density, open circuit voltage and overall efficiency. The general trend follows the expected literature scenario, which is a gain in V_{OC} values compensating the decrease in J_{SC} . It was shown that the Fermi level of a semiconductor realigns over the time and is attributed to an increase in open-circuit voltage. At the same time, dye dissociation from the surface (as evidenced by the bleaching) and an increase in electron recombination are observed.

Table 3.12. Parameters for DSCs with electrolytes E2b and E2e over the period of 40 days. All DSCs were fully masked.

| Electrolyte | DSC | Day | $J_{SC} / \text{mA cm}^{-2}$ | V_{OC} / mV | $ff / \%$ | $\eta / \%$ |
|-------------|-----|-----|------------------------------|----------------------|-----------|-------------|
| E2b | 1 | 0 | 2.58 | 292 | 63 | 0.47 |
| | | 5 | 2.54 | 401 | 52 | 0.53 |
| | | 14 | 2.19 | 425 | 58 | 0.54 |
| | | 25 | 1.85 | 446 | 63 | 0.52 |
| | | 40 | 1.35 | 469 | 67 | 0.43 |
| E2b | 2 | 0 | 2.38 | 326 | 65 | 0.51 |
| | | 5 | 2.32 | 403 | 60 | 0.56 |
| | | 14 | 2.17 | 421 | 59 | 0.54 |
| | | 25 | 2.07 | 457 | 62 | 0.59 |
| | | 40 | 1.73 | 460 | 64 | 0.51 |
| E2b | 3 | 0 | 2.34 | 374 | 65 | 0.57 |
| | | 5 | 2.15 | 428 | 62 | 0.57 |
| | | 14 | 2.04 | 441 | 61 | 0.55 |
| | | 25 | 1.88 | 469 | 64 | 0.57 |
| | | 40 | 1.53 | 470 | 66 | 0.48 |
| E2e | 1 | 0 | 2.51 | 308 | 63 | 0.49 |
| | | 5 | 2.16 | 385 | 63 | 0.53 |
| | | 14 | 1.95 | 418 | 65 | 0.53 |
| | | 25 | 1.76 | 436 | 66 | 0.50 |
| | | 40 | 1.46 | 446 | 66 | 0.43 |
| E2e | 2 | 0 | 2.78 | 307 | 62 | 0.53 |
| | | 5 | 2.17 | 387 | 61 | 0.52 |
| | | 14 | 1.73 | 435 | 64 | 0.48 |
| | | 25 | 1.32 | 461 | 68 | 0.41 |
| | | 40 | 0.90 | 466 | 71 | 0.29 |
| E2e | 3 | 0 | 2.61 | 315 | 62 | 0.51 |
| | | 5 | 2.19 | 379 | 61 | 0.50 |
| | | 14 | 1.97 | 418 | 63 | 0.52 |
| | | 25 | 1.70 | 437 | 65 | 0.48 |
| | | 40 | 1.32 | 446 | 67 | 0.40 |



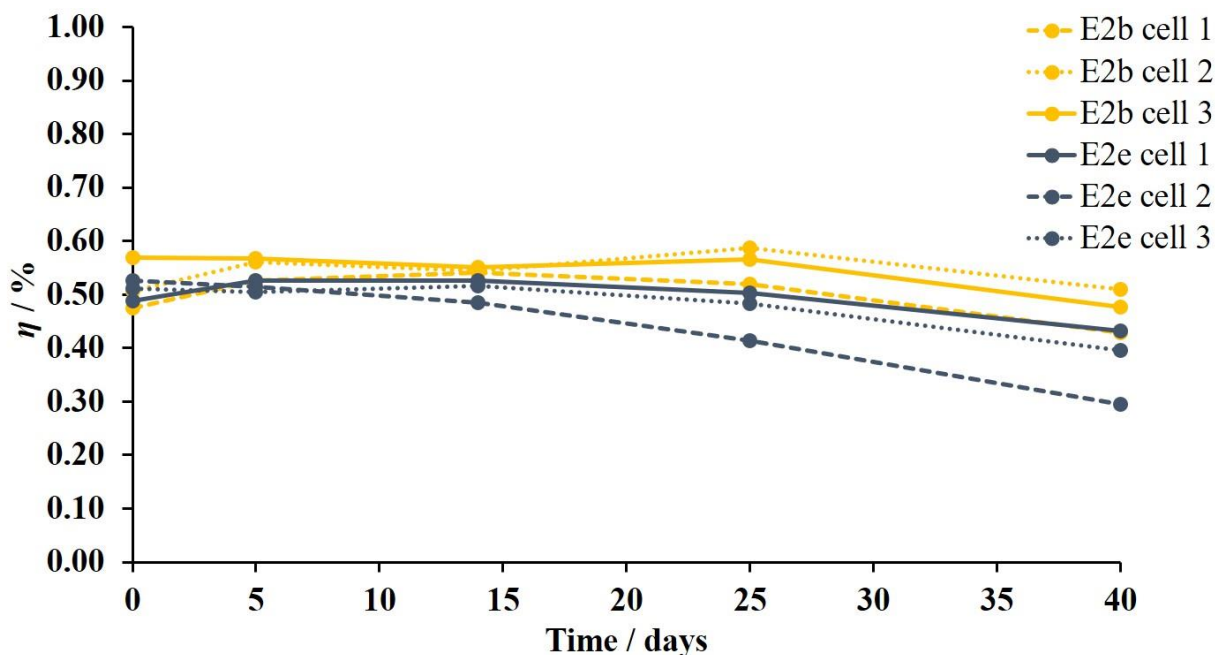


Figure 3.19. Variation in DSC parameters over a 40-day period with electrolytes E2b and E2e. Lines between the dots are added only for guiding the eye.

3.1.7 Summary: Solvents and additives

The studies in this chapter have shown that the use of 3-methoxypropionitrile instead of MeCN as the solvent for the electrolyte led to an improvement in the short-circuit current density and an enhanced photoconversion efficiency. The increase in J_{SC} was followed by a small increase of 20 mV in the open-circuit voltage for the electrolyte with BMII IL. For PDMII-based electrolyte V_{OC} was not affected and only significant gain in J_{SC} resulted in the PCE improvement. Thus, the further investigations were performed with MPN as a solvent for electrolytes. The four ionic liquids (BMII, PDMII, BMIPF, EMIMPF) were investigated with and without additives like MBI and TBP. There was no significant difference observed between MBI and TBI at concentration from 0.10 M to 0.01 M. On the other hand, electrolyte with 0.50 M TBP performed better due to increased V_{OC} value compared to the same concentration of MBI. Most of ILs have shown better results in the absence of heterocyclic additives except EMIMPF IL. The removal of the MBI additive resulted in detrimental falling of V_{OC} . The best performing electrolyte compositions were E2c and E2b with 0.01 M of MBI and without MBI, respectively. Both have PDMII as IL and MPN as a solvent.

3.2 Investigations of the effect of lithium salts and ionic liquid concentration

3.2.1 The effect of lithium salts in electrolyte

Lithium salts are a further class of common additives for electrolytes. Due to the adsorption possibilities of the Li^+ ion on the surface, their presence has an influence on the conduction band (CB) of the semiconductor and shifts it towards positive potentials.¹⁶⁷ This effect leads to an enhanced electron injection from the excited dye to the semiconductor. On the other hand, it lowers the potential of a cell since the positive shift of CB decreases the gap between the Fermi level of the semiconductor and energy level on the redox couple. In the case of LiI, the counterion also contributes to the potential of iodide/triiodide redox couple, which is used for iron(II) dyes. For a deeper understanding of the counterion impact on the system, the effect of Li^+ additives was investigated using the salts LiI and LiPF_6 . In section 3.1.4, it was shown that the influence of additives MBI and TBP can be entirely changed depending on the ionic liquid incorporated in the electrolyte system. Thus, numerous electrolyte combinations were screened with different ionic liquids in the presence of lithium salts (Figure 3.20). For this study, additives MBI and TBP were not added in electrolytes, since in sections 3.1.2 and 3.1.4 it was shown that their presence was not beneficial for DSCs performance. Electrolyte compositions are given in Table 3.13. For each electrolyte multiple DSCs were manufactured (Table 3.14, Figure 3.21), but, for convenience, only those with close to average values will be discussed.

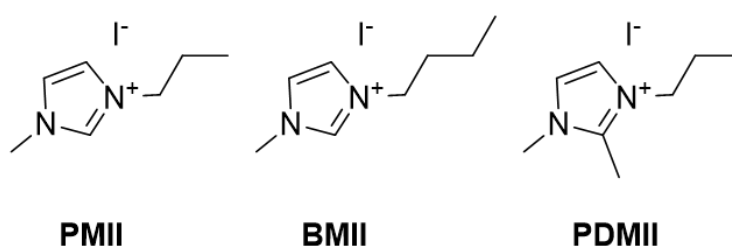


Figure 3.20. Structures of ILs used in this study.

Table 3.13. Electrolyte compositions with various Li^+ salts and IL concentrations. MPN was used as a solvent.

| Electrolyte | LiI / M | LiPF_6 / M | I_2 / M | IL / M |
|-------------|---------|---------------------|------------------|-------------|
| PMIIa | 0.10 | – | 0.05 | PMII / 0.60 |
| PMIIb | – | 0.10 | 0.05 | PMII / 0.60 |
| PMIIc | 0.18 | – | 0.05 | PMII / 0.60 |
| PMIId | – | 0.18 | 0.05 | PMII / 0.60 |

Third Chapter

| | | | | |
|--------|------|------|------|--------------|
| BMIIa | 0.10 | – | 0.05 | BMII / 0.60 |
| BMIIb | – | 0.10 | 0.05 | BMII / 0.60 |
| BMIIc | 0.18 | – | 0.05 | BMII / 0.60 |
| BMIIId | – | 0.18 | 0.05 | BMII / 0.60 |
| BMIIe | 0.26 | – | 0.05 | BMII / 0.60 |
| BMIIIf | 0.34 | – | 0.05 | BMII / 0.60 |
| BMIIg | 0.18 | – | 0.05 | BMII / 0.52 |
| BMIIh | 0.26 | – | 0.05 | BMII / 0.44 |
| BMIIi | 0.34 | – | 0.05 | BMII / 0.36 |
| PDMIIe | – | 0.10 | 0.05 | PDMII / 0.60 |
| PDMIIa | 0.18 | – | 0.05 | PDMII / 0.60 |
| PDMIIb | 0.18 | – | 0.05 | PDMII / 0.52 |
| PMIIe | 0.18 | – | 0.05 | PMII / 0.52 |
| PMIIIf | 0.18 | – | 0.05 | PMII / 0.44 |

Table 3.14. Parameters for multiple DSC devices with different electrolytes. All DSCs were fully masked.

| Electrolyte | $J_{sc} / \text{mA cm}^{-2}$ | V_{oc} / mV | $ff / \%$ | $\eta / \%$ | Rel. $\eta / \%$ ¹ |
|--------------|------------------------------|----------------------|-----------|-------------|-------------------------------|
| PMIIa cell 1 | 2.34 | 371 | 66 | 0.57 | 10.2 |
| PMIIa cell 2 | 2.26 | 354 | 66 | 0.53 | 9.5 |
| PMIIa cell 3 | 2.41 | 355 | 65 | 0.56 | 10.0 |
| PMIIa cell 4 | 2.69 | 373 | 63 | 0.63 | 11.3 |
| PMIIb cell 1 | 2.71 | 264 | 57 | 0.41 | 7.3 |
| PMIIb cell 2 | 2.35 | 285 | 60 | 0.40 | 7.1 |
| PMIIb cell 3 | 2.66 | 265 | 58 | 0.41 | 7.3 |
| PMIIb cell 4 | 2.77 | 288 | 60 | 0.48 | 8.6 |
| PMIIc cell 1 | 3.01 | 315 | 62 | 0.59 | 10.5 |
| PMIIc cell 2 | 2.98 | 270 | 62 | 0.50 | 8.9 |
| PMIIc cell 3 | 2.98 | 318 | 63 | 0.59 | 10.5 |
| PMIId cell 1 | 3.91 | 281 | 53 | 0.59 | 10.5 |
| PMIId cell 2 | 3.44 | 296 | 54 | 0.55 | 9.8 |
| PMIId cell 3 | 3.45 | 301 | 56 | 0.58 | 10.4 |
| PMIId cell 4 | 2.85 | 284 | 60 | 0.48 | 8.6 |
| BMIIa cell 1 | 2.42 | 374 | 61 | 0.55 | 9.8 |
| BMIIa cell 2 | 2.38 | 340 | 64 | 0.52 | 9.3 |

Third Chapter

| | | | | | |
|---------------|------|-----|----|------|------|
| BMIIa cell 3 | 2.20 | 366 | 63 | 0.51 | 9.1 |
| BMIIa cell 4 | 2.18 | 318 | 64 | 0.45 | 8.0 |
| BMIIb cell 1 | 1.77 | 359 | 62 | 0.39 | 6.9 |
| BMIIb cell 2 | 1.54 | 361 | 65 | 0.37 | 6.6 |
| BMIIb cell 3 | 1.56 | 366 | 66 | 0.38 | 6.8 |
| BMIIb cell 4 | 1.57 | 372 | 66 | 0.38 | 6.8 |
| BMIIc cell 1 | 3.40 | 301 | 59 | 0.61 | 10.9 |
| BMIIc cell 2 | 3.56 | 311 | 57 | 0.63 | 11.3 |
| BMIIc cell 3 | 3.51 | 291 | 58 | 0.59 | 10.5 |
| BMIIc cell 4 | 3.40 | 294 | 60 | 0.60 | 10.7 |
| BMII d cell 1 | 3.13 | 315 | 59 | 0.58 | 10.4 |
| BMII d cell 2 | 2.65 | 313 | 62 | 0.51 | 9.1 |
| BMII d cell 3 | 2.92 | 307 | 61 | 0.55 | 9.8 |
| BMII d cell 4 | 3.10 | 330 | 60 | 0.61 | 10.9 |
| BMII e cell 1 | 3.02 | 299 | 62 | 0.56 | 10.0 |
| BMII e cell 2 | 2.79 | 288 | 64 | 0.51 | 9.1 |
| BMII e cell 3 | 3.08 | 286 | 62 | 0.55 | 9.8 |
| BMII e cell 4 | 3.10 | 306 | 63 | 0.60 | 10.7 |
| BMII f cell 1 | 3.45 | 307 | 60 | 0.64 | 11.4 |
| BMII f cell 2 | 3.49 | 302 | 62 | 0.65 | 11.6 |
| BMII f cell 3 | 3.38 | 298 | 61 | 0.62 | 11.1 |
| BMII f cell 4 | 3.46 | 292 | 61 | 0.61 | 10.9 |
| BMII g cell 1 | 3.33 | 298 | 62 | 0.62 | 11.1 |
| BMII g cell 2 | 3.03 | 272 | 63 | 0.52 | 9.3 |
| BMII g cell 3 | 3.62 | 293 | 60 | 0.64 | 11.4 |
| BMII g cell 4 | 3.35 | 277 | 61 | 0.57 | 10.2 |
| BMII h cell 1 | 3.46 | 301 | 60 | 0.63 | 11.3 |
| BMII h cell 2 | 3.58 | 263 | 47 | 0.44 | 7.9 |
| BMII h cell 3 | 3.86 | 311 | 55 | 0.66 | 11.8 |
| BMII h cell 4 | 3.32 | 281 | 58 | 0.54 | 9.6 |
| BMII i cell 1 | 3.61 | 264 | 62 | 0.59 | 10.5 |
| BMII i cell 2 | 3.98 | 264 | 61 | 0.64 | 11.4 |
| BMII i cell 3 | 3.49 | 246 | 60 | 0.52 | 9.3 |

Third Chapter

| | | | | | |
|---------------|-------|-----|----|------|------|
| BMIi cell 4 | 3.78 | 220 | 60 | 0.50 | 8.9 |
| PDMIIe cell 1 | 2.44 | 317 | 58 | 0.45 | 8.0 |
| PDMIIe cell 2 | 2.86 | 293 | 47 | 0.40 | 7.1 |
| PDMIIe cell 3 | 2.93 | 300 | 58 | 0.51 | 9.1 |
| PDMIIe cell 4 | 2.68 | 298 | 57 | 0.45 | 8.1 |
| PDMIIa cell 1 | 3.27 | 348 | 58 | 0.66 | 11.8 |
| PDMIIa cell 2 | 3.41 | 346 | 54 | 0.64 | 11.4 |
| PDMIIb cell 1 | 3.21 | 337 | 57 | 0.62 | 11.1 |
| PDMIIb cell 2 | 3.01 | 318 | 60 | 0.57 | 10.2 |
| PMIIe cell 1 | 2.80 | 368 | 62 | 0.64 | 11.4 |
| PMIIe cell 2 | 2.71 | 390 | 60 | 0.64 | 11.4 |
| PMIIe cell 3 | 2.80 | 360 | 62 | 0.62 | 11.1 |
| PMIIe cell 4 | 2.70 | 366 | 63 | 0.62 | 11.1 |
| PMIIf cell 1 | 2.27 | 344 | 63 | 0.49 | 8.8 |
| PMIIf cell 2 | 2.14 | 364 | 64 | 0.49 | 8.8 |
| PMIIf cell 3 | 2.22 | 366 | 63 | 0.51 | 9.2 |
| PMIIf cell 4 | 2.32 | 346 | 62 | 0.49 | 8.8 |
| N719 | 12.53 | 654 | 68 | 5.60 | 100 |

[†] Relative to a value of η for N719 set at 100%.

In our previous investigations on electrolytes, a 0.10 M LiI concentration without additives was used. These conditions were set as a starting point. In Table 3.13 electrolyte composition PMIIa and PMIIb as well as BMIIa and BMIIb are presented, which differ only in the Li^+ salt used (LiI or LiPF_6). Interestingly, the trend observed for J_{SC} values is different for the ionic liquids PMII and BMII using either LiI or LiPF_6 . While the J_{SC} value increased from 2.34 to 2.66 mA cm^{-2} for PMIIb, it decreased from 2.42 to 1.77 mA cm^{-2} for BMIIb. For PMII IL the V_{OC} drop with more than 100 mV is observed, while in case of BMII IL the change of lithium salt did not affect the potential (Figures 3.21 and 3.22). At the same time, a fall in fill factor is observed for both electrolytes, which results in lower overall efficiencies.

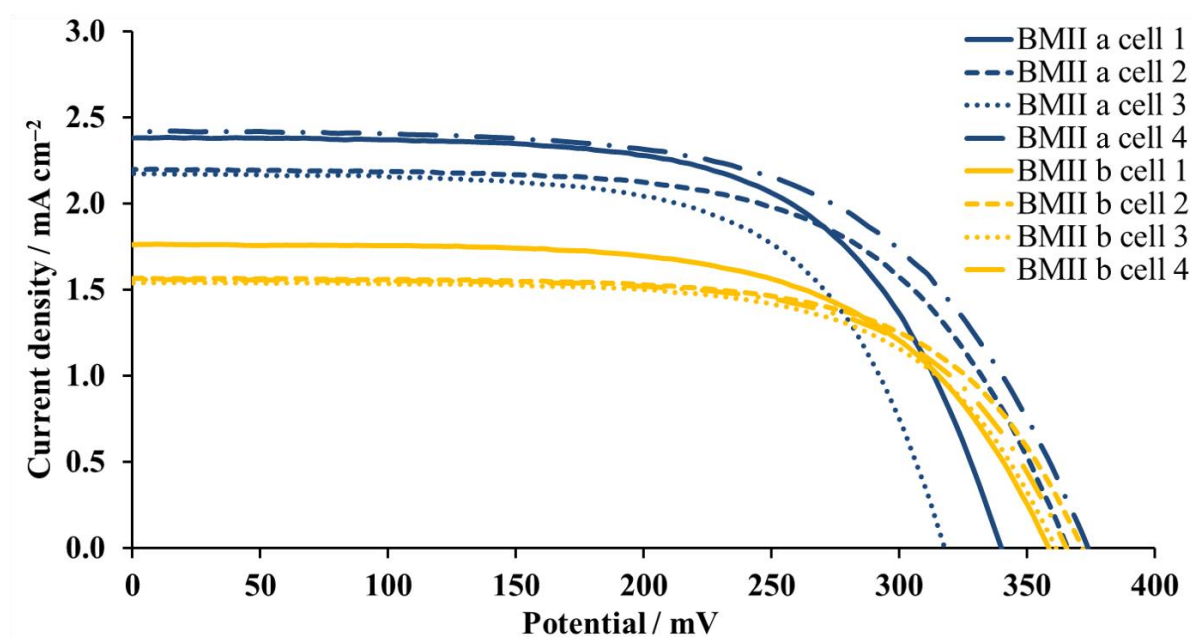


Figure 3.21. *J-V* curves for multiple DSCs with electrolytes BMIIa and BMIIb to show the reproducibility.

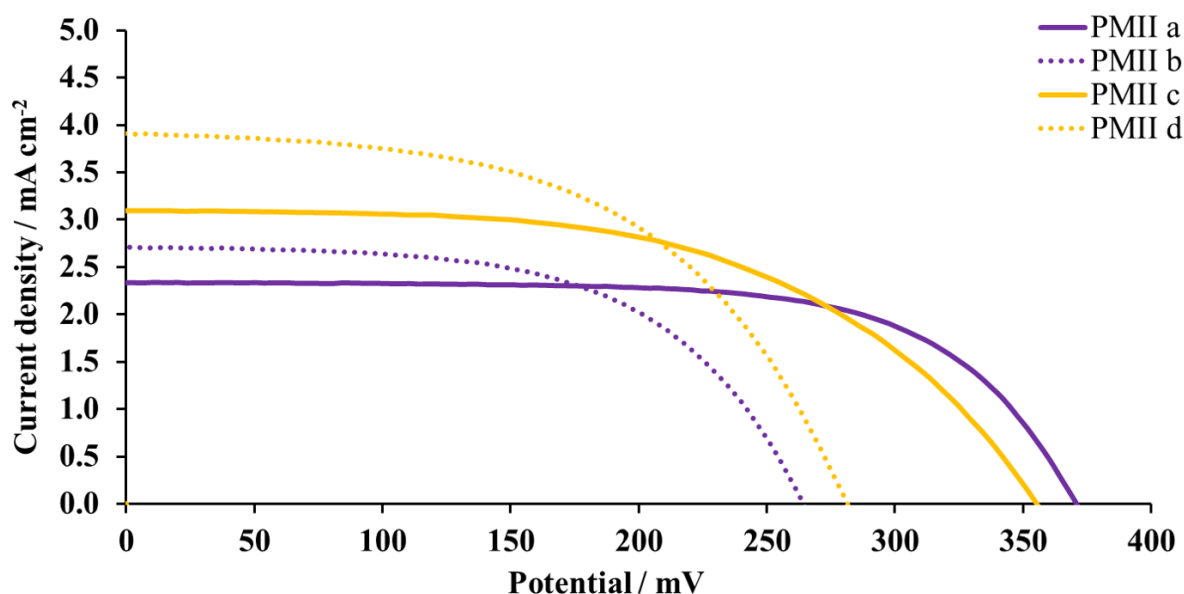


Figure 3.22. *J-V* curves for DSCs with electrolytes PMIIa, PMIIb, PMIIc and PMIIId. Solid lines refer to electrolytes with LiI, dotted lines refer to electrolytes with LiPF₆.

An increase in Li⁺-concentration has a positive effect on overall DSC performance for both salts LiI and LiPF₆. Comparing electrolytes PMIIa and PMIIc with 0.10 M or 0.18 M of LiI, respectively, an increase in short circuit density is observed for increased salt loading. Despite the change in V_{OC} from 371 to 315 mV, the positive influence of V_{OC} resulted in higher PCE of 0.59% for electrolyte PMIIc. On going from electrolyte BMIIa to BMIIc, the same trends in J_{SC} and V_{OC} are observed and result in a higher overall efficiency of 0.61% (10.9% with a respect to N719 set at 100%). The change in LiPF₆ concentration from 0.10 M to 0.18 M reveals a more apparent difference in J_{SC} values for PMIIb and PMIIId. 0.18 M LiPF₆ concentration results in more than

Third Chapter

1.0 mA cm⁻² increase in J_{SC} for PMIID. Higher LiPF₆ concentration has a positive influence on V_{OC} as well and increases the value from 264 to 281 mV going from PMIIb to PMIID electrolyte. Both J_{SC} and V_{OC} contributed to the higher PCE value of 0.59% for PMIID. The change in LiPF₆ concentration for BMII IL resulted in an enhanced value in J_{SC} but also to a decrease in V_{OC} for BMIID electrolyte. The improvement in J_{SC} overcompensates the opposing effect of a reduction in open-circuit potential and leads to 0.58% PCE for BMIID compared to 0.39% for BMIIb. For the electrolyte based on PDMII IL the increase of LiI concentration improved the PCE to 0.66% due to the significant enhance of J_{SC} from 2.31 to 3.27 mA cm⁻² compared to E2b electrolyte. The slight increase in V_{OC} results in the value of 348 mV.

Electrolytes PMIIc and PMIID both contain a Li⁺-concentration of 0.18 M, but different counterions (I⁻ or PF₆⁻, respectively). A lower J_{SC} of 3.01 mA cm⁻² in combination with a higher V_{OC} of 315 mV for PMIIc compared to 3.91 mA cm⁻² J_{SC} and 281 mV V_{OC} for PMIID result in a similar efficiency of 0.59% (10.5% relative to N719 set at 100%) for both electrolytes. However, an opposite trend is observed for electrolytes BMIIc and BMIID. Both electrolytes contain 0.18 M Li⁺ but differ in the counterion. An enhanced J_{SC} value of 3.40 mA cm⁻² for BMIIc lead to a slightly better PCE of 0.61% compared to 0.58% for BMIID. It is important to note that the change from LiI to LiPF₆ has an influence on both J_{SC} and V_{OC} . Thus, not only can the CB of the semiconductor be affected by the choice of counterion, but also the energy level of the redox shuttle of an electrolyte. Since DSCs based on electrolytes with LiI have a better performance than with LiPF₆, we continued with a closer investigation of the impact of different Li⁺ concentrations using LiI.

An increase of LiI concentration from 0.18 M to 0.26 M in the presence of BMII IL resulted in lower DSC performance. The change is followed by loss in J_{SC} from 3.40 to 3.02 mA cm⁻² but no change in V_{OC} . This results in 0.56% PCE (10.0% relative to N719). A further change to 0.34 M of LiI in BMIIe electrolyte leads to an enhanced J_{SC} value of 3.45 mA cm⁻² and V_{OC} of 307 mV and thus to a PCE of 0.64%. The J - V trends for electrolytes BMIIc, BMIIe and BMIIe are significant, because an improvement in either J_{SC} or V_{OC} is typically followed by a decrease in V_{OC} or J_{SC} , respectively (Figure 3.23).

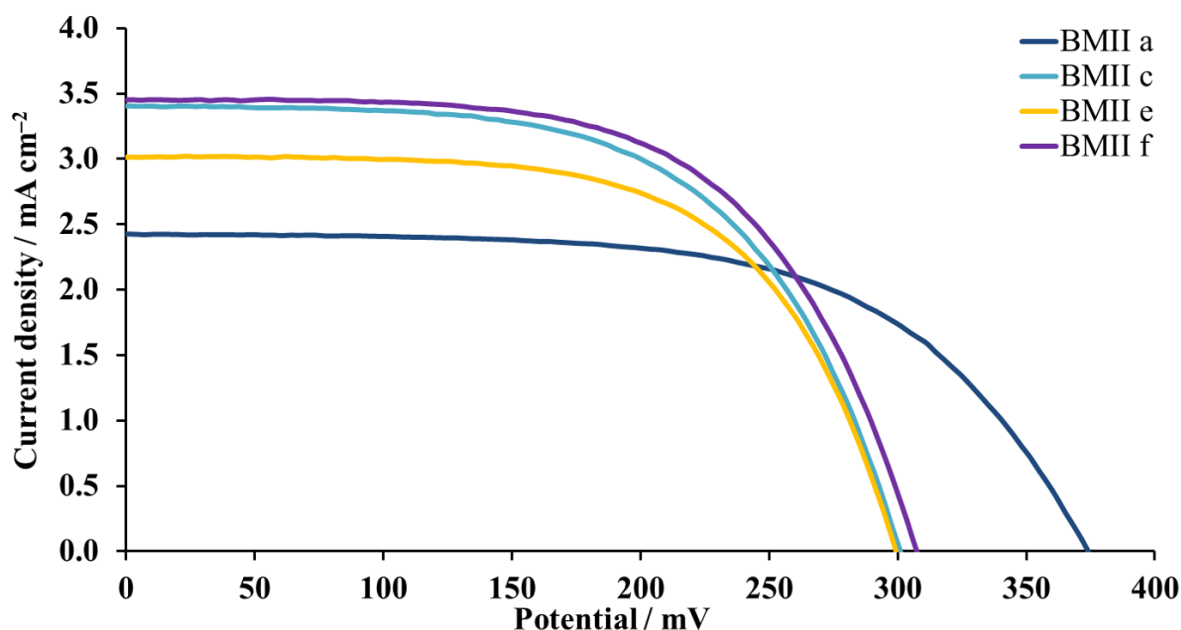


Figure 3.23. J - V curves for DSCs with electrolytes BMIIa, BMIIc, BMIIe and BMII f.

Since this investigation focused on the influence of different Li^+ -concentrations, it is critical that the concentration of I^- is constant. It is important to note, that in cases of ILs and Li^+ salts with an iodide counterion, both iodide sources contribute I^- to the redox couple. The original BMIIa electrolyte contains 0.1 M LiI and 0.6 M BMII with a total concentration of 0.7 M iodide. With an increase of LiI in the electrolyte, the total iodide concentration increased as well. Therefore, we decreased the amount of IL present in an electrolyte proportionally to the added amount of LiI to keep the I^- concentration constant. From electrolyte BMIIa to BMIIg, BMIIh and BMIIi, the concentration of LiI increases from 0.1 M to 0.18 M, 0.26 M and 0.34 M and concentration of IL decreases from 0.6 M to 0.52 M, 0.44 M and 0.36 M, respectively. The J_{SC} values improved in the range of 2.42-3.61 mA cm^{-2} and V_{OC} decreased from 374 to 264 mV. Interestingly, up to a concentration of 0.26 M LiI and 0.44 M BMII a rise in PCE is observed from 0.55 to 0.63% for BMIIh. A further change to higher LiI and lower BMII concentrations for BMIIi electrolyte results in a loss in PCE to 0.59% due to the drop in V_{OC} from 301 to 264 mV. However, despite the different concentrations of LiI and BMII electrolytes BMIIg and BMIIh have similar PCE of 0.62 and 0.63%, respectively.

The electrolytes E2b and PDMIIe differ only in their Li^+ salt counterion (I^- or PF_6^-) with the same concentration of 0.1 M. The presence of LiPF_6 decreased the values of V_{OC} and ff and leads to a PCE of 0.45% despite a small increase in J_{SC} (Figure 3.24). A higher concentration of LiI for PDMIIa electrolyte proved beneficial and lead to an increase of both J_{SC} and V_{OC} . This results in a PCE value of 0.66% and corresponds to a relative efficiency of 11.8% with respect to N719 set

at 100%. In the case of PDMII IL, the change in IL concentration resulted in a small decrease in V_{OC} of 11 mV. This led to lower a PCE value of 0.62%.

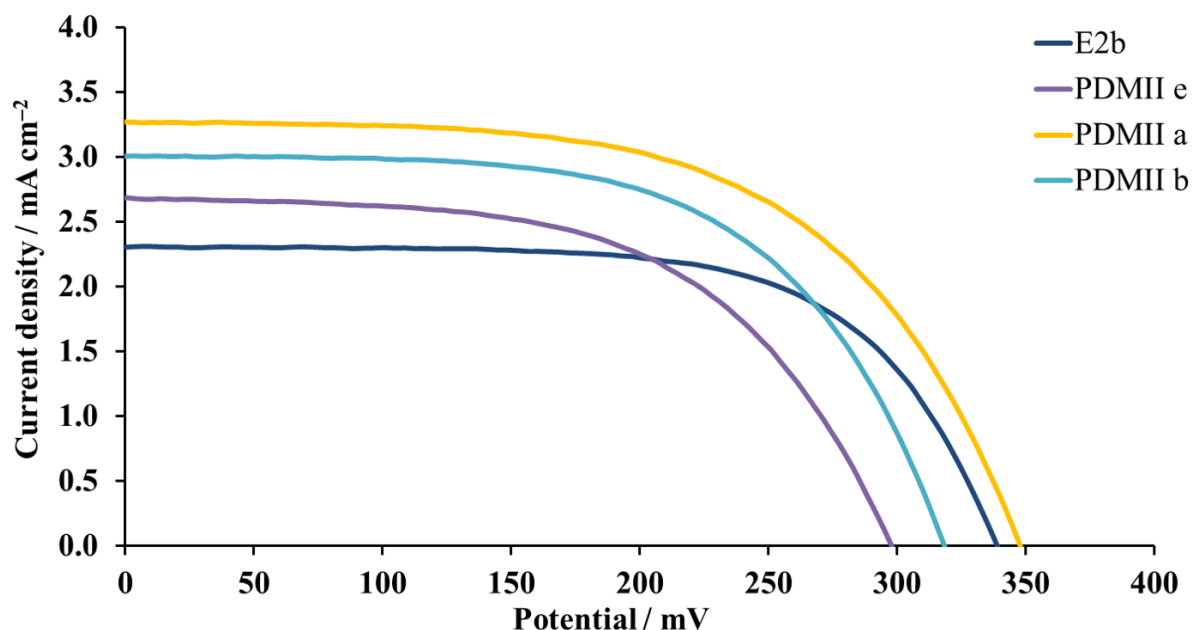


Figure 3.24. J - V curves for DSCs with electrolytes based on PDMII IL.

The observed trend for PMII IL is similar to the BMII based electrolytes. An improvement of 0.46 mA cm^{-2} in J_{SC} values is observed on going from PMIIa to PMIIe electrolyte and this leads to a higher PCE of 0.64% (11.4% relative to N719 set at 100%). The open-circuit voltage shows no significant change. Further decrease of PMII from 0.52 to 0.44 M without an appropriate increase of LiI resulted in lower PCE of 0.49% with corresponding loss in both J_{SC} and V_{OC} .

3.2.2 The EQE and EIS study of Li^+ ion influence on DSCs

DSCs with electrolytes listed in Table 3.13 (PMIIa-BMIId) all exhibited a broad EQE spectra in the range of 430-570 nm. These results were consistent with the EQE discussed in section 3.5. All EQE_{max} values are presented in Table 3.15. Figures 3.25 and 3.26 demonstrate the reproducibility of multiple DSCs in terms of EQE measurements.

Table 3.15. EQE_{max} values for multiple DSCs for each electrolyte.

| Electrolyte | $\text{EQE}_{\text{max}} / \%$ | | | | EQE_{max} average / % | Wavelength range ¹ / nm |
|-------------|--------------------------------|--------|--------|--------|--|---------------------------------------|
| | cell 1 | cell 2 | cell 3 | cell 4 | | |
| PMIIa | 17 | 18 | 18 | 19 | 18 | 470-510 |

| | | | | | | |
|--------|----|----|----|----|----|---------|
| PMIIb | 15 | 18 | 17 | 18 | 17 | 460-490 |
| PMIIc | 24 | 21 | 21 | 12 | 20 | 450-510 |
| PMIId | 26 | 27 | 24 | 21 | 24 | 460-510 |
| BMIIa | 18 | 16 | 16 | 18 | 17 | 440-460 |
| BMI Ib | 17 | 12 | 14 | 15 | 15 | 460 |
| BMI Ic | 24 | 25 | 24 | 23 | 24 | 470-480 |
| BMI Id | 18 | 22 | 19 | 20 | 20 | 470 |
| BMI Ie | 24 | 24 | 24 | 25 | 24 | 490-500 |
| BMI If | 21 | 22 | 21 | 22 | 21 | 490-500 |
| BMI Ig | 21 | 25 | 24 | 24 | 23 | 480-500 |
| BMI Ih | 24 | 25 | 30 | 21 | 25 | 480 |
| BMI Ii | 25 | 27 | 24 | 27 | 26 | 480-500 |

[†] The range of λ_{\max} for multiple DSCs.

The values of EQE_{\max} were not affected by Li^+ counterion and were $\approx 15\text{-}19\%$ at λ_{\max} 460-510 nm for electrolytes PMIIa and PMIIb for a set of four DSCs for each electrolyte. The similarity of EQE spectra for PMIIa and PMIIb can be seen in Figure 3.25. Higher concentration of Li^+ salts resulted in the increased up to 21-24% EQE_{\max} at λ_{\max} in the range of 450-510 nm for PMIIc (with one outlier cells with 12% EQE_{\max}) and 21-27% at λ_{\max} in the range of 460-510 nm for PMIId (Table 3.15).

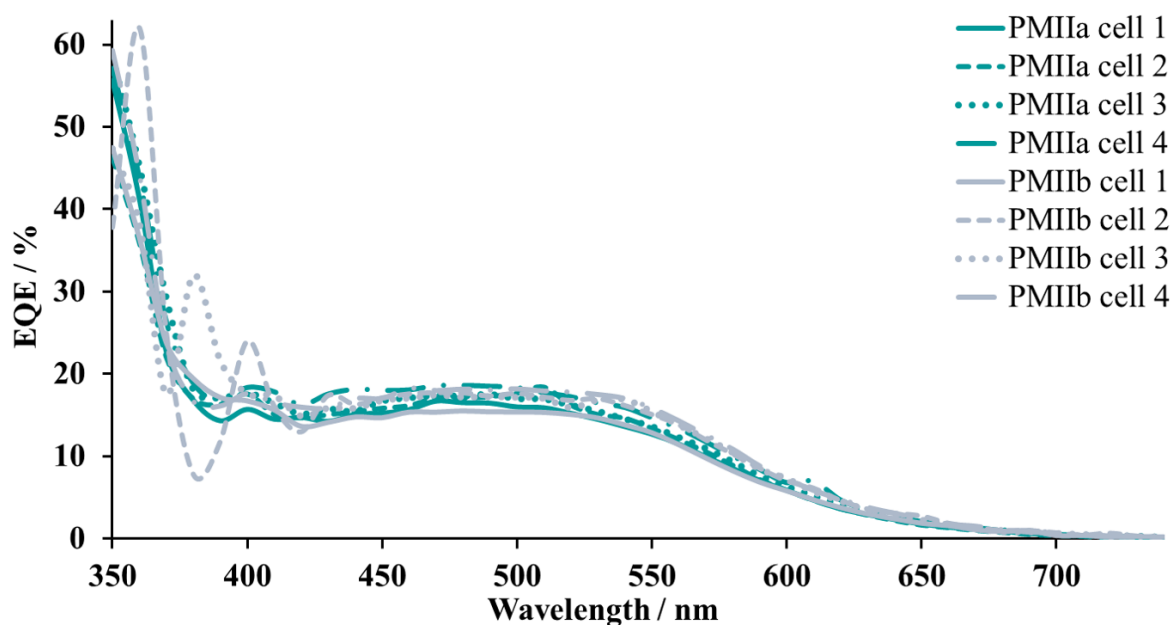


Figure 3.25. EQE spectra for multiple DSCs with electrolytes PMIIa and PMIIb to show reproducibility.

DSCs with electrolytes BMIIa and BMIIb had slightly lower EQE_{max} of $\approx 12-18\%$ with the λ_{max} slightly shifted in the short wavelength region (440-460 nm) than PMIIa and PMIIb (Table 3.15, Figure 3.26). For electrolytes with BMII IL, enhanced Li^+ concentrations also led to higher EQE_{max} values of $\approx 23-25\%$ for BMIIc (λ_{max} is in the region 470-480 nm) and of $\approx 18-22\%$ for BMII d at $\lambda_{max} = 470$ nm (Figure 3.27). A similar influence of Li^+ concentration on J_{SC} was observed.

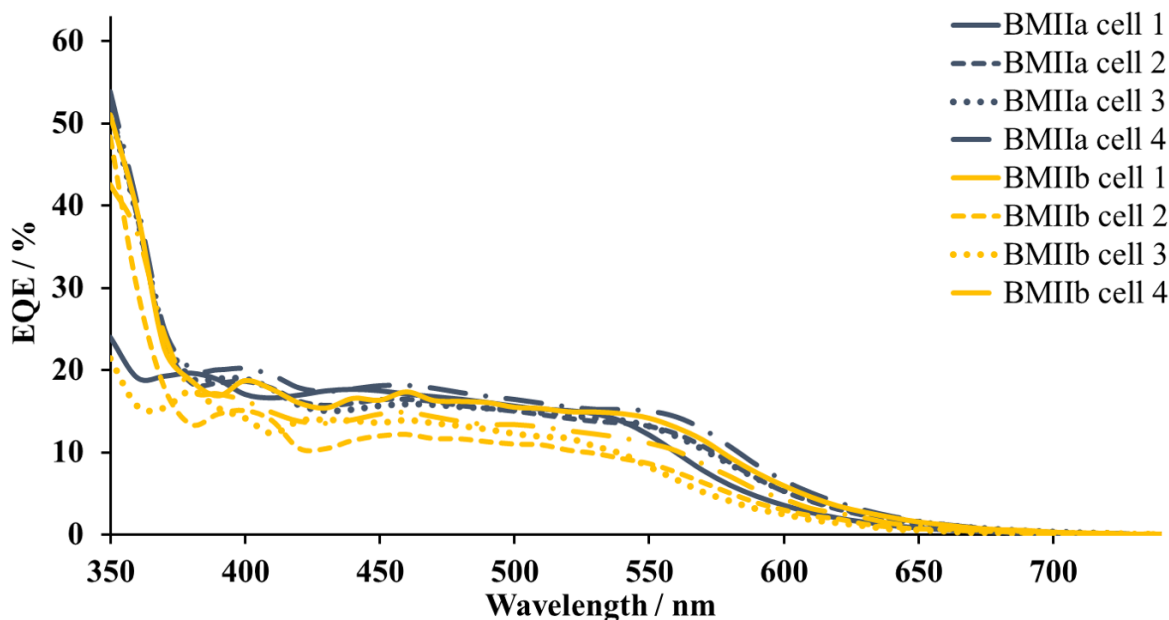


Figure 3.26. EQE spectra for multiple DSCs with electrolytes BMIIa and BMIIb to show reproducibility.

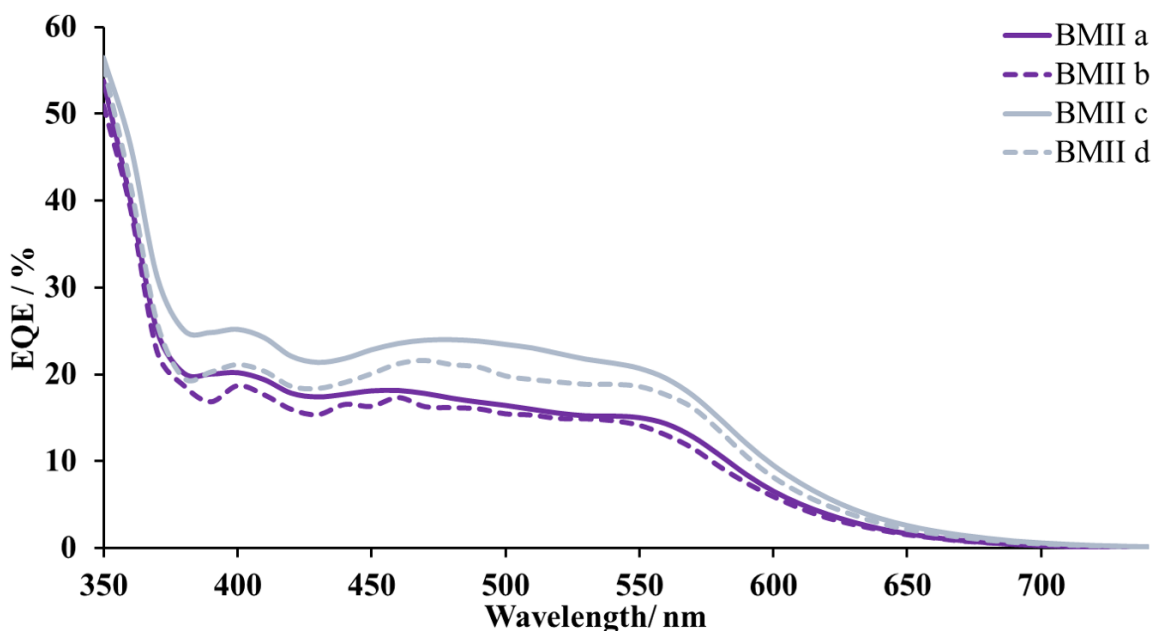


Figure 3.27. EQE spectra for DSCs with electrolytes BMIIa, BMIIb, BMIIc, BMII d.

The increase from 0.26 to 0.34 M of LiI concentration in the electrolytes had a positive effect on the short-circuit current density and had a similar reflection in EQE spectra. The EQE_{max} was

approximately 24% for BMIIe and was approximately 21-22% for BMII f at λ_{\max} 490-510 nm (Figure 3.28). On the example of electrolytes BMIIg, BMIIh, and BMIIi the influence of Li^+ ions from 0.18 M to 0.34 M due to the constant concentration of I^- can be illustrated. On going from BMIIg to BMIIi, the EQE_{\max} increased from $\approx 23\%$ to $\approx 26\%$ at λ_{\max} 480-500 nm.

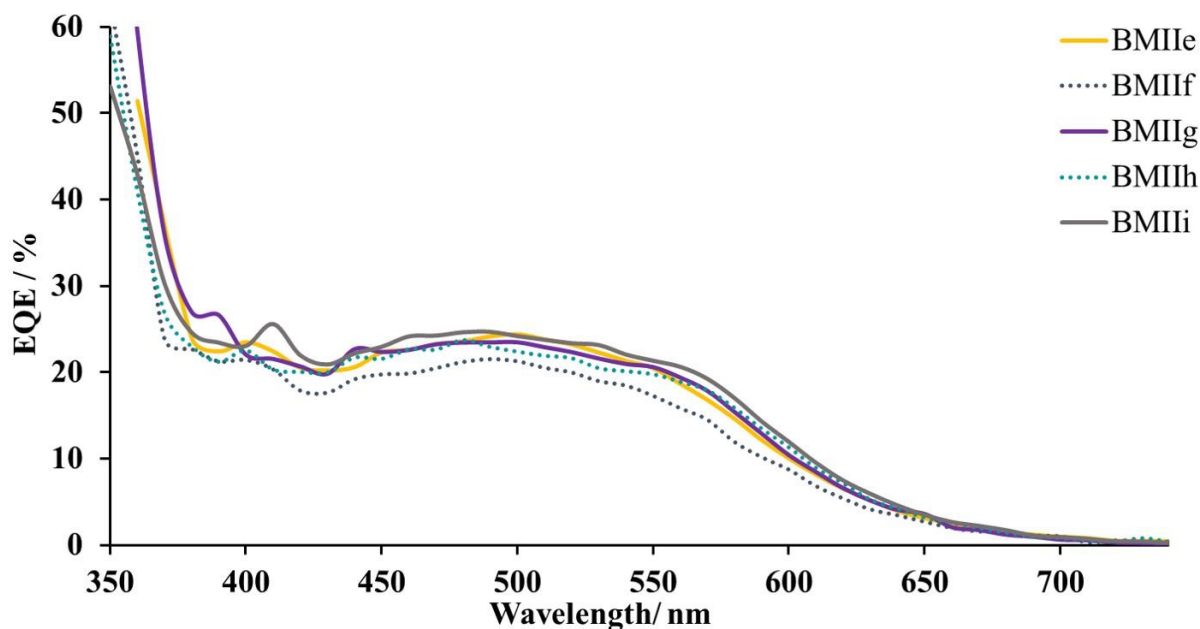


Figure 3.28. EQE spectra for DSCs with electrolytes BMIIe, BMII f, BMIIg, BMIIh and BMIIi.

For a deeper understanding of the LiI influence on the Fe(II)-sensitized DSC, EIS measurements were performed (Table 3.16). In Second Chapter the necessity of multiple devices for EIS measurements was examined. Thus, the data in Table 3.16 are presented for multiple DSCs, but only the average numbers will be discussed. The parameters of the counter electrodes stay constant for all the DSCs (R_s , R_{Pt} and C_{Pt}).

Table 3.16. EIS parameters for multiple DSCs using electrolytes based on BMII IL with different concentration of LiI.

| Electrolyte ^I | R_{rec} / Ω | $C_{\mu} / \mu F$ | R_{tr} / Ω | τ / ms | τ_t / ms | $L_d / \mu m$ | R_s / Ω | R_{Pt} / Ω | $C_{Pt} / \mu F$ |
|--------------------------|--------------------|-------------------|-------------------|-------------|---------------|---------------|----------------|-------------------|------------------|
| BMIIa cell 1 | 161 | 288 | 19 | 47 | 5 | 35 | 14 | 6 | 7 |
| BMIIa cell 2 | 199 | 233 | 32 | 46 | 7 | 30 | 13 | 3 | 9 |
| BMIIa cell 3 | 191 | 214 | 38 | 41 | 8 | 27 | 12 | 5 | 9 |
| BMIIa cell 4 | 192 | 384 | 9 | 74 | 3 | 56 | 14 | 4 | 6 |
| BMIIc cell 1 | 169 | 307 | 13 | 52 | 4 | 43 | 13 | 8 | 6 |
| BMIIc cell 2 | 160 | 506 | 6 | 81 | 3 | 63 | 14 | 8 | 5 |
| BMIIc cell 3 | 157 | 352 | 11 | 55 | 4 | 46 | 14 | 9 | 5 |
| BMIIc cell 4 | 122 | 267 | 17 | 33 | 5 | 32 | 14 | 9 | 5 |

| | | | | | | | | | |
|---------------------------|-----|-----|-----|-----|----|----|----|----|---|
| BMIIe cell 1 | 130 | 214 | 109 | 28 | 23 | 13 | 12 | 6 | 7 |
| BMIIe cell 2 | 151 | 245 | 80 | 37 | 20 | 16 | 14 | 8 | 7 |
| BMIIe cell 3 | 141 | 226 | 101 | 32 | 23 | 14 | 12 | 7 | 9 |
| BMIIe cell 4 | 150 | 258 | 69 | 39 | 18 | 18 | 11 | 11 | 7 |
| BMIIIf cell 1 | 152 | 374 | 26 | 57 | 10 | 29 | 16 | 11 | 5 |
| BMIIIf cell 2 | 140 | 307 | 45 | 43 | 14 | 21 | 16 | 7 | 6 |
| BMIIIf cell 3 | 169 | 328 | 38 | 56 | 12 | 25 | 15 | 10 | 6 |
| BMIIIf cell 4 | 142 | 292 | 45 | 41 | 13 | 21 | 13 | 11 | 6 |
| BMIIh cell 1 | 144 | 378 | 23 | 54 | 9 | 30 | 12 | 12 | 5 |
| BMIIh cell 2 | 180 | 403 | 19 | 72 | 8 | 36 | 12 | 8 | 8 |
| BMIIh cell 3 | 197 | 590 | 7 | 116 | 4 | 65 | 12 | 8 | 5 |
| BMIIh cell 4 | 187 | 279 | 46 | 52 | 13 | 24 | 14 | 10 | 6 |
| BMIIi cell 1 | 99 | 302 | 40 | 30 | 12 | 19 | 11 | 10 | 6 |
| BMIIi cell 2 | 103 | 369 | 19 | 38 | 7 | 28 | 11 | 9 | 6 |
| BMIIi cell 3 | 108 | 241 | 66 | 26 | 16 | 15 | 16 | 13 | 7 |
| BMIIi cell 4 | 86 | 223 | 76 | 19 | 17 | 13 | 11 | 10 | 7 |
| BMIIa _{average} | 186 | 280 | 25 | 52 | 6 | 37 | 13 | 5 | 8 |
| BMIIc _{average} | 152 | 358 | 12 | 55 | 4 | 46 | 14 | 9 | 5 |
| BMIIe _{average} | 143 | 236 | 90 | 34 | 21 | 15 | 12 | 8 | 8 |
| BMIIIf _{average} | 151 | 325 | 39 | 49 | 12 | 24 | 15 | 10 | 6 |
| BMIIh _{average} | 177 | 413 | 24 | 74 | 9 | 39 | 13 | 10 | 6 |
| BMIIi _{average} | 99 | 284 | 50 | 28 | 13 | 19 | 12 | 11 | 7 |

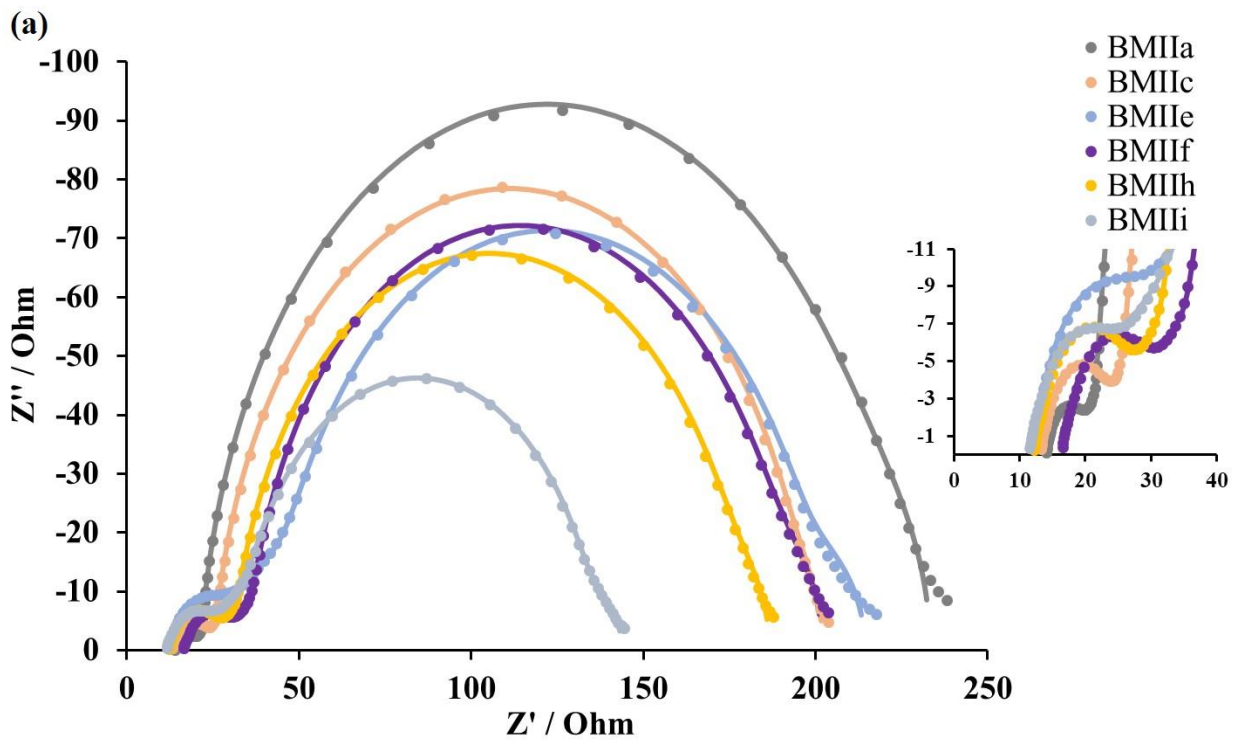
¹ *average* – the sum of all values for a given parameter divided by the number of cells.

The increase of Li⁺ ion concentration up to 0.26 M is followed by a decrease in recombination resistance from 186 to 143 Ω (Figure 3.29a). The trend for chemical capacitance is not linear and on going from BMIIa to BMIIc C_{μ} increases to 358 μF and then decreases to 236 μF for BMIIe. The transport resistance has a similar trend from 0.1 M to 0.18 M LiI with a decrease from 25 to 12 Ω , but then an increase up to 90 Ω for 0.26 M LiI. For 0.34 M LiI values of R_{rec} and C_{μ} increase again to 151 Ω and 325 μF , respectively, while R_{tr} decreases to 39 Ω .

As was discussed above, the diffusion length, transport time and electron lifetime play an important role in the DSC system. According to previously reported EIS measurements, high Li⁺ ion concentrations in the electrolyte can considerably increase L_d in the case of DSC with ruthenium(II)-based Z907 dye.¹⁰⁷ However, we observed the opposite trend for NHC iron(II) dye.

In the presence of 0.6 M of BMII L_d values increase from 37 to 46 μm from 0.1 M to 0.18 M of LiI and then decrease to 15 μm for 0.26 M of LiI. At the same time, τ decreases from 52 to 34 ms, while τ_t increases from 6 to 21 ms for electrolytes BMIIa, BMIIc and BMIIe. Since the charge lifetime is inversely correlated to the maximum frequency f_{max} , the Bode plot shows the same trend in τ values (Figure 3.29b). Electrolyte BMII f is an exception from this trend as the increase from 0.26 to 0.34 M in LiI concentration leads to enhanced values of L_d and τ and reduced τ_t .

In the case of DSCs with a constant 0.7 M iodide ion concentration (electrolytes BMIIh and BMIIi), the EIS data are consistent with trends in J_{SC} and V_{OC} . The decrease in the BMII concentration from 0.60 to 0.44 M with retained 0.26 M of LiI leads to a higher J_{SC} , which is associated with lower R_{tr} and higher C_{μ} . The further increase in the LiI concentration to 0.34 M and a corresponding decrease of the BMII concentration to 0.36 M (BMIIi electrolyte) lead to lower R_{rec} and C_{μ} values, but higher R_{tr} compared to electrolyte BMIIh.



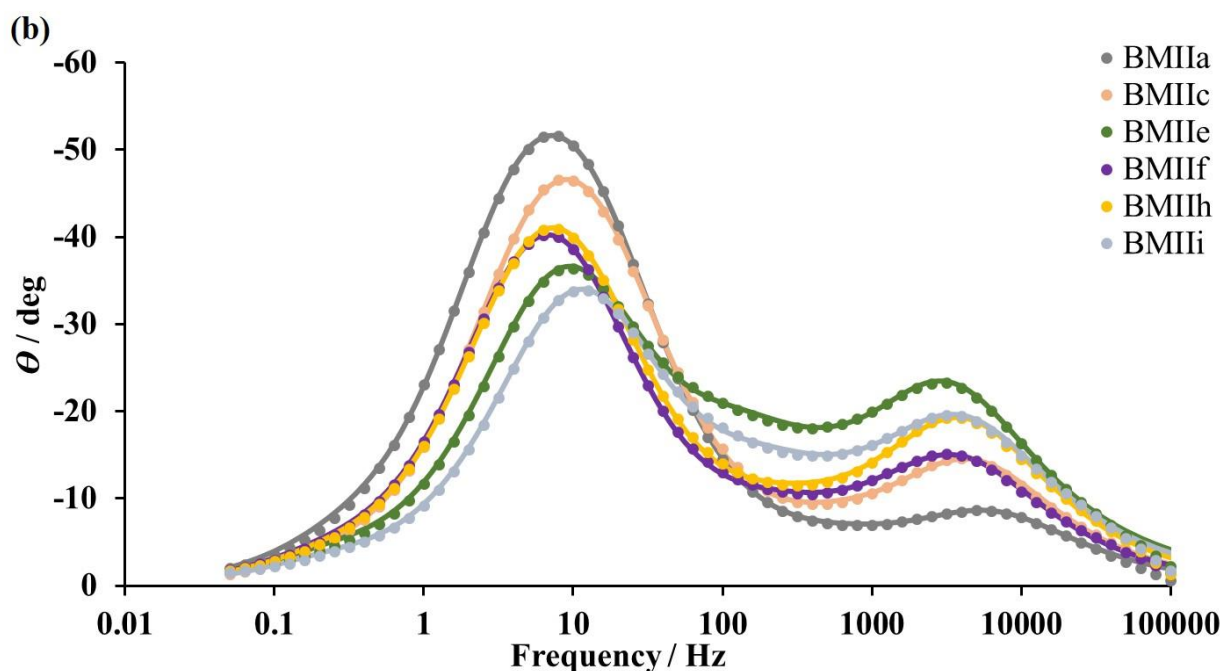


Figure 3.29. EIS plot of DSCs with electrolytes BMIIa, BMIIc, BMIIe, BMII f, BMIIh and BMIIi; a. Nyquist plot with expansion of high frequency region; b. Bode plot. Dotted lines represent experimental data, solid lines represent fitted data.

3.2.3 The effect of increased IL concentration in electrolyte

It is well established that electrolytes with IL as a medium are a beneficial alternative to ones with volatile organic solvents. On the other hand, it is hard to introduce a solvent-free electrolyte into a device due to the high viscosity of ILs. Moreover, not all ILs are liquids at room temperature. Thus, the necessity for the organic solvent is still there. We decided to radically increase the concentration of IL in our system in order to decrease the amount of organic solvent and examine the effect of high IL concentration on the DSC outcome.

The electrolyte compositions are shown in Table 3.17. All electrolytes have 1.50 M of corresponding IL. Multiple DSC devices were manufactured to show the reproducibility of measurements, but the discussion will focus only on one device with parameters closest to average (Table 3.18).

Table 3.17. Electrolyte compositions with 1.50 M concentration of different ILs. MPN was used as a solvent.

| Electrolyte | LiI / M | LiPF ₆ / M | I ₂ / M | IL / M |
|-------------|---------|-----------------------|--------------------|-------------|
| BMIIj | 0.10 | – | 0.05 | BMII / 1.50 |
| BMIIk | 0.18 | – | 0.05 | BMII / 1.50 |
| BMIII | – | 0.10 | 0.05 | BMII / 1.50 |

Third Chapter

| | | | | |
|--------|------|------|------|--------------|
| BMIIm | – | 0.18 | 0.05 | BMII / 1.50 |
| PMIIg | 0.18 | – | 0.05 | PMII / 1.50 |
| PDMIIc | 0.18 | – | 0.05 | PDMII / 1.50 |

Electrolytes BMIIj and BMIIk differ only in LiI concentration of 0.10 and 0.18 M, respectively. DSCs with 0.18 M LiI have PCE of 0.55% (9.7% relative to N719) and DSCs with 0.18 M LiI have PCE of 0.46% (8.1% relative to N719). The increase of BMII to 1.5 M resulted in decrease of PCE values for both BMIIj and BMIIk electrolytes compare to BMIIa and BMIIc with 0.6 M concentration (Table 3.14). The LiI trend stays the same: higher concentration results in higher PCE in the presence of 1.5 M of BMII in electrolyte.

At the 0.6 M concentration of BMII the change from LiI to LiPF₆ had a negative influence on DSC performance and resulted in lower PCE. On going from BMIIj to BMIII (0.1 M LiPF₆), the J_{SC} value increases from 2.04 to 4.16 mA cm⁻² and leads to enhanced PCE of 0.57% (Figure 3.30). Greater LiPF₆ concentration of 0.18 M results in 0.49% of PCE for electrolyte BMIIm. It is important to note, that for 0.1 M LiPF₆ higher BMII concentration improved the DSC performance compared to 0.39% with 0.6 M IL, but in the case of 0.18 M LiPF₆ the PCE value does not show any changes (Figure 3.30).

Table 3.18. Parameters for multiple DSCs with different electrolytes. Electrolyte compositions are presented in Table 3.17. All DSCs were fully masked.

| Electrolyte | $J_{SC} / \text{mA cm}^{-2}$ | V_{OC} / mV | $ff / \%$ | $\eta / \%$ | Rel. $\eta / \%$¹ |
|--------------------|--|--|-----------------------------|-------------------------------|--|
| BMIJ cell 1 | 2.07 | 356 | 62 | 0.46 | 8.0 |
| BMIJ cell 2 | 1.95 | 363 | 66 | 0.47 | 8.2 |
| BMIJ cell 3 | 1.93 | 349 | 66 | 0.45 | 7.9 |
| BMIJ cell 4 | 2.04 | 367 | 62 | 0.46 | 8.1 |
| BMIIk cell 1 | 3.02 | 311 | 61 | 0.57 | 10.1 |
| BMIIk cell 2 | 3.06 | 292 | 62 | 0.55 | 9.7 |
| BMIIk cell 3 | 2.88 | 289 | 62 | 0.52 | 9.1 |
| BMIIk cell 4 | 3.06 | 299 | 60 | 0.55 | 9.7 |
| BMIII cell 1 | 4.16 | 281 | 49 | 0.57 | 10.0 |
| BMIII cell 2 | 3.79 | 299 | 50 | 0.57 | 10.0 |
| BMIIm cell 1 | 4.25 | 237 | 47 | 0.47 | 8.3 |
| BMIIm cell 2 | 3.91 | 268 | 47 | 0.49 | 8.6 |
| PMIIg cell 1 | 2.71 | 324 | 61 | 0.54 | 9.4 |
| PMIIg cell 2 | 2.76 | 356 | 56 | 0.55 | 9.7 |

| | | | | | |
|---------------|-------|-----|----|------|-----|
| PMIIg cell 3 | 2.81 | 340 | 58 | 0.56 | 9.8 |
| PMIIg cell 4 | 2.65 | 327 | 63 | 0.54 | 9.5 |
| PDMIIc cell 1 | 2.82 | 274 | 60 | 0.46 | 8.1 |
| PDMIIc cell 2 | 2.63 | 283 | 53 | 0.40 | 7.0 |
| PDMIIc cell 3 | 2.89 | 287 | 60 | 0.50 | 8.8 |
| PDMIIc cell 4 | 2.93 | 285 | 58 | 0.49 | 8.6 |
| N719 | 13.92 | 653 | 63 | 5.70 | 100 |

¹ Relative to a value of η for N719 set at 100%.

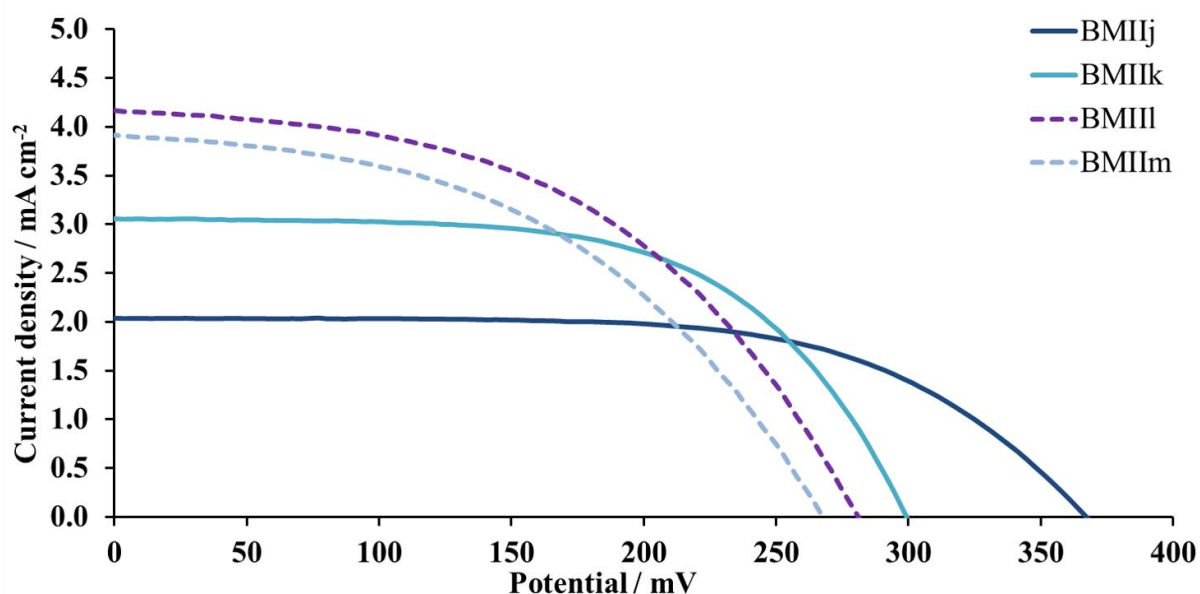


Figure 3.30. J - V curves for DSCs with electrolytes BMIIj, BMIIk, BMIII and BMIIIm.

In Figure 3.31, the dependency of J_{SC} and relative η on lithium salt concentration at different BMII concentrations is presented. In the case of an iodide anion, the linear dependency for both 0.60 and 1.50 M IL concentrations could be observed. The improvement in J_{SC} is followed by higher PCE values for all BMII concentrations in the presence of an increased amount of lithium iodide. For LiPF_6 salt, the trend for 1.50 M BMII is an opposite than for 0.60 M. The combination of increased IL and Li^+ salt concentration resulted in lower relative efficiency compared to the same amount of LiPF_6 in the presence of 0.60 M BMII.

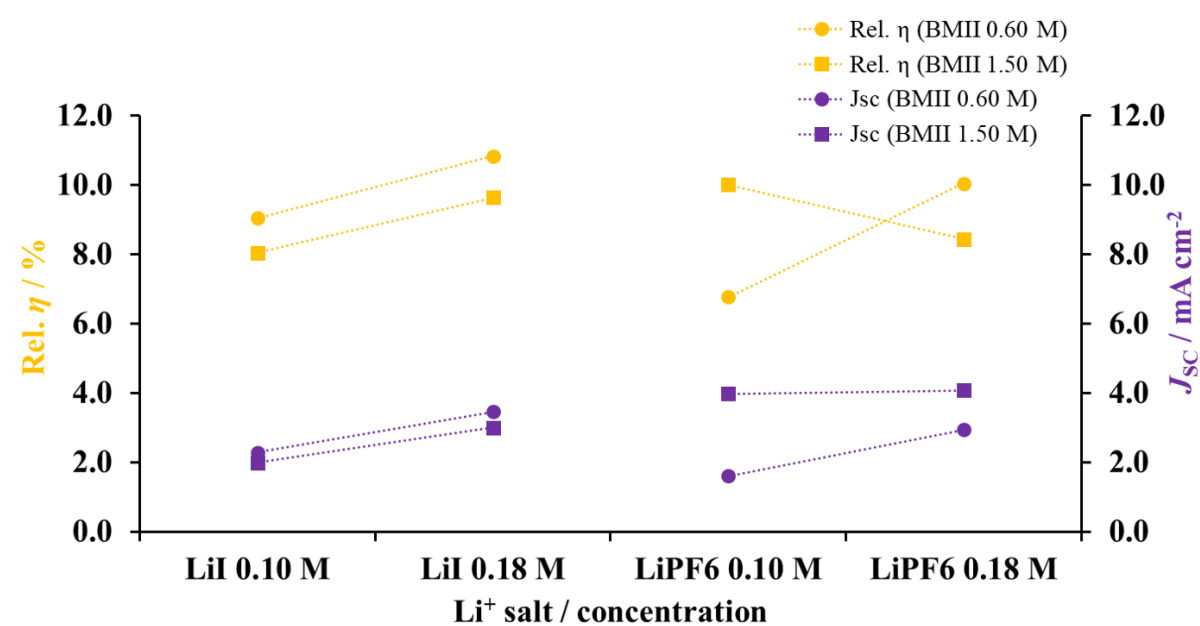


Figure 3.31. Relative η and J_{sc} for DSCs with BMII-based electrolytes in the presence of Li^+ salts to illustrate the influence of BMII concentration. Dotted lines are added to guide the eye.

Electrolytes PMIIc and PMIIg differ only in PMII concentration (0.6 M and 1.5 M, respectively, Table 3.17) with retained electrolyte composition. On going from PMIIc to PMIIg, the open-circuit voltage increases from 315 to 356 mV (Table 3.18). At the same time, decreased values of J_{sc} and ff lead to a lower PCE of 0.55% compared to 0.59% for PMIIc (Figure 3.31). In the case of PDMII IL the change of IL concentration results in decrease in both J_{sc} and V_{oc} . Thus, PDMIIc PCE value of 0.46% is much lower compared to 0.66% for electrolyte with 0.6 M PDMII concentration.

In Figure 3.32, the overall comparison of concentration influence of three ILs is presented with constant LiI quantity of 0.18 M.

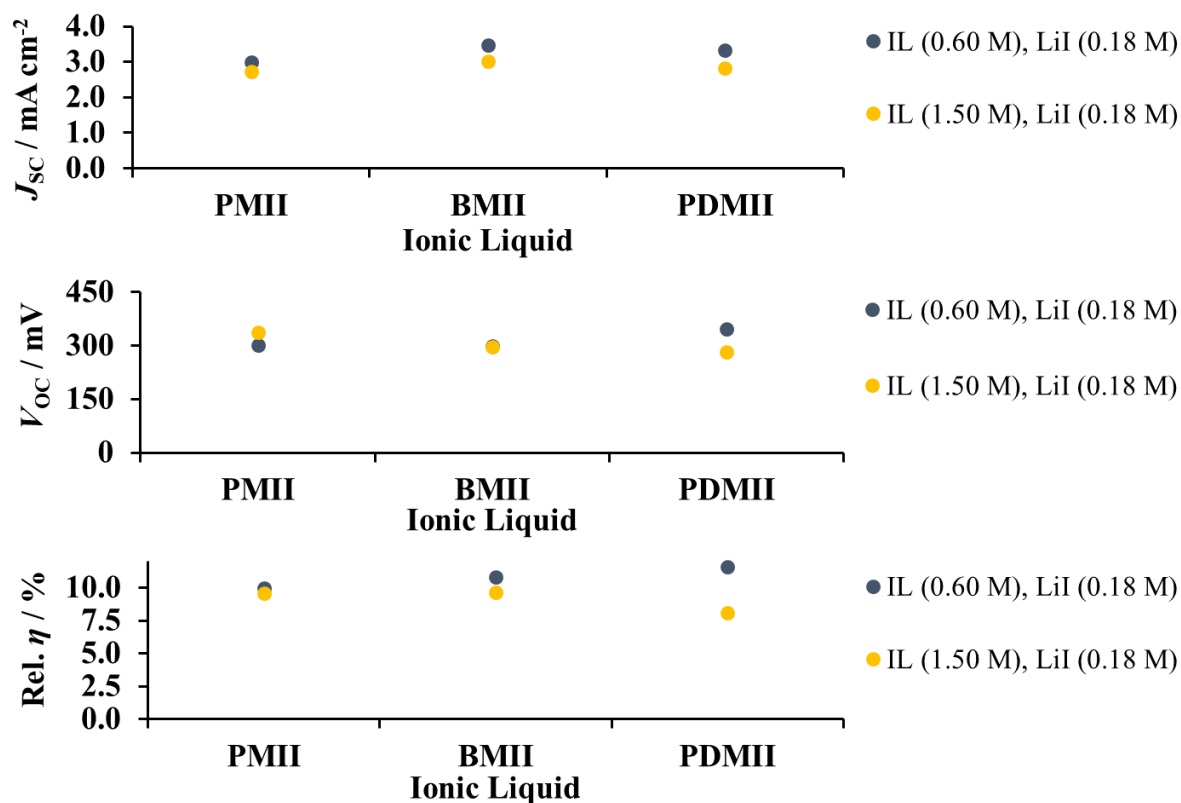


Figure 3.32. J_{sc} , V_{oc} and relative η (to N719) average values for DSCs based on PMII, BMII or PDMII ILs in the presence of LiI to illustrate the influence of ILs concentration.

For all ILs the increase in concentration led to slightly lower short-circuit current density values. In the case of the open circuit voltage, higher IL concentration resulted in increased values for PMII and did not lead to any changes for BMII. For PDMII, the 1.5 M concentration was also not beneficial for V_{oc} and led to lower voltage values. Overall, higher IL concentrations did not show any advantages in photoconversion efficiencies for all DSCs sets. For PMII relative to N719 efficiency had no significant changes on going from 0.60 to 1.50 M IL. For BMII and PDMII higher concentration led to lower relative efficiencies for both ILs.

3.2.4 Summary: Li^+ salts and IL concentration

An increase in the Li^+ ion concentration had a positive effect on the PCE for all ILs. The DSCs containing electrolytes BMIIc and BMIIe had similar J - V plot profiles with a slightly higher PCE for BMIIe. EQE and EIS data confirmed this trend. It was also shown that too high or too low an IL concentration negatively affected a PCE. Based on these results, 0.18 M LiI was considered as the optimal additive in combination with 0.60 M IL and was used for the following investigations.

3.3 Influence of structure of IL on a DSC operation

3.3.1 The change in an alkyl chain length of 1-alkyl-3-methylimidazolium iodide

ILs play an important role in a DSC operation. They contribute to DSC stability over time and affect the mass transport of a cell. The most common ILs employed in electrolytes are imidazolium salts. The length of an alkyl chain of 1-alkyl-3-methylimidazolium iodide family alters the viscosity, diffusion properties and conductivity. For example, 1-alkyl-3-methylimidazolium iodides with longer side chain have higher viscosity, where alkyl representing *n*-butyl, *n*-hexyl, and *n*-octyl.¹⁶⁸ At the same time, high viscosity of ILs brings limitations on the redox couple diffusion.¹⁶⁹ Despite the use of 1-alkyl-3-methylimidazolium iodides in combination with 3-methoxypropionitrile as an organic solvent, the ion diffusion is still strongly affected by the structure of the IL. Therefore, this structure is expected to bring significant changes in DSC performances.

Five ILs with different alkyl chain lengths were employed in our study: 1,3-dimethylimidazolium iodide, 1-ethyl-3-methylimidazolium iodide, 1-propyl-3-methylimidazolium iodide, 1-butyl-3-methylimidazolium iodide, 1-hexyl-3-methylimidazolium iodide and 1-dodecyl-3-methylimidazolium iodide (Figure 3.33). Parameters for DSC with electrolytes based on given ILs are presented in Table 3.19. Four DSCs were measured for each electrolyte, but the most representative will be discussed.

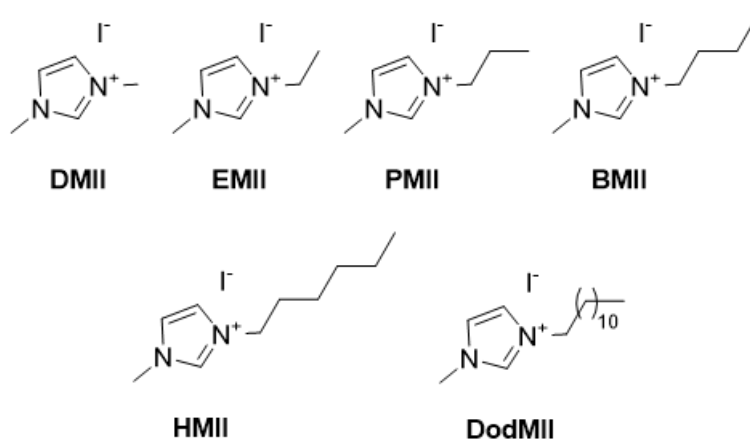


Figure 3.33. Structures of ILs with different alkyl chain length.

Table 3.19. Parameters for DSC using electrolytes with 1-alkyl-3-methylimidazolium iodide with different side chain length. Electrolyte compositions are LiI (0.18 M), I₂ (0.05 M), IL (0.60 M) in MPN.

| Electrolyte¹ | $J_{SC} / \text{mA cm}^{-2}$ | V_{OC} / mV | $ff / \%$ | $\eta / \%$ | Rel. $\eta / \%$² |
|--------------------------------|--|--|-----------------------------|-------------------------------|--|
| DMII cell 1 | 2.31 | 362 | 63 | 0.53 | 9.5 |
| DMII cell 2 | 2.35 | 348 | 62 | 0.50 | 8.9 |
| DMII cell 3 | 2.55 | 366 | 60 | 0.56 | 10.0 |
| DMII cell 4 | 2.29 | 370 | 62 | 0.52 | 9.3 |
| EMII cell 1 | 2.47 | 344 | 62 | 0.52 | 9.3 |
| EMII cell 2 | 2.63 | 344 | 61 | 0.55 | 9.8 |
| EMII cell 3 | 2.25 | 316 | 62 | 0.44 | 7.9 |
| EMII cell 4 | 2.53 | 306 | 62 | 0.48 | 8.6 |
| PMIIC cell 1 | 3.01 | 315 | 62 | 0.59 | 10.5 |
| PMIIC cell 2 | 2.98 | 270 | 62 | 0.50 | 8.9 |
| PMIIC cell 3 | 2.98 | 318 | 63 | 0.59 | 10.5 |
| BMIIC cell 1 | 3.40 | 301 | 59 | 0.61 | 10.9 |
| BMIIC cell 2 | 3.56 | 311 | 57 | 0.63 | 11.3 |
| BMIIC cell 3 | 3.51 | 291 | 58 | 0.59 | 10.5 |
| BMIIC cell 4 | 3.40 | 294 | 60 | 0.60 | 10.7 |
| HMII cell 1 | 3.14 | 316 | 60 | 0.60 | 10.7 |
| HMII cell 2 | 3.00 | 317 | 62 | 0.59 | 10.5 |
| HMII cell 3 | 3.05 | 333 | 62 | 0.63 | 11.3 |
| HMII cell 4 | 3.13 | 317 | 61 | 0.61 | 10.9 |
| DodMII cell 1 ³ | 2.74 | 278 | 62 | 0.47 | 7.5 |
| DodMII cell 2 | 3.04 | 317 | 56 | 0.54 | 8.6 |
| DodMII cell 3 | 2.41 | 287 | 60 | 0.41 | 6.5 |
| DodMII cell 4 | 2.74 | 268 | 59 | 0.43 | 6.9 |
| N719 | 12.53 | 654 | 68 | 5.60 | 100 |

¹ Parameters for electrolytes PMIIC and BMIIC are shown from Table 3.14 for convenience; ² Relative to a value of η for N719 set at 100%; ³ DSCs with DodMII electrolyte were built with a difference of several months and reference N719 values on this day were $J_{SC} = 15.36 \text{ mA cm}^{-2}$, $V_{OC} = 654 \text{ mV}$, $ff = 62\%$, $\eta = 6.27\%$.

As the alkyl chain is lengthened, an increase in PCE is observed. On going from methyl to *n*-butyl substituent the values of J_{SC} increase from 2.31 to 3.40 mA cm^{-2} (Figure 3.34). Despite the reduction in potential from 326 to 301 mV, higher J_{SC} lead to a 0.61% of PCE (10.9% relative to N719 set to 100%) for BMIIC electrolyte. Interestingly, the presence of longer alkyl chain does not lead to a further increase in an overall performance after a chain length of *n*-hexyl. Electrolyte

HMII has a similar PCE of 0.60% as for BMIIc, due to a slight increase in V_{OC} of 316 mV which is countered by a loss in J_{SC} . Further increase in the side alkyl chain to *n*-dodecyl did not show any advantages. The decrease in both J_{SC} and V_{OC} is observed compared to HMII is observed. The overall photoconversion efficiency of DSCs with DodMII electrolyte is the lowest in the sequence ($PCE_{average} = 0.47\%$, 7.5% relative to N719). The value of ff is not affected by the length of an alkyl substituent and stays more or less constant for all electrolytes.

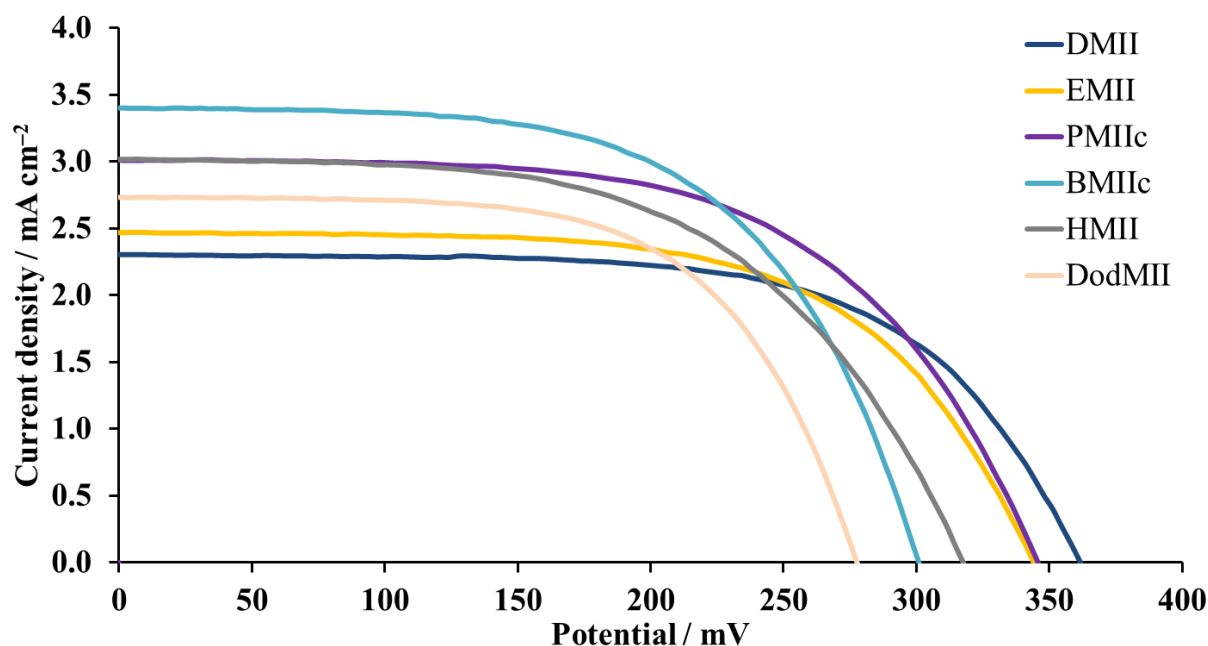


Figure 3.34. J - V curves for DSCs with electrolytes based on ILs of 1-alkyl-3-methylimidazolium iodide family.

The EQE spectra were recorded for DSCs with different side-chain length (Table 3.20). For all DSCs the spectra cover a broad range of wavelengths as expected for the NHC iron(II) dye. The trend in EQE is consistent with J_{SC} and EQE_{max} enhances from methyl ($\approx 17\%$ at $\lambda_{max} = 470$ to 490 nm) to *n*-butyl side chain up to $\approx 24\%$ at $\lambda_{max} = 430$ to 570 nm. As was observed on the example of J - V curves, the further extension to *n*-hexyl chain does not lead to any beneficial effects. The value of EQE_{max} for HMII ($\approx 20\%$) is the same as for the EMII-based electrolyte. Further increase of *n*-alkyl chain to *n*-dodecyl has no influence on EQE spectra and DSCs with DodMII electrolyte have comparable EQE_{max} to HMII.

Table 3.20. EQE_{max} values for multiple DSCs of each set.

| Electrolyte | $EQE_{max} / \%$ | | | | EQE_{max} average / % | Wavelength range ¹ / nm |
|-------------|------------------|--------|--------|----------------|----------------------------|---------------------------------------|
| | cell 1 | cell 2 | cell 3 | cell 4 | | |
| DMII | 15 | 17 | 19 | – ² | 17 | 470-490 |
| EMII | 19 | 20 | 17 | 22 | 19 | 480-500 |

Third Chapter

| | | | | | | |
|--------|----|----|----|----------------|----|---------|
| PMIIC | 24 | 21 | 21 | – ³ | 22 | 450-490 |
| BMIIC | 24 | 23 | 25 | 24 | 24 | 470-480 |
| HMII | 20 | 21 | 20 | 21 | 20 | 480-500 |
| DodMII | 19 | 21 | 11 | 21 | 18 | 490-500 |

¹ The range of λ_{\max} for multiple DSCs; ² Although the cells performed well, good EQE spectra could not be obtained; ³ Only three working cells were used from this set for all measurements.

The EIS parameters with their average values are shown in Table 3.21 and are consistent with the observed trends in J - V curves. In Figure 3.35, impedance spectra are presented. EIS experiments were carried out for multiple DSCs, but only average values will be discussed. Series resistance as well as platinum counter electrode resistance and capacitance stay constant for all DSCs.

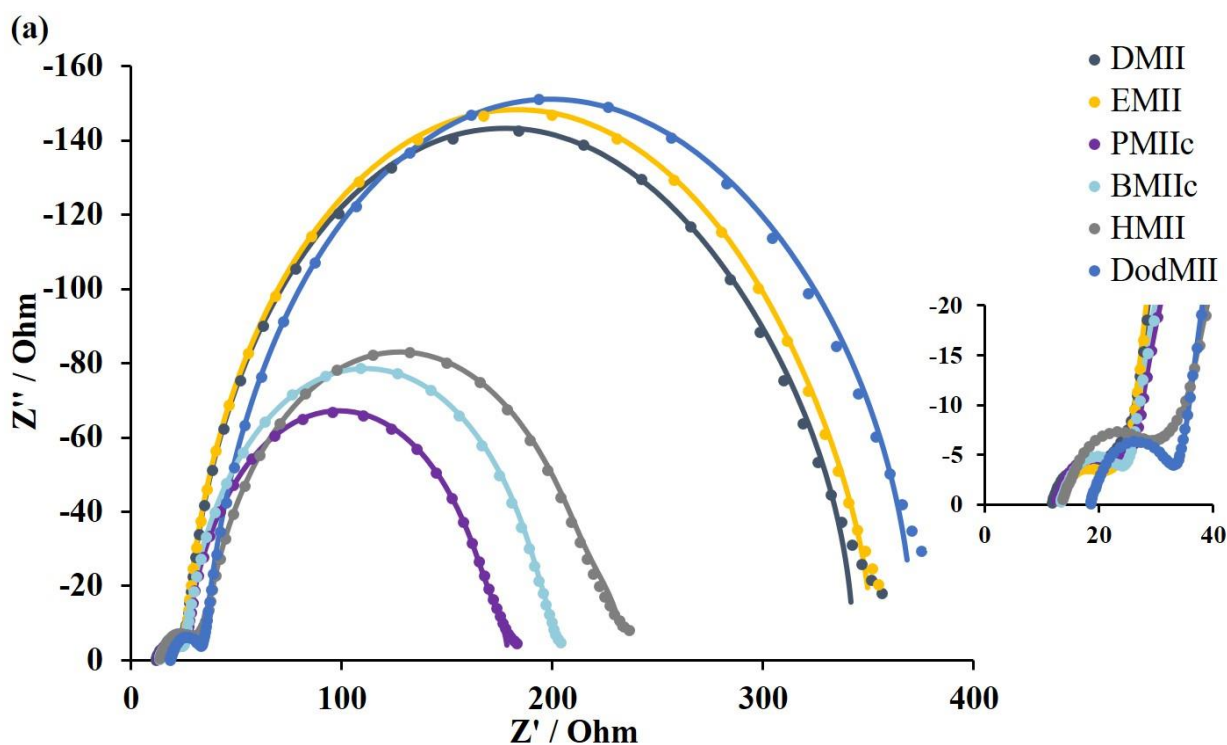
Table 3.21. EIS parameters for DSC using electrolytes with 1-alkyl-3-methylimidazolium iodide with different side chain length.

| Electrolyte | R_{rec} / Ω | $C_{\mu} / \mu\text{F}$ | R_{tr} / Ω | τ / ms | τ_t / ms | $L_d / \mu\text{m}$ | R_s / Ω | R_{Pt} / Ω | $C_{\text{Pt}} / \mu\text{F}$ |
|---------------------------------------|---------------------------|-------------------------|--------------------------|--------------------|----------------------|---------------------|----------------|--------------------------|-------------------------------|
| DMII cell 1 | 266 | 484 | 10 | 129 | 5 | 61 | 11 | 6 | 6 |
| DMII cell 2 | 269 | 416 | 22 | 112 | 9 | 42 | 12 | 6 | 7 |
| DMII cell 3 | 381 | 768 | 4 | 293 | 3 | 122 | 13 | 4 | 6 |
| DMII cell 4 | 337 | 363 | 26 | 122 | 9 | 43 | 12 | 5 | 7 |
| EMII cell 1 | 331 | 472 | 12 | 156 | 6 | 62 | 11 | 8 | 5 |
| EMII cell 2 | 299 | 464 | 19 | 139 | 9 | 48 | 13 | 6 | 5 |
| PMIIC cell 1 | 134 | 405 | 8 | 54 | 3 | 48 | 13 | 8 | 6 |
| PMIIC cell 2 | 141 | 297 | 19 | 42 | 6 | 33 | 12 | 8 | 5 |
| PMIIC cell 3 | 134 | 266 | 26 | 36 | 7 | 27 | 15 | 10 | 7 |
| HMII cell 1 | 164 | 329 | 35 | 54 | 12 | 26 | 14 | 10 | 5 |
| HMII cell 2 | 179 | 330 | 32 | 59 | 11 | 28 | 13 | 10 | 5 |
| HMII cell 3 | 155 | 256 | 62 | 40 | 16 | 19 | 12 | 13 | 6 |
| HMII cell 4 | 179 | 328 | 30 | 59 | 10 | 29 | 13 | 11 | 5 |
| DodMII cell 1 | 218 | 301 | 26 | 66 | 8 | 35 | 12 | 10 | 6 |
| DodMII cell 2 | 281 | 687 | 10 | 193 | 7 | 63 | 19 | 11 | 6 |
| DodMII cell 3 | 243 | 239 | 69 | 58 | 17 | 23 | 14 | 14 | 7 |
| DodMII cell 4 | 182 | 100 | 20 | 18 | 2 | 36 | 13 | 32 | 7 |
| DMII _{average} | 313 | 508 | 16 | 164 | 7 | 67 | 12 | 5 | 7 |
| EMII _{average} | 315 | 468 | 16 | 148 | 8 | 55 | 12 | 7 | 5 |
| PMIIC _{average} | 136 | 323 | 18 | 44 | 5 | 36 | 13 | 9 | 6 |
| BMIIC _{average} ¹ | 152 | 358 | 12 | 55 | 4 | 46 | 14 | 9 | 5 |

| | | | | | | | | | |
|----------------------------------|-----|-----|----|----|----|----|----|----|---|
| $\text{HMII}_{\text{average}}$ | 169 | 311 | 40 | 53 | 12 | 26 | 13 | 11 | 5 |
| $\text{DodMII}_{\text{average}}$ | 231 | 332 | 31 | 84 | 8 | 39 | 14 | 17 | 6 |

[†] Parameters for electrolyte $\text{BMIIc}_{\text{average}}$ are presented from Table 3.16 for convenience.

The recombination and transport resistances do not change on going from methyl to *n*-ethyl group, but the chemical capacitance decreases from 508 to 468 μF . This explains the observation of only a small deviation in J_{SC} and V_{OC} values for the respective DSC sets and leads to a comparable PCE. The similarity of DMII and EMII impedance spectra can be seen in Figure 3.35 in both Nyquist and Bode plots. The change to an *n*-propyl substituent results in a decrease in both R_{rec} and C_{μ} , what leads to enhanced short-circuit current density. The extension to an *n*-butyl chain results in increased values of recombination resistance and chemical capacitance, but lower transport resistance. The combination of these parameters results in higher J_{SC} and as consequence higher PCE compared to PMIIc electrolyte. In case of *n*-hexyl side chain an increase in R_{rec} as well as R_{tr} in combination with lower C_{μ} values lead to similar DSC efficiencies as for BMIIc. Remarkably, values of diffusion length, electron lifetime and electron transport time are consistent with each other for all sets of DSCs. The trend in τ can be seen in the Bode plot (Figure 3.35b).



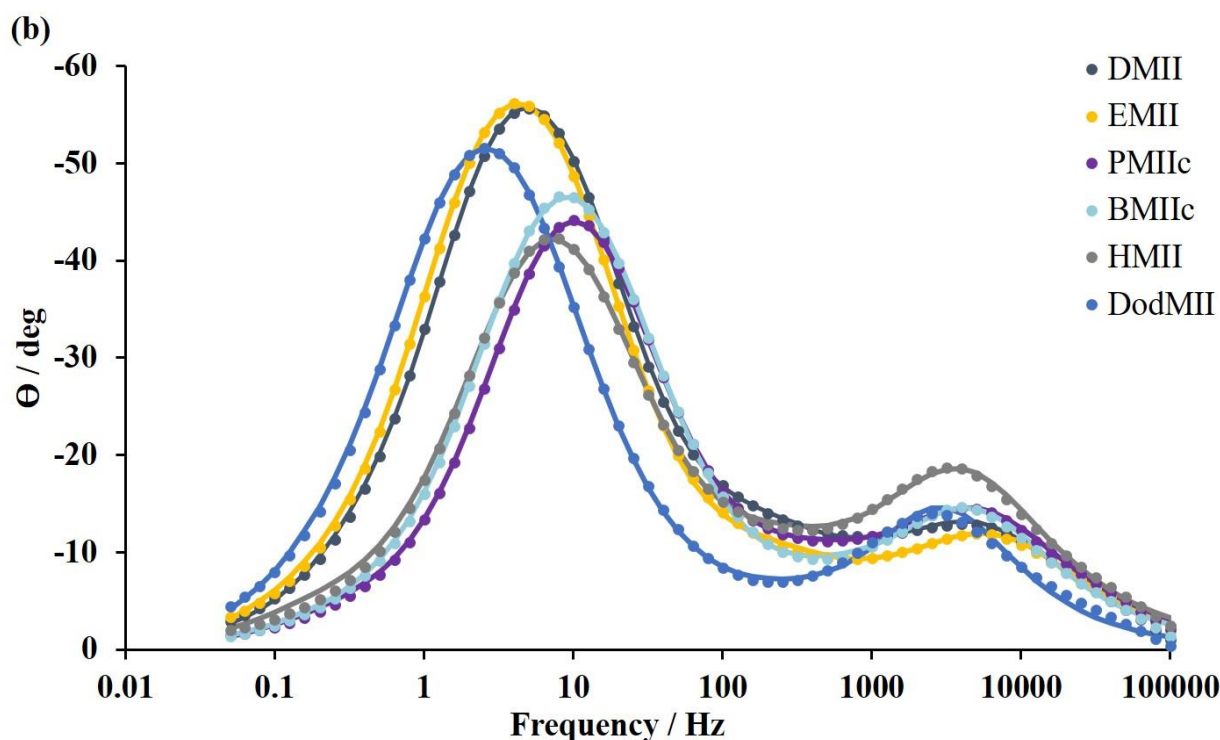


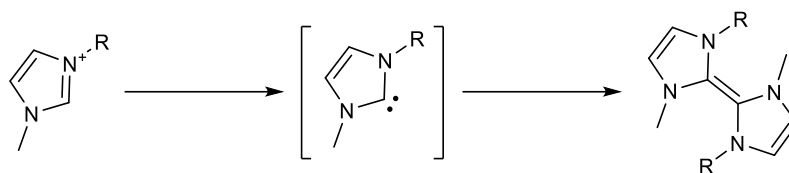
Figure 3.35. EIS plots for DSCs with electrolytes DMII, EMII, PMIIc, HMII and DodMII: a. Nyquist plot with expansion of high frequency region; b. Bode plot.

Interestingly, two groups of electrolytes could be extracted based on EIS and J - V parameters. Electrolytes DMII and EMII have similar ranges of R_{rec} ($\approx 314 \Omega$) and C_{μ} (468-508 μF), while PMIIc, BMIIc and HMII have same parameters in the ranges of 136-169 Ω for R_{rec} and 311-358 μF for C_{μ} . The same trend can be observed for DSC performances. For electrolytes DMII and EMII average J_{SC} value is 2.42 mA cm^{-2} and average PCE of 0.51%. At the same time electrolytes PMIIc-HMII have an average J_{SC} value of 3.20 mA cm^{-2} and average PCE of 0.59%. Thus, electrolytes with 1-alkyl-3-methylimidazolium iodide IL, where alkyl group is n -propyl or longer, have more favorable electron injection into the semiconductor. On the other hand, an n -hexyl chain is less suitable than an n -butyl one. This can be confirmed with values of L_d and τ_t . It is known that the optimal diffusion length has to be around three times greater than the thickness of the TiO_2 layer (d is $\approx 12 \mu\text{m}$). For HMII the decrease in the L_d value in combination with an increased τ_t lead to a less efficient electron collection on the back of an electrode.

Low transport resistance and transport time values and optimal diffusion length for BMII-based DSCs represent a small electron loss in the semiconductor and result in good performing DSCs.

3.3.2 The influence of a methyl group in the 2-position in imidazolium-based IL

Despite the broad use of imidazolium derivatives as ILs in electrolytes for DSCs, they can degrade under temperature or irradiation conditions. Because of the activated position between two nitrogen atoms, imidazolium core has a potential to form a dimer or generate a highly reactive free carbene moiety (Scheme 3.6). Under the basic conditions the ring-opening can occur. One way to avoid these types of undesired reactions is to protect the 2-position with the methyl group, which will prevent the deprotonation.



Scheme 3.6. Possible rearrangement of imidazolium-based IL.¹⁷⁰

Therefore, 1-propyl-3-methylimidazolium iodide, 1-butyl-3-methylimidazolium iodide and 1-hexyl-3-methylimidazolium iodide ILs were compared to the corresponding ILs with additional methyl group in 2-position: 1-propyl-2,3-dimethylimidazolium iodide (PDMII), 1-butyl-2,3-dimethylimidazolium iodide (BDMII) and 1-hexyl-2,3-dimethylimidazolium iodide (HDMII, Figure 3.36). The electrolyte composition for all DSCs was LiI (0.18 M), I₂ (0.05 M), IL (0.6 M) in MPN. In Table 3.22 parameters for multiple DSCs are presented, but solely values for the most representative cells will be discussed.

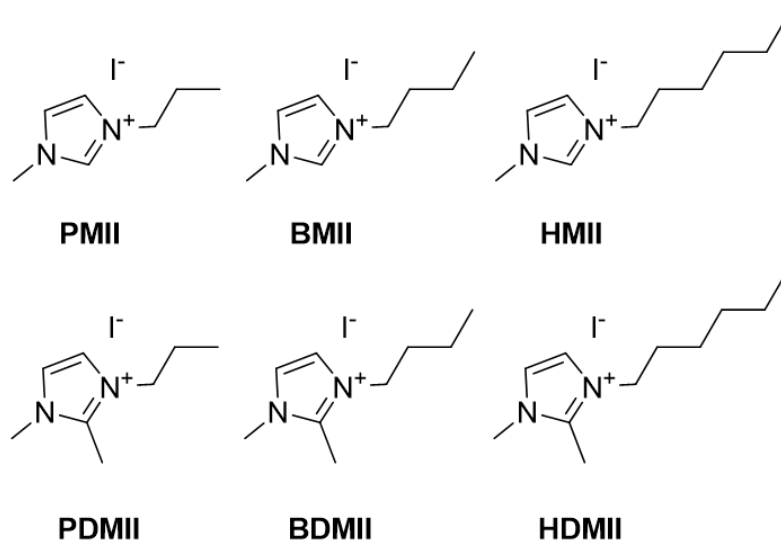


Figure 3.36. Structures of various 1-alkyl-3-methylimidazolium iodide and 1-alkyl-2,3-methylimidazolium iodide ILs.

Table 3.22. Parameters for DSCs with different ILs employed in electrolytes. All DSCs were fully masked.

| Electrolyte¹ | $J_{SC} / \text{mA cm}^{-2}$ | V_{OC} / mV | $ff / \%$ | $\eta / \%$ | Rel. $\eta / \%$² |
|--------------------------------|--|--|-----------------------------|-------------------------------|--|
| PMIIc cell 1 | 3.01 | 315 | 62 | 0.59 | 10.5 |
| PMIIc cell 2 | 2.98 | 270 | 62 | 0.50 | 8.9 |
| PMIIc cell 3 | 2.98 | 318 | 63 | 0.59 | 10.5 |
| PDMIIa cell 1 | 3.27 | 348 | 58 | 0.66 | 11.8 |
| PDMIIa cell 2 | 3.41 | 346 | 54 | 0.64 | 11.4 |
| BMIIC cell 1 | 3.40 | 301 | 59 | 0.61 | 10.9 |
| BMIIC cell 2 | 3.56 | 311 | 57 | 0.63 | 11.3 |
| BMIIC cell 3 | 3.51 | 291 | 58 | 0.59 | 10.5 |
| BMIIC cell 4 | 3.40 | 294 | 60 | 0.60 | 10.7 |
| BDMIIc cell 1 | 3.70 | 279 | 58 | 0.60 | 10.7 |
| BDMIIc cell 2 | 3.30 | 321 | 61 | 0.64 | 11.5 |
| BDMIIc cell 3 | 3.37 | 295 | 61 | 0.61 | 10.9 |
| BDMIIc cell 4 | 3.53 | 263 | 59 | 0.55 | 9.8 |
| HMII cell 1 | 3.14 | 316 | 60 | 0.60 | 10.7 |
| HMII cell 2 | 3.00 | 317 | 62 | 0.59 | 10.5 |
| HMII cell 3 | 3.05 | 333 | 62 | 0.63 | 11.3 |
| HMII cell 4 | 3.13 | 317 | 61 | 0.61 | 10.9 |
| HDMII cell 1 | 3.00 | 303 | 63 | 0.57 | 10.2 |
| HDMII cell 2 | 3.04 | 254 | 60 | 0.46 | 8.2 |
| HDMII cell 3 | 3.04 | 282 | 62 | 0.53 | 9.5 |
| HDMII cell 4 | 2.87 | 302 | 63 | 0.55 | 9.8 |
| N719 | 12.53 | 654 | 68 | 5.60 | 100 |

¹ Parameters for electrolytes PMIIc, PDMIIa and BMIIC are presented from Table 3.14 for convenience; ² Relative to a value of η for N719 set at 100%.

On going from PMII to PDMII IL the increase in both short-circuit current density and open-circuit voltage can be observed. J_{SC} value changed from 3.01 for PMII to 3.27 mA cm^{-2} for PDMII. In case of V_{OC} , the values enhanced up to 438 mV for PDMII IL compared to 315 mV for PMII. These changes correspond to higher PCE for PDMII of 0.66%.

The performances of DSCs with BMII and BDMII do not differ. The average PCE is 0.6% for both ILs. Despite the change in the structure, the DSCs containing BDMII had same average J_{SC} of 3.5 mA cm^{-2} and similar V_{OC} values, which are only 10 mV smaller, than the average for BMII. It is an interesting observation, because at room temperature (ca. 22 °C in our laboratories) these

ILs are in different states: BMII is a liquid, while BDMII is a solid. This difference could expectedly lead to variable ionic conductivity and mass transport properties. However, identical trends in DSC parameters show that the structural differentiation does not have any effect on the DSC performance.

The comparison between HMII and HDMII resulted in better PCE for HMII IL in the range of 0.60-0.63%. PCE values for HDMII lay between 0.46 and 0.57%. The difference could be explained by the higher V_{OC} for HMII, which is 320 mV (average for 4 cells) compared to 285 mV (average) for HDMII. At the same time, the short-circuit current density stayed the same, around 3.0 mA cm^{-2} for both ILs.

The overall PCE trend for all ILs is shown in Figure 3.37, where the blue colour corresponds to mono-methylated and yellow corresponds to bis-methylated imidazolium ring. Average values of multiple DSCs were used for all parameters.

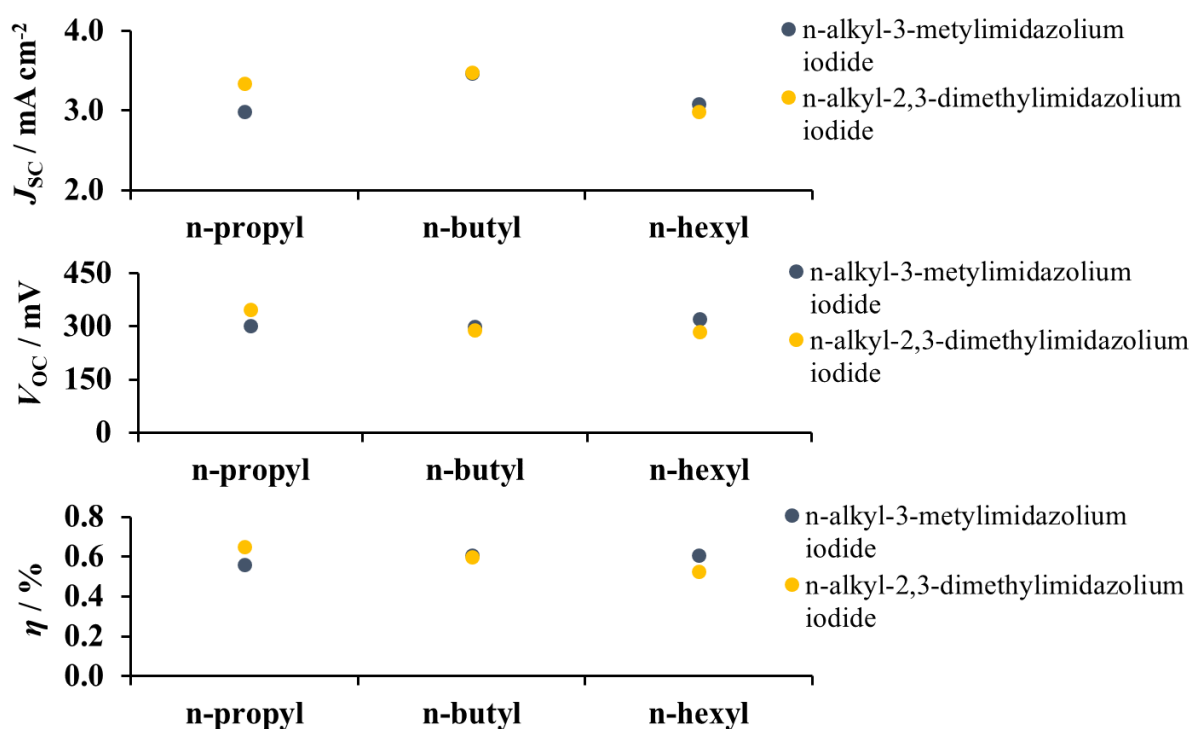


Figure 3.37. J_{sc} , V_{oc} and η average values for DSCs based on *n*-alkyl-3-methylimidazolium iodide or *n*-alkyl-2,3-dimethylimidazolium iodide to illustrate the influence of IL structure.

For the *n*-propyl side chain, the presence of the additional methyl group led to an increase in both J_{SC} and V_{OC} values. This effect had a direct impact on photoconversion efficiency and resulted in a higher η for PDMII than PMII. The data for 1-butyl-3-methylimidazolium iodide are very similar to those for cells with BDMII and indicate the similar performance of DSCs based on these ILs. When a *n*-hexyl chain is incorporated, both J_{SC} and V_{OC} had a small decrease in values on going

from HMII to HDMII and, thus, a lower η was observed for the IL with two methyl groups in the structure.

3.3.3 The influence of IL counterion on DSC performance

A high quantity of imidazolium iodide in an electrolyte results in increased Γ^- concentrations, which contribute to the redox shuttle and result in faster dye regeneration. At the same time, too high amounts of iodide ion lead to a loss of the photocurrent due to the effective quenching of dye and sequential ineffective electron injection into the semiconductor.⁸⁸ In order to overcome this drawback, we decided to investigate the impact of ILs with different counterions.

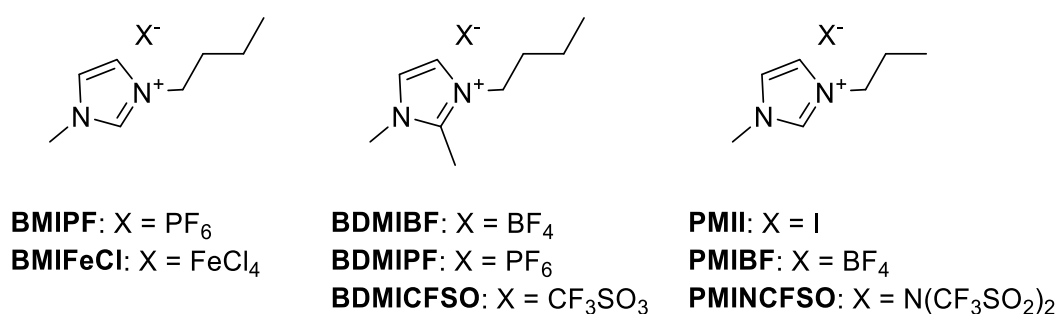


Figure 3.38. Structures of ILs with different counterions used in this study.

Following compounds were chosen for the investigations: 1-butyl-3-methylimidazolium tetrachloroferrate and hexafluorophosphate, 1-butyl-2,3-dimethylimidazolium ILs with tetrafluoroborate, hexafluorophosphate and trifluoromethanesulfonate counterions and 1-propyl-3-methylimidazolium ILs with tetrafluoroborate, bis(trifluoromethylsulfonyl)imide and iodide counterions (Figure 3.38). The performances of DSCs containing the electrolytes with different ILs are summarized in Table 3.23. The electrolyte composition was LiI 0.18 M, I₂ 0.05 M and IL 0.6 M in MPN.

Table 3.23. Parameters for multiple DSCs using electrolytes based on imidazolium ILs with different counterions. All DSCs were fully masked.

| Electrolyte | $J_{sc} / \text{mA cm}^{-2}$ | V_{oc} / mV | $ff / \%$ | $\eta / \%$ | Rel. $\eta / \%$ ¹ |
|-----------------|------------------------------|----------------------|-----------|-------------|-------------------------------|
| BDMIBF cell 1 | 3.80 | 266 | 41 | 0.41 | 7.3 |
| BDMIBF cell 2 | 4.09 | 251 | 39 | 0.40 | 7.1 |
| BDMIPF cell 1 | 2.84 | 351 | 58 | 0.57 | 10.2 |
| BDMIPF cell 2 | 2.83 | 346 | 57 | 0.56 | 10.0 |
| BDMICFSO cell 1 | 2.22 | 385 | 66 | 0.56 | 10.0 |

| | | | | | |
|------------------|-------|-----|----|------|------------------|
| BDMICFSO cell 2 | 2.07 | 387 | 67 | 0.54 | 9.6 |
| PMIBF cell 1 | 4.90 | 244 | 30 | 0.35 | 6.3 |
| PMIBF cell 2 | 3.34 | 248 | 26 | 0.21 | 3.8 |
| PMINCFISO cell 1 | 2.84 | 316 | 62 | 0.56 | 10.0 |
| PMINCFISO cell 2 | 2.88 | 311 | 61 | 0.55 | 9.8 |
| BMIPF cell 1 | 1.17 | 142 | 31 | 0.05 | 0.8 ² |
| BMIPF cell 2 | 1.84 | 187 | 31 | 0.11 | 1.5 |
| BMIPF cell 3 | 1.52 | 224 | 37 | 0.12 | 1.8 |
| BMIPF cell 4 | 0.73 | 305 | 48 | 0.11 | 1.6 |
| BMIFeCl | – | – | – | – | – |
| N719 | 12.53 | 654 | 68 | 5.60 | 100 |

¹ Relative to a value of η for N719 set at 100%. ² DSCs with BMIPF electrolyte were built with a difference of several months and reference N719 values on this day were $J_{SC} = 13.83 \text{ mA cm}^{-2}$, $V_{OC} = 736 \text{ mV}$, $ff = 67\%$, $\eta = 6.81\%$.

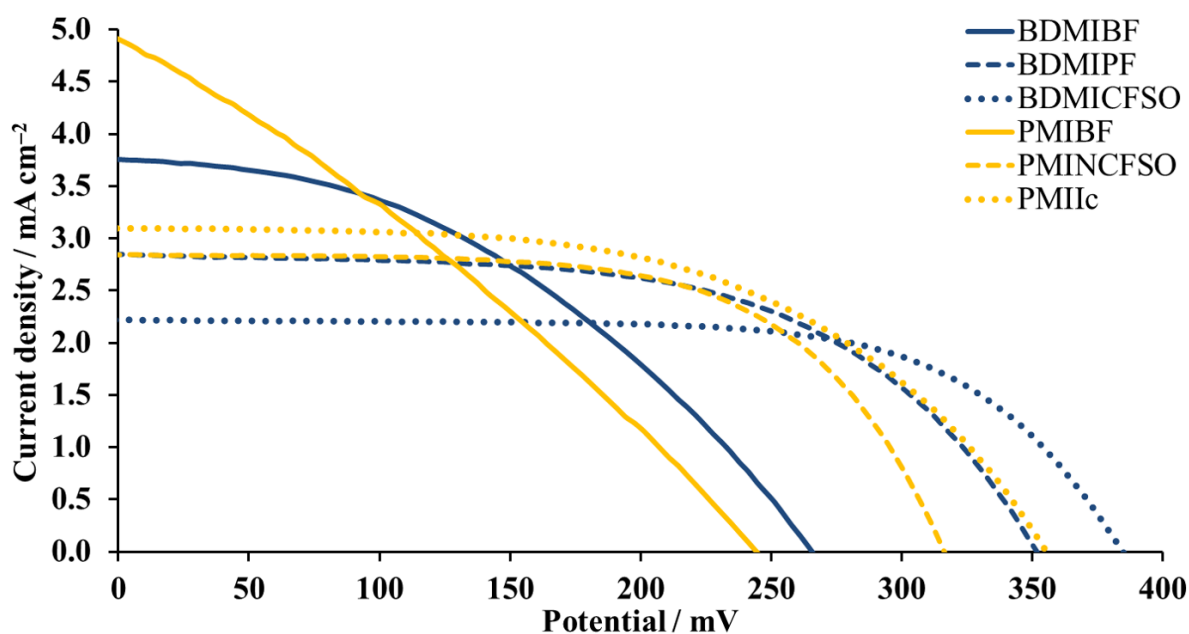


Figure 3.39. J - V curves for DSCs with electrolytes based on [BDMII]⁺ and [PMI]⁺ ILs with different counterions.

In the series of [BDMI]⁺ ILs with [BF₄]⁻, [PF₆]⁻ and [CF₃SO₃]⁻ counterions, J_{SC} values fall from 3.80 to 2.22 mA cm⁻², while open circuit voltage enhances from 266 to 385 mV (Figure 3.39). In the [PMI]⁺ series, the observed trend is the same. On going from [BF₄]⁻ to [N(CF₃SO₂)₂]⁻ and to I⁻ an increase in V_{OC} is followed by a decrease in J_{SC} . This results in a better photoconversion efficiency of 0.56% for PMINCFISO electrolyte than 0.35% for PMIBF. The highest PCE of 0.59% is observed for electrolyte PMIIc and translates to a relative efficiency of 10.5% with respect to N719 set at 100% (Table 3.23).

Third Chapter

Interestingly, for [BDMI]⁺ the change from [PF₆]⁻ to [CF₃SO₃]⁻ has only a little effect on the DSC efficiencies (0.57 and 0.56%). For [PMI]⁺ there is a moderate gain in performance from 0.35 to 0.56% (6.3 and 10.0% relative to N719) on going from [N(CF₃SO₂)₂]⁻ to I⁻ counterion as a consequence of enhanced J_{SC} value of 3.01 mA cm⁻² while retaining V_{OC} .

The presence of [BF₄]⁻ counterions is not beneficial in either of the BDMIBF or PMIBF electrolytes. Despite high short-circuit current densities values, low V_{OC} values of 266 and 264 mV in combination with low ff values of 41 and 30% lead to PCE values of 0.41 and 0.35% for BDMIBF and PMIBF, respectively.

DSCs containing the electrolyte with BMIPF have the lowest performance in the series except BMiFeCl. DSCs with 1-butyl-3-methylimidazolium hexafluorophosphate have J_{SC} values <2.00 mA cm⁻². The J - V curves for devices with these ILs were not especially reproducible, and this is often the case in our study of the iron(II) NHC sensitized cells with small PCE values.

DSCs with the BMiFeCl electrolyte in which the 1-butyl-3-methylimidazolium salt has tetrachloroferrate as counterion, do not have any current going through cell. It is important to note that the electrolyte had a dark red colour, but during DSC irradiation it turned bright pink. We have no explanation for this observation.

3.3.4 The influence of mixed counterions of 1-alkyl-3-methylimidazolium ILs

As was discussed above, high concentrations of I⁻ in the electrolyte provoke dye quenching and decrease electron injection. Thus, the use of ILs with different counterions can decrease the iodide concentration in the system while retaining the quantity of imidazolium cation. At the same time in section 3.3.3, it was shown that the change of the imidazolium salt counterion from iodide to non-halide ions did not lead to an increase in PCE values. However, anomalous high short-circuit current densities were observed for ILs with the [BF₄]⁻ counter ion. We therefore considered it of interest to combine the benefits of ILs with the different anion and try the electrolytes with binary ionic liquids.

Compositions for tested electrolytes with mixed ILs are presented in Table 3.24. 1-propyl-3-methylimidazole iodide, 1-butyl-3-methylimidazole iodide, 1-propyl-3-methylimidazole tetrafluoroborate and 1-butyl-3-methylimidazole hexafluorophosphate were chosen as ionic liquid components.

Third Chapter

Table 3.24. Electrolyte composition based on binary ionic liquids used for DSCs manufacturing. The solvent was MPN for all systems. $[\text{Im}]^+[\text{I}]^-$ is an imidazolium-based IL with iodide counterion; $[\text{Im}]^+[\text{X}]^-$ is imidazolium-based IL with any counterion except iodide.

| Electrolyte | $[\text{Im}]^+[\text{I}]^- / \text{M}$ | $[\text{Im}]^+[\text{X}]^- / \text{M}$ | LiI / M | I_2 / M |
|-------------|--|--|-------------------------|-------------------------|
| PMII-BFa | PMII / 0.52 | PMIBF ₄ / 0.08 | 0.18 | 0.05 |
| PMII-BFb | PMII / 0.52 | PMIBF ₄ / 0.04 | 0.18 | 0.05 |
| BMII-PFa | BMII / 0.52 | BMIPF ₆ / 0.08 | 0.18 | 0.05 |
| BMII-PFb | BMII / 0.52 | BMIPF ₆ / 0.04 | 0.18 | 0.05 |
| BMIPF | – | BMIPF ₆ / 0.60 | 0.18 | 0.05 |

The starting point was an PMIIc electrolyte containing 0.60 M IL . In section 3.2.3, it was shown that higher IL concentrations are not beneficial for DSCs, so it was decided to keep the total IL concentration as 0.60 M in all electrolytes. The combinations of PMII and PMIBF as well as BMII and BMIPF ILs were tested. The photovoltaic parameters are presented in Table 3.25 where entries 1, 2, 3, 4, 5 correspond to PMII-BFa, PMII-BFb, BMII-PFa, BMII-PFb and BMIPF electrolytes, respectively. In the following discussion the average values of J - V parameters will be considered for an appropriate comparison of DSCs sets between each other.

Table 3.25. Parameters for DSCs using mixed ILs in electrolytes. All DSCs were fully masked.

| Entry | Electrolyte | $J_{sc} / \text{mA cm}^{-2}$ | V_{oc} / mV | $ff / \%$ | $\eta / \%$ | Rel. $\eta / \% ^I$ |
|-------|-----------------|------------------------------|----------------------|-----------|-------------|---------------------|
| 1 | PMII-BFa cell 1 | 2.83 | 283 | 57 | 0.46 | 7.0 |
| | PMII-BFa cell 2 | 3.15 | 251 | 57 | 0.45 | 6.8 |
| | PMII-BFa cell 3 | 2.99 | 242 | 58 | 0.42 | 6.4 |
| | PMII-BFa cell 4 | 3.50 | 224 | 57 | 0.45 | 6.9 |
| 2 | PMII-BFb cell 1 | 2.53 | 305 | 62 | 0.48 | 7.3 |
| | PMII-BFb cell 2 | 2.47 | 301 | 64 | 0.48 | 7.3 |
| | PMII-BFb cell 3 | 2.72 | 279 | 65 | 0.49 | 7.5 |
| | PMII-BFb cell 4 | 2.58 | 299 | 67 | 0.52 | 8.0 |
| 3 | BMII-PFa cell 1 | 2.47 | 308 | 61 | 0.46 | 7.0 |
| | BMII-PFa cell 2 | 2.56 | 310 | 62 | 0.49 | 7.5 |
| | BMII-PFa cell 3 | 2.34 | 312 | 66 | 0.48 | 7.3 |
| | BMII-PFa cell 4 | 2.98 | 290 | 63 | 0.55 | 8.4 |
| 4 | BMII-PFb cell 1 | 2.50 | 294 | 59 | 0.43 | 6.6 |
| | BMII-PFb cell 2 | 2.67 | 294 | 59 | 0.46 | 7.0 |
| | BMII-PFb cell 3 | 2.79 | 282 | 64 | 0.50 | 7.6 |

| | | | | | | |
|---|-----------------------------|-------|-----|----|------|-----|
| | BMII-PFb cell 4 | 2.84 | 282 | 66 | 0.53 | 8.1 |
| 5 | BMIPF cell 1 | 1.17 | 142 | 31 | 0.05 | 0.8 |
| | BMIPF cell 2 | 1.84 | 187 | 31 | 0.11 | 1.7 |
| | BMIPF cell 3 | 1.52 | 224 | 37 | 0.12 | 1.8 |
| | BMIPF cell 4 | 0.73 | 305 | 48 | 0.11 | 1.7 |
| – | PMII-BFa _{average} | 3.12 | 250 | 57 | 0.45 | 6.8 |
| – | PMII-BFb _{average} | 2.58 | 296 | 65 | 0.49 | 7.5 |
| – | BMII-PFa _{average} | 2.59 | 305 | 63 | 0.50 | 7.6 |
| – | BMII-PFb _{average} | 2.70 | 288 | 62 | 0.48 | 7.3 |
| – | BMIPF _{average} | 1.32 | 214 | 36 | 0.10 | 1.5 |
| – | N719 | 13.90 | 717 | 66 | 6.54 | 100 |

¹ Relative to a value of η for N719 set at 100%.

The electrolyte PMII-BFa contains 0.52 M PMII and 0.08 M PMIBF₄. For this electrolyte, an increase in J_{SC} was observed compared to PMIIc, but the average value of 3.12 mA cm⁻² is lower than that for the PMIBF. For V_{OC} with higher values were observed for PMII-BFa than for PMIIc electrolyte. The overall efficiency decreases with addition of PMIBF₄ despite the increase in short-circuit current density. The opposite trend is observed for PMII-BFb. The lower 0.04 M concentrations of [BF₄]⁻ led to lower current density values, but higher potential and, thus, higher PCE compared to 0.08 M BMIBF₄ in the electrolyte.

In Figure 3.40, the overview of average values for J_{SC} , V_{OC} and relative η for all DSCs sets is presented.

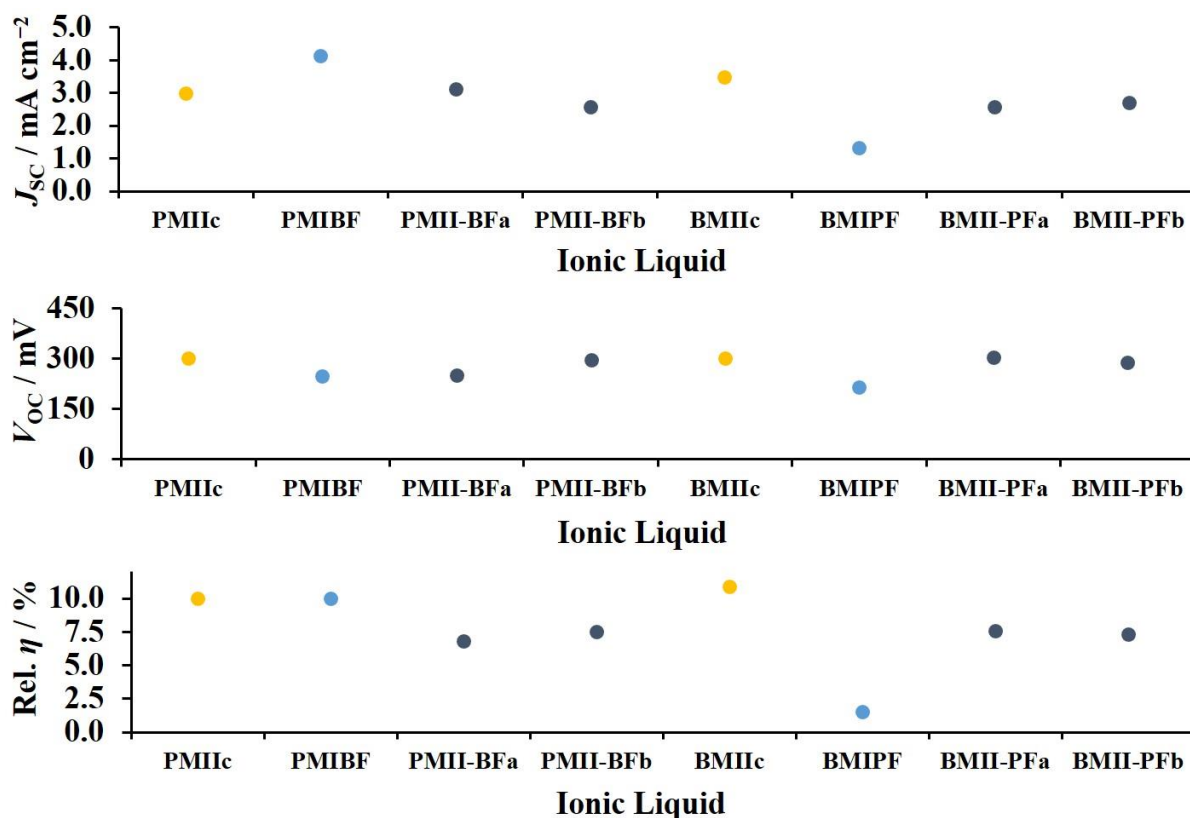


Figure 3.40. J_{sc} , V_{oc} and relative η average values for DSCs based on electrolytes with mixed ILs to illustrate the influence of imidazolium anion. The total concentration of IL is always 0.60 M. The retained electrolyte composition is 0.18 M LiI, 0.05 M I₂ in MPN. The detailed electrolyte compositions are presented in Table 3.24. Yellow dots correspond to iodine counterion, bright blue to [BF₄]⁻ in case of [PMI]⁺ and [PF₆]⁻ in case of [BMI]⁺. Dark blue dots correspond to electrolytes with mixed ILs. *Note:* For PMIBF electrolyte the good reproducibility was achieved for J_{sc} and V_{oc} values, but due to the deviations in ff , the reproducibility of the set was relatively low in terms of relative efficiency (6.3 and 3.8%) and, thus, average relative η cannot be directly compared to other electrolytes' values.

The average relative efficiency of DSCs with BMIPF electrolyte was dramatically low compared to BMIIc (relative η 1.5% and 10.6%, respectively, Figure 3.40). The addition of 0.08 M BMIPF₆ IL to 0.52 M BMII (electrolyte BMI-PFa, Table 3.24) did not improve the efficiency compared to BMIIc and decreased the values of J_{sc} . The V_{oc} values remained the same for both electrolytes. Reducing the BMIPF₆ concentration to 0.04 M (Table 3.24, electrolyte BMII-PFb) did not lead to significant changes in PCE on going from BMI-PFa to BMI-PFb electrolyte.

Overall, the mixture of ILs in electrolyte is beneficial compared to only [Im]⁺[X]⁻ (where X ≠ I), but the performance of DSCs with mixed ILs is still lower than that with only iodide as a counter ion for IL.

3.3.5 Summary: The influence of *n*-alkyl substituents and counterions of ILs

Our investigations have shown that the increase in the length of the alkyl side chain in imidazolium ILs has a positive effect on DSC performance. The two best performing electrolytes were based on PMII and BMII ILs. However, the optimal side chain for 1-alkyl-3-methylimidazolium iodide is *n*-butyl and the further increase in length to *n*-hexyl does not have any benefits. This conclusion is confirmed in the EQE spectra and EIS measurements. The presence of additional methyl group in 2-position for PMII and BMII ILs leads to higher PCE for PDMII and similar PCE of $\approx 0.61\%$ in case of BDMII. In case of HMII, the changes in the structure led to lower average performance of 0.52%. These experiments have shown that for imidazolium ILs with longer *n*-alkyl side chains starting from *n*-butyl, an additional methyl group is not beneficial. The further adjustments were done with counterions of ILs of imidazolium family. The counterion change has resulted in high V_{OC} values for BDMICFSO and PMINCFISO electrolytes, while $[BF_4]^-$ containing ILs are not advantageous despite high J_{SC} values. The combination of ILs with different counterions did not improve the DSC photovoltaic performance despite high J_{SC} values. The best overall performances were achieved with $[PDMI]^+$ ionic liquid with I^- counterion.

3.4 Influence of iodine concentration on DSCs performance

3.4.1 Motivation

All electrolytes in our study have the iodide/triiodide redox couple, which can be described as in Equation 3.1. In solution, iodine and iodide form triiodide. In detail the interaction between redox shuttle and dye is described in First Chapter, section 1.4.4.



The triiodide concentration is of importance for well performing dye-sensitized solar cell and directly affects V_{OC} values due to the redox potential of the electrolyte.¹⁷¹ Triiodide concentration depends on the iodine concentration according to Equation 3.1. Usually, the formation constant for triiodide is high in organic solvents. At the same time, the concentration of iodide ions is also much higher than that of iodine.⁸⁴ For example, electrolyte PDMIIa consists of LiI, I_2 and PDMII. The total concentration of I^- is 0.78 M (LiI 0.18 M in combination with PDMII 0.60 M), while the starting concentration of iodine is just 0.05 M before the injection of electrolyte into the DSC device.

It has been demonstrated using the dye N719 that an increase in I_2 concentration has a direct influence on the short-circuit current density.¹⁷² The optimal iodine concentration for the electrolyte in acetonitrile was 0.03 M (remaining electrolyte composition, i.e. excluding iodine, is 1.00 M PMII, 0.10 M guanidinium thiocyanate, 0.50 M MBI in MeCN). On going from lower to higher iodine concentration (0.03 M \rightarrow 0.20 M \rightarrow 0.50 M), a positive shift of the redox potential was observed. Despite this shift, the V_{OC} values were not affected by varying iodine concentrations. Interestingly, the usage of 1-ethyl-3-methylimidazolium tetracyanoborate (EMIBCN) IL as a solvent led to a different trend and 0.20 M I_2 was the most beneficial concentration. It was also shown that the effective diffusion coefficient for triiodide was in a good agreement with the literature for IL electrolyte, while for MeCN media it was one order of magnitude lower than expected.¹⁷²

Two main differences between acetonitrile and EMIBCN are their density and their viscosity, which has a great influence on ion diffusion in the electrolyte. In Table 3.26, the densities of MeCN, EMIBCN and MPN are presented. As expected, EMIBCN as an IL has the highest density and acetonitrile has the lowest, while MPN (which is commonly used in our systems) has a density

which is in between these two solvents. The same trend for chosen solvents is observed in viscosity.

Table 3.26. Solvent densities at room temperature.

| Solvent | Density [g/mL at 25°C] | Viscosity [mPa s] ¹ |
|--|------------------------|--------------------------------|
| Acetonitrile | 0.786 | 0.37 / 298 K |
| 1-Ethyl-3-methylimidazolium tetracyanoborate | 1.294 | 19.8 / 293 K |
| 3-Methoxypropionitrile | 0.937 | 2.5 / 298 K |

¹ 1 cP = 1 mPa s

The triiodide diffusion capability directly contributes to DSC efficiency. Since the viscosity of electrolyte media directly influences the transport of the redox shuttle, and viscous solvents can retard the ion diffusion¹⁷², higher iodine concentrations can help to overcome this limitation. At the same time, more recombination processes can occur. Hence, the optimal iodine concentration needs to be found for the best possible electrolyte combination.

In our previous investigations we had shown that IL structure highly influences the iron(II)-based DSC photovoltaic performance. Therefore, various concentrations of iodine were tested for FeNHC-based DSCs in the presence of different ILs with MPN as an electrolyte solvent.

3.4.2 Comparison of electrolytes with 0.05 M and 0.10 M I₂

In Table 3.27, parameters extracted from *J-V* curves for various electrolytes with 0.10 M iodine concentration are presented. The ruthenium(II) dye N719 was used as a reference. 1,3-Dimethylimidazole iodide, 1-ethyl-3-methylimidazole iodide, 1-propyl-3-methylimidazole iodide, 1-butyl-3-methylimidazole iodide, 1-hexyl-3-methylimidazole iodide, 1-propyl-2,3-dimethylimidazole iodide, 1-butyl-2,3-dimethylimidazole iodide and 1-hexyl-2,3-dimethylimidazole iodide were chosen as ionic liquid components in electrolytes (Table 3.27, electrolytes DMIIa (entry 1), EMIIa (entry 2), PMIIg (entry 3), BMIIo (entry 4), HMIIa (entry 5), PDMIIe (entry 6), BDMIIb (entry 7), HDMIIa (entry 8) and PDMIIId (entry 9)). The composition was LiI 0.18 M, I₂ 0.10 M and IL 0.60 M in MPN for all electrolytes except PDMIIId, where 0.5 M

MBI was added. In 2020, Becker *et al.* published the statistical investigations of the reproducibility of DSCs (the investigation is presented in Chapter 2).¹⁷³ It was shown that multiple DSCs are required for representative data. It is convenient to use average values of multiple DSCs for the comparison between the cells instead of data collected for one device. Thus, in the following discussion the average values of J - V parameters will be considered for appropriate comparison of DSCs sets between each other.

Table 3.27. Parameters for sets of multiple DSCs using electrolytes with 1-alkyl-3-methylimidazolium iodide or 1-alkyl-2,3-dimethylimidazolium iodide with different side chain length and increased iodine concentration. Electrolyte composition is LiI (0.18 M), I₂ (0.10 M), IL (0.60 M) in MPN everywhere, except PDMIIId. In the end of the Table, average data are presented for each parameter. All DSCs were fully masked.

| Entry | Electrolyte | $J_{sc} / \text{mA cm}^{-2}$ | V_{oc} / mV | $ff / \%$ | $\eta / \%$ | Rel. $\eta / \%$ ¹ |
|-------|---------------|------------------------------|----------------------|-----------|-------------|-------------------------------|
| 1 | DMIIa cell 1 | 3.94 | 282 | 61 | 0.67 | 10.8 |
| | DMIIa cell 2 | 3.70 | 285 | 60 | 0.64 | 10.3 |
| | DMIIa cell 3 | 3.93 | 275 | 58 | 0.62 | 10.0 |
| | DMIIa cell 4 | 3.70 | 296 | 61 | 0.67 | 10.8 |
| 2 | EMIIa cell 1 | 3.50 | 211 | 41 | 0.30 | 4.8 |
| | EMIIa cell 2 | 4.69 | 234 | 48 | 0.53 | 8.6 |
| | EMIIa cell 3 | 2.86 | 173 | 38 | 0.19 | 3.1 |
| | EMIIa cell 4 | 4.39 | 187 | 40 | 0.33 | 5.3 |
| 3 | PMIIg cell 1 | 2.55 | 288 | 64 | 0.47 | 7.6 |
| | PMIIg cell 2 | 2.37 | 297 | 64 | 0.45 | 7.3 |
| | PMIIg cell 3 | 2.53 | 297 | 63 | 0.48 | 7.7 |
| | PMIIg cell 4 | 2.48 | 306 | 63 | 0.47 | 7.7 |
| 4 | BMIIo cell 1 | 2.45 | 274 | 64 | 0.43 | 6.9 |
| | BMIIo cell 2 | 2.19 | 263 | 64 | 0.37 | 6.0 |
| | BMIIo cell 3 | 2.56 | 275 | 64 | 0.45 | 7.3 |
| | BMIIo cell 4 | 2.48 | 266 | 63 | 0.42 | 6.7 |
| 5 | HMIIa cell 1 | 2.95 | 164 | 32 | 0.16 | 2.6 |
| | HMIIa cell 2 | 2.84 | 166 | 32 | 0.15 | 2.4 |
| | HMIIa cell 3 | 2.10 | 115 | 29 | 0.07 | 1.1 |
| | HMIIa cell 4 | 2.52 | 138 | 29 | 0.10 | 1.6 |
| 6 | PDMIIe cell 1 | 3.51 | 171 | 47 | 0.28 | 4.5 |
| | PDMIIe cell 2 | 3.69 | 156 | 42 | 0.24 | 3.9 |
| | PDMIIe cell 3 | 3.34 | 154 | 43 | 0.22 | 3.6 |

| | | | | | | |
|---|-----------------------------|------|-----|----|------|------|
| | PDMIIe cell 4 | 3.45 | 144 | 39 | 0.20 | 3.2 |
| 7 | BDMIIb cell 1 | 2.56 | 283 | 61 | 0.44 | 7.2 |
| | BDMIIb cell 2 | 2.59 | 262 | 60 | 0.40 | 6.5 |
| | BDMIIb cell 3 | 2.59 | 282 | 60 | 0.44 | 7.1 |
| | BDMIIb cell 4 | 2.45 | 260 | 61 | 0.39 | 6.2 |
| 8 | HDMIIa cell 1 | 2.45 | 251 | 57 | 0.35 | 5.7 |
| | HDMIIa cell 2 | 2.59 | 229 | 56 | 0.33 | 5.3 |
| | HDMIIa cell 3 | 2.51 | 229 | 56 | 0.32 | 5.2 |
| | HDMIIa cell 4 | 2.76 | 259 | 52 | 0.38 | 6.1 |
| 9 | PDMIIId cell 1 ² | 0.07 | 285 | 51 | 0.01 | 0.2 |
| | PDMIIId cell 2 | 0.07 | 278 | 50 | 0.01 | 0.2 |
| – | DMIIa _{average} | 3.82 | 285 | 60 | 0.65 | 10.5 |
| – | EMIIa _{average} | 3.86 | 201 | 42 | 0.34 | 5.5 |
| – | PMIIg _{average} | 2.48 | 297 | 63 | 0.47 | 7.6 |
| – | BMIIo _{average} | 2.42 | 269 | 64 | 0.42 | 6.7 |
| – | HMIIa _{average} | 2.60 | 146 | 31 | 0.12 | 1.9 |
| – | PDMIIe _{average} | 3.50 | 156 | 43 | 0.24 | 3.8 |
| – | BDMIIb _{average} | 2.55 | 272 | 60 | 0.42 | 6.8 |
| – | HDMIIa _{average} | 2.58 | 242 | 55 | 0.35 | 5.6 |
| – | PDMIIId _{average} | 0.07 | 282 | 51 | 0.01 | 0.2 |

¹ Relative to average N719 efficiency of 6.19% from all N719 values (6.22, 6.21 and 6.14%) during DSCs measurements;

² Electrolyte contains MBI and the composition is LiI (0.18 M), I₂ (0.10 M), MBI (0.50 M), IL (0.60 M) in MPN.

The short-circuit current density values are remarkably similar for electrolytes DMIIa and EMIIa with 3.82 and 3.86 mA cm⁻², respectively (Table 3.27, entries 1 and 2). Then, a decrease in J_{SC} is observed for the electrolytes with PMII (2.48 mA cm⁻²; entry 3) and BMII (2.42 mA cm⁻²; entry 4) ILs compared to 3.86 mA cm⁻² for EMIIa. The J_{SC} value of 2.60 mA cm⁻² for the cell containing HMIIa (entry 5) is comparable to those with the PMIIg and BMIIo electrolytes. The open circuit voltage is in the same range of 297-269 mV for all 1-alkyl-3-methylimidazolium iodide-based electrolytes except for EMII and HMII ILs. The lowest value of 146 mV is observed for HMIIa while for EMIIa it is 201 mV. The trends in values of ff and PCE follow the same pattern as the trend in V_{OC} values, in which the lowest result is found for HMIIa. Remarkably, the set of DSCs with the highest PCE of 0.65% contains the IL with the shortest alkyl (methyl) group (Table 3.27, entry 1).

Third Chapter

On going from ILs with a 1-alkyl-3-methylimidazolium core to ILs with an additional methyl group (1-alkyl-2,3-methylimidazolium iodide), changes in performance are observed. For example, DSCs with PDMII IL (entry 6) have higher J_{SC} of 3.50 mA cm^{-2} compared to those with PMII. At the same time, the decrease in V_{OC} and ff resulted in lower overall PCE. For BDMIIb electrolyte (entry 7) no significant changes were observed compared to BMIIo (entry 4) and, thus, the same PCE of 0.42% is seen for both electrolytes. In case of HDMII IL (entry 8), the trend in J - V parameters is different. The short-circuit current density stays constant, while V_{OC} and ff values show an increase compared to HMII. This change has a positive outcome leading to higher PCE.

In our previous investigations, PDMII IL had one the highest PCE with 0.05 M I_2 compared to other ILs (Chapter Three, part 3.2, section 3.2.1). Since DSCs with the PDMIIe electrolyte have low open circuit voltage values but promising J_{SC} values, it was decided to enhance the efficiency with an addition of MBI to electrolyte. MBI is a known agent to improve the open circuit voltage.^{174, 175} Therefore, 0.5 M MBI was added in the electrolyte composition. Unfortunately, the increase in V_{OC} occurred together with dramatic reduction in J_{SC} , which resulted in PCE of 0.01% only (0.2% relative to N719).

As discussed above, not only the iodine concentration influenced the overall efficiencies of DSCs. The DSC performance was influenced by the IL structure in combination with I_2 concentration in the electrolyte composition. Hence, the trend for electrolytes with 0.10 M iodine is significantly different compared to those with 0.05 M I_2 (Figure 3.41).

The open circuit voltage is the difference between the Fermi level of a semiconductor and the redox potential of electrolyte. According to the Nernst Equation the increase in iodide ion concentration would cause a negative shift of the I^-/I_3^- potential, consequently reducing the V_{OC} .¹⁷¹ In the case of open circuit voltage, the increase in iodine concentration to 0.10 M resulted in lower values for all ILs compared to 0.05 M I_2 . Only PMII IL has a comparable potential for 0.05 M and 0.10 M I_2 . It is important to note that with 0.05 M I_2 , the average V_{OC} values for all three ILs were in the range of 362-321 mV, while with 0.10 M I_2 the difference became more obvious. Considering this aspect, values of 201, 297 and 146 mV were measured for EMIIa, PMIIg and HMIIa, respectively. The fall in potential can be assigned to changes in the molar ratio of iodide/triiodide.

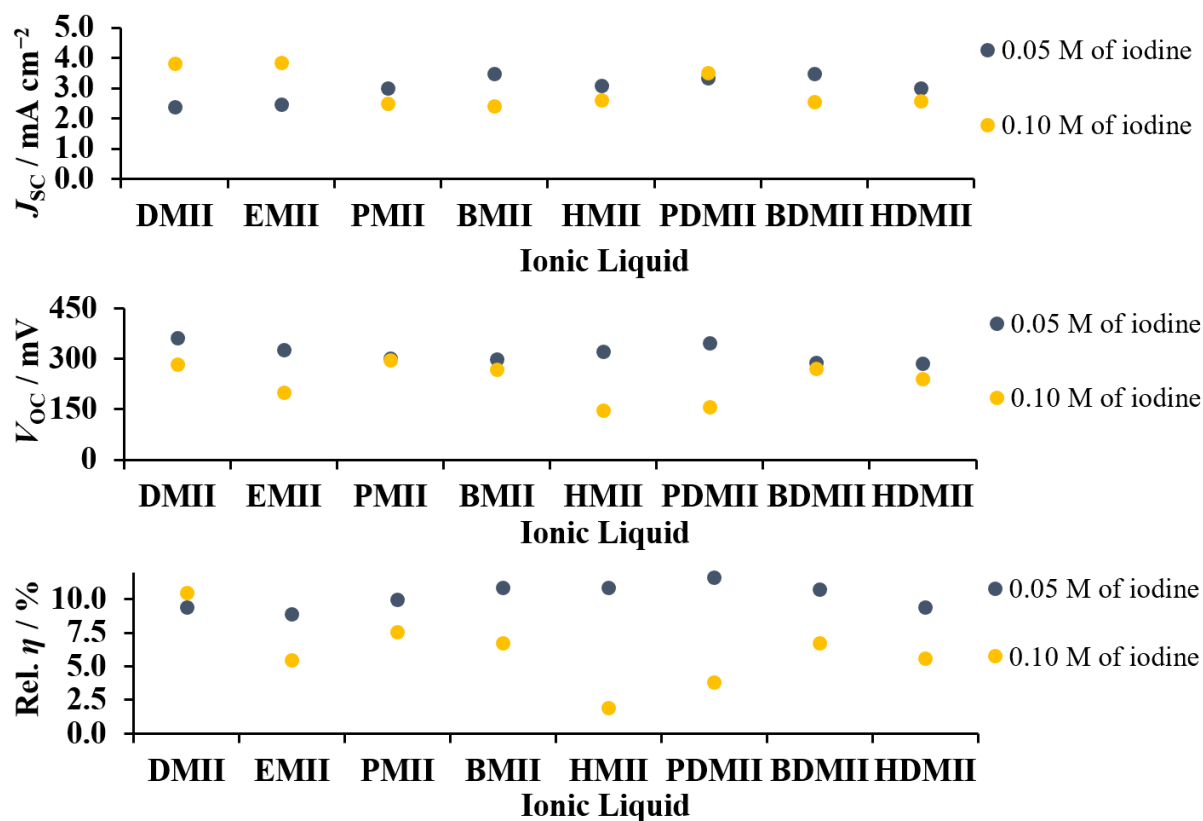


Figure 3.41. J_{SC} , V_{OC} and relative η average values for DSCs based on electrolytes with 0.05 or 0.10 M I_2 and *n*-alkyl-3-methylimidazolium or *n*-alkyl-2,3-dimethylimidazolium iodide to illustrate the influence of iodine concentration. The retained electrolyte composition is 0.18 M LiI, 0.60 M IL in MPN. The average values for electrolytes with 0.05 I_2 are calculated from the Table 3.14.

For J_{SC} , higher values were obtained with an increased concentration of iodine only for DMII and EMII ILs. With PDMII IL, there was almost no change in J_{SC} (3.34 and 3.50 mA cm^{-2} for 0.05 and 0.10 M I_2) with different iodine concentrations. In the case of HMII IL as well as HDMII based electrolytes, the change in J_{SC} is less than 0.5 mA cm^{-2} (3.08 and 2.60 mA cm^{-2} for HMII with 0.05 and 0.10 M I_2 ; 2.99 and 2.58 mA cm^{-2} for HDMII with 0.05 and 0.10 M I_2). The trend in PCE is for all ILs except DMII and DSCs containing electrolytes with lower iodine quantities have higher performances. The η_{average} increased from 0.53 to 0.65% (9.4 to 10.5% relative to N719, Figure 3.41). Thus, in terms of photoconversion efficiency, the DMIIa electrolyte has the highest potential.

3.4.3 EIS measurements of DSCs with 0.10 M I_2

For a deeper understanding of the electrolyte differences, EIS measurements were performed. In Table 3.28, data for multiple DSCs are presented with average values for each parameter. Only average values will be used for data comparison in the following discussion. For fitting

Third Chapter

experimental EIS data electric circuit model 1 was used, which was shown in First Chapter. The model includes transmission line impedance and Nernst diffusion impedance represented by a Warburg impedance.

Table 3.28. EIS parameters for DSCs with 0.10 M I₂ in electrolytes.

| Entry | Electrolyte | R_{rec} / Ω | C_{μ} / μF | R_{tr} / Ω | τ / ms | τ_t / ms | L_d / μm | R_d / Ω | R_s / Ω | R_{Pt} / Ω | C_{Pt} / μF |
|-------|---------------|-------------------------|------------------------------|------------------------|-------------|------------------|--------------------------|---------------------|---------------------|------------------------|-----------------------------|
| 1 | DMIIa cell 1 | 86 | 428 | 20 | 37 | 8 | 25 | 10 | 9 | 5 | 6 |
| | DMIIa cell 2 | 115 | 385 | 33 | 44 | 13 | 23 | 21 | 9 | 5 | 6 |
| | DMIIa cell 3 | 127 | 477 | 16 | 60 | 8 | 34 | 15 | 9 | 4 | 6 |
| | DMIIa cell 4 | 124 | 363 | 34 | 45 | 12 | 23 | 14 | 11 | 5 | 6 |
| 2 | EMIIa cell 1 | 284 | 1796 | 2 | 510 | 4 | 133 | 22 | 11 | 8 | 6 |
| | EMIIa cell 2 | 88 | 1256 | 2 | 111 | 3 | 76 | 37 | 11 | 7 | 5 |
| | EMIIa cell 3 | 252 | 1306 | 1 | 329 | 1 | 191 | 44 | 11 | 4 | 6 |
| | EMIIa cell 4 | 184 | 1764 | 1 | 325 | 2 | 147 | 10 | 11 | 5 | 6 |
| 3 | PMIIg cell 1 | 188 | 355 | 19 | 67 | 7 | 38 | 42 | 12 | 5 | 6 |
| | PMIIg cell 2 | 248 | 335 | 30 | 83 | 10 | 35 | 72 | 11 | 4 | 7 |
| | PMIIg cell 3 | 248 | 383 | 17 | 95 | 6 | 46 | 65 | 11 | 4 | 6 |
| | PMIIg cell 4 | 231 | 328 | 24 | 76 | 8 | 37 | 61 | 11 | 5 | 6 |
| 4 | BMIIo cell 1 | 195 | 431 | 12 | 84 | 5 | 48 | 41 | 15 | 5 | 5 |
| | BMIIo cell 2 | 192 | 309 | 32 | 59 | 10 | 29 | 55 | 14 | 5 | 5 |
| | BMIIo cell 3 | 195 | 402 | 16 | 78 | 6 | 42 | 51 | 11 | 6 | 5 |
| | BMIIo cell 4 | 164 | 259 | 49 | 42 | 13 | 22 | 41 | 12 | 6 | 6 |
| 5 | HMIIa cell 1 | 382 | 2582 | 3 | 986 | 7 | 147 | 72 | 12 | 15 | 6 |
| | HMIIa cell 2 | 374 | 2435 | 1 | 910 | 2 | 238 | 87 | 11 | 10 | 6 |
| | HMIIa cell 3 | 457 | 2849 | 1 | 13000 | 2 | 344 | 83 | 11 | 8 | 7 |
| | HMIIa cell 4 | 376 | 2845 | 1 | 1068 | 3 | 233 | 77 | 11 | 13 | 6 |
| 6 | PDMIIe cell 1 | 182 | 954 | 2 | 174 | 2 | 115 | 33 | 13 | 6 | 5 |
| | PDMIIe cell 2 | 241 | 1324 | 2 | 320 | 3 | 132 | 21 | 12 | 7 | 5 |
| | PDMIIe cell 3 | 297 | 1136 | 3 | 338 | 3 | 127 | 15 | 13 | 7 | 5 |
| | PDMIIe cell 4 | 239 | 1250 | 2 | 298 | 3 | 122 | 11 | 11 | 5 | 5 |
| 7 | BDMIIb cell 1 | 244 | 407 | 13 | 99 | 5 | 52 | 48 | 12 | 6 | 5 |
| | BDMIIb cell 2 | 249 | 459 | 9 | 114 | 4 | 64 | 57 | 13 | 9 | 5 |
| | BDMIIb cell 3 | 196 | 485 | 7 | 95 | 3 | 63 | 43 | 13 | 6 | 5 |

| | | | | | | | | | | | |
|---|---------------------------|-----|------|----|------|----|-----|----|----|----|---|
| 8 | HDMIIa cell 1 | 215 | 367 | 22 | 79 | 8 | 38 | 18 | 12 | 12 | 5 |
| | HDMIIa cell 2 | 164 | 319 | 28 | 52 | 9 | 29 | 21 | 12 | 8 | 5 |
| | HDMIIa cell 3 | 329 | 328 | 28 | 108 | 9 | 41 | 44 | 12 | 8 | 6 |
| | HDMIIa cell 4 | 251 | 396 | 23 | 100 | 9 | 40 | 22 | 12 | 10 | 6 |
| – | DMIIa _{average} | 113 | 413 | 26 | 47 | 10 | 26 | 15 | 10 | 4 | 6 |
| – | EMIIa _{average} | 202 | 1531 | 2 | 319 | 3 | 137 | 28 | 11 | 6 | 6 |
| – | PMIIg _{average} | 229 | 350 | 22 | 80 | 8 | 39 | 60 | 11 | 4 | 6 |
| – | BMIIo _{average} | 186 | 350 | 27 | 66 | 8 | 36 | 47 | 13 | 6 | 5 |
| – | HMIIa _{average} | 397 | 2678 | 1 | 3991 | 3 | 240 | 80 | 11 | 12 | 6 |
| – | PDMIIe _{average} | 240 | 1166 | 2 | 282 | 3 | 124 | 20 | 12 | 6 | 5 |
| – | BDMIIb _{average} | 230 | 450 | 9 | 103 | 4 | 60 | 49 | 13 | 7 | 5 |
| – | HDMIIa _{average} | 240 | 352 | 25 | 85 | 9 | 37 | 26 | 12 | 9 | 6 |

The series resistance R_s stays constant (as expected) for all the DSCs and thus, the observed variation in performances and ff values cannot be assigned to this. The parameters R_{Pt} and C_{Pt} , which are attributed to the platinum counter electrode, are constant for most DSCs as well. Exceptions are the HMIIa and HDMIIa sets. These cells have the highest R_{Pt} values of 12 and 9 Ω , respectively, which is also seen in the Bode plot (Figure 3.42, high frequency region). The difference in R_{Pt} can be a result of different interfacial contact formation between the platinum layer and the electrolyte.¹⁷⁶ The variation in ff values can be a consequence of the same cause.¹⁷⁶ The process of triiodide catalytic reduction at the counter electrode is associated with a voltage loss due to the overpotential. This has a response in a DSC fill factor decrease.¹³⁴

The transport of the redox shuttle through the electrolyte media is diffusion-driven and of key importance for an efficient DSC performance.¹⁴⁷ High iodide concentrations are required for rapid dye regeneration, meaning that I^- is in excess to I_3^- . Low triiodide concentration limits the mass transport in solar cells, but in contrast to this, an excess of I_3^- may lead to an increase of recombination processes at the photoanode. An excess of I_3^- ($\lambda_{max} \approx 350$ nm) also leads to increased light absorption, but no electron injection.¹³⁴ In the Nyquist plot, the electrolyte contribution can be observed in the low f region (Figure 3.43). The diffusion resistance R_d in the electrolyte can give an inside look into the electron transfer and needs to be considered together with the charge transfer resistance R_{Pt} at the counter electrode. The overall trend can be described as longer alkyl chains introduced into the IL correspond to higher R_d values (15 Ω for DMII compared to 80 Ω for HMII, Table 3.28, entries 1 and 5). The exception is BMII IL (entry 4),

whose R_d average value falls between those of EMIIa and PMIIg. The highest diffusion resistance corresponds to the highest R_{Pt} value for HMIIa electrolyte (entry 5). For ILs with an additional methyl group, the R_d values are in the range of 20-49 Ω (entries 6-8). The greatest diffusion resistance corresponds to the BDMIIb electrolyte (entry 7). Interestingly, this did not affect R_{Pt} , whose value is comparable to other DSC sets.

Another important parameter, which varies between cells, is the electron lifetime τ . The longest τ is observed for HMIIa and the shortest for DMIIa electrolyte. The tendency for changes in τ is illustrated in the Bode plot (Figure 3.42, low frequency region), since τ is inversely related to the maximum frequency.^{134, 144} The electron lifetime is in agreement with the transport time τ_t , which must be lower than τ in order to ensure that there is effective transport of electrons through the TiO_2 .¹⁴⁷ The diffusion length L_d is another crucial parameter for the efficient electron transport in the semiconductor and should be longer than the active layer thickness.¹⁷⁷ For all electrolytes L_d is longer than the TiO_2 layer thickness ($\approx 12 \mu m$) and follows the τ trend for all electrolytes.

A similar tendency for τ is observed for the chemical capacitance C_{μ} and recombination resistance R_{rec} . These trends are expected, because τ is directly related to these parameters.¹³⁴ The increase of R_{rec} from 1,3-dimethylimidazolium iodide to 1-hexyl-3-methylimidazolium iodide is observed in both the Bode and Nyquist plots (Figures 3.42 and 3.43). The deviation in recombination resistance for other ILs is not critical and does not have a significant impact on PCE as it can be seen in Table 3.27.

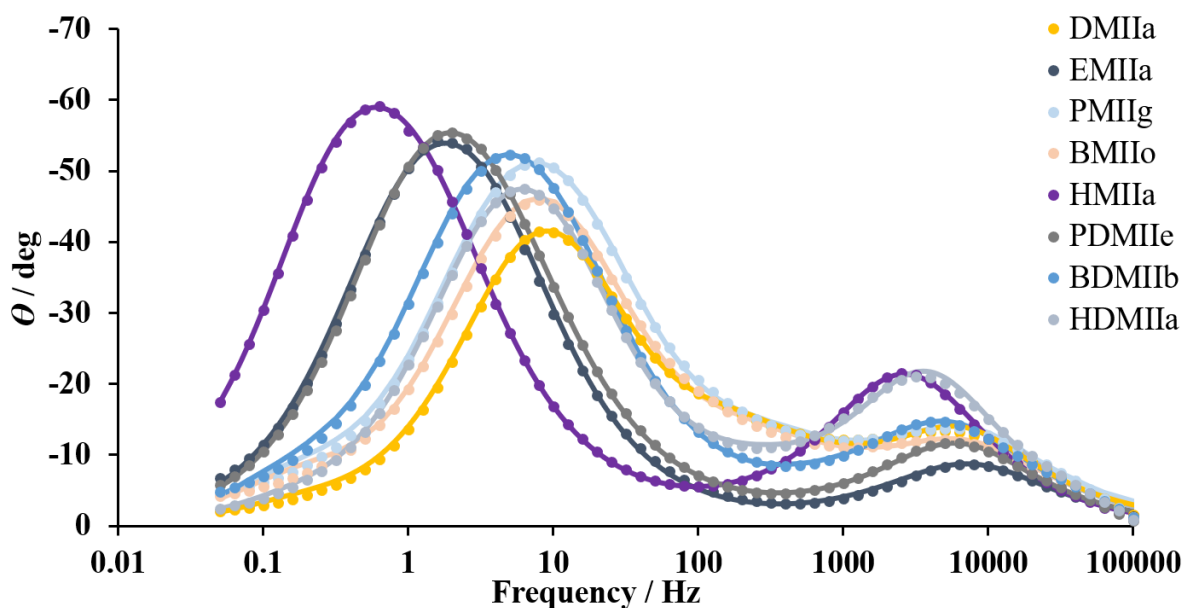


Figure 3.42. Bode plot of the most representative cells from each DSCs set with 0.10 M I_2 .

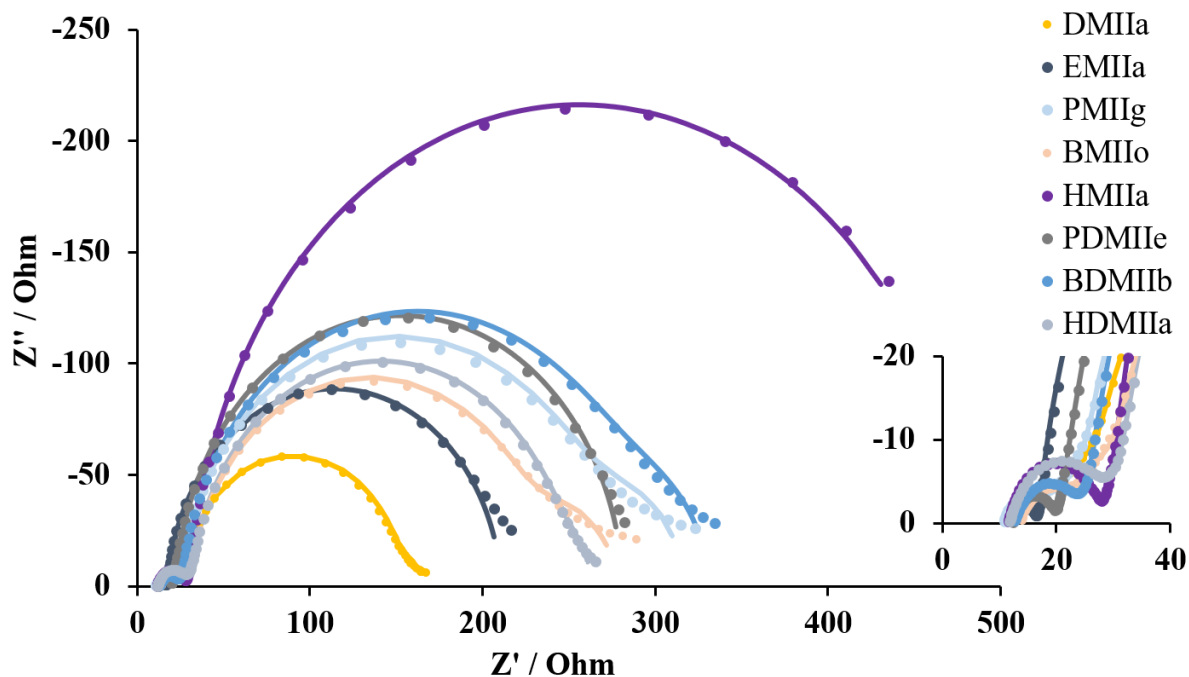


Figure 3.43. Nyquist plot of the most representative cells from each DSCs set with 0.10 M I₂ with the expansion of high frequency region.

Chemical capacitance C_{μ} values are comparable for all DSCs, except for the three sets which contain EMII, HMII and PDMII. EMII and PDMII have remarkably high J_{SC} values ($\sim 3.50 \text{ mA cm}^{-2}$), while all three sets have rather low open-circuit voltage values (146-201 mV). Overall, this results in insufficient photoconversion. Interestingly, these cells have minimal values of transport resistance R_t . For the other electrolytes, R_t is in the range 22-27 Ω except for BDMII, which has an average value of 9 Ω .

A higher iodine concentration of 0.10 M in the electrolyte resulted in a different impedance response compared to those with 0.05 M I₂ (Tables 3.28 and 3.29). While R_{Pt} and C_{Pt} stay constant, the diffusion resistance shows significant differences for all ILs. The values of R_d increased for all electrolytes, except for EMII and HMII, which had no considerable changes, and DMII IL, whose value decreased. The reduction of R_{rec} brought a beneficial impact to J_{SC} . For the EMIIa electrolyte, a spectacular increase in chemical capacitance as well as a decrease in R_{tr} are responsible for the higher J_{SC} . Unfortunately, typically the beneficial changes in C_{μ} result in a decrease in V_{OC} and the EMIIa set was not an exception. In the case of PMII and BMII ILs, changes in I₂ concentration resulted in increased values of the recombination resistance and thus lower J_{SC} . For the BMIIo electrolyte, a slight increase in ff is observed. However, the rise in chemical capacitance for HMIIa is followed by an increase in recombination resistance compared to HMII electrolyte. The values of ff decreased by a factor of two. At the same time, significant increase in R_d from 18 to 80 Ω is seen.

Table 3.29. EIS parameters for electrolytes with 0.05 M I₂ from Table 3.20 are shown for convenience.

| Electrolyte | R_{rec} / C_μ / μF | R_{tr} / τ / ms | τ_t / L_d / R_d / R_s / R_{Pt} / C_{Pt} / | Ω | Ω | ms | μm | Ω | Ω | Ω | μF |
|--------------------------|---|--------------------------------|--|----------|----------|-----------|-----------|----------|----------|----------|-----------|
| DMII _{average} | 313 | 508 | 16 | 164 | 7 | 67 | 43 | 12 | 5 | 7 | |
| EMII _{average} | 315 | 468 | 16 | 148 | 8 | 55 | 36 | 12 | 7 | 5 | |
| PMIIC _{average} | 136 | 323 | 18 | 44 | 5 | 36 | 10 | 13 | 9 | 6 | |
| BMIIC _{average} | 152 | 358 | 12 | 55 | 4 | 46 | 10 | 14 | 9 | 5 | |
| HMIIC _{average} | 169 | 311 | 40 | 53 | 12 | 26 | 18 | 13 | 11 | 5 | |

Overall, the increase in iodine concentration led to significant changes not only in *J-V* plot for all ILs, but also in impedance. The most beneficial changes were observed for DMII IL. Interesting trends were seen for EMII, HMII and PDMII ILs with radical increase in chemical capacitance values. Moreover, it was noticed that the structure of IL had an impact on the electrolyte/counter electrode interface, what results in different trends in *R_{Pt}*.

3.4.4 Further iodine concentration study for electrolytes with DMII, EMII and PDMII ionic liquids

For a deeper understanding of the iodine concentration impact in the electrolyte, three ILs were chosen for more detailed study: DMII, EMII and PDMII. The electrolytes can be separated into three families, each based on DMII, EMII or PDMII IL. In each family three DSC sets were measured – without iodine, with 0.02 M I₂, or with 0.20 M I₂. The remaining electrolyte composition was the same for all electrolytes (for complete electrolyte compositions see Table 3.30).

Table 3.30. Electrolyte compositions with various iodine concentrations and DMII, EMII or PDMII IL. MPN was used as a solvent.

| Electrolyte | [Im]⁺[I]⁻ / M | LiI / M | I₂ / M |
|--------------------|--|----------------|--------------------------|
| DMIIb | DMII / 0.60 | 0.18 | – |
| DMIIc | DMII / 0.60 | 0.18 | 0.02 |
| DMIIId | DMII / 0.60 | 0.18 | 0.20 |
| EMIIb | EMII / 0.60 | 0.18 | – |
| EMIIc | EMII / 0.60 | 0.18 | 0.02 |
| EMIIId | EMII / 0.60 | 0.18 | 0.20 |
| PDMIIIf | PDMII / 0.60 | 0.18 | – |

| | | | |
|--------|--------------|------|------|
| PDMIIg | PDMII / 0.60 | 0.18 | 0.02 |
| PDMIIh | PDMII / 0.60 | 0.18 | 0.20 |

Multiple DSCs were built for each electrolyte set and their photovoltaic parameters are presented in Table 3.31. The ruthenium(II) dye N719 was used as a reference. Entries 1, 2 and 3 correspond to electrolytes with DMII IL, entries 4, 5 and 6 to EMII and entries 7, 8 and 9 to PDMII IL. For each set average values were determined and will be described in the following discussion.

Table 3.31. Parameters and average values for multiple DSCs with various electrolytes. All DSCs were fully masked.

| Entry | Electrolyte | $J_{SC} / \text{mA cm}^{-2}$ | V_{OC} / mV | $ff / \%$ | $\eta / \%$ | Rel. $\eta / \%$ ¹ |
|-------|---------------|------------------------------|----------------------|-----------|-------------|-------------------------------|
| 1 | DMIIb cell 1 | 3.02 | 316 | 50 | 0.48 | 7.5 |
| | DMIIb cell 2 | 3.28 | 294 | 52 | 0.50 | 7.7 |
| | DMIIb cell 3 | 3.06 | 285 | 52 | 0.46 | 7.1 |
| | DMIIb cell 4 | 3.15 | 294 | 50 | 0.47 | 7.3 |
| 2 | DMIIc cell 1 | 3.14 | 296 | 56 | 0.52 | 8.1 |
| | DMIIc cell 2 | 3.25 | 298 | 55 | 0.53 | 8.3 |
| | DMIIc cell 3 | 3.06 | 305 | 55 | 0.51 | 8.0 |
| | DMIIc cell 4 | 3.23 | 300 | 55 | 0.53 | 8.3 |
| 3 | DMIIId cell 1 | 2.51 | 291 | 63 | 0.46 | 7.2 |
| | DMIIId cell 2 | 2.91 | 261 | 58 | 0.44 | 6.9 |
| | DMIIId cell 3 | 2.84 | 282 | 60 | 0.48 | 7.5 |
| | DMIIId cell 4 | 2.78 | 279 | 61 | 0.47 | 7.3 |
| 4 | EMIIb cell 1 | 3.42 | 281 | 51 | 0.49 | 7.7 |
| | EMIIb cell 2 | 3.22 | 294 | 52 | 0.49 | 7.7 |
| | EMIIb cell 3 | 3.24 | 282 | 50 | 0.45 | 7.1 |
| | EMIIb cell 4 | 3.42 | 286 | 48 | 0.47 | 7.3 |
| 5 | EMIIc cell 1 | 3.18 | 293 | 56 | 0.52 | 8.1 |
| | EMIIc cell 2 | 3.18 | 298 | 56 | 0.53 | 8.3 |
| | EMIIc cell 3 | 3.22 | 286 | 56 | 0.51 | 8.0 |
| | EMIIc cell 4 | 2.83 | 283 | 57 | 0.45 | 7.1 |
| 6 | EMIIId cell 1 | 2.32 | 274 | 64 | 0.40 | 6.3 |
| | EMIIId cell 2 | 2.41 | 272 | 63 | 0.42 | 6.5 |
| | EMIIId cell 3 | 2.78 | 276 | 64 | 0.49 | 7.7 |
| | EMIIId cell 4 | 2.74 | 267 | 64 | 0.47 | 7.3 |

Third Chapter

| | | | | | | |
|---|---------------------------------------|------|-----|----|------|-----|
| 7 | PDMII _f cell 1 | 3.57 | 326 | 46 | 0.53 | 8.3 |
| | PDMII _f cell 2 | 3.48 | 311 | 40 | 0.43 | 6.7 |
| | PDMII _f cell 3 | 3.63 | 316 | 45 | 0.52 | 8.0 |
| | PDMII _f cell 4 | 3.56 | 314 | 43 | 0.48 | 7.5 |
| 8 | PDMII _g cell 1 | 3.25 | 276 | 59 | 0.53 | 8.3 |
| | PDMII _g cell 2 | 3.12 | 290 | 58 | 0.52 | 8.1 |
| | PDMII _g cell 3 | 3.20 | 275 | 60 | 0.52 | 8.2 |
| | PDMII _g cell 4 | 3.31 | 267 | 57 | 0.51 | 7.9 |
| 9 | PDMII _h cell 1 | 2.61 | 282 | 65 | 0.48 | 7.4 |
| | PDMII _h cell 2 | 2.62 | 271 | 64 | 0.46 | 7.1 |
| | PDMII _h cell 3 | 2.63 | 266 | 64 | 0.45 | 7.0 |
| | PDMII _h cell 4 | 2.48 | 295 | 65 | 0.47 | 7.4 |
| – | DMII _b _{average} | 3.13 | 297 | 51 | 0.47 | 7.4 |
| – | DMII _c _{average} | 3.17 | 300 | 55 | 0.52 | 8.2 |
| – | DMII _d _{average} | 2.76 | 278 | 60 | 0.46 | 7.2 |
| – | EMII _b _{average} | 3.32 | 286 | 50 | 0.48 | 7.4 |
| – | EMII _c _{average} | 3.10 | 290 | 56 | 0.50 | 7.9 |
| – | EMII _d _{average} | 2.56 | 272 | 64 | 0.45 | 7.0 |
| – | PDMII _f _{average} | 3.56 | 317 | 43 | 0.49 | 7.7 |
| – | PDMII _g _{average} | 3.22 | 277 | 58 | 0.52 | 8.1 |
| – | PDMII _h _{average} | 2.59 | 278 | 64 | 0.46 | 7.2 |

[†] Relative to N719 efficiency of 6.41% (duplicate cells performed the same) set as 100%.

For all ILs, an identical trend in *ff* can be observed on going from electrolytes with no iodine to 0.02 M and to 0.20 M I₂. For electrolytes without iodine, the lowest fill factor values were measured. Higher iodine concentration led to an increase in *ff* values. The most significant changes occurred in PDMII systems, where the values changed from 43% for PDMII_f electrolyte (no I₂) to 58% for PDMII_g (0.02 M I₂) followed by the further increase to 65% for PDMII_h (0.20 M I₂). Interestingly, the same fill factor value as for PDMII_f is observed for PDMII_e electrolyte with 0.10 M I₂ in it (Figure 3.44, PDMII).

A similar trend as for PDMII is found for EMII IL. The *ff* values increase in the following order: 0.00 → 0.02 → 0.05 → 0.20 M I₂ with on outlier concentration of 0.10 M (Figure 3.44, EMII). This observation will be discussed in the EIS section below.

The lowest variance in ff is observed for DMII IL (Figure 3.44, DMII) and follows the discussed trend for all iodine concentrations with one exception. The average fill factor value of 62% is observed for DMII electrolyte with 0.05 M I_2 , which is slightly higher than 60% for 0.20 M I_2 (Table 3.31, DMII_{average}). The lowest ff values correspond to DMIIb electrolyte without iodine.

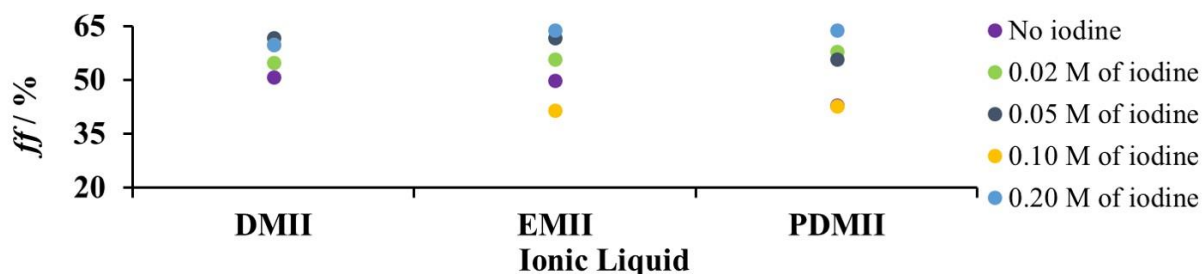


Figure 3.44. The changes in average fill factor values for DSCs with different ILs in electrolytes.

For DMII IL, the values of J_{SC} and V_{OC} had almost no changes looking at values from electrolyte DMIIb to DMIIc. However, with 0.20 M iodine concentration the decrease is observed in both short-circuit current density and potential. Due to the increase in fill factor for DMII_d, the photoconversion efficiency is 0.46% (7.2% relative to N719 set as 100%) and is similar to DMIIb. The highest photoconversion efficiency for cells with the electrolyte with DMII is observed for DMIIa with 0.10 M I_2 , and this is a result of these DSCs having the greatest J_{SC} values for this set (Figure 3.45, DMII).

For EMII IL, no significant changes in potential were observed on going from EMIIb to EMIIc electrolyte. The ten times higher iodine concentration resulted in a lower V_{OC} value for EMII_d compared to EMIIc. The J_{SC} values for EMII electrolytes are inversely related to the fill factor trend and decrease with higher iodine concentration (Table 3.31). Overall, the fall in short-circuit current density and potential result in a decrease of PCE on going from 0.02 to 0.20 M I_2 (7.0% for EMII_d compared to 7.9% for EMIIc, respectively, relative to N719 set as 100%, entries 5 and 6). The highest relative efficiency is observed for the DSCs with the EMII electrolyte with 0.05 M iodine despite the lowest J_{SC} in the EMII set (Figure 3.45, EMII).

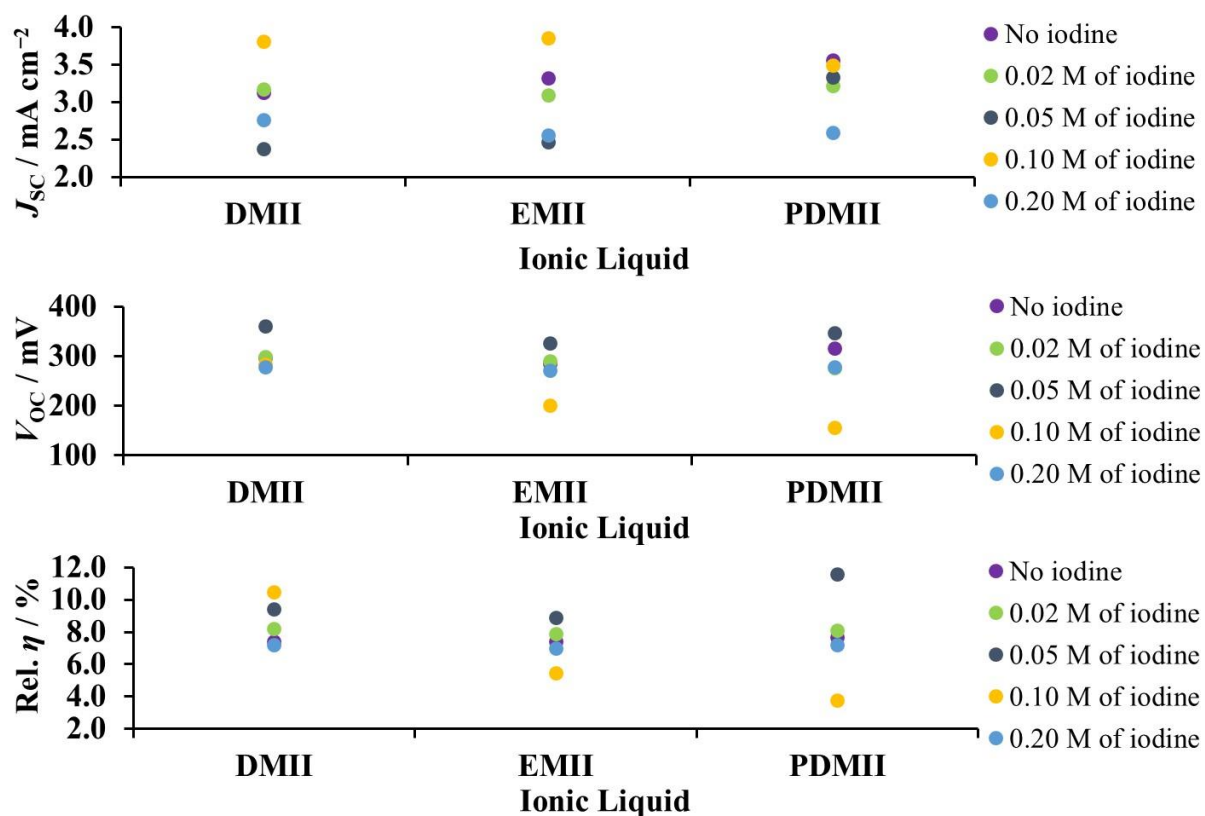


Figure 3.45. The changes in J_{sc} , V_{oc} and relative η average values for DSCs with different ILs in electrolytes.

For PDMII, IL changes in J_{sc} and ff follow the EMII trend for PDMIIg, PDMIIh and PDMIIi electrolytes. The trend in J - V curves is illustrated in Figure 3.46. Remarkably, high short-circuit current density and open circuit voltage for PDMIIi are offset by low fill factor and lead as a consequence to comparable PCE values to PDMIIg and PDMIIh electrolytes. The greatest efficiency difference is observed for 0.05 and 0.10 M I_2 in PDMII based electrolytes with 0.65 (11.6 % relative to N719) and 0.25% (3.8% relative to N719), respectively (Figure 3.45).

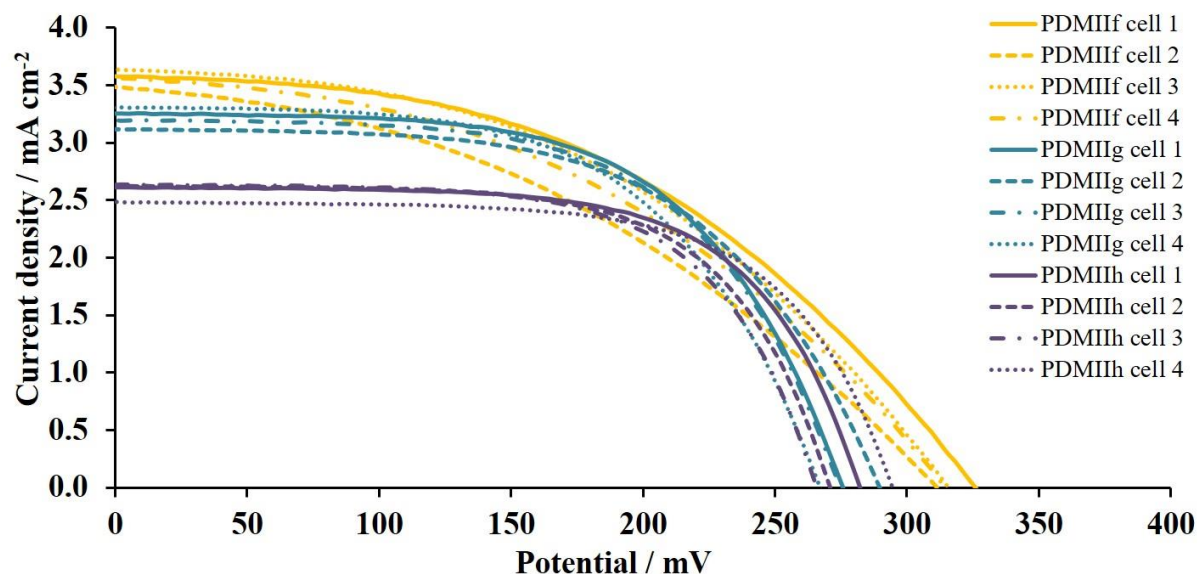


Figure 3.46. *J-V* curves for multiple DSCs with electrolytes PDMIIf (no I₂), PDMIIg (0.02 M I₂) and PDMIHh (0.20 M I₂).

3.4.5 EQE measurements of DSCs with 0.02 M, 0.20 M and no iodine in electrolytes

An EQE measurement offers a better understanding of photocurrent limitations in a solar cell device (First Chapter, section 3.2). For our solar cells, the EQE curves were measured between 350-740 nm, which is the typical working range for DSCs.¹³⁷ The results of these measurements are presented in Table 3.32. Multiple DSCs were measured for each set and average values for EQE_{max} were determined. Only average values will be used in the following discussion. It is important to note, that EQE_{max} will be considered in the visible region from $\lambda > 430$ nm, since in the low wavelength region of visible light the absorbance of triiodide affects to the EQE values.^{178, 179} Due to the low photon flux in the triiodide range this EQE region has low reproducibility for all DSCs and is not taken into the count.

Table 3.32. The results of EQE measurements.

| Electrolyte | EQE _{max} / % | | | | EQE _{max} average / % | Wavelength range ¹ / nm |
|-------------|------------------------|----------------|--------|--------|-----------------------------------|---------------------------------------|
| | cell 1 | cell 2 | cell 3 | cell 4 | | |
| DMIIf | 19 | 21 | 18 | 23 | 20 | 450-490 |
| DMIIc | 24 | 32 | 20 | 23 | 25 | 460-480 |
| DMIIh | 17 | 20 | 23 | 22 | 21 | 480-510 |
| EMIIb | 30 | – ² | 26 | 23 | 27 | 450-470 |
| EMIIc | 21 | 16 | 25 | 19 | 20 | 450-490 |

| | | | | | | |
|---------|----|----------------|----|----|----|---------|
| EMIIId | 18 | 15 | 20 | 20 | 18 | 470-500 |
| PDMIIIf | 31 | – ² | 25 | 24 | 27 | 450-470 |
| PDMIIg | 20 | 20 | 20 | 21 | 20 | 480-510 |
| PDMIIh | 20 | 20 | 23 | 19 | 20 | 490-500 |

¹ The range of λ_{\max} for multiple DSCs. ² Although the cells performed well, good EQE spectra could not be obtained.

All DSCs had their EQE_{\max} values in the range of 450-510 nm. DMII IL DSCs without iodine in the electrolyte show the same $\text{EQE}_{\max\text{average}}$ as the DMIIId set with 0.20 M I_2 (20 and 21%, respectively, Table 3.32). The highest $\text{EQE}_{\max\text{average}}$ value of 25% for DMII IL is observed for DMIIb with 0.02 M I_2 . For EMII IL the trend is more obvious and $\text{EQE}_{\max\text{average}}$ decreases from no iodine in the electrolyte to a concentration of 0.20 M. The greatest step is observed from EMIIb to EMIIc electrolyte changing from 27 to 20%, respectively. EMIIId follows the trend and has 18% $\text{EQE}_{\max\text{average}}$. This can be seen in Figure 3.47.

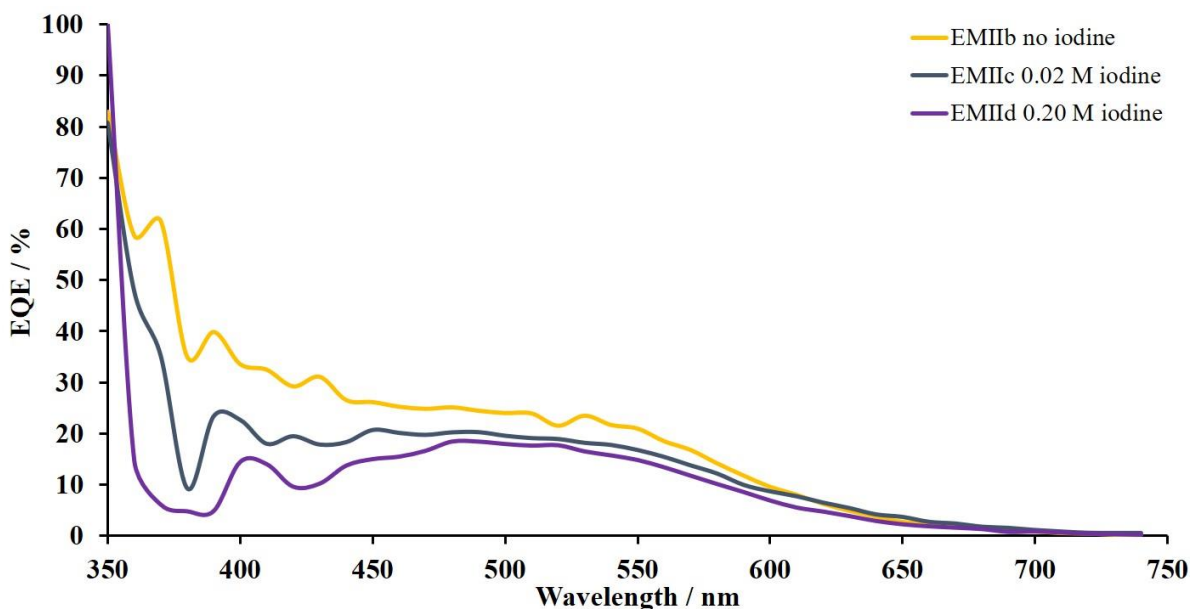


Figure 3.47. EQE curves of most representative DSCs from each set with EMIIb, EMIIc and EMIIId electrolytes.

For PDMII IL the highest $\text{EQE}_{\max\text{average}}$ is observed like for EMII IL for electrolyte without iodine (Table 3.32, PDMIIIf). It is also in agreement with J_{SC} . For PDMIIg and PDMIIh the same $\text{EQE}_{\max\text{average}}$ of 20% is observed. Interestingly, J_{SC} values for PDMIIh are significantly lower than for PDMIIg (Table 3.31, entries 9 and 8). This can be an indication for the differences in electron transport and collection for these two systems.

The variation in parameters and EQE spectra for different DSC sets can be attributed to several electron processes and EIS measurements were conducted for a better insight.

3.4.6 EIS measurements of DSCs with 0.02 M, 0.20 M and no iodine in electrolytes

EIS measurements were conducted for DSCs with three electrolyte families, based on DMII, EMII or PDMII IL containing 0.00, 0.02 or 0.20 M I₂ (for complete electrolyte compositions see Table 3.30). The impedance was measured for multiple DSCs for each set, but only average values of each parameter will be reviewed in the following discussion (Table 3.33).

Table 3.33. EIS parameters for DSCs with 0.00, 0.20 and 0.20 M I₂ in electrolytes.

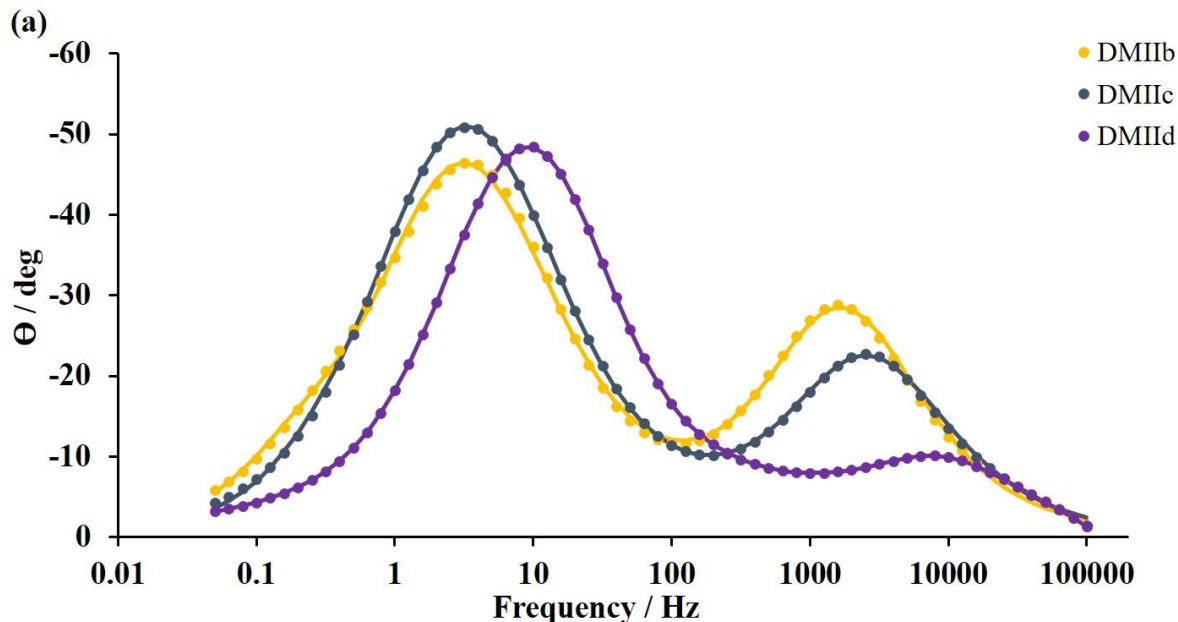
| Entry | Electrolyte | R_{rec} / Ω | C_{μ} / μF | R_{tr} / Ω | τ / ms | τ_t / ms | L_d / μm | R_d / Ω | R_s / Ω | R_{Pt} / Ω | C_{Pt} / μF |
|-------|---------------|-------------------------|------------------------------|------------------------|----------------|------------------|--------------------------|---------------------|---------------------|------------------------|-----------------------------|
| 1 | DMIIb cell 1 | 304 | 526 | 8 | 160 | 4 | 76 | 88 | 12 | 23 | 7 |
| | DMIIb cell 2 | 230 | 608 | 6 | 140 | 4 | 73 | 133 | 12 | 23 | 7 |
| | DMIIb cell 3 | 196 | 417 | 6 | 82 | 3 | 66 | 140 | 14 | 25 | 8 |
| 2 | DMIIc cell 1 | 286 | 587 | 12 | 168 | 7 | 58 | 18 | 13 | 21 | 5 |
| | DMIIc cell 2 | 275 | 724 | 4 | 199 | 3 | 94 | 39 | 12 | 23 | 6 |
| | DMIIc cell 3 | 263 | 570 | 3 | 150 | 1 | 123 | 85 | 13 | 18 | 6 |
| | DMIIc cell 4 | 252 | 622 | 11 | 157 | 7 | 58 | 16 | 12 | 13 | 6 |
| 3 | DMII d cell 1 | 146 | 325 | 16 | 47 | 5 | 36 | 27 | 10 | 3 | 8 |
| | DMII d cell 2 | 147 | 353 | 12 | 52 | 4 | 43 | 21 | 12 | 5 | 5 |
| | DMII d cell 3 | 150 | 367 | 12 | 55 | 4 | 43 | 24 | 12 | 4 | 5 |
| | DMII d cell 4 | 152 | 382 | 9 | 58 | 3 | 50 | 26 | 11 | 4 | 5 |
| 4 | EMIIb cell 1 | 207 | 605 | 10 | 125 | 6 | 55 | 124 | 12 | 29 | 8 |
| | EMIIb cell 2 | 212 | 725 | 7 | 153 | 5 | 68 | 125 | 12 | 27 | 8 |
| | EMIIb cell 3 | 165 | 829 | 7 | 137 | 6 | 58 | 163 | 11 | 32 | 8 |
| | EMIIb cell 4 | 183 | 628 | 16 | 115 | 10 | 41 | 140 | 13 | 43 | 7 |
| 5 | EMIIc cell 1 | 253 | 587 | 8 | 148 | 5 | 68 | 30 | 13 | 11 | 7 |
| | EMIIc cell 2 | 243 | 641 | 5 | 156 | 3 | 83 | 31 | 15 | 9 | 6 |
| | EMIIc cell 3 | 251 | 654 | 8 | 164 | 5 | 67 | 32 | 13 | 17 | 6 |
| | EMIIc cell 4 | 202 | 590 | 6 | 119 | 3 | 73 | 34 | 12 | 10 | 5 |
| 6 | EMII d cell 1 | 133 | 207 | 52 | 27 | 11 | 19 | 10 | 11 | 2 | 8 |
| | EMII d cell 2 | 101 | 185 | 65 | 19 | 12 | 15 | 10 | 13 | 3 | 8 |
| | EMII d cell 3 | 105 | 172 | 63 | 18 | 11 | 15 | 10 | 12 | 2 | 8 |
| | EMII d cell 4 | 96 | 193 | 61 | 19 | 12 | 15 | 9 | 11 | 4 | 7 |

| | | | | | | | | | | | |
|---|---------------------------------------|-----|------|----|-----|----|----|-----|----|----|---|
| 7 | PDMII _f cell 1 | 268 | 1243 | 10 | 333 | 12 | 64 | 214 | 12 | 34 | 9 |
| | PDMII _f cell 2 | 221 | 1275 | 13 | 282 | 16 | 50 | 296 | 12 | 57 | 7 |
| | PDMII _f cell 3 | 240 | 1255 | 10 | 301 | 12 | 60 | 239 | 14 | 37 | 9 |
| | PDMII _f cell 4 | 204 | 1403 | 11 | 286 | 15 | 52 | 274 | 15 | 47 | 8 |
| 8 | PDMII _g cell 1 | 157 | 314 | 23 | 49 | 7 | 31 | 20 | 11 | 18 | 6 |
| | PDMII _g cell 2 | 172 | 355 | 35 | 61 | 12 | 27 | 23 | 11 | 29 | 7 |
| | PDMII _g cell 3 | 173 | 314 | 22 | 54 | 7 | 33 | 21 | 12 | 13 | 7 |
| | PDMII _g cell 4 | 170 | 377 | 16 | 64 | 6 | 39 | 20 | 11 | 20 | 6 |
| 9 | PDMII _h cell 1 | 121 | 225 | 44 | 27 | 10 | 20 | 9 | 11 | 5 | 6 |
| | PDMII _h cell 2 | 148 | 169 | 82 | 25 | 14 | 16 | 13 | 11 | 5 | 8 |
| | PDMII _h cell 3 | 94 | 184 | 61 | 17 | 11 | 15 | 8 | 12 | 5 | 7 |
| – | DMII _b _{average} | 243 | 517 | 7 | 127 | 3 | 72 | 120 | 13 | 24 | 7 |
| – | DMII _c _{average} | 269 | 626 | 7 | 168 | 5 | 83 | 40 | 12 | 19 | 6 |
| – | DMII _d _{average} | 149 | 357 | 12 | 53 | 4 | 43 | 24 | 11 | 4 | 6 |
| – | EMII _b _{average} | 192 | 697 | 10 | 133 | 7 | 55 | 138 | 12 | 33 | 8 |
| – | EMII _c _{average} | 237 | 618 | 7 | 147 | 4 | 73 | 32 | 13 | 12 | 6 |
| – | EMII _d _{average} | 109 | 189 | 60 | 21 | 11 | 16 | 10 | 12 | 3 | 8 |
| – | PDMII _f _{average} | 233 | 1294 | 11 | 300 | 14 | 57 | 256 | 13 | 44 | 8 |
| – | PDMII _g _{average} | 168 | 340 | 24 | 57 | 8 | 32 | 21 | 11 | 20 | 6 |
| – | PDMII _h _{average} | 121 | 193 | 62 | 23 | 12 | 17 | 10 | 11 | 5 | 7 |

Before starting the evaluation, it is important to note that the series resistance stays constant for all DSCs as well as the capacitance attributed to the platinum counter electrode. At the same time, a similar tendency is observed for all ILs for the charge transfer resistance at the platinum counter electrode and charge diffusion resistance in the electrolyte. Independent of the structure of the IL, the DSCs without iodine have the greatest R_{Pt} and R_d values. With an addition of 0.02 M I_2 , a decrease is observed for both parameters. Further increase of iodine concentration to 0.20 M is followed by a drop in R_{Pt} and R_d values. The trend in resistance at the counter electrode is inversely proportional to the trend in the fill factor. The lowest values of ff correspond to electrolytes without iodine. The R_{Pt} changes can be illustrated with the help of a Bode plot (Figure 3.48, right peak, a – electrolytes with DMII IL, b – with EMII IL, c – with PDMII; the yellow colour corresponds to electrolytes without iodine, blue – to electrolytes with 0.02 M and purple – to 0.20 M iodine concentration). The shift of the right peak from lower to higher frequencies going from 0.00 to 0.20 M I_2 is credited to a decrease in the charge transfer time¹⁸⁰ and is observed for electrolytes

with all three ILs. The structure of the IL influences the EIS response for DSCs as well. Thus, an electrolyte with no iodine and shorter alkyl chain (DMII) has a lower R_d , than electrolyte EMIIb (120 and 138 Ω , respectively, Table 3.33). PDMIIc has the average value of 256 Ω , which is two times higher than that for EMIIb. On the other hand, PDMIIh and EMIIId with 0.20 M I_2 show lower R_d values of 10 Ω compared to DMIIId (24 Ω , Table 3.33).

The diffusion length L_d was also affected by changes in the electrolyte compositions. In the case of the DMII family, electrolytes without iodine and with 0.02 M I_2 have a higher L_d , at least by a factor of 6, than the active layer thickness d (L_d is for DMIIc slightly longer than for DMIIb). For DMIIId, a significant decrease was observed, but still, the diffusion length is 3.5 times longer than the thickness of the TiO_2 layer. In case of EMII IL, the highest diffusion length of 73 μm is observed for 0.02 M I_2 and 55 μm is observed for the electrolyte without iodine. High concentrations of iodine resulted in a short $L_{daverage}$ of 17 μm , which is comparable to the semiconductor thickness ($d \approx 12 \mu m$). For the PDMII family, the trend in L_d is linear in the order PDMIIg – PDMIIg – PDMIIh and for the highest I_2 concentration the shortest diffusion length is observed. Similar average values as for EMIIb and PDMIIc were detected ($\approx 56 \mu m$) as well as for EMIIId and PDMIIh ($\approx 16 \mu m$).



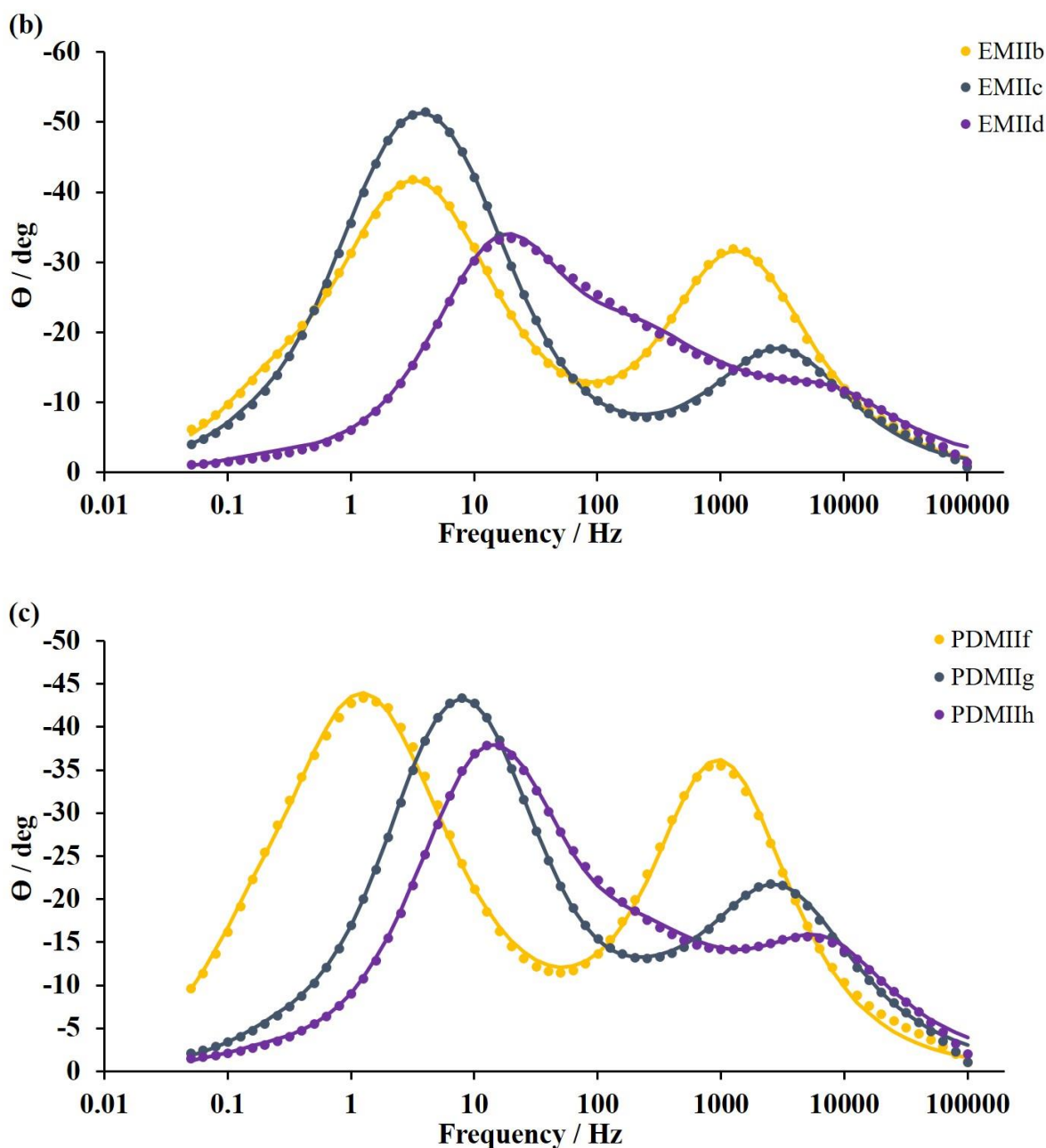


Figure 3.48. EIS Bode plots for DSCs with three electrolyte families; (a) electrolytes with DMII IL; (b) electrolytes with EMII IL; (c) electrolytes with PDMII IL; yellow colour corresponds to electrolytes without iodine, blue – to electrolytes with 0.02 M and purple – to 0.20 M.

However, when L_d becomes shorter than the active layer thickness, the so-called Gerischer impedance (Z_G) overtakes the diffusion-recombination impedance model.¹⁷⁷ Typically, when a large recombination rate is observed, the diffusion-recombination impedance needs to be changed to the Gerischer impedance.¹⁴⁶ In this case, the transport resistance R_{tr} becomes significantly larger than the recombination resistance R_{rec} and the recombination time is shorter than the diffusion time through the active layer.^{146, 181} Practically, R_{rec} , R_{tr} and C_μ parameters cannot be extracted in the presence of Z_G ($L_d \ll d$), and L_d of $\approx 0.5d$ is the limit to obtain them. Thus, the diffusion-recombination impedance model used in this study is suitable for EIS fitting despite comparable

values of L_d and d for EMIIId and PDMIIh electrolytes. At the same time, the experimental curve shapes for EMIIId and PDMIIh also change in the Z_G direction (Figure 3.49, Figure 3.48b, c). The effect is particularly seen for the EMIIId electrolyte (Figure 3.48b, EMIIId).

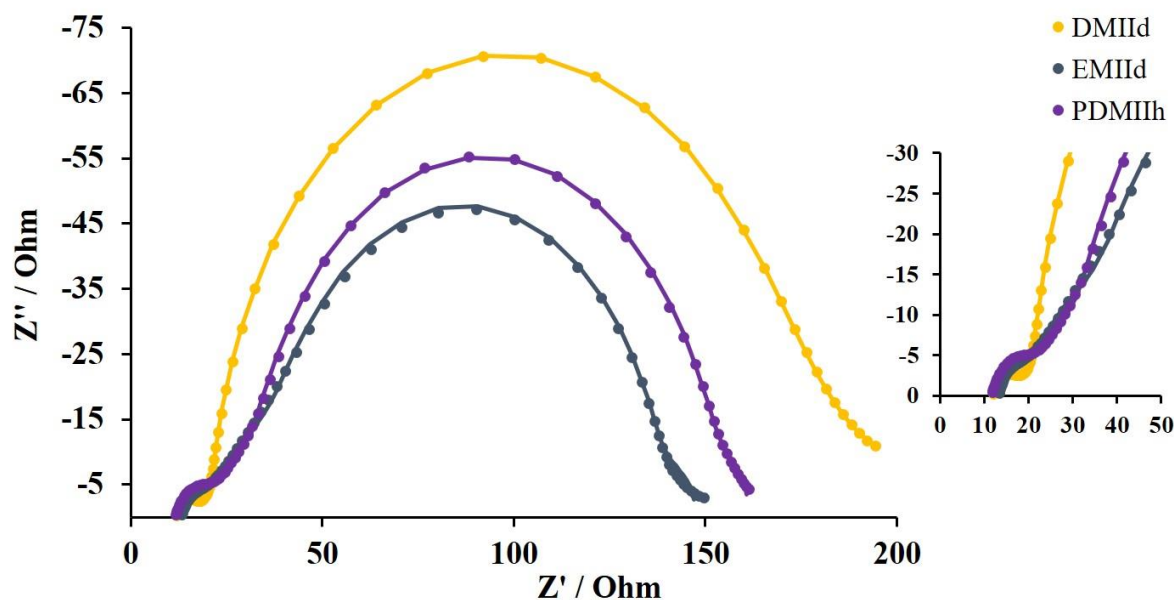


Figure 3.49. The Nyquist plot with high frequency region expansion of the of DSCs with DMIIId, EMIIId and PDMIIh electrolytes to demonstrate the change in spectra profile depending on IL structure.

For all DSC sets, the electron lifetime significantly decreased from electrolyte with no I_2 to 0.20 M I_2 . This trend can be noticed in the Bode plot due to the shift of left peaks to higher frequencies (Figure 3.48a, b, c) and particularly seen for PDMII IL (Figure 3.48c). Nevertheless, τ is considerably larger than τ_i for all electrolytes. The transport resistance increases for all electrolyte families on going from 0.00 to 0.20 M I_2 . Interestingly, the lowest R_{tr} for 0.20 M I_2 is observed for DMII IL ($\approx 12 \Omega$, Table 3.33, entry 3) indicating an efficient transport compared to EMIIId and PDMIIh ($\approx 60 \Omega$, Table 3.33, entries 6 and 9, respectively).

The lowest values of chemical capacitance as well as recombination resistance are observed for 0.20 M I_2 for all electrolytes (Table 3.33). Remarkably, C_μ for PDMIIIf supports high values of J_{SC} and EQE_{max} . The dramatic fall in C_μ on going to PDMIIg (0.02 M I_2) has a response in lower J_{SC} and EQE_{max} for this electrolyte. The further decrease in capacitance results in J_{SC} changes but does not affect the EQE performance. The recombination resistance follows the C_μ trend and supports the observed short-circuit density changes. From EMIIb to EMIIc the fluctuation in C_μ is not substantial, but in combination with an increase in R_{rec} results to lower J_{SC} and EQE_{max} values. For EMIIId, R_{rec} and C_μ both decrease and lead to a consistent drop in J_{SC} and EQE_{max} . In the case of the DMII set, the small rise in R_{rec} can be seen in combination with $\approx 110 \mu F$ increase in C_μ from DMIIb to DMIIc. This leads to $\approx 5\%$ higher EQE_{max} for DSCs with 0.02 M I_2 compared to no

Third Chapter

iodine in the electrolyte. For 0.20 M I₂, a drop in both R_{rec} and C_{μ} is observed and followed by lowering of J_{SC} and EQE_{max} values (Tables 3.31 and 3.32).

In total, iodine concentration significantly influences most of the electronic processes in DSC for all ILs. The main trends were observed for resistance in the electrolyte, counter electrode resistance, transport resistance and electron diffusion length in semiconductor.

3.4.7 Summary: Electrolytes with different iodine concentration

The concentration of iodine has an influence on various crucial interfacial processes occurring in a DSC. Four iodine concentrations (0.00, 0.02, 0.10 and 0.20 M) were tested in combination with different ILs in electrolytes for iron(II)-based DSCs. Short-circuit current density, open circuit potential and fill factor were influenced by changes in I₂ concentration for all IL used in this study. The most dramatic changes were observed for HMII IL. Insufficient HMIIa performance was linked to low V_{OC} and fill factor values. The limiting processes correlated to increased electrolyte diffusion resistance and charge transfer resistance at the platinum counter electrode. Interestingly, the IL with shortest alkyl-chains like DMII and EMII got an increase in J_{SC} on going from 0.05 to 0.10 M I₂ compared to IL with longer side chains.

In the example of DMII, EMII and PDMII ILs, it was shown that lower concentrations of iodine reduced the transport resistance in the semiconductor in the photoanode. At the same time, higher I₂ concentrations led to a decrease in diffusion resistance in electrolyte as well as in platinum counter electrode resistance. The electron lifetime and diffusion length were also affected by iodine concentration and decreased on going from 0.00 to 0.20 M I₂. The EQE measurements had shown the highest values for DSCs without iodine in electrolyte for all ILs. Similar trend is observed in J_{SC} for DMII, EMII and PDMII ILs. Considering all aspects, in this study DMII was the best performing IL not only in terms of PCE, but also had the most promising impedance profile.

4. Conclusion

During this study, the optimization of iron(II)-sensitized DSCs was conducted. First investigations had started with $[\text{Fe}(\text{III}-5)(\text{Phtpy})]^{2+}$ complexes as sensitizers. Two principal strategies were used for dye assembly on the semiconductor surface – SALSAC and stepwise approaches. It was shown that the choice of dye assembling strategy led to differences in the performance. Significant variations were not observed in case of V_{OC} , but twice higher values for J_{SC} were obtained with the SALSAC strategy compared to the stepwise one. Interestingly, lower absorbance in ssUV-Vis was observed for the SALSAC approach. Moreover, it was shown that the electrolyte composition is of key importance. The first built devices had shown no performance with the electrolyte Stnd II PF (0.10 M LiI, 0.05 M I_2 , 0.60 M 1-butyl-3-methylimidazolium hexafluorophosphate and 0.50 M 1-methylbenzimidazole in 3-methoxypropionitrile). The change from 0.05 to 0.10 M I_2 played a crucial role and a PCE of 0.05% was detected with J_{SC} of 0.14 mA cm^{-2} and V_{OC} of 445 mV. Compared to well-performing Ru-based sensitizers, the performance is dramatically lower, but to our knowledge it was the first performing DSC based on a $[\text{Fe}(\text{III}-5)(\text{Phtpy})]^{2+}$ complex. However, further investigations on electrolyte composition and push-pull design did not lead to enhancement of performance.

The continuation of electrolyte studies was done with an iron(II) NHC complex as a sensitizer and chenodeoxycholic acid as a co-adsorbent. Iodide/triiodide was used as a redox shuttle. Changes in the electrolyte as well as solvent (from MeCN to MPN) were beneficial for the PCE of these devices. The four ionic liquids (BMII, PDMII, BMIPF, EMIMPF) were investigated and the DSCs with PDMII IL in the electrolyte exhibited the best performance within the set (PCE of 0.57%, 9.3% relative to N719). Moreover, the influence of MBI and TBP additives in the electrolyte was studied. DSCs with PDMII-based electrolytes with MBI and TBP at different concentrations (0.50, 0.10, 0.05 M for TBP and 0.50, 0.10, 0.05, 0.01 M for MBI) were measured. DSCs with TBP had slightly higher PCE at 0.5 M concentration compared to the same concentration of MBI. This could be explained with higher open circuit voltage values as J_{SC} was not affected by changing TBP to MBI. No significant differences were observed between TBP and MBI at other concentrations. Electrolytes without additives were tested and, despite the decrease in V_{OC} , higher PCE values were observed for all ILs except EMIMPF. The best performing electrolyte compositions were E2c and E2b with 0.01 M of MBI and without MBI, respectively. At this point, the highest PCE for the iron(II) NHC complex was achieved, as the previously published performance was 0.13% for this dye.

Third Chapter

Further investigations were conducted on the electrolyte composition. Various concentrations of Li^+ salts (LiI and LiPF_6) were tested in the presence of PMII, BMII and PDMII ILs. An increase in the Li^+ ion concentration had a positive effect on the PCE for all ILs. However, the counterion for the Li^+ -salt affected both J_{SC} and V_{OC} indicating not only the interaction with CB, but also influencing the energy of the redox couple. These findings were confirmed with EQE and EIS measurements. Furthermore, the concentration of IL was studied. It was also shown that too high or too low concentrations of IL negatively affected the PCE. Based on these results, 0.18 M LiI was considered as the optimal additive in combination with 0.60 M IL and was used for the following investigations.

The structure of IL plays a crucial role in the electrolyte composition. Six ILs (DMII, EMII, PMII, BMII, HMII and DodMII) were tested at a constant concentration of 0.60 M. It was shown that an increase in the alkyl chain length of the imidazolium ILs positively influenced the DSC performance. The optimal side chain was *n*-butyl as the further increase to *n*-hexyl resulted in similar PCE as for BMII. Electrolyte with 1-dodecyl-3-methylimidazolium iodide had lower PCE compared to HMII due to decreased J_{SC} values. This conclusion was confirmed in the EQE spectra and EIS measurements. HMII and DodMII had the highest values of transport resistance in this investigation. The presence of an additional methyl group in the 2-position for PMII and BMII ILs resulted in higher PCE for PDMII (0.59% for PMII and 0.66% for PDMII) and similar PCE of $\approx 0.61\%$ in case of BDMII. In the case of HMII, changes in the structure led to a lower average performance of 0.53% compared to 0.61%. These experiments have shown that an additional methyl group is not beneficial for imidazolium ILs with longer side chains starting from *n*-butyl. The further alterations were done with counterions of imidazolium ILs. A change in the counterion resulted in high V_{OC} values for BDMICFSO and PMINCFSO electrolytes, while $[\text{BF}_4]^-$ containing ILs are not advantageous despite significantly high J_{SC} values (4.09 mA cm^{-2} for BDMIBF). The overall best performances were achieved for $[\text{PDMI}]^+$ IL with I^- counterion. The combination of ILs with different counterions did not improve the DSC photovoltaic performance.

As it was shown on the example of the $[\text{Fe}(\text{III}-5)(\text{Phtpy})]^{2+}$ complex, the iodine concentration had an essential contribution to the PCE of solar devices. In this study, four iodine concentrations (0.00, 0.02, 0.10 and 0.20 M) were tested in combination with different ILs in electrolytes. All parameters like short-circuit current density, open circuit potential and fill factor were influenced by changes in the iodine concentration independently from the IL structure. According to EQE_{max} and J_{SC} values, the highest photocurrent was achieved for DSCs without or with the lowest iodine concentration, except for DMII and EMII ILs. Electrolytes with these ILs had the highest J_{SC}

Third Chapter

values with 0.10 M I₂. The most dramatic changes were observed for HMII IL. Insufficient HMIIa performance was attributed to low V_{OC} and fill factor values. An increased electrolyte diffusion resistance and charge transfer resistance at the platinum counter electrode were observed with 0.10 M I₂. Lower concentrations of iodine reduced the transport resistance in the semiconductor of the photoanode for DMII, EMII and PDMII ILs. The decrease in diffusion resistance in the electrolyte and in the platinum counter electrode resistance was observed at higher I₂ concentrations. The electron lifetime and diffusion length decreased from 0.00 to 0.20 M I₂.

In conclusion, our findings revealed an electrolyte with 0.18 M LiI, 0.05 M I₂, 0.60 M PDMII in MPN as the best performing one with a PCE of 0.66% for an iron(II) NHC sensitizer. However, several other electrolytes (e.g., with DMII, PMII or BMII ILs) had comparable performances and could be used as promising alternatives.

Fourth Chapter

1. Motivation

An alternative dye structure (IV-1), which could increase the sigma-donation to the metal centre, is presented in Figure 4.1. It differs from dye I-4, which has been discussed in Third Chapter, solely in the imidazolium moiety. Due to the saturated backbone structure of the imidazolium moiety, the ligand's donative abilities should be increased without negatively influencing other parts of the molecule.

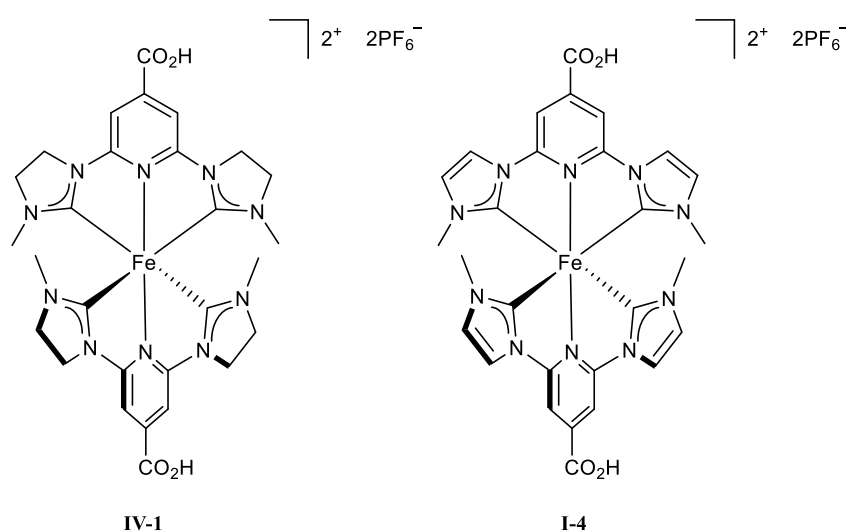
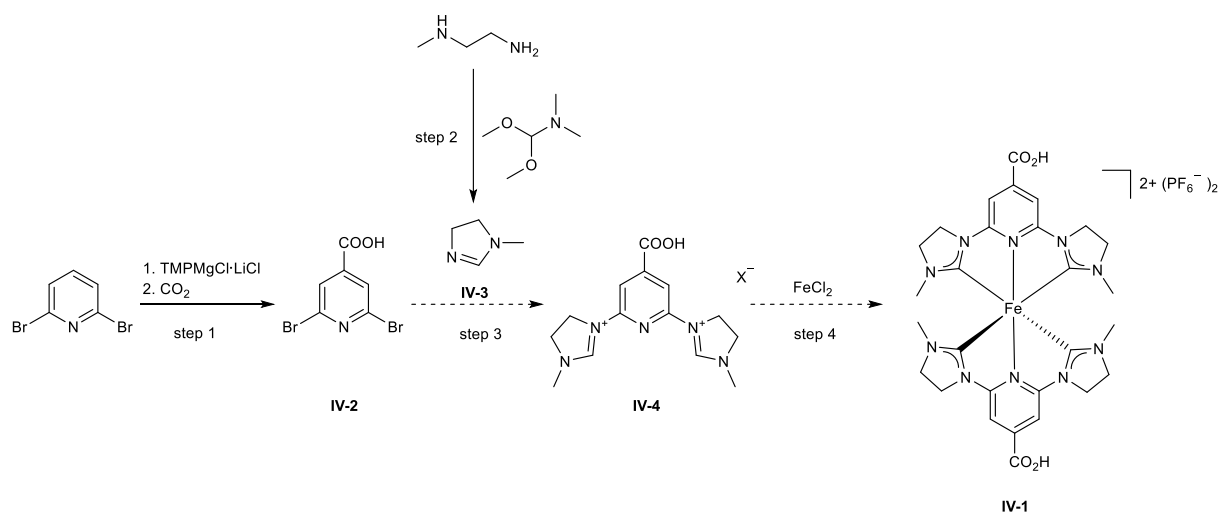


Figure 4.1. Structures of proposed dye IV-1 and dye I-4.

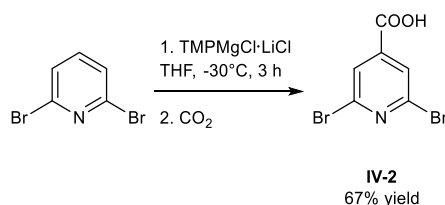
The proposed synthetic route is shown in Scheme 4.1 and was designed on the previously published synthesis of I-4.⁸³ As a first step, 2,6-dibromoisonicotinic acid IV-2 was synthesised from 2,6-dibromopyridine *via* magnesiation and following quenching using dry ice. Then, it was planned to introduce 1-methyl-4,5-dihydroimidazole (IV-3), which was synthesised in advance from *N*-methylethanediamine and *N,N*-dimethylformamide dimethyl acetal, to the pyridine ring *via* a bis-substitution reaction. Finally, the obtained ligand would be complexed with iron(II) chloride to afford the target compound IV-1.



Scheme 4.1. Synthetic route to obtain target complex IV-1. Solid arrows show reactions with isolated compounds, dashed arrows show transformations without isolated compounds.

2. Discussion

First, 2,6-dibromopyridine was metalated using the non-nucleophilic amide base $\text{TMPMgCl}\cdot\text{LiCl}$ (TMP = 2,2,6,6-tetramethylpiperidynyl). The following quenching with dry ice afforded 2,6-dibromoisonicotinic acid IV-2 (Scheme 4.2).

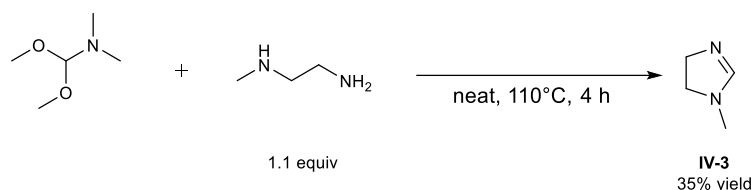


Scheme 4.2. Synthesis of 2,6-dibromoisonicotinic acid (IV-2).

The reaction was based on the previously published functionalization of 2,6-dibromopyridine *via* magnesiation with $\text{TMPMgCl}\cdot\text{LiCl}$ base and subsequent quenching with iodine as an electrophile.¹⁸² The main challenge of the reaction appeared to be the upscaling. A 2.00 mmol reaction scale resulted in the similar yield as 1.00 mmol, 48% and 50%, respectively (Table 4.1, entries 1 and 2). The further upscaling to 5.00 mmol led to lower yield of 33% (entry 3). It was observed that longer metalation times led to higher conversion of starting material and consequently to better yields. Quenching of the reaction with dry ice after 1 h of metalation resulted in 33% yield (5.00 mmol scale, Table 4.1, entry 3) and after 3 h in 67% (4.00 mmol scale, entry 4). Thus, 4.00 mmol scale and 3 h of metalation time were considered as suitable conditions for conducting the reaction.

Table 4.1. Overview on the 2,6-dibromoisonicotinic acid synthesis.

| Entry | Metalation time | Scale | Yield |
|-------|-----------------|-----------|-------|
| 1 | 1 h | 1.00 mmol | 48% |
| 2 | 1 h | 2.00 mmol | 50% |
| 3 | 1 h | 5.00 mmol | 33% |
| 4 | 3 h | 4.00 mmol | 67% |



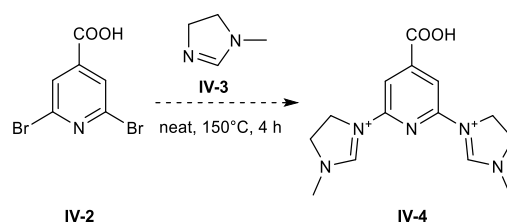
Scheme 4.3. Synthesis of 1-methyl-4,5-dihydroimidazole (IV-3).

1-Methyl-4,5-dihydroimidazole (IV-3), the second reactant used in the subsequent coupling reaction, was prepared from *N*-methylethanediamine and *N,N*-dimethylformamide dimethyl acetal neat at 110°C for 4 h (Scheme 4.3). It was observed that the increase of acetal equivalents from 1.00 to 1.10 resulted in an increased yield from 27 % to 35 % (Table 4.2).

Table 4.2. Influence of *N,N*-dimethylformamide dimethyl acetal equivalents on the condensation yield.

| Entry | <i>N,N</i> -Dimethylformamide dimethyl acetal equivalents | Yield |
|-------|---|-------|
| 1 | 1.00 | 27% |
| 2 | 1.10 | 35% |

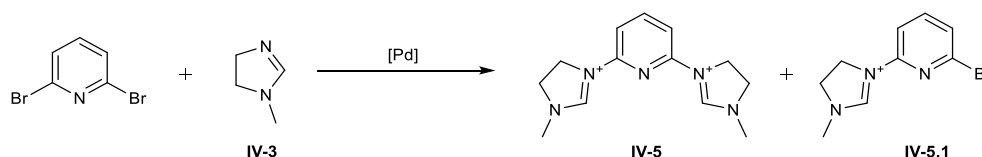
As a next step, the substitution reaction of 2,6-dibromoisonicotinic acid (IV-2) and 1-methyl-4,5-dihydroimidazole (IV-3) was explored according to the analogous approach for ligand III-13 but with 1-methylimidazole under neat conditions at 150°C (Scheme 4.4). The reaction between IV-2 and 1-methylimidazole was previously published⁸³ and used for the I-4 synthesis (Third Chapter, section 3, Scheme 3.5).

Scheme 4.4. Direct synthesis of IV-4 *via* nucleophilic aromatic substitution. Dashed arrow shows transformations without isolated compound.

Fourth Chapter

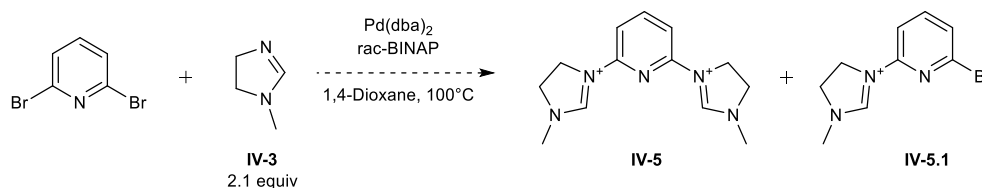
However, the neat substitution reaction did not lead to the desired transformation and resulted in a black sticky solid, which stuck to the bottom of the flask. From this, only starting material could be isolated. To avoid formation of the black solid and to improve reactivity, it was decided to carry the reaction out with solvent present. DMF was chosen because it can solubilise the IV-2 starting material. Trying to overcome the challenges by using DMF as well as increasing the reaction time (from 4 h to 72 h) did not improve the outcome either and the target compound was not obtained (only starting material was recovered).

The direct substitution was not further investigated at this stage anymore and it was decided to evaluate transition metal catalysed cross-coupling between 2,6-dibromopyridine and 1-methyl-4,5-dihydroimidazole (IV-3) as an alternative pathway (Scheme 4.5).



Scheme 4.5. Transition metal catalyzed cross-coupling of 2,6-dibromopyridine and IV-3 as alternative synthetic pathway.

One of the most common ways to form a C-N bond is Buchwald-Hartwig amination.¹⁸³ It is important to note that generation of quaternary ammonium cations *via* cross-coupling is not trivial. Mainly, these types of moiety are generated *via* substitution or ring-formation reactions.¹⁸⁴⁻¹⁸⁸ Thus, the primary goal at this stage was to successfully synthesise and identify the target compound and not to optimise the reaction. Due to the moderate yield of the 2,6-dibromoisonicotinic acid (IV-2) preparation and the limited scalability of its synthesis (4.00 mmol, Table 4.1), commercially available 2,6-dibromopyridine was chosen as model substrate (due to the structural similarity) before using the acid IV-2 as an actual target reactant. Monitoring of reactions was primarily done by ¹H NMR spectroscopy and/or ESI-MS. Therefore, results could not be quantified in terms of conversion percentage. Instead, reaction mixtures were analysed based on the presence of the target compound. As a starting point, a commonly used catalyst system for Buchwald-Hartwig cross-coupling was chosen.¹⁸³



Scheme 4.6. Cross-coupling reaction between 2,6-dibromopyridine and 1-methyl-4,5-dihydroimidazole (IV-3) using baseline conditions.

Fourth Chapter

Table 4.3. The baseline conditions were 2,6-dibromopyridine (1.00 equiv), 1-methyl-4,5-dihydroimidazole (IV-3, 2.10 equiv), Pd(dba)₂, rac-BINAP in 1,4-dioxane heated under inert conditions at 100°C for 72 h; the scale of reactions was not exceeding 0.50 mmol if not stated different.

| Entry | [Pd] ligand | / Time | Additional conditions | Observations |
|-------|----------------|--------|---|---|
| 1 | 10% / 20% | 72 h | - | Starting material, IV-5 and IV-5.1 products are present. |
| 2 | 10% / 20% | 168 h | - | Starting material, IV-5 and IV-5.1 products are present. |
| 3 | - | 168 h | - | No conversion, only starting material is observed. |
| 4 | 20% / 40% | 72 h | - | Starting material, IV-5 and IV-5.1 products are present. New species with carbene centre are observed. |
| 5 | 40% / 80% | 72 h | - | IV-5 and IV-5.1 products are present. |
| 6 | 20% / 40% | 3 h | 120°C, MW | Starting material, IV-5 and IV-5.1 products are present. |
| 7 | 20% / 40% | 72 h | The scale was increased from 0.50 to 1.00 mmol. | No target compound IV-5 was observed, mono-coupled product IV-5.1 and hydrolysed mono-coupled product IV-5.2 are present. |
| 8 | 20% / 40% | 72 h | IV-5.1 was used as a starting material, 1.10 equiv of IV-3. | IV-5 and IV-5.1 products are present. |
| 9 | 20% / 40% | 72 h | 1.00 equiv of IV-3. | IV-5 and IV-5.1 products are present. |
| 10 | 20% / 40% | 120 h | 8.40 equiv of IV-3. | IV-5 is observed, no presence of IV-5.1. |
| 11 | 10% / 20% | 120 h | Premix of catalyst, 8.40 equiv of IV-3. | IV-5 is observed, no presence of IV-5.1. |
| 12 | 5% / 10% | 120 h | Premix of catalyst, 8.40 equiv of IV-3. | No target compound IV-5 was observed. |

MW – microwave irradiation.

Fourth Chapter

The initial reaction (Table 4.3, entry 1) between 2,6-dibromopyridine and IV-3 led to a mixture of mono- and bis-coupled products (IV-5.1 and IV-5, respectively, Scheme 4.6). The products were detected by ESI-MS in the crude mixture (Figure 4.2). At the same time, only starting material was mainly present in the ^1H NMR spectrum and no IV-5 was observed in spectrum. It indicated that despite formation of target product IV-5, the conversion was not sufficient after 72 h at 100°C . After purification by flash chromatography, IV-5 and IV-5.1 were isolated in a 1:1 ratio (as seen in the ^1H -NMR spectrum, Figure 4.3).

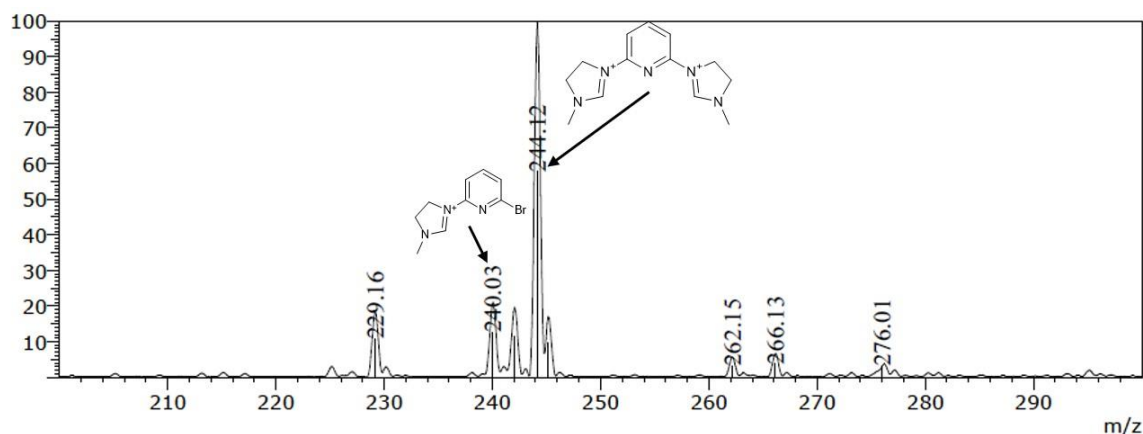


Figure 4.2. Section of ESI-MS spectrum of crude mixture (Table 4.3, entry 1).

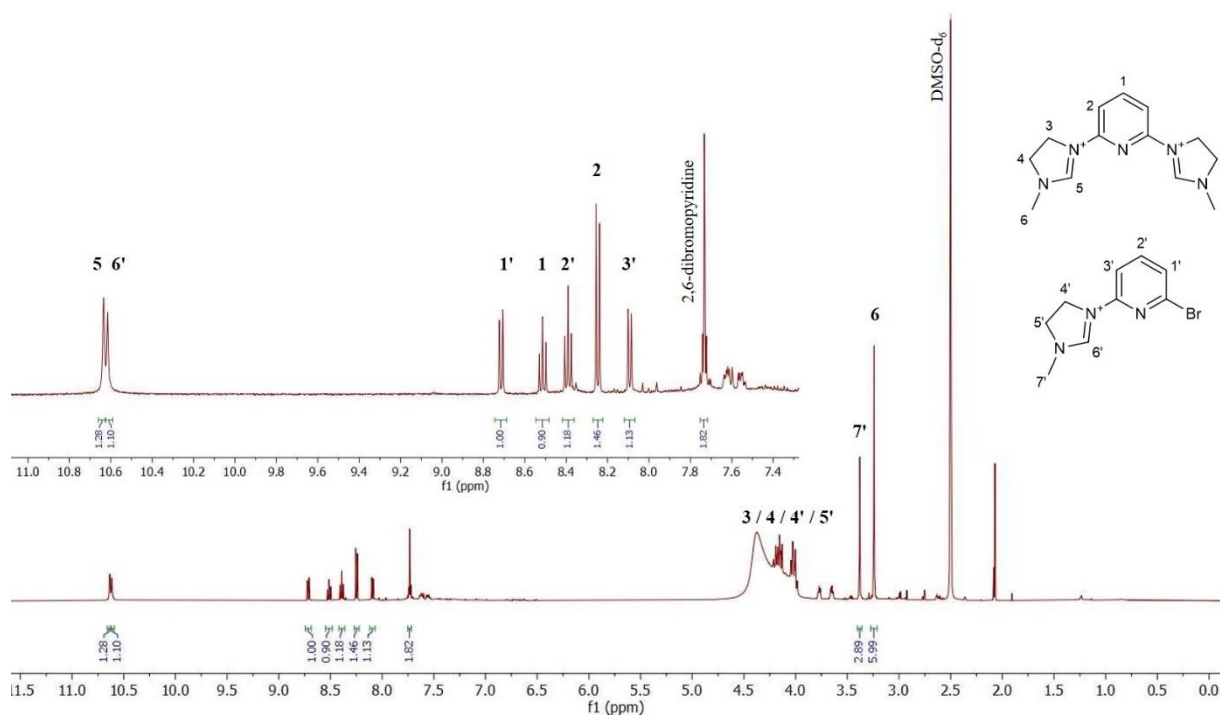


Figure 4.3. ^1H NMR spectrum of the IV-5/IV-5.1 mixture in DMSO-d_6 with the expansion of aromatic region (Table 4.3, entry 1).

The initial conditions resulted in numerous by-products and the target molecule was found as a minor compound. The mono- and bis-coupled products were isolated only in a marginal yield. Despite a starting scale of 0.42 mmol 2,6-dibromopyridine, just enough material for an NMR spectroscopic analysis was isolated. Due to the similar structure of mono- and bis-coupled products (Scheme 4.6), it proved to be complicated to separate them by flash chromatography. The most promising eluent mixture, which was identified for separation, was MeCN / sat. aq. NH_4PF_6 (50 : 1.5; v:v). Even so, an effective separation of mono- and bis-coupled products IV-5.1 and IV-5 was not possible. To achieve a further conversion of the mono-coupled intermediate, the reaction time was increased from 72 to 168 h (7 days; Table 4.3, entry 2). Despite a longer reaction time, the molecular masses of mono-coupled derivative and starting material were still observed in the ESI-MS and the mono-coupled species was isolated in a small quantity exclusively in the following workup. The ^1H NMR spectrum of the product is shown in Figure 4.4. The solution in the NMR tube was, unfortunately, of a low concentration despite the fact that the whole isolated compound was used for the NMR sample.

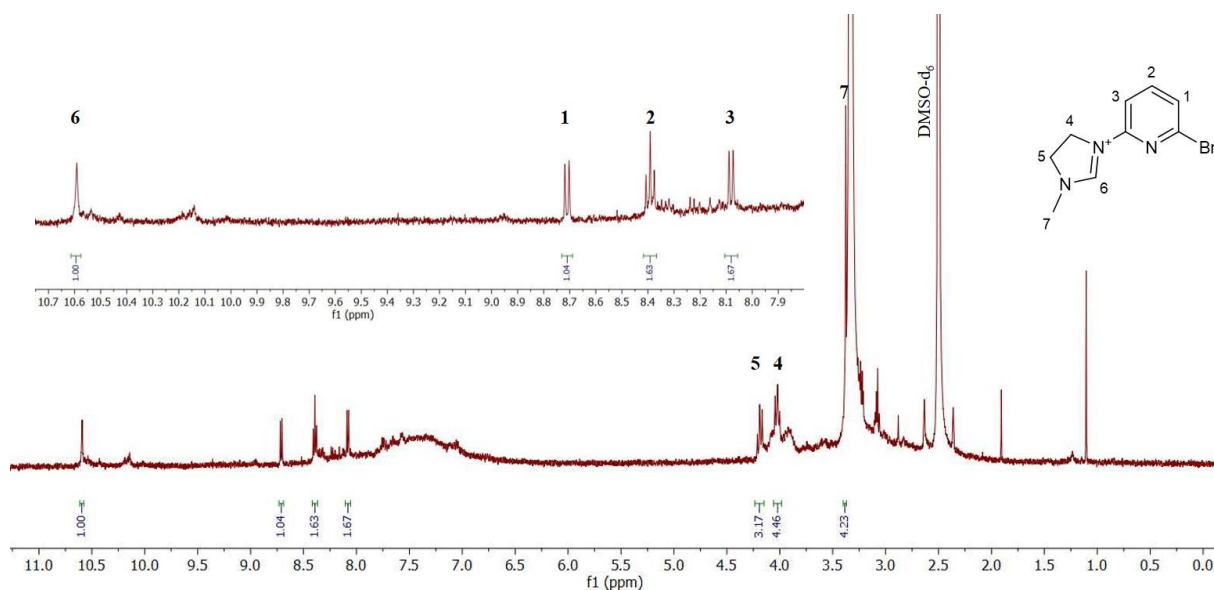
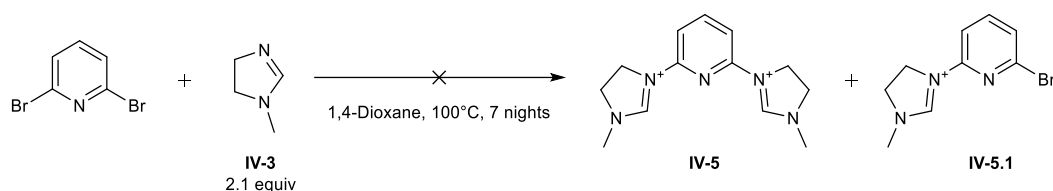


Figure 4.4. ^1H NMR spectrum of IV-5.1 in DMSO-d_6 with the expansion of aromatic region (Table 4.3, entry 2).

In order to find out if the reaction actually requires the use of a catalyst (generally needed for cross couplings) or if the conducted reaction proceeds *via* a substitution, a test trial was performed under the same conditions in the absence of a catalytic system (Table 4.3, entry 3, Scheme 4.7). The absence of mono- and bis-coupled product masses in the ESI-MS confirmed that this reaction indeed proceeds *via* a catalytic pathway.



Scheme 4.7. The test reaction between 2,6-dibromopyridine and 1-methyl-4,5-dihydroimidazole IV-3 in the absence of catalytic system.

So far only insufficient conversion to target compound IV-5 had been achieved. Typically, a colour change of the reaction mixture from red to yellow was observed after addition of IV-3. This could be the result of coordination of 1-methyl-4,5-dihydroimidazole (IV-3) to the [Pd] species, that partially quenches further catalytic activity. Incomplete conversion of the starting material 2,6-dibromopyridine confirmed this suggestion. In order to overcome this issue, the catalytic system loading was increased from 10 to 20 mol% for the Pd-source and from 20 to 40 mol% for the *rac*-BINAP ligand, while the other parameters remained unchanged (Table 4.3, entry 4).

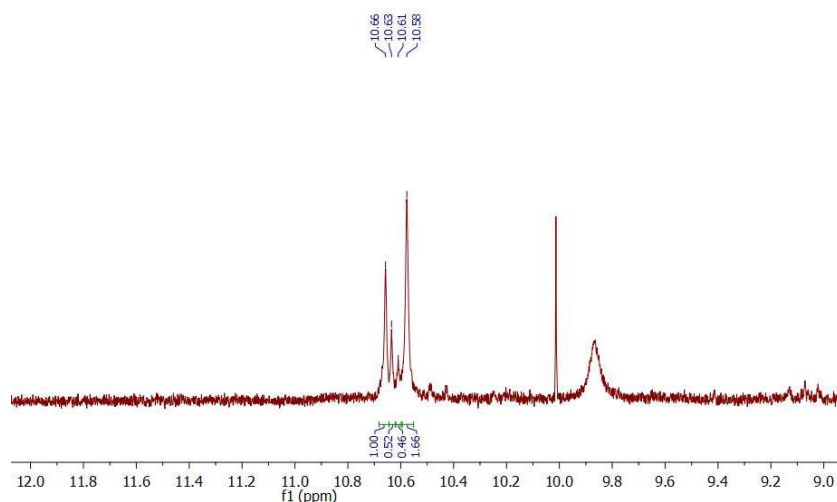


Figure 4.5. ^1H NMR spectrum of cross-coupling reaction entry 4, Table 4.3 in DMSO-d_6 . Peaks at 10.66 and 10.63 ppm correspond to carbene centres of IV-5 and IV-5.1, respectively. Peaks at 10.61 and 10.58 ppm correspond to new generated species.

As can be seen in the ^1H NMR spectrum in Figure 4.5, new species were generated besides the target compound IV-5 after the load increase of catalytic system. At the same time, starting material as well as mono-coupled product IV-5.1 were still observed. Further increase of Pd-source from 20 to 40 mol% and of *rac*-BINAP ligand from 40 to 80 mol% led to full conversion of 2,6-dibromopyridine, but no peaks corresponding to carbene centres of IV-5, IV-5.1, or the debrominated monocoupling product were observed by ^1H NMR spectroscopic analysis (Table 4.3, entry 5). The ESI-MS spectrum of the crude mixture is presented in Figure 4.6, showing (despite the catalyst increase) only the minor presence of the mono- and bis-coupling products.

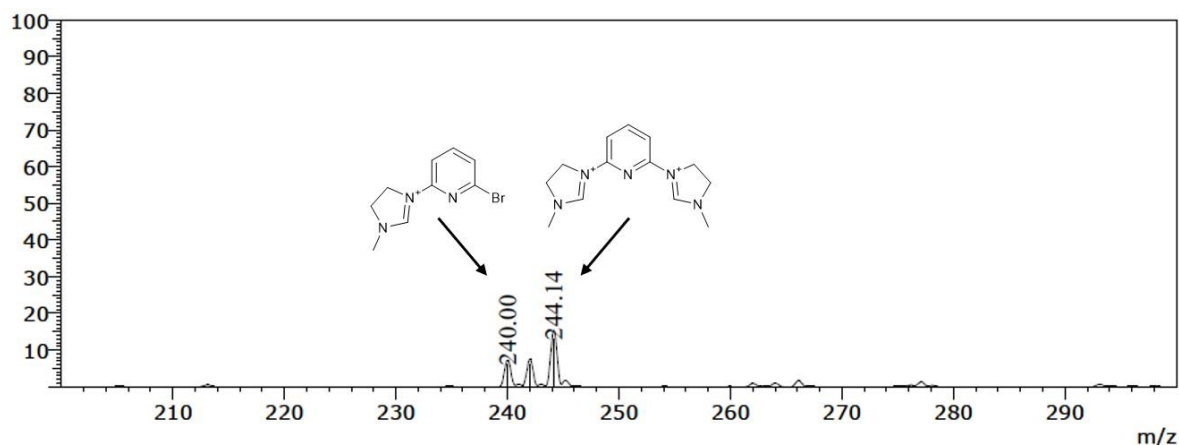
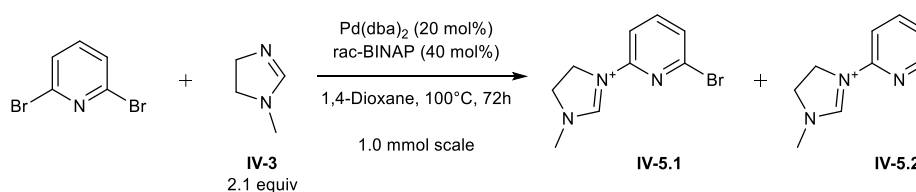


Figure 4.6. Section of ESI-MS spectrum of crude mixture (Table 4.3, entry 5).

With the aim of further increasing the starting material conversion, microwave irradiation at 120 °C was applied. The load of [Pd]/ligand catalytic system was 20/40 mol% (Table 4.3, entry 6). After 3 h the target compound IV-5 was observed by ESI-MS in the crude mixture with mono-coupled product IV-5.1 and starting material 2,6-dibromopyridine. Longer reaction times resulted in the formation of more side products but did not positively influence the conversion to IV-5.

Due to the screening character of the study, the scale of reactions was not exceeding 0.50 mmol at this point. This aspect made the isolation of IV-5 more challenging since the target compound was observed only in traces. To make a potential isolation more practical, the scale of reaction was increased to 1.00 mmol (Table 4.3, entry 7). The same conditions were used as for entry 4 ($\text{Pd}(\text{dba})_2$ (20 mol%), *rac*-BINAP (40 mol%) in 1,4-dioxane heated under inert conditions at 100 °C for 72 h). Interestingly, no target compound was observed in this case and only mono-coupled compound IV-5.1 and its hydrolysed derivative IV-5.2 were found (Scheme 4.8).



Scheme 4.8. Cross-coupling reaction at 1.00 mmol scale.

It was decided to introduce the obtained product IV-5.1 into a second cross-coupling reaction with 1-methyl-4,5-dihydroimidazole (IV-3) in order to gain the target product IV-5. Because of the similar structures of IV-5.1 and IV-5.2, these compounds could not be effectively separated by flash chromatography purification either and were obtained in a 1:1 mixture (Figure 4.7).

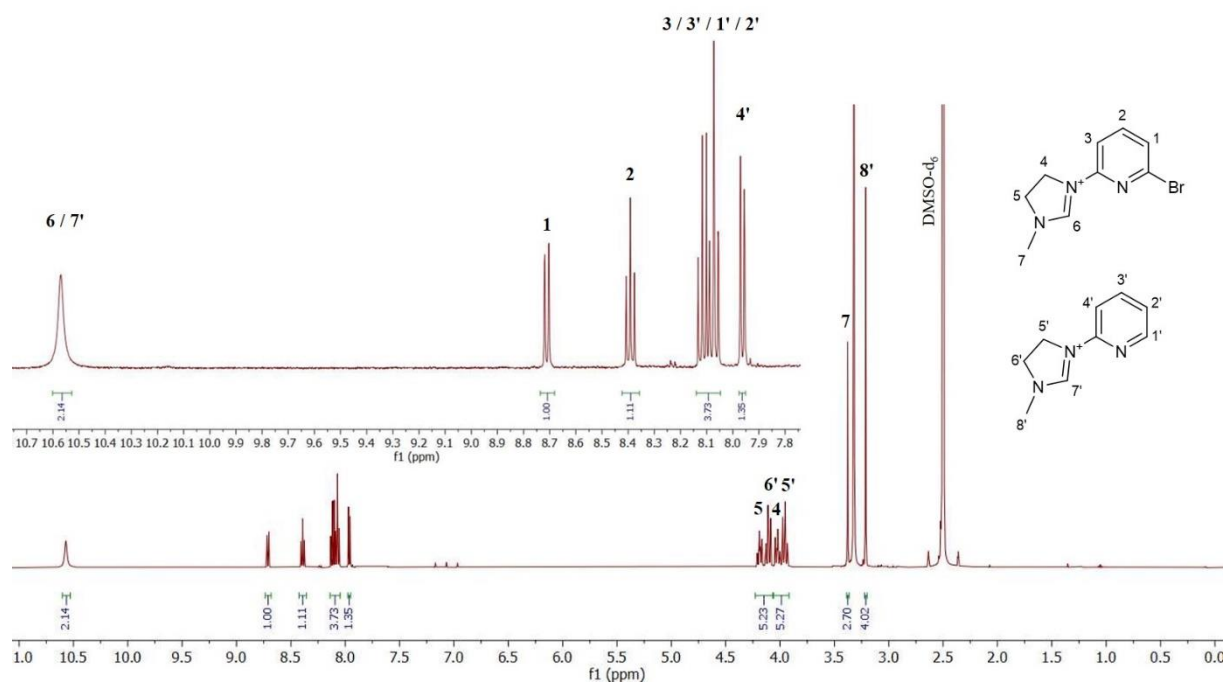
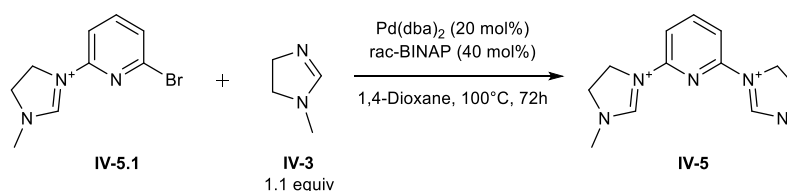


Figure 4.7. ¹H NMR spectrum of IV-5.1 and IV-5.2 in DMSO-d₆ with the expansion of aromatic region (Table 4.3, entry 7).

Since IV-5.2 does not have a halogen functionality, which could be transformed in a cross-coupling reaction, the mixture of products was used directly for the next step (Scheme 4.9).



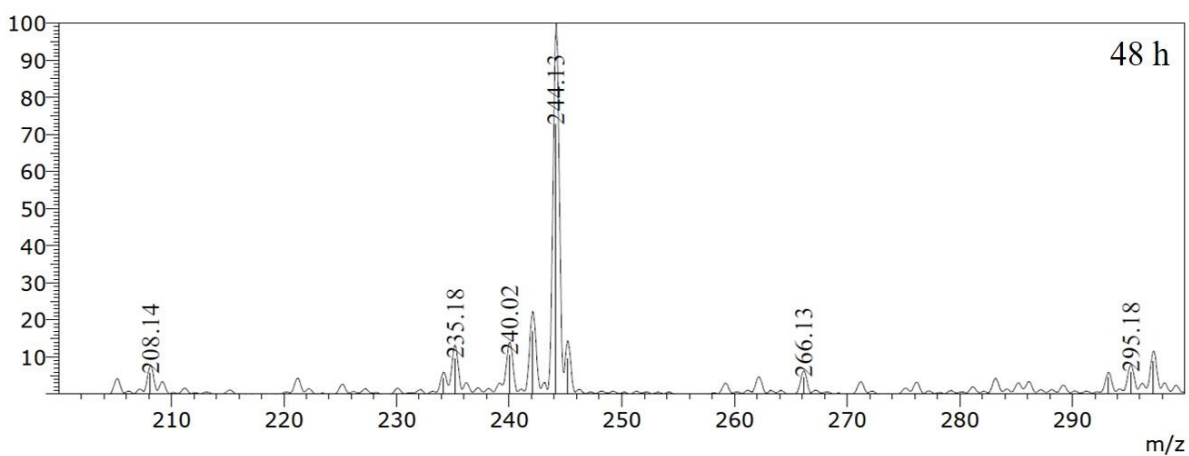
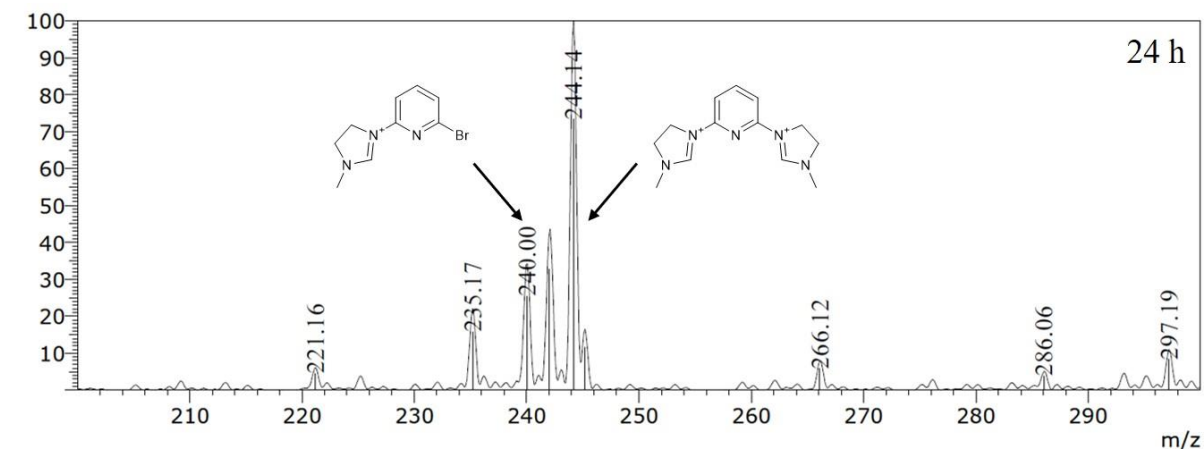
Scheme 4.9. Follow-up cross-coupling reaction between IV-5.1 and IV-3.

The reaction was carried out under the same conditions as the first coupling, but in the presence of only 1.10 equiv IV-3 (Table 4.3, entry 8). Despite an incomplete conversion of IV-5.1, the product IV-5 was observed in the mixture by ESI-MS. Thus, it was shown that mono-coupled compound IV-5.1 can react further after isolation, but due to the low concentration of IV-5 compared to the additionally formed side-products, the compound was not detected by ¹H NMR spectroscopic analysis.

Since a mixture of mono- and bis-coupled products was so far always obtained and no sufficient separation of these compounds was perceived, it was decided to perform the synthesis only with 1.00 equiv IV-3 to isolate first the mono-coupling product IV-5.1 and further react it in a second cross-coupling reaction afterwards (Table 4.3, entry 9). Interestingly, both products IV-5.1 and IV-5 were formed during the first cross-coupling, despite the use of only 1.00 equiv IV-3. Thus, IV-3 was already consumed before all of the 2,6-dibromopyridine starting material could be

Fourth Chapter

converted. Since mainly by-products were generated in the reaction, IV-5 and IV-5.1 were detected only by ESI-MS and could not be observed in the corresponding ^1H NMR spectrum. After this observation, an excess of 1-methyl-4,5-dihydroimidazole (IV-3) was used (Table 4.3, entry 10). The reaction time took 120 h for the full conversion of 2,6-dibromopyridine and to achieve the largest possible transformation of IV-5.1 to IV-5 (Figure 4.8). However, the target compound was still the minor component and many by-products were generated according to ^1H NMR spectroscopic analysis. Therefore, IV-5 could be detected only by ESI-MS.



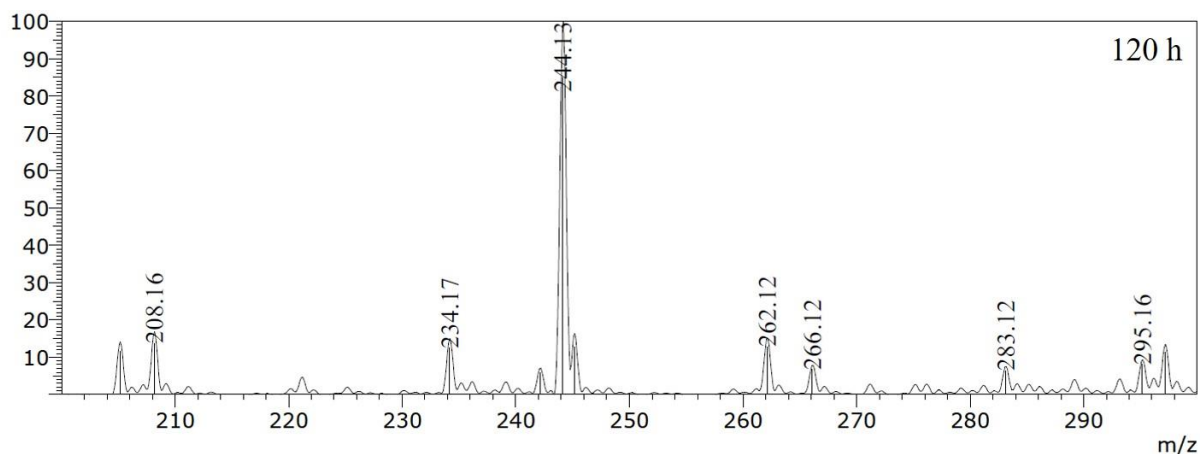
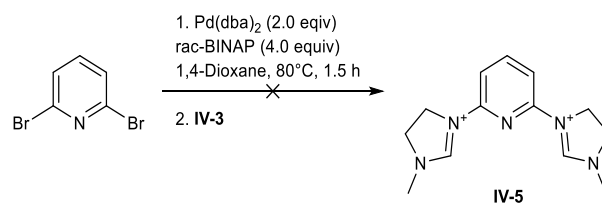


Figure 4.8. Section of ESI-MS spectra of crude mixture after 24 h, 48 h and 120 h (Table 4.3, entry 10) to monitor the conversion of IV-5.1.

As already discussed above, higher catalyst loadings tended to lead to the formation of more side-products. Hence, the amount of palladium salt/ligand was decreased back to 10/20 mol% in the presence of 8.40 equiv of 1-methyl-4,5-dihydroimidazole (Table 4.3, entry 11). Despite the absence of IV-5.1 in the mixture, the target compound IV-5 was still observed only in traces compared to numerous by-products. In order to check if it is possible to reduce side-products by the load of palladium complex/ligand, the charged quantity was decreased further to 5/10 mol% (Table 4.3, entry 12). The experiment had shown that no IV-5 or IV-5.1 was generated.

For a deeper understanding of the catalytic process, a test experiment was performed (Scheme 4.10). In order to find out if [Pd] interferes with the imidazolium carbene centre, 2,6-dibromopyridine was heated to 80°C with 2.00 equiv Pd(dba)₂ and 4.00 equiv rac-BINAP in the absence of dihydroimidazole IV-3 to avoid the reaction of palladium with dihydroimidazole before the oxidative insertion step. The stoichiometric load of the catalytic system was used to monitor the conversion of 2,6-dibromopyridine. It was observed that after 1.5 h no traces of starting material were present, and IV-3 was added. The reaction was stirred at the same temperature overnight. Ultimately, no traces of target compound were observed. This could be an indication of side-reaction processes that occurred before the addition of IV-3.



Scheme 4.10. The test trial of IV-5 synthesis with premixed catalytic system with 2,6-dibromopyridine.

At this point of the investigation, reaction conversions were typically incomplete, and IV-5 was generated as a minor product. Therefore, further investigations on the actual cross-coupling system

were conducted. The two additional catalytic systems Pd(OAc)₂/BrettPhos and Pd(dppf)Cl₂/PPh₃ were tested, which are also common for Buchwald-Hartwig aminations (Table 4.4).¹⁸³ In the case of the Pd(OAc)₂/BrettPhos system, no target compound was observed in the reaction mixture after 48 h at 100°C (Table 4.4 entry 1). The Pd(dppf)Cl₂/PPh₃ combination resulted under the same conditions in mono-coupled product IV-5.1, but no IV-5 was present (Table 4.4, entry 2, Figure 4.9).

Table 4.4. The baseline conditions were 2,6-dibromopyridine (1.00 equiv), 1-methyl-4,5-dihydroimidazole (IV-3, 2.10 equiv), [Pd]/ligand in 1,4-dioxane heated under inert conditions at 100°C for 48 h; the scale of reactions was not exceeding 0.50 mmol.

| Entry | [Pd] source / mol% | Ligand / mol% | Solvent | Additional conditions | Observations |
|-------|------------------------------|-----------------------|-------------|-----------------------|--|
| 1 | Pd(OAc) ₂ / 10 | BrettPhos / 20 | 1,4-Dioxane | 100°C, 48 h | No traces of target product IV-5. |
| 2 | Pd(dppf)Cl ₂ / 10 | PPh ₃ / 20 | 1,4-Dioxane | 100°C, 48 h | Only mono-coupled product IV-5.1 is present. |

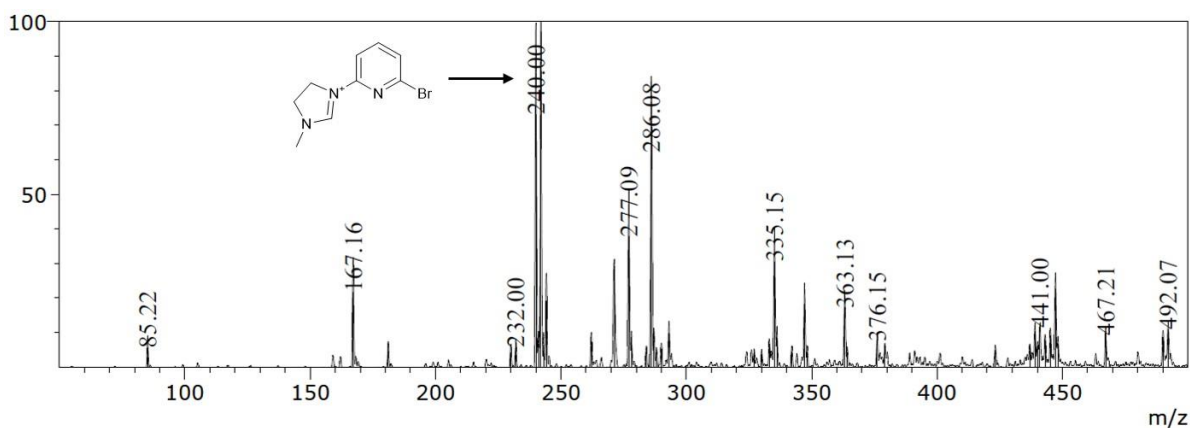
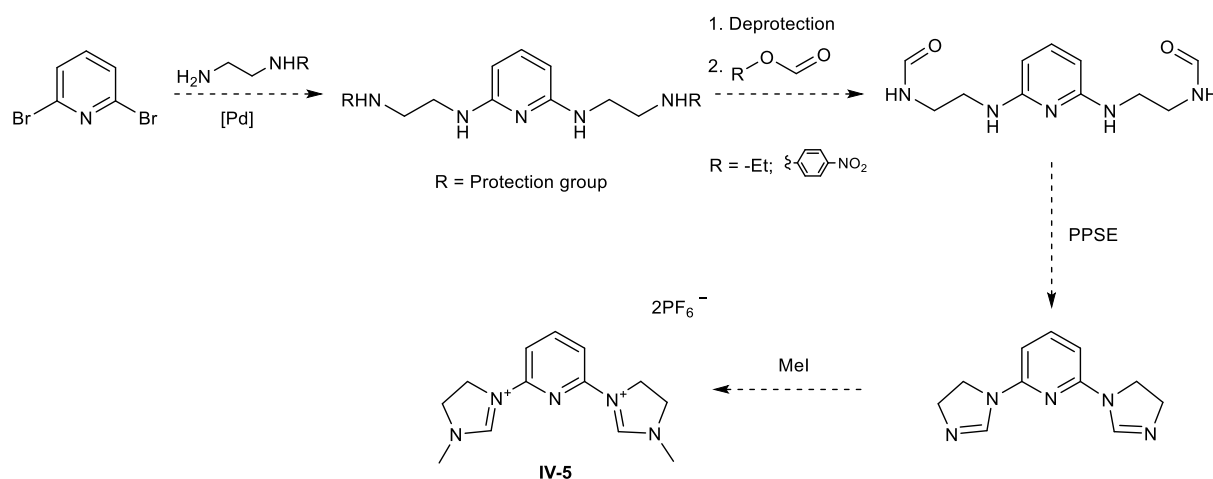


Figure 4.9. ESI-MS spectrum of crude mixture using Pd(dppf)Cl₂/PPh₃ as catalytic system (Table 4.4, entry 2).

Due to the limited success of the cross-coupling between 2,6-dibromopyridine and IV-3, it was decided to change the synthetic strategy. The new synthetic route is shown in Scheme 4.11.

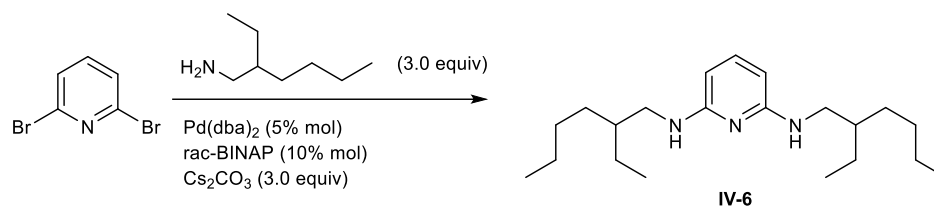


Scheme 4.11. Alternative synthetic route for IV-5. Dashed arrows show transformations without isolated compounds.

First, monoprotected ethylenediamine (EDA) is introduced to the pyridine ring. Then, the deprotection is carried out and amine moiety is formylated. The synthesis will be completed by the imidazole ring closure. Starting with the first step, a C-N bond formation is required. It is known that secondary amines are more effectively coupled than primary amines due to competitive β -hydride elimination.¹⁸⁹ This process results in the formation of a reduced arene, which comes from the Ar-Pd^{II}-H intermediate.¹⁸⁹ Nevertheless, several catalytic systems based on Pd(OAc)₂ and Pd(dba)₂¹⁹⁰⁻¹⁹² were found effective also for primary amines, which became the starting point for the following studies. Reaction progress and outcome were monitored by ¹H NMR spectroscopy and/or ESI-MS analysis. Therefore, results could not be quantified in terms of conversion percentage. Instead, reaction mixtures were analysed only for the presence of the target compound.

Coupling of the two model substrates 2,6-dibromopyridine and the primary amine 2-ethylhexan-1-amine was first tested in an initial baseline experiment (Scheme 4.12). Based on the literature, Pd(dba)₂ was kept as a suitable [Pd] source for cross-coupling with primary amine. The reaction was conducted with the catalytic system Pd(dba)₂/BINAP and Cs₂CO₃ as base in THF. The reaction was performed at 65°C overnight under inert conditions. The target product IV-6 was observed in ESI-MS and as one of the major compounds in ¹H NMR. This proof-of-concept experiment with commercially available compounds had shown that the pathway *via* cross-coupling would be possible and results in the formation of the target product. Interestingly, conducting the same reaction under microwave irradiation (90°C, 1 h) did not lead to the target product and only side-products were observed.

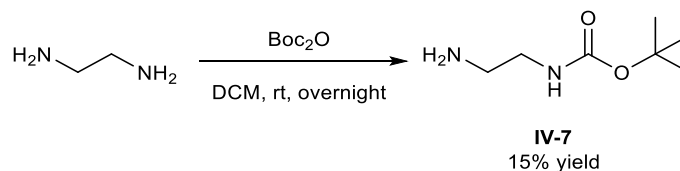
Fourth Chapter



Scheme 4.12. Proof-of-concept cross-coupling of 2,6-dibromopyridine and primary amine 2-ethylhexan-1-amine.

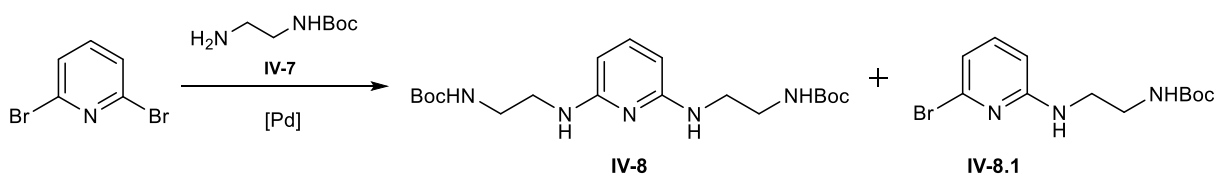
The proof-of-concept reaction was carried out successfully and the same conditions were applied for the use of N-Boc-ethylenediamine (BocEDA; IV-7), which was identified as a potential substrate of the newly designed synthetic route. EDA can form complexes with various metal ions including palladium and, thus, monoprotected ethylenediamine was used for the synthesis.^{193, 194}

BocEDA (IV-7) was synthesised according to a literature procedure from EDA and Boc anhydride in 15% yield (Scheme 4.13).¹⁹⁵



Scheme 4.13. Synthesis of N-Boc-ethylenediamine (IV-7).

Then, BocEDA was further converted in the Buchwald-Hartwig amination with 2,6-dibromopyridine (Scheme 4.14).



Scheme 4.14. Buchwald-Hartwig amination of 2,6-dibromopyridine and BocEDA (IV-7).

Table 4.5. Experiments on the Buchwald-Hartwig amination of 2,6-dibromopyridine and BocEDA.

| Entry | [Pd] source / mol% | Ligand / mol% | Base / equiv | Solvent | Additional conditions | Observations |
|-------|--------------------------|----------------|--|---------|-----------------------|---|
| 1 | Pd(dba) ₂ / 5 | rac-BINAP / 10 | Cs ₂ CO ₃ / 3.00 | THF | 65°C, ON | Compounds IV-8 and IV-8.1 as well as 2,6-dibromopyridine are present. Numerous by-products. |
| 2 | Pd(dba) ₂ / 5 | rac-BINAP / 10 | Cs ₂ CO ₃ / 3.00 | THF | 65°C, ON ¹ | IV-8 is present. Full conversion of starting material. Numerous by-products were formed. |
| 3 | Pd(dba) ₂ / 5 | rac-BINAP / 10 | Cs ₂ CO ₃ / 3.00 | THF | 90°C, 1 h, MW | Full conversion of starting material, minimal conversion to IV-8. |
| 4 | Pd(dba) ₂ / 5 | rac-BINAP / 10 | Cs ₂ CO ₃ / 3.00 | Toluene | 110°C, 1 h, MW | Full conversion of starting material, minimal conversion to IV-8. |
| 5 | Pd(dba) ₂ / 5 | rac-BINAP / 10 | KO ^t Bu / 3.30 | Toluene | 100°C, ON | Only mono-coupled product IV-8.1 is present. |

All reactions were carried out under inert conditions, ON – overnight, MW – microwave irradiation; ¹ All compounds except BocEDA were mixed and stirred for 40 min at rt, then BocEDA was added, and the reaction was heated to 65°C ON.

Cross-coupling of 2,6-dibromopyridine and IV-7 was carried in an initial experiment in the presence of Cs₂CO₃ at 65°C in THF. Under these conditions, the reaction resulted in numerous products among which the target compound IV-8 and the mono-coupling product IV-8.1 were present (Table 4.5, entry 1). The successful formation of target product could be detected by ¹H NMR spectroscopy and ESI-MS analysis. Additionally, the mono-coupled product IV-8.1 and 2,6-dibromopyridine were detected by ESI-MS analysis in the crude mixture. Products IV-8 and

Fourth Chapter

IV-8.1 could not be separated by standard purification (flash chromatography) because of their structural similarities (Figure 4.10).

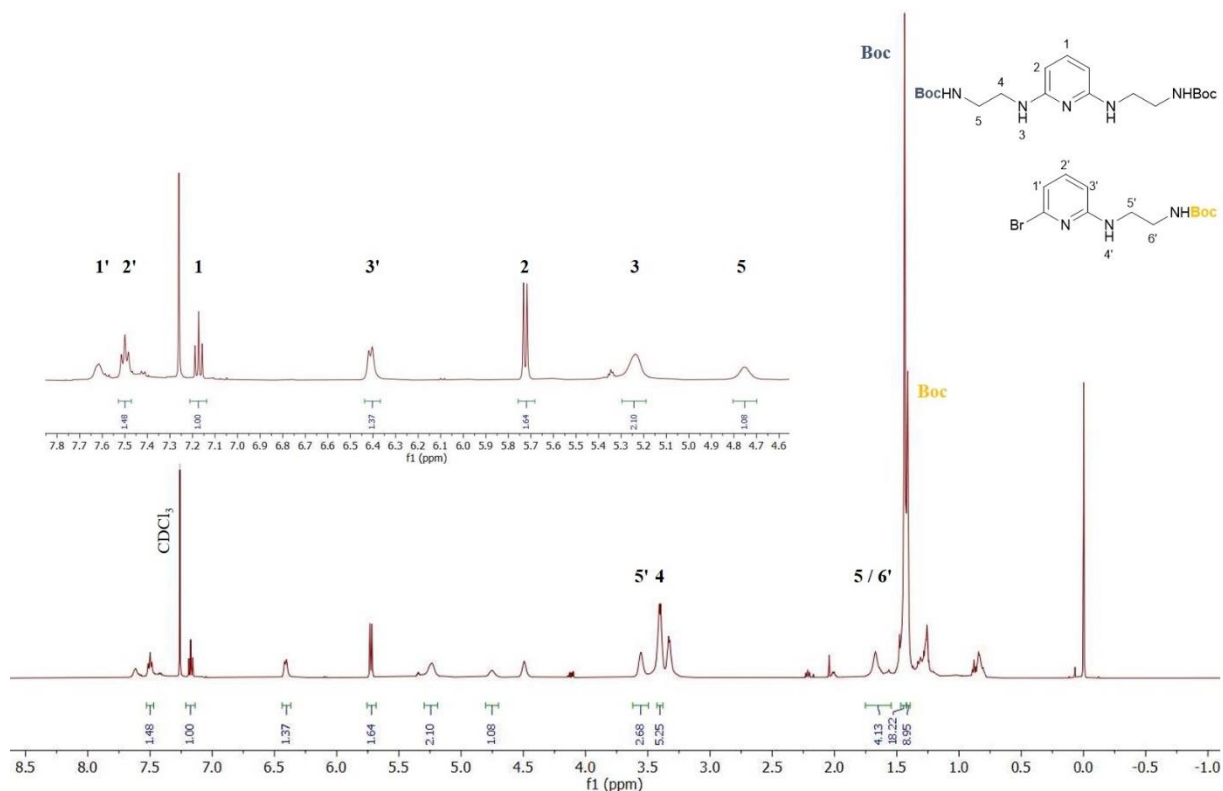


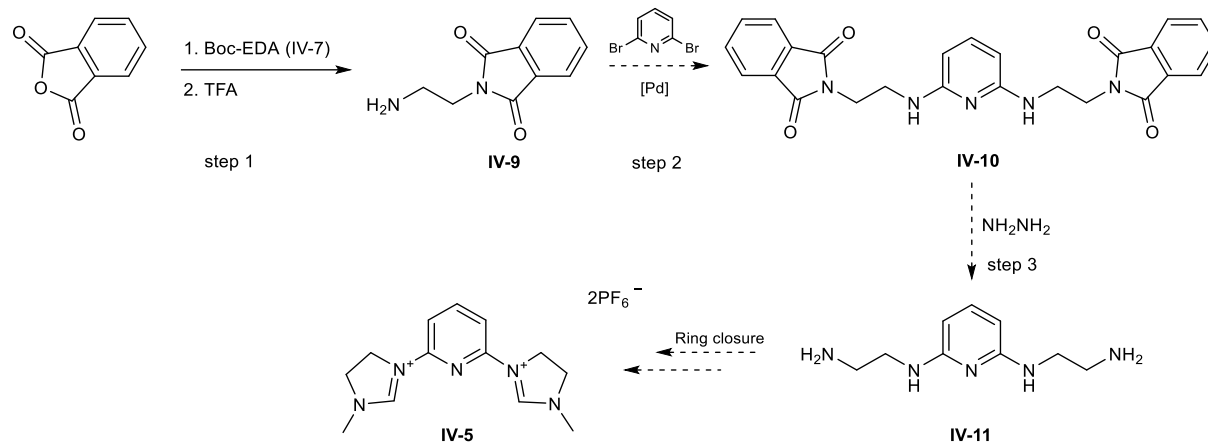
Figure 4.10. ¹H NMR spectrum of IV-8 and IV-8.1 in CDCl₃ with the expansion of aromatic region (Table 4.5, entry 1).

Since the reaction was carried out at 65°C overnight, various side-products could be generated by an early coordination of the amine to palladium before the oxidative insertion occurred. This aspect could result in numerous side-reactions. To avoid potential formation of such in-situ adducts, the reaction was repeated with a different addition sequence of the relevant components (Table 4.5, entry 2). All reagents except BocEDA were mixed in THF and stirred for 40 minutes at room temperature. Then, the amine was added and the reaction was heated to 65°C and stirred at this temperature overnight. Analysis by ESI-MS revealed that IV-8 was present in the crude mixture among other side-products. However, it could not be detected *via* ¹H NMR analysis anymore. These first trials demonstrated that 2,6-dibromopyridine and BocEDA (IV-7) converted under the given conditions to various side-products and less selective to IV-8 when pre-mixing reaction components without IV-7.

After the observations described above, it was decided to minimize the reaction time by using a microwave reactor. It was anticipated that it will reduce the amount of by-products and increase the conversion to the target compound (Table 4.5 entry 3). Despite full conversion of starting material after 1 h at 90°C, IV-8 was observed *via* ESI-MS, but not detected in the ¹H NMR

spectrum indicating that only traces of compound were present in the mixture. For an understanding of solvent-related impacts and the influence of a broader temperature range, the reaction was conducted in toluene in combination with an elevated temperature of 110°C (Table 4.5, entry 4). After 1 h under microwave conditions, a similar outcome as for the previous experiments was observed (full conversion of starting material, but only traces of IV-8). Interestingly, the change of base from Cs₂CO₃ to KO^tBu resulted only in mono-coupled product IV-8.1 as well as some side-products, but no IV-8 was observed in the reaction mixture (Table 4.5, entry 5).

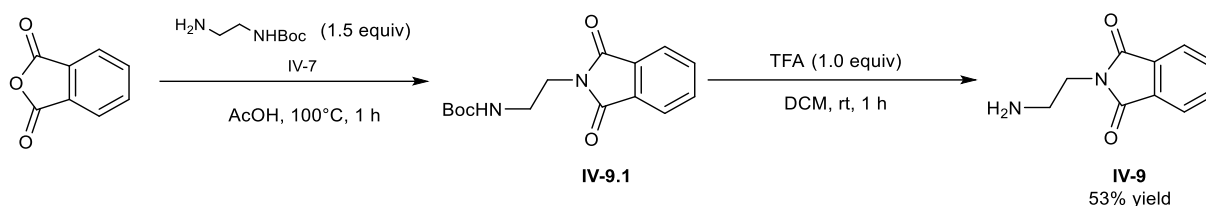
The experiments listed in Table 4.5 showed an overall high conversion of 2,6-dibromopyridine under the applied conditions, but, since the desired product IV-8 was only found in traces, the desired selectivity of the reaction remained as major challenge. A potential explanation for these findings is that BocEDA may coordinate to palladium and functions rather as ligand and not as reactant. To reduce potential coordination properties, the *tert*-butoxycarbonyl protecting group was replaced by a phthalimide moiety affording amine IV-9. The route of corresponding synthesis is presented in Scheme 4.15.



Scheme 4.15. Alternative synthetic path using a phthalimide-protected amine to afford target compound IV-5. Solid arrows show reactions with isolated compounds, dashed arrows show transformations without isolated compounds.

Based on the new synthetic pathway, compound IV-9 could be synthesized according to a literature procedure from BocEDA (IV-7) and phthalic anhydride in 53% yield over two steps (Scheme 4.16).¹⁹⁶

Fourth Chapter



Scheme 4.16. Synthesis of phthalimide-protected EDA (IV-9).

Afterwards, IV-9 was reacted with the model substrate 2,6-dibromopyridine in a Buchwald-Hartwig amination to obtain the double substituted product IV-10. In a third step, the protecting groups are cleaved with a standard protocol (use of hydrazine) and the free amine IV-11 will be proceeded in a cyclization reaction to the target compound IV-5, as already presented in Scheme 4.15. In Table 4.6 the experiments to prepare the bis-coupling product IV-10 are summarized. The trials were started with the same initial conditions for cross-coupling as for the use of BocEDA, but with an increased catalyst load (Table 4.6 entry 1). Despite the relatively high load of catalyst, no conversion of starting materials was observed after overnight reaction at 65°C in THF. As for BocEDA, the solvent was changed from THF to toluene and the temperature was increased to 110°C (Table 4.6, entry 2). Still, no conversion was observed after stirring overnight. The usage of microwave irradiation and higher temperature (170°C) resulted in the consumption of IV-9, but 2,6-dibromopyridine was still present in the mixture among other side-products, which was confirmed by ESI-MS and ¹H NMR spectroscopic analysis (Table 4.6, entry 3).

Table 4.6. Experiments on the Buchwald-Hartwig amination of 2,6-dibromopyridine and IV-9.

| Entry | [Pd] source / mol% | Ligand / mol% | Base / equiv | Solvent | Additional conditions | Observations |
|-------|---------------------------|----------------|--|---------|-----------------------|---|
| 1 | Pd(dba) ₂ / 10 | rac-BINAP / 20 | Cs ₂ CO ₃ / 3.00 | THF | 65°C, ON | No reaction, only starting materials are present. |
| 2 | Pd(dba) ₂ / 5 | rac-BINAP / 10 | Cs ₂ CO ₃ / 3.00 | Toluene | 110°C, ON | No reaction, only starting materials are present. |
| 3 | Pd(dba) ₂ / 5 | rac-BINAP / 10 | Cs ₂ CO ₃ / 3.00 | Toluene | 170°C, 1.5 h, MW | 2,6-dibromopyridine is present, no IV-9 in the mixture. |

Fourth Chapter

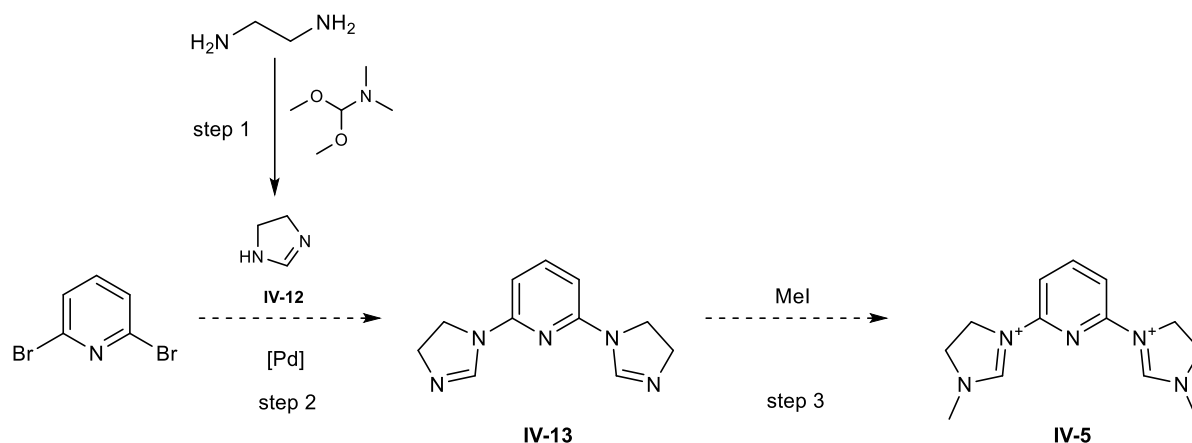
| | | | | | | |
|---|-----------------------------|-------------------|---|-----------------|-----------|---|
| 4 | Pd(dba) ₂ / 5 | rac-BINAP / 10 | Cs ₂ CO ₃ / 3.00 | 1,4- Dioxane | 100°C, ON | 2,6-dibromo- pyridine and target compound IV-10 are present. |
| 5 | Pd(dba) ₂ / 5 | rac-BINAP / 10 | KO ^t Bu / 3.00 | 1,4- Dioxane | 100°C, ON | 2,6-dibromo- pyridine and target compound IV-10 are present. |

All reactions were carried out under inert conditions, ON – overnight, MW – microwave irradiation.

The change of solvent to 1,4-dioxane, which is another common solvent for Buchwald-Hartwig amination, brought positive changes (Table 4.6 entry 4). Despite residual 2,6-dibromopyridine after stirring at 100°C overnight, the target product IV-10 was observed in the ESI-MS spectrum of the reaction mixture. However, ¹H NMR analysis revealed only numerous side-products and 2,6-dibromopyridine, and no signals that could be assigned to the target compound could be detected. In case of BocEDA, the change of base resulted solely in mono-coupling product along with other side-products (Table 4.6, entry 5). Thus, it was of interest to check if a base change will have a major influence on the reaction outcome. The substitution of caesium carbonate with potassium *tert*-butoxide led to a similar crude mixture containing IV-10 and 2,6-dibromopyridine. Despite the presence of target product IV-10 in ESI-MS, its actual formation was insufficient under the investigated conditions and numerous side-product were observed by ¹H NMR analysis.

Various limitations like insufficient conversion and formation of numerous side-products negatively affected the cross-coupling of 2,6-dibromopyridine with IV-3, IV-7 and IV-9. Thus, it was decided to focus directly on the use of 4,5-dihydro-1H-imidazole (IV-12), which has a secondary amine functionality. As was discussed above, secondary amines are common Buchwald-Hartwig coupling substrates and react more effectively than primary amines. The general synthetic path is shown in Scheme 4.17.

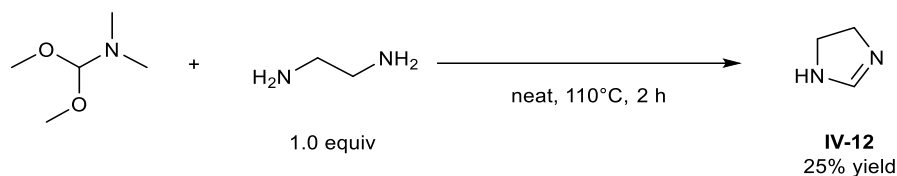
Fourth Chapter



Scheme 4.17. Alternative synthetic path to obtain IV-5. Solid arrows show reactions with isolated compounds, dashed arrows show transformations without isolated compounds.

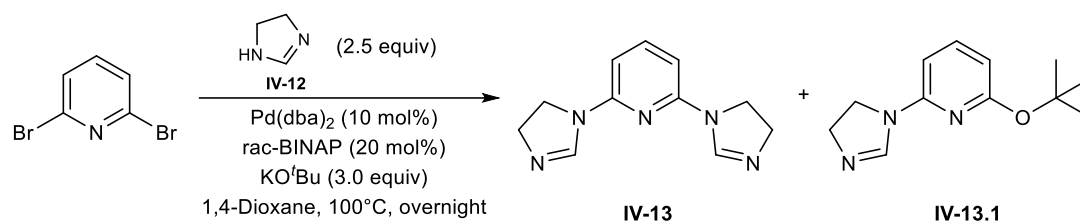
The first step describes the actual formation of 4,5-dihydro-1H-imidazole (IV-12), which will be further reacted in the subsequent cross-coupling with 2,6-dibromopyridine. The cross-coupling product IV-13 then needs to be methylated to afford the target compound IV-5.

The synthesis of IV-12 was performed according to a literature procedure, which was already used for the IV-3 preparation.¹⁹⁷ The reaction between N,N-dimethylformamide dimethyl acetal and EDA was carried out neat and afforded the product IV-12 as an amorphous solid in up to 25% yield (Scheme 4.18).



Scheme 4.18. Synthesis of 4,5-dihydro-1H-imidazole IV-12 from N,N-dimethylformamide dimethylacetal and EDA.

Since the Pd(dba)₂/rac-BINAP catalytic system showed the most promising results for coupling IV-3 (Table 4.3, entries 1 and 4), it was used for IV-12 as well. The secondary amine functionality requires a deprotonation step in the catalytic cycle. Therefore, KO^tBu was used as a base in this reaction (Scheme 4.19).



Scheme 4.19. Buchwald-Hartwig cross-coupling of 2,6-dibromopyridine and IV-12 to afford IV-13.

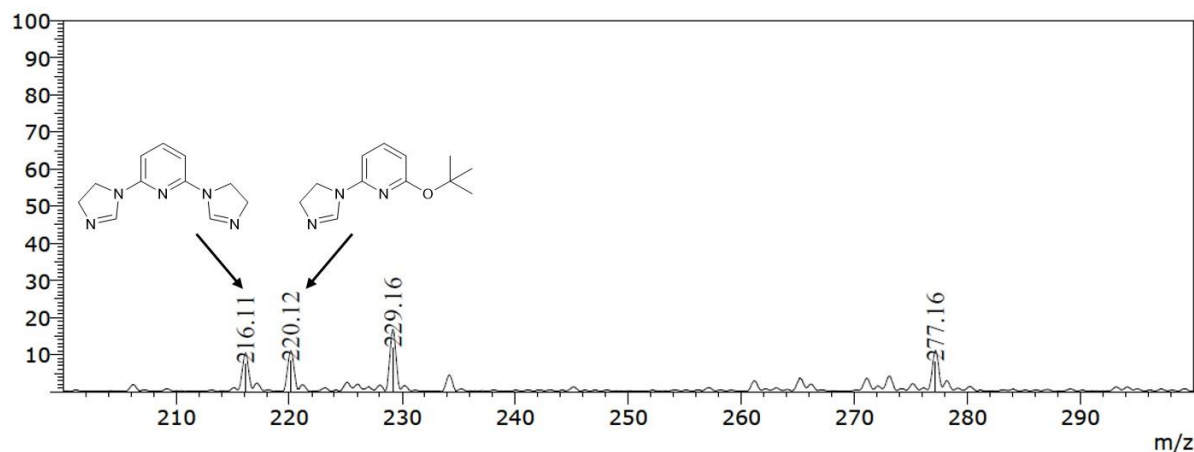
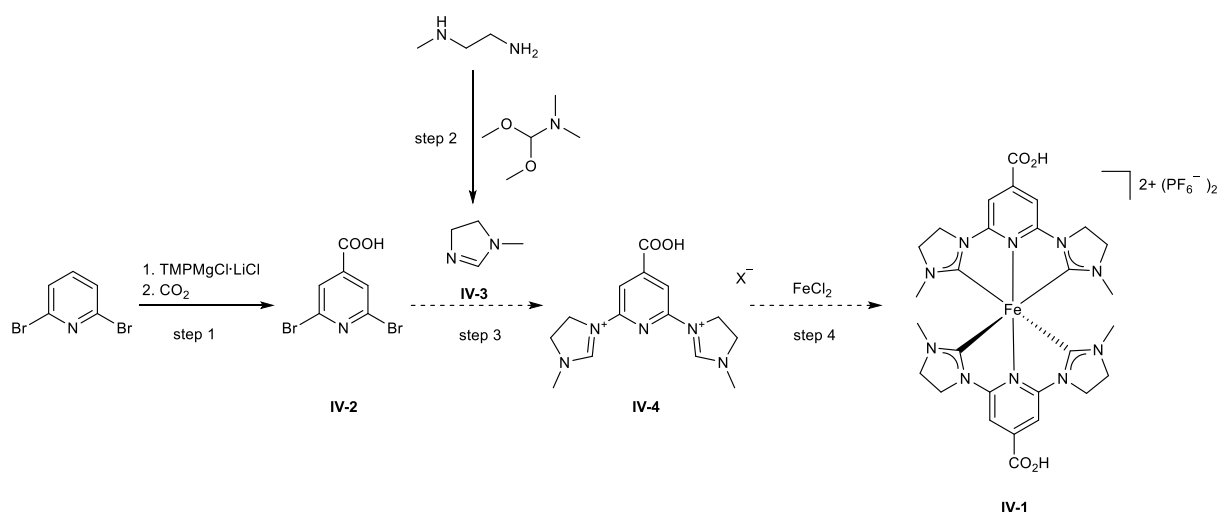


Figure 4.11. Section of ESI-MS spectrum of crude reaction mixture presented in Scheme 4.19.

According to ESI-MS analysis, the crude mixture contained the target compound IV-13 together with product IV-13.1, which was formed by mono-coupling and substitution of bromine with *tert*-butoxide (Figure 4.11). The reaction has so far not been further optimised, but the preliminary results demonstrated a high potential for achieving selective formation of IV-13 by additional optimisation. The absence of a quaternary ammonium cation should be beneficial for the purification. Moreover, the base choice needs to be carefully studied. It should not have nucleophilic properties to avoid aromatic substitution at the pyridine ring. Furthermore, the base could also deprotonate IV-12 and generate free carbene provoking various side-reactions.

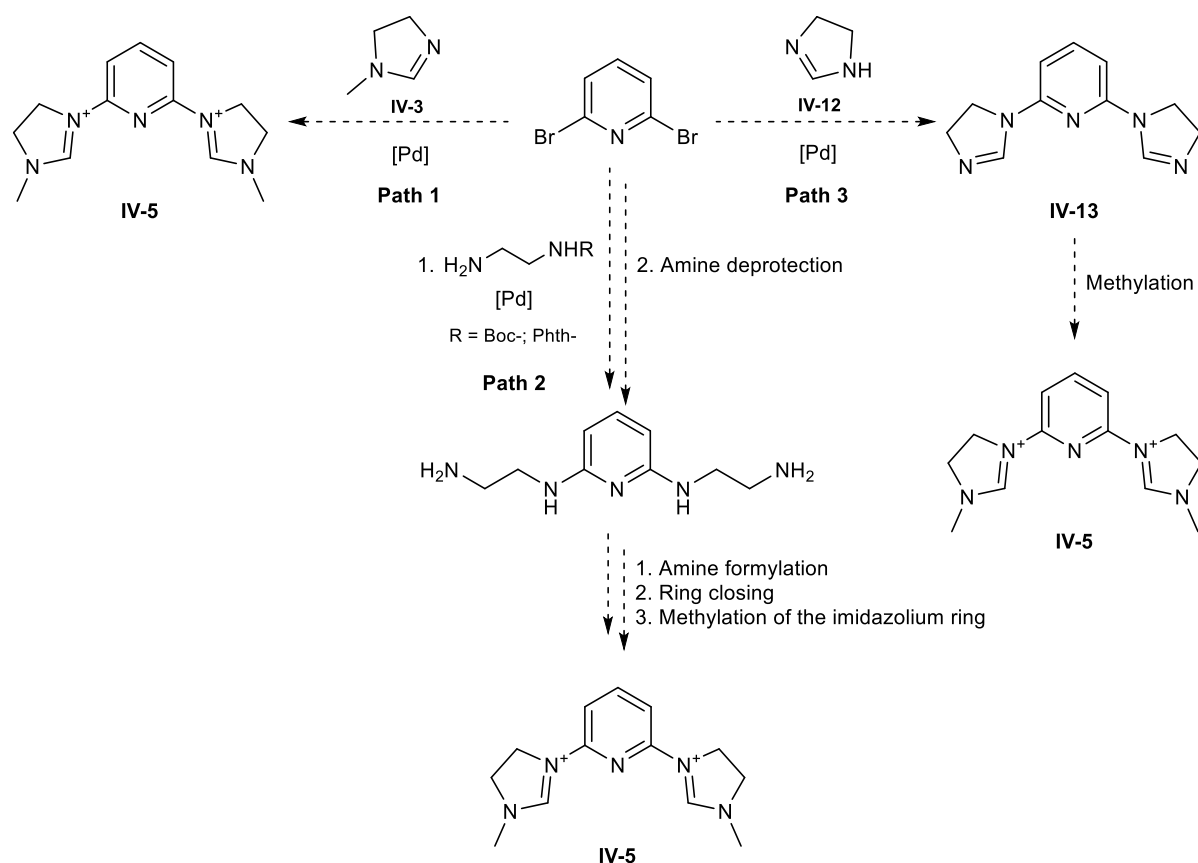
3. Summary and Outlook



Scheme 4.20. Proposed synthetic route to achieve alternative dye IV-1.

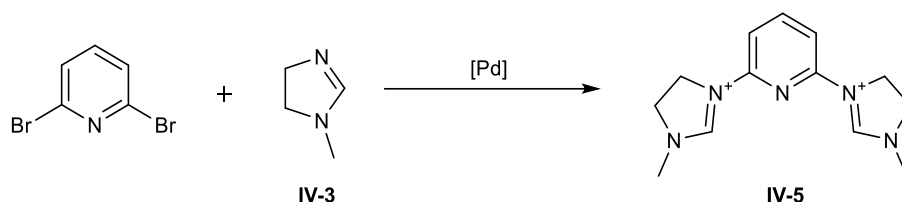
The goal was to design and synthesize an alternative dye molecule (IV-1), which would increase the sigma-donation on the metal centre (Scheme 4.20). The designed synthetic route was an analogue of the IV-4 synthesis and included the preparation of 2,6-dibromoisonicotinic acid IV-2, which would be further involved in a *bis*-substitution reaction with 1-methyl-4,5-dihydroimidazole IV-3 to give the bis-coupling product IV-4. IV-3 had to be synthesised from *N*-methylethanediamine and *N,N*-dimethylformamide dimethyl acetal in advance. Ligand IV-4 would have been converted in a final complexation reaction with iron(II) chloride to afford the target complex IV-1. Unfortunately, not all steps in this strategy were achieved.

The aromatic substitution was a limiting factor of the synthesis and the strategy had to be changed to cross-coupling. Several synthetic routes, which are presented in Scheme 4.21, were designed to obtain the final intermediate IV-5. Due to scale up limitations of the 2,6-dibromoisonicotinic acid preparation, the study was performed on commercially available 2,6-dibromopyridine.



Scheme 4.21. All synthetic pathways to obtain IV-5 *via* cross-coupling investigated in this study.

The first route proposed a Buchwald-Hartwig amination between 2,6-dibromopyridine and 1-methyl-4,5-dihydroimidazole (IV-3) as a coupling substrate (Scheme 4.22).



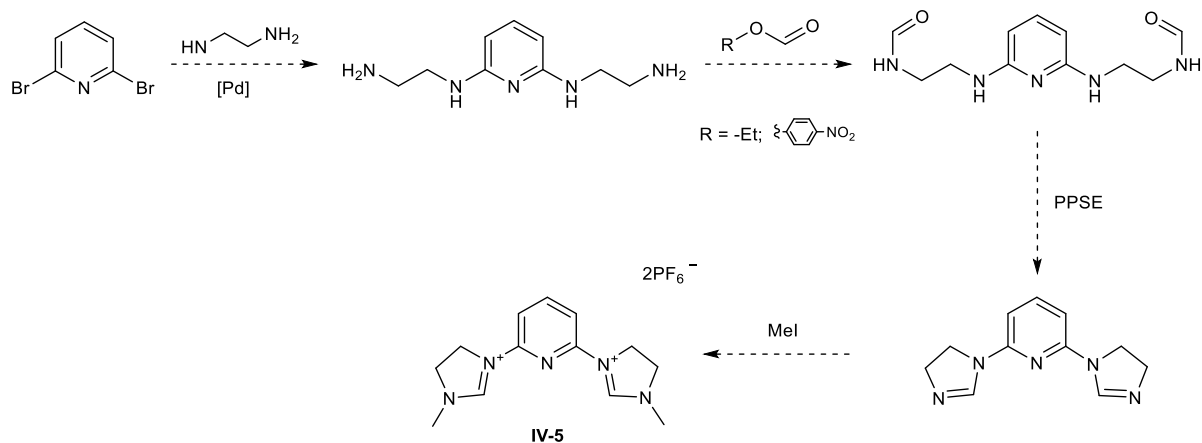
Scheme 4.22. Synthetic path to give IV-5 *via* direct cross-coupling between 2,6-dibromopyridine and 1-methyl-4,5-dihydroimidazole (IV-3).

It was shown that large catalyst amounts (from 10 mol% palladium complex on) and long reaction times (not less than 72 h) are required to form the target product at least for analytical identification *via* ESI-MS analysis. In most of the cases, the mono-coupled product IV-5.1 was formed in combination with IV-5. The most promising conditions were Pd(dba)₂ 10 mol%, rac-BINAP 20 mol%, IV-3 2.10 equiv in 1,4-dioxane, heated to 100°C under inert conditions. Despite insufficient conversion to the target product, it was the only conditions that resulted in an isolated mixture of IV-5 and IV-5.1. Other attempts led only to IV-5.1 or to traces of IV-5, which could not be isolated. The formation of a carbene centre *via* deprotonation of IV-3 presented a particular

Fourth Chapter

challenge as it presumably led to the formation of various side-products. Moreover, the second oxidative insertion may be challenging as in most of the cases the mono-coupled product was observed.

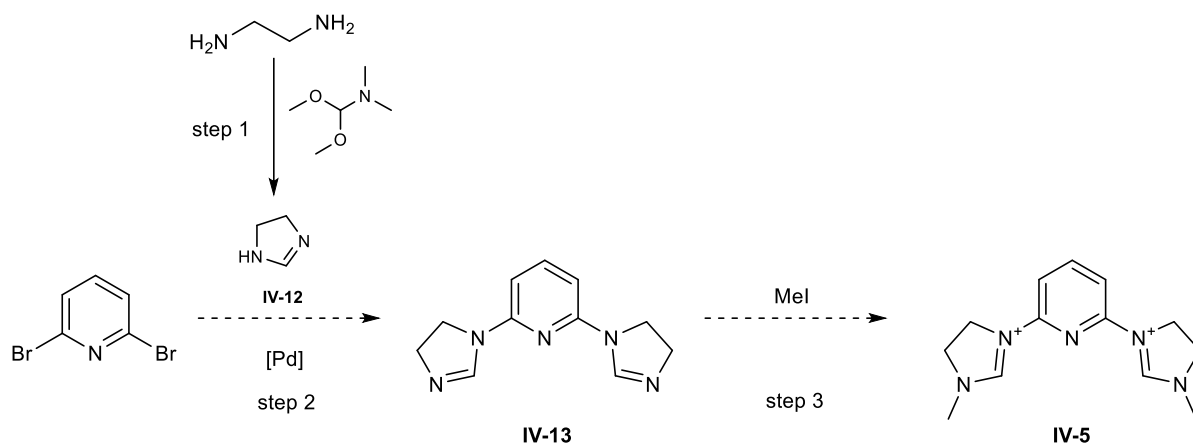
The second pathway included a Buchwald-Hartwig amination between 2,6-dibromopyridine and ethylenediamine, followed by formylation and ring closure to give IV-5 (Scheme 4.23).



Scheme 4.23. Synthetic pathway to give IV-5 via Buchwald-Hartwig amination between 2,6-dibromopyridine and ethylenediamine, followed by formylation and ring closure.

Monoprotected EDA was used to avoid coordination on palladium and was synthesised in advance. Two protective groups were tested – Boc and phthalimide. Various attempts were made to optimize the synthetic conditions for successfully coupling either the Boc- or phthalimide-protected amines, but the target product could ultimately not be isolated. As for the previous path, the mono- and bis-coupled products were forming during the reaction. In case of Boc-protection, a mixture of mono- and bis-coupled products could be isolated, but for the phthalimide-protected amine the target compound was observed only via ESI-MS analysis.

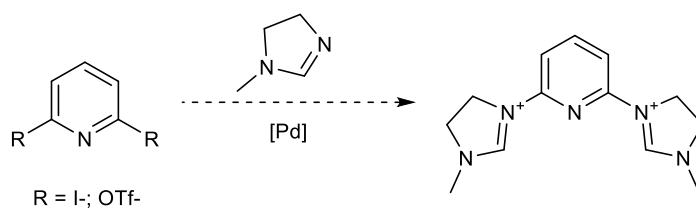
The third synthetic pathway included a Buchwald-Hartwig amination of 2,6-dibromopyridine with the secondary amine substrate 4,5-dihydro-1H-imidazole (Scheme 4.24).



Scheme 4.24. Synthetic pathway to give IV-5 *via* cross-coupling between 2,6-dibromopyridine and 4,5-dihydro-1H-imidazole (IV-12), followed by methylation of intermediate IV-13.

4,5-Dihydro-1H-imidazole (IV-12) was synthesized in advance from N,N-dimethylformamide dimethyl acetal and EDA. The cross-coupling of 2,6-dibromopyridine and IV-12 led to product IV-13, which could be detected by ESI-MS analysis.

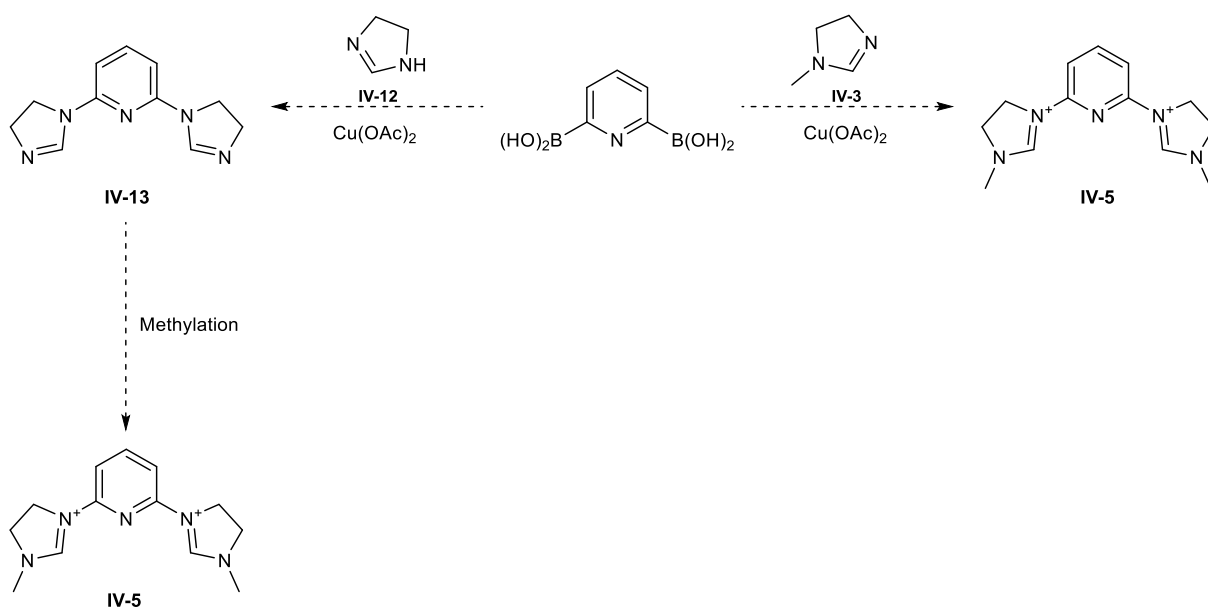
The Buchwald-Hartwig amination proved to be a challenging step in the synthesis towards the target ligand IV-5. Despite the insufficient conversion and selectivity as well as challenges with the actual isolation, it was demonstrated that the desired product can in principle be formed *via* a cross-coupling reaction. Moreover, it was shown that a catalyst is required for the product formation. For a successful preparation of target compound IV-5, further efforts on synthetic route definition and reaction optimization are still required. One possibility to overcome conversion limitations in the cross-coupling step could be the substitution of bromine with iodine or triflate (Scheme 4.25). Using a more favourable leaving group might facilitate the oxidative insertion and allow a more effective second palladium insertion. Moreover, it was found on the example of Pd₂(dba)₃ that commercially available Pd complexes can contain significant amount of Pd nanoparticles.¹⁹⁸ Utilization of Pd₂(dba)₃ of unknown purity resulted in reduced catalytic activity in the homogeneous phase as well as unexpected heterocatalytic activity of Pd nanoparticles may occur. This aspect needs to be considered for future investigations.



Scheme 4.25. Synthetic path to give IV-5 *via* direct cross-coupling between 2,6-disubstituted pyridine and 1-methyl-4,5-dihydroimidazole using different pyridine functionalities.

Fourth Chapter

Due to the challenging usage of palladium, the application of the copper-catalysed Chan-Lam coupling, which is based on reaction of aryl boronic acids with amines, could offer considerable benefits (Scheme 4.26). A further advantage of this coupling compared to the Buchwald-Hartwig amination is the possibility to conduct experiments under aerobic conditions.¹⁹⁹ Moreover, several copper-catalysed cross-coupling reactions of arylboronic acids with imidazoles are known in the literature.^{200, 201} Finally, iridium-catalysed alkylations of aromatic amines may offer an opportunity for the synthesis of precursors IV-8 or IV-10 that would allow further investigation of the ring closure pathway.²⁰²



Scheme 4.26. Synthetic route *via* copper-catalysed Chan-Lam coupling to afford target compound IV-5.

Fifth Chapter

Experimental part

1. General considerations

Current density-voltage (J - V) measurements were made by irradiating from the photoanode side with a LOT Quantum Design LS0811 instrument ($100 \text{ mW cm}^{-2} = 1 \text{ sun at AM 1.5}$) and the simulated light power was calibrated with a silicon reference cell.

The EQE measurements were performed on a Spe-Quest quantum efficiency setup from Rera Systems (Netherlands) equipped with a 100W halogen lamp (QTH) and a lambda 300 grating monochromator from Lot Oriel. The monochromatic light was modulated to 1 Hz using a chopper wheel from ThorLabs. The cell response was amplified with a large dynamic range IV converter from CVI Melles Griot and then measured with a SR830 DSP Lock-In amplifier from Stanford Research.

Solid-state UV-Vis spectra were measured on VARIAN Cary-5000 spectrophotometer. The transparent TiO_2 electrodes were measured as reference.

For the EIS measurements a ModuLab® XM PhotoEchem photoelectrochemical measurement system from Solartron Analytical was used. The impedance was measured at the open-circuit potential of the cell at a light intensity of 22 mW cm^{-2} (590 nm) in the frequency range 0.05 Hz to 100 kHz using an amplitude of 10 mV. The impedance data were analysed and fitted using ZView® software from Scribner Associates Inc.

^1H , $^{13}\text{C}\{1\text{H}\}$ and $^{31}\text{P}\{1\text{H}\}$ NMR spectra were recorded on Bruker Avance III-400 or 500 NMR spectrometers; spectra were recorded at 295 K. Chemical shifts were referenced to the residual solvent peaks. ^1H and $^{13}\text{C}\{1\text{H}\}$ NMR were referenced with respect to $\delta(\text{TMS}) = 0 \text{ ppm}$ and $^{31}\text{P}\{1\text{H}\}$ NMR chemical shifts were referenced with respect to $\delta(85\% \text{ aqueous H}_3\text{PO}_4) = 0 \text{ ppm}$.

Microwave reactions were performed in a Biotage Initiator 8 reactor.

Dyes N719 and SQ2 were purchased from Solaronix.

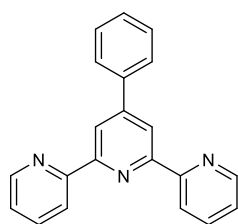
Commercial working electrodes (opaque) and platinum counter electrodes (Test Cell Platinum Electrodes Drilled) were obtained from Solaronix as well as hot-melt sealing foil (Test Cell Gaskets, made from Meltonix 1170-60 sealing film, 60 microns thick). The conducting silver paint (colloidal suspension, 0.5 troy oz.) was obtained from SPI.

Starting materials for synthesis were obtained in reagent grade from Avocado Research Chemicals Ltd, Sigma-Aldrich, Fluorochem, Alfa-Aesar, TCI, Carl Roth and Acros Organics. Dry solvents (crown cap or AcroSeal®) were purchased from Acros Organics. HPLC grade solvents were used for solar cells manufacturing, and ESI-MS analyses. HPLC grade solvents were purchased from HPLC VWR and J.T. Baker. NMR solvents were obtained from Cambridge Isotope Laboratories Inc. and Apollo. Fluka silica gel 60 was used for flash chromatography. Thin layer chromatography (TLC) was performed with aluminium sheets covered with silica gel 60 (Merck).

2. Synthesis of ligands and complexes

2.1 Synthesis of terpyridine compounds

4'-Phenyl-2,2':6',2''-terpyridine (III-2)



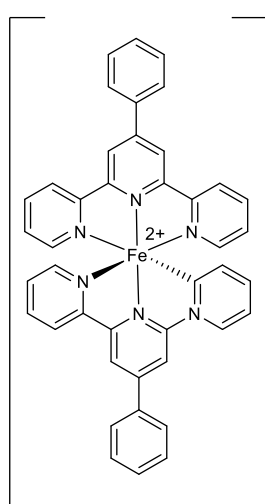
2- Acetylpyridine (2.0 equiv, 2.00 mmol, 0.22 mL) was added to benzaldehyde (1.0 equiv, 1.00 mmol, 0.10 mL) in EtOH (10 mL). Then KOH (2.0 equiv, 2.00 mmol, 112 mg) was added followed by addition of aq. NH₃ solution (28 wt%, 4.0 equiv, 4.00 mmol, 0.55 mL). The reaction mixture was stirred for 4 h at rt. Afterwards the precipitation was collected by filtration and washed with EtOH

(3 x 5 mL). Then the crude product was recrystallized. MeOH (10 mL) was added and the mixture was heated up to reflux followed by the addition of chloroform until everything was dissolved. Afterwards the reaction mixture was cooled to rt, the solid was collected and dried under vacuum. 4'-Phenyl-2,2':6',2''-terpyridine was obtained as an off-white solid (0.45 mmol, 140 mg, 45%).

The NMR is in agreement with the literature.²⁰³

¹H-NMR (500 MHz, CDCl₃) δ / ppm: 8.75 (s, 2H), 8.73 (ddd, J = 4.8, 1.9, 0.9 Hz, 2H), 8.68 (dt, J = 7.9, 1.1 Hz, 2H), 7.93 – 7.85 (m, 4H), 7.54 – 7.48 (m, 2H), 7.49 – 7.42 (m, 1H), 7.35 (ddd, J = 7.5, 4.8, 1.2 Hz, 2H).

¹³C-NMR (126 MHz, CDCl₃) δ / ppm: 156.28, 155.93, 150.35, 149.13, 138.51, 136.85, 128.99, 128.90, 127.34, 123.80, 121.35, 118.93.

$[\text{Fe}(\text{Phtpy})_2][\text{PF}_6]_2$ (III-1)

2PF_6^- $\text{FeCl}_2 \cdot 4\text{H}_2\text{O}$ (1.0 equiv, 0.13 mmol, 26.0 mg) and Phtpy (III-2, 2.0 equiv, 0.26 mmol, 81.0 mg) were dissolved in MeOH (8.0 mL). The reaction mixture was stirred for 30 min at rt. Then NH_4PF_6 (2.0 equiv, 0.26 mmol, 42.7 mg) was added and the mixture was stirred for 2 h until a purple precipitate was formed. The obtained crude product was filtered over Celite and washed with water (3 x 10 mL), EtOH (3 x 10 mL) and MTBE (3 x 15 mL) sequentially. The purple solid was redissolved with MeCN and the solvent was removed under reduced pressure to obtain $[\text{Fe}(\text{Phtpy})_2][\text{PF}_6]_2$ as purple solid (0.11 mmol, 105 mg, 83%).

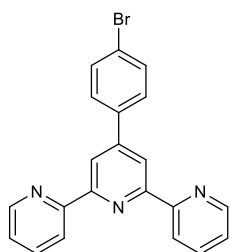
The NMR is in agreement with the literature.²⁰⁴

$^1\text{H-NMR}$ (500 MHz, CD_3CN) δ / ppm: 9.19 (s, 4H), 8.62 (dt, $J = 8.1, 1.0$ Hz, 4H), 8.35 – 8.31 (m, 4H), 7.91 (td, $J = 7.8, 1.5$ Hz, 4H), 7.85 – 7.80 (m, 4H), 7.77 – 7.72 (m, 2H), 7.20 (ddd, $J = 5.6, 1.5, 0.7$ Hz, 4H), 7.09 (ddd, $J = 7.2, 5.6, 1.3$ Hz, 4H).

$^{13}\text{C-NMR}$ (126 MHz, CD_3CN) δ / ppm: 160.90, 158.61, 153.66, 151.08, 139.31, 137.31, 131.32, 130.35, 128.50, 127.87, 124.40, 122.24.

$^{19}\text{F-NMR}$ (471 MHz, CD_3CN) δ / ppm: -72.92 (d, $J = 706.5$ Hz).

4'-(4-Bromophenyl)-2,2':6',2''-terpyridine (III-3)



2-Acetylpyridine (2.0 equiv, 40.0 mmol, 4.5 mL) was added to 4-bromobenzaldehyde (1.0 equiv, 20.0 mmol, 3.70 g) in EtOH (100 mL) at rt. Then KOH (2.0 equiv, 40.0 mmol, 2.24 g) was added followed by addition of aq. NH_3 solution (32 wt%, 2.5 equiv, 50.0 mmol, 6.0 mL). The reaction mixture was stirred for 4 h at rt. Afterwards the precipitation was collected by

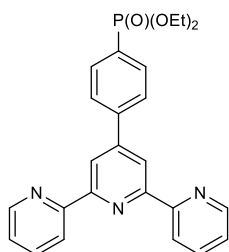
filtration and washed with EtOH (3 x 15 mL). Then the crude product was recrystallized. MeOH (20 mL) was added and the mixture was heated up to reflux followed by the addition of chloroform until everything was dissolved. Afterwards the reaction mixture was cooled to rt, the solid was collected and dried under vacuum. 4'-(4-bromophenyl)-2,2':6',2''-terpyridine was obtained as a white solid (9.74 mmol, 3.78 g, 49%).

The NMR is in agreement with the literature.²⁰³

$^1\text{H-NMR}$ (400 MHz, CDCl_3) δ / ppm: 8.73 (ddd, $J = 4.8, 1.8, 0.9$ Hz, 2H), 8.70 (s, 2H), 8.67 (dt, $J = 8.0, 1.1$ Hz, 2H), 7.89 (ddd, $J = 8.0, 7.5, 1.8$ Hz, 2H), 7.81 – 7.76 (m, 2H), 7.67 – 7.62 (m, 2H), 7.36 (ddd, $J = 7.5, 4.8, 1.2$ Hz, 2H).

$^{13}\text{C-NMR}$ (101 MHz, CDCl_3) δ / ppm: 156.24, 156.19, 149.29, 149.22, 137.56, 137.06, 132.24, 129.04, 124.09, 123.61, 121.52, 118.71.

Diethyl (4-([2,2':6',2''-terpyridin]-4'-yl)phenyl) phosphonate (III-4)



A microwave vial was charged with 4'-(4-bromophenyl)-2,2':6',2''-terpyridine (III-3, 1.0 equiv, 1.15 mmol, 0.45 g), $\text{Pd}(\text{PPh}_3)_4$ (5% mol, 0.05 mmol, 0.66 g) and Cs_2CO_3 (5.0 equiv, 5.75 mmol, 1.87 g). The vial was evaporated and refilled with nitrogen. Diethyl phosphite (4.0 equiv, 4.60 mmol, 0.59 mL) was dissolved in dry THF (10 mL) and the

solution was bubbled with nitrogen. Afterwards the THF solution was added to the terpyridine mixture, the vial was sealed and reacted in a microwave for 90 min at 110°C . After complete reaction, the mixture was filtered over Celite and the solvent was evaporated under reduced pressure. The violet residue was recrystallized from a minimum amount of MeCN and the obtained crystals were washed with cold Et_2O (3 x 10 mL) to give diethyl (4-([2,2':6',2''-terpyridin]-4'-yl)phenyl) phosphonate as a white solid (0.51 mmol, 226 mg, 44%).

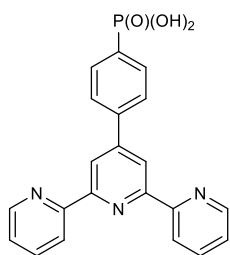
The NMR is in agreement with the literature.²⁰⁵

$^1\text{H-NMR}$ (400 MHz, CDCl_3) δ / ppm: 8.75 (s, 2H), 8.74 (ddd, $J = 4.8, 1.8, 0.9$ Hz, 2H), 8.68 (dt, $J = 8.0, 1.1$ Hz, 2H), 8.03 – 7.93 (m, 4H), 7.89 (ddd, $J = 8.0, 7.5, 1.8$ Hz, 2H), 7.37 (ddd, $J = 7.5, 4.8, 1.2$ Hz, 2H), 4.26 – 4.07 (m, 4H), 1.36 (td, $J = 7.1, 0.5$ Hz, 6H).

$^1\text{H NMR}$ (400 MHz, Acetone- d_6) δ 8.85 (s, 2H), 8.78 – 8.72 (m, 4H), 8.13 – 7.98 (m, 6H), 7.52 – 7.46 (m, 2H), 4.23 – 4.06 (m, 4H), 1.33 (t, $J = 7.1$ Hz, 6H).

$^{31}\text{P-NMR}$ (162 MHz, Acetone- d_6) δ / ppm: 17.04.

4-([2,2':6',2''-Terpyridin]-4'-yl)phenyl)phosphonic acid (III-5)



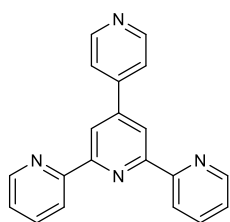
The hydrolysis of phosphonate III-4 was carried out according to a literature procedure.²⁰⁵

III-4 (1.0 equiv, 0.49 mmol, 218 mg) was suspended in anhydrous CH_2Cl_2 (1.5 mL) under nitrogen. TMSBr (4.0 equiv, 1.96 mmol, 0.26 mL) was added and the reaction mixture was stirred overnight at rt. Then the solvent was evaporated under reduced pressure and MeOH (10 mL) was added. The suspension was stirred for 2 h at rt. The white solid was filtered, washed with EtOH (3 x 10 mL), acetone (3 x 10 mL) and dried under vacuum. Afterwards the crude product was dissolved in 10% NaOH aq. solution (4.5 mL) and precipitated by acidifying the solution with 10% HCl aq. solution to pH 3. The white precipitate was filtered, washed with water (3 x 10 mL), EtOH (3 x 10 mL), acetone (3 x 10 mL) and dried under vacuum to obtain 4-([2,2':6',2''-terpyridin]-4'-yl)phenyl)phosphonic acid as a white solid (0.34 mmol, 134 mg, 70%).

$^1\text{H-NMR}$ (500 MHz, DMSO-d_6) δ / ppm: 8.90 (d, $J = 8.1$ Hz, 2H), 8.88 – 8.86 (m, 4H), 8.28 (t, $J = 8.0$ Hz, 2H), 8.11 (dd, $J = 8.1, 3.0$ Hz, 2H), 7.93 – 7.87 (m, 2H), 7.74 (dd, $J = 7.6, 5.0$ Hz, 2H). (OH-groups were not observed in the NMR spectrum).

$^{31}\text{P-NMR}$ (202 MHz, DMSO-d_6) δ / ppm: 11.83.

4'-(Pyridine-4-yl)-2,2':6',2''-terpyridine (III-6)



2-Acetylpyridine (2.0 equiv, 10.0 mmol, 1.1 mL) was added to 4-pyridinecarboxaldehyde (1.0 equiv, 5.00 mmol, 0.48 mL) in EtOH (50 mL).

Then KOH (2.5 equiv, 12.5 mmol, 701 mg) was added followed by addition of aq. NH_3 solution (32 wt%, 4.0 equiv, 20.0 mmol, 1.2 mL). The brown reaction mixture was stirred for 4 h at rt. Afterwards the precipitation was

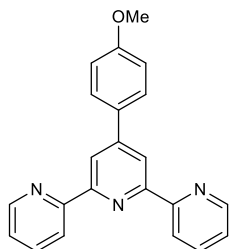
collected by filtration and washed with EtOH (3 x 10 mL). The crude product was recrystallized from chloroform to obtain 4'-(pyridine-4-yl)-2,2':6',2''-terpyridine as white solid (0.98 mmol, 303 mg, 20%).

The NMR is in agreement with the literature.²⁰⁶

$^1\text{H-NMR}$ (400 MHz, CDCl_3) δ / ppm: 8.78 – 8.76 (m, 4H), 8.74 (ddd, $J = 4.8, 1.8, 0.9$ Hz, 2H), 8.68 (dt, $J = 8.0, 1.1$ Hz, 2H), 7.93 – 7.87 (m, 2H), 7.79 (dt, $J = 4.5, 1.6$ Hz, 2H), 7.38 (ddt, $J = 7.7, 5.0, 1.5$ Hz, 2H).

^{13}C -NMR (101 MHz, CDCl_3) δ / ppm: 156.57, 155.90, 150.73, 149.37, 147.68, 146.13, 137.12, 124.27, 121.86, 121.53, 118.83.

4'-(4-Methoxyphenyl)-2,2':6',2''-terpyridine (III-7)



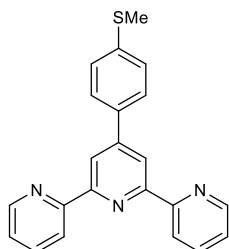
2-Acetylpyridine (2.0 equiv, 5.00 mmol, 0.56 mL) was added to *p*-anisaldehyde (1.0 equiv, 2.50 mmol, 0.30 mL) in EtOH (25 mL). Then KOH (2.5 equiv, 6.25 mmol, 351 mg) was added followed by addition of aq. NH_3 solution (32 wt%, 4.0 equiv, 10.0 mmol, 1.2 mL). The yellow reaction mixture was stirred for 72 h at rt. Afterwards the precipitation was collected by filtration and washed with EtOH (3 x 10 mL). Then the crude product was recrystallized. MeOH (10 mL) was added and the mixture was heated up to reflux followed by the addition of chloroform until everything was dissolved. Afterwards the reaction mixture was cooled to rt, and the solid was collected and air dried. 4'-(4-Methoxyphenyl)-2,2':6',2''-terpyridine was obtained as off-white solid (0.75 mmol, 253 mg, 30%).

The NMR is in agreement with the literature.²⁰⁷

^1H -NMR (500 MHz, CDCl_3) δ / ppm: 8.73 (ddd, $J = 4.8, 1.8, 0.9$ Hz, 2H), 8.71 (s, 2H), 8.67 (dt, $J = 8.0, 1.1$ Hz, 2H), 7.91 – 7.84 (m, 4H), 7.34 (ddd, $J = 7.5, 4.7, 1.2$ Hz, 2H), 7.06 – 7.01 (m, 2H), 3.88 (s, 3H).

^{13}C -NMR (126 MHz, CDCl_3) δ / ppm: 160.65, 156.53, 155.98, 149.91, 149.24, 136.98, 130.91, 128.68, 123.89, 121.50, 118.43, 114.46, 55.53.

4'-(4-Methylthiophenyl)-2,2':6',2''-terpyridine (III-8)



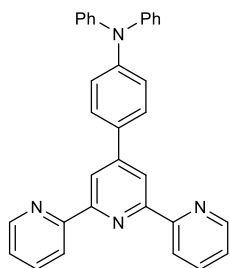
2-Acetylpyridine (2.0 equiv, 2.50 mmol, 0.28 mL) was added to 4-(methylthio)benzaldehyde (1.0 equiv, 1.25 mmol, 0.17 mL) in EtOH (10 mL). Then KOH (2.5 equiv, 3.13 mmol, 351 mg) was added followed by addition of aq. NH_3 solution (32 wt%, 4.0 equiv, 5.00 mmol, 0.60 mL). The reaction mixture was stirred for 12 h under reflux conditions. Afterwards the precipitation was collected by filtration, washed with EtOH (3 x 10 mL) and air dried to obtain 4'-(4-methylthiophenyl)-2,2':6',2''-terpyridine as beige solid (0.42 mmol, 1150 mg, 34%).

The NMR is in agreement with the literature.²⁰⁸

$^1\text{H-NMR}$ (500 MHz, CDCl_3) δ / ppm: 8.75 – 8.71 (m, 4H), 8.67 (dt, $J = 8.0, 1.1$ Hz, 2H), 7.91 – 7.83 (m, 4H), 7.40 – 7.33 (m, 4H), 2.55 (s, 3H).

$^{13}\text{C-NMR}$ (126 MHz, CDCl_3) δ / ppm: 156.42, 156.12, 149.71, 149.28, 140.21, 137.02, 135.09, 127.76, 126.67, 123.97, 121.52, 118.55, 15.69.

4'-(*N,N*-Diphenylanilin-4-yl)-2,2':6',2''-terpyridine (III-9)



2-Acetylpyridine (2.0 equiv, 2.00 mmol, 0.22 mL) was added to a suspension of 4-(diphenylamino)benzaldehyde (1.0 equiv, 1.00 mmol, 273 mg) in EtOH (20 mL). Then KOH (2.5 equiv, 2.50 mmol, 140 mg) was added followed by addition of aq. NH_3 solution (32 wt%, 8.0 equiv, 8.00 mmol, 0.96 mL). The reaction mixture was stirred for 12 h under reflux conditions. Afterwards the mixture was cooled down to rt. The solvent was evaporated under reduced pressure until dryness and acetone (10 mL) was added to the residue. The obtained suspension was filtrated, the solid was collected and air dried resulting in the target product. The acetone fraction was purified by flash chromatography on silica gel with petroleum ether/MTBE (8:2) as eluent. Afterwards, the product was filtered over silica with the same solvent mixture to obtain 4'-(*N,N*-diphenylanilin-4-yl)-2,2':6',2''-terpyridine as a -yellow solid (0.21 mmol, 98.0 mg, 21%).

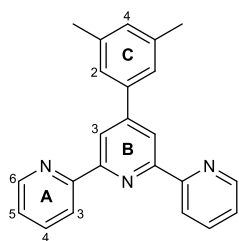
The NMR is in agreement with the literature.²⁰⁹

The NMR is in agreement with the literature.²⁰⁹

$^1\text{H-NMR}$ (500 MHz, CDCl_3) δ / ppm: 8.72 (ddd, $J = 5.0, 2.0, 1.0$ Hz, 2H), 8.71 (s, 2H), 8.67 (dt, $J = 7.9, 1.1$ Hz, 2H), 7.87 (td, $J = 7.7, 1.8$ Hz, 2H), 7.81 – 7.77 (m, 2H), 7.34 (ddd, $J = 7.4, 4.8, 1.2$ Hz, 2H), 7.32 – 7.27 (m, 4H), 7.20 – 7.14 (m, 6H), 7.08 (td, $J = 7.3, 1.2$ Hz, 2H).

$^{13}\text{C-NMR}$ (126 MHz, CDCl_3) δ / ppm: 156.54, 156.00, 149.88, 149.26, 148.93, 147.54, 136.97, 131.97, 129.52, 128.27, 124.95, 123.89, 123.51, 123.28, 121.48, 118.43. (Two carbon peaks of the phenyl moiety from the diphenylanilin group are not observed due to signal overlap).

4'-(3,5-Dimethylphenyl)-2,2':6',2''-terpyridine (III-10)



2-Acetylpyridine (2.0 equiv, 1.00 mmol, 0.11 mL) was added to 3,5-dimethylbenzaldehyde (1.0 equiv, 0.50 mmol, 0.07 mL) in EtOH (10 mL). Then KOH (2.5 equiv, 1.25 mmol, 70.1 mg) was added followed by addition of aq. NH₃ solution (32 wt%, 8.0 equiv, 4.00 mmol, 0.48 mL). The reaction mixture was stirred for 72 h under reflux conditions. Afterwards the mixture was cooled down to rt and filtered. The solvent was evaporated under reduced pressure and the obtained crude product was crystallized. MeOH (10 mL) was added and the mixture was heated up to reflux followed by the addition of chloroform until everything was dissolved. Afterwards the reaction mixture was cooled to rt, the solid was collected and air dried. 4'-(3,5-Dimethylphenyl)-2,2':6',2''-terpyridine as beige solid (0.15 mmol, 51.0 mg, 30%).

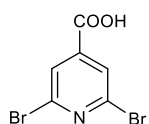
¹H-NMR (500 MHz, CDCl₃) δ / ppm: 8.75 (ddd, $J = 4.8, 1.8, 0.9$ Hz, 2H, H^{A6}), 8.72 (s, 2H, H^{B3}), 8.68 (dt, $J = 7.9, 1.1$ Hz, 2H, H^{A3}), 7.88 (td, $J = 7.7, 1.8$ Hz, 2H, H^{A4}), 7.53 (dd, $J = 1.5, 0.8$ Hz, 2H, H^{C2}), 7.35 (ddd, $J = 7.5, 4.7, 1.2$ Hz, 2H, H^{A5}), 7.10 – 7.09 (dd, $J = 1.6, 0.8$ Hz, 1H, H^{C4}), 2.42 (s, 6H, H^{Me}).

¹³C-NMR (126 MHz, CDCl₃) δ / ppm: 156.53, 155.92, 150.77, 149.26, 138.62, 138.50, 136.99, 130.83, 125.30, 123.91, 121.55, 119.04, 21.51 (C^{Me}).

ESI-MS m/z 360.15 [M + Na]⁺ (calc. 337.42).

2.2 Synthesis towards *N*-heterocyclic carbene compounds

2,6-Dibromoisonicotinic acid (III-11)



The acid was synthesized according to the literature procedure used as reference.¹⁸²

A flame-dried flask was charged with 2,6-dibromopyridine (1.0 equiv, 5.00 mmol, 1.18 g) under nitrogen. The flask was evaporated and refilled with nitrogen. Anhydrous THF (50 mL) was added and the solution was cooled to -30°C. TMPMgCl·LiCl (1.2 equiv, 6.00 mmol, 6.0 mL) was added dropwise for 15 min and the reaction mixture was stirred at the same temperature for 3 h. Afterwards the reaction was quenched with dry ice until gas evolution stopped and the mixture was allowed to warm to rt overnight. The pH was adjusted (pH \approx 12) with 1M NaOH solution and the mixture was extracted with AcOEt (3 x 15 mL). The aq. layer was acidified with 1M H₂SO₄ to pH = 2 and extracted with AcOEt (3 x 15 mL). The combined organic fractions were

Fifth Chapter

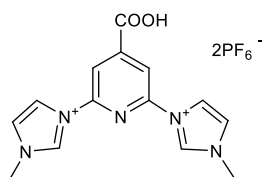
dried over Mg_2SO_4 and the solvent was removed under reduced pressure to obtain 2,6-dibromoisonicotinic acid as white solid (1.65 mmol, 462 mg, 33%).

The NMR is in agreement with the literature.²¹⁰

$^1\text{H-NMR}$ (500 MHz, DMSO-d_6) δ / ppm: 14.24 (br. s, 1H), 7.97 (s, 2H).

$^{13}\text{C-NMR}$ (126 MHz, DMSO-d_6) δ / ppm: 163.50, 143.67, 140.80, 126.73.

2,6-Bis(3-methylimidazolium-1-yl)pyridine-4-carboxylate hexafluorophosphate (I-8)



The salt was synthesized according to a literature procedure.⁸³

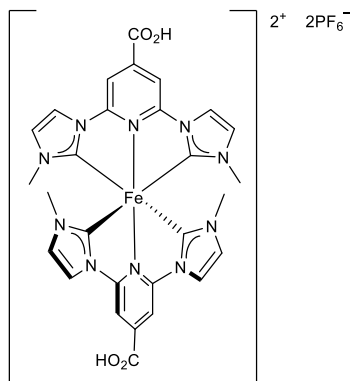
A pressure vial was charged with 2,6-dibromoisonicotinic acid (1.0 equiv, 0.98 mmol, 276 mg) and 1-methylimidazole (12.8 equiv, 12.5 mmol, 1 mL).

The vial was sealed and the reaction mixture was stirred for 4 h at 150°C . Once the reaction cooled down to rt, water (5 mL) was added and NH_4PF_6 sat. aq. solution (10 mL) was added. The mixture was acidified with 1M H_2SO_4 to $\text{pH} = 2$. The precipitate was collected *via* filtration, washed with water (3 x 10 mL) and MTBE (3 x 10 mL) and dried under high vacuum at 70°C for 16 h to obtain 2,6-bis(3-methylimidazolium-1-yl)pyridine-4-carboxylate hexafluorophosphate as beige solid (0.44 mmol, 254 mg, 45%).

$^1\text{H-NMR}$ (500 MHz, DMSO-d_6) δ / ppm: 10.41 (d, $J = 1.6$ Hz, 2H), 8.85 (t, $J = 1.9$ Hz, 2H), 8.53 (s, 2H), 8.04 (t, $J = 1.8$ Hz, 2H), 4.01 (s, 6H). (Proton from carboxylic acid was not observed).

$^{13}\text{C-NMR}$ (126 MHz, DMSO-d_6) δ / ppm: 163.79, 145.62, 136.64, 124.82, 119.27, 113.54, 36.52. (One tertiary carbon peak is not visible due to the overlap with another tertiary carbon peak).

Bis(2,6-bis(3-methylimidazol-1-ylidene)pyridine-4-carboxylic acid)iron(II) dihexafluorophosphate (I-4)



The iron(II) NHC complex was synthesized according to an adapted literature procedure.⁸³

A flask was charged with anhydrous FeCl_2 (1.0 equiv, 0.17 mmol, 21.7 mg) and the ligand I-8 (2.0 equiv, 0.34 mmol, 197 mg) under nitrogen. DMF (4.0 mL) was added followed by KO^tBu (1M solution in THF, 4.2 equiv, 0.72 mmol, 0.72 mL). The reaction mixture was

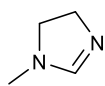
Fifth Chapter

stirred at rt overnight. 1M H₂SO₄ was added to adjust the pH to 2, then HPF₆ (3% aq. solution, 10 mL) was added until the precipitate started to form. The precipitate was collected *via* filtration, washed with water (3 x 10 mL) and MTBE (3 x 10 mL) to obtain bis(2,6-bis(3-methylimidazol-1-ylidene)pyridine-4-carboxylic acid)iron(II) dihexafluorophosphate as dark red solid (0.10 mmol, 87.8 mg, 56%).

¹H-NMR (500 MHz, CD₃CN) δ / ppm: 8.29 (s, 4H), 8.15 (d, $J = 2.3$ Hz, 4H), 7.00 (d, $J = 2.2$ Hz, 4H), 2.49 (s, 12H). (Protons from carboxylic acids were not observed).

¹³C-NMR (126 MHz, CD₃CN) δ / ppm: 199.71, 165.10, 155.25, 140.48, 127.83, 117.80, 105.81, 35.65.

1-Methyl-4,5-dihydro-imidazole (IV-3)



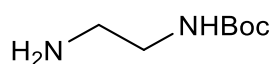
Compound IV-3 was synthesized according to an adapted literature procedure.¹⁹⁷

N,N-Dimethylformamide dimethylacetal (1.10 equiv, 29.7 mmol, 3.95 mL) was added to *N*-methylethylenediamine (1.0 equiv, 27.0 mmol, 2.38 mL) and the mixture was heated neat at 110°C for 4 h. Afterwards, the mixture was distilled (45°C/10 mbar) to give 1-methyl-4,5-dihydroimidazole as a colourless oil (9.36 mmol, 787 mg, 35%).

¹H-NMR (500 MHz, CDCl₃) δ / ppm: 6.73 (s, 1H), 3.79 (t, $J = 9.8$ Hz, 2H), 3.13 (t, $J = 10.3$ Hz, 2H), 2.80 (d, $J = 1.2$ Hz, 3H).

¹³C-NMR (126 MHz, CDCl₃) δ / ppm: 158.70, 55.69, 51.08, 34.42.

N-Boc-Ethylenediamine (IV-7)



Compound IV-7 was synthesized according to a literature procedure.¹⁹⁵

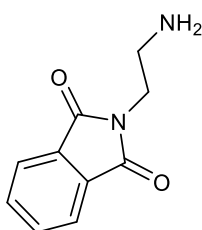
Di-*tert*-butyl dicarbonate (1.0 equiv, 18.3 mmol, 3.92 mL) was dissolved in CH₂Cl₂ (300 mL). This mixture was added dropwise over 6 h to a solution of ethylenediamine (6.0 equiv, 110 mmol, 7.33 mL) in CH₂Cl₂ (40 mL) under vigorous stirring. Then the mixture was stirred at rt for 24 h. Afterwards the solvent was removed under reduced pressure. 1M Na₂CO₃ aq. solution (350 mL) was added to the residual oil. The solution was extracted with CH₂Cl₂ (3 x 100 mL). The combined organic fractions were dried over Mg₂SO₄ and the solvent was evaporated under reduced pressure to give *N*-Boc-Ethylenediamine as a colourless oil (2.81 mmol, 450 mg, 15%).

Fifth Chapter

$^1\text{H-NMR}$ (500 MHz, CDCl_3) δ / ppm: 5.22 – 5.08 (br. s, 1H), 3.16 – 3.07 (m, 2H), 2.75 (t, $J = 5.9$ Hz, 2H), 2.05 – 1.92 (br. S, 2H), 1.38 (s, 9H).

$^{13}\text{C-NMR}$ (126 MHz, CDCl_3) δ / ppm: 156.33, 43.57, 42.02, 28.54. (Tertiary carbon peak was not observed).

N-(2-Amino-ethyl)-phthalimide (IV-9)

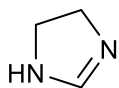


Compound IV-9 was synthesized according to an adapted literature procedure.¹⁹⁶

Phthalic anhydride (1.0 equiv, 15 mmol, 1.45 mL) was dissolved in acetic acid (10 mL). Then IV-7 (1.5 equiv, 22.5 mmol, 3.57 mL) was added. The reaction mixture was stirred for 1.5 h at 100°C. Afterwards the reaction was cooled to rt. Water (150 mL) was added and the mixture was extracted with CH_2Cl_2 (3 x 30 mL). The combined organic fractions were washed with water (30 mL), dried over Mg_2SO_4 and the solvent was evaporated under reduced pressure. The intermediate product was purified by flash chromatography on silica gel with cyclohexane/AcOEt (4:1) as eluent. Afterwards the obtained white solid was dissolved in CH_2Cl_2 (250 mL). Trifluoroacetic acid (100 mL) was added to the solution and the reaction mixture was stirred at rt for 1 h. Then the solvent and acid were removed under reduced pressure to afford a beige solid. The solid was stirred for 15 min in EtOH (50 mL) and filtered. The product was filtered and dried under vacuum to give *N*-(2-Amino-ethyl)-phthalimide as a white solid (8.00 mmol, 1523 mg, 53%).

$^1\text{H-NMR}$ (500 MHz, DMSO-d_6) δ / ppm: 7.95 – 7.80 (m, 4H), 3.84 (t, $J = 5.8$ Hz, 2H), 3.09 (t, $J = 5.9$ Hz, 2H). (Peak corresponding to the free amino-group, was not observed).

4,5-Dihydro-imidazole (IV-12)



Compound IV-12 was synthesized according to an adapted literature procedure.¹⁹⁷

N,N-Dimethylformamide dimethylacetal (1.00 equiv, 22.0 mmol, 2.92 mL) was added to ethylenediamine (1.0 equiv, 22.0 mmol, 1.47 mL) and the mixture was heated neat at 110°C for 2 h. Afterwards, the mixture was evaporated. and the yellow residue was purified by flash chromatography on silica gel with $\text{CH}_2\text{Cl}_2/\text{MeOH}$ (9:1) as eluent to give 4,5-dihydro-imidazole as an amorphous colourless solid (5.54 mmol, 388 mg, 25%).

Fifth Chapter

The NMR is in agreement with the literature.²¹¹ (Note: Compound was reported and initially measured in D₂O. Due to observed decomposition (hydrolysis) in this solvent, it was reanalysed in DMSO-d₆)

¹H-NMR (500 MHz, D₂O) δ / ppm: 8.09 – 8.08 (br. 1H), 3.55 – 3.52 (br. 4H).

¹H-NMR (500 MHz, DMSO-d₆) δ / ppm: 6.98 (br. s, 1H), 3.33 (br. s, 4H).

ESI-MS m/z 71.08 [M + H]⁺ (calc. 70.10).

Sixth Chapter

Summary and Outlook

The statistical study of EIS measurements had shown that it is important to perform EIS measurements on multiple cells to confirm that representative impedance data are collected. SQ2 served as an example of a dye, which had a wide deviation in experimental data as well as in fitted parameters. This illustrated how diverse parameters could be obtained within one set of devices with identical components and fabrication. There is a strong tendency in the DSC literature to present EIS data for only one solar device for a given dye, which may lead to erroneous data evaluation. Our study had shown that performing EIS measurements on at least four DSCs could serve as a good practice in order to determine reasonable average values.

The optimization of DSCs sensitized with iron(II) complexes was conducted. First investigations had started with $[\text{Fe(III-5)(Phtpy)}]^{2+}$ complexes as sensitizers. It was shown that the dye assembling strategy influences the PCE of the device. Significant variations were not observed in case of V_{OC} , but higher values for J_{SC} were obtained with the SALSAC strategy compared to the stepwise one. The careful choice of electrolyte composition led to our knowledge to the first performing DSC based on a $[\text{Fe(III-5)(Phtpy)}]^{2+}$ complex. A PCE of 0.05% was detected with J_{SC} of 0.14 mA cm^{-2} and V_{OC} of 445 mV in the presence of electrolyte Std II A (0.10 M LiI, 0.10 M I_2 , 0.60 M 1-butyl-3-methylimidazolium hexafluorophosphate and 0.50 M 1-methylbenzimidazole in 3-methoxypropionitrile).

The continuation of electrolyte studies was done with DSCs sensitized with an iron(II) NHC complex and chenodeoxycholic acid. The redox shuttle was always iodide/triiodide. Changes in solvent from MeCN to MPN were beneficial for the DSCs performance. It was shown that for the iron(II) MHC dyes the presence of additives like MBI and TBP is not advantageous. The removal of these additives resulted in a significant increase of J_{SC} values. Numerous ionic liquids were screened with various counter ions. On the example of DMII, EMII, PMII, BMII, HMII and DodMII as well as PDMII, BDMII, HDMII the influence of structural differences of ILs was studied. It was shown that longer alkyl chains (from methyl to *n*-butyl) can be beneficial. However, the further increase to *n*-hexyl and *n*-dodecyl led to the decrease in PCE compared to BMII. The presence of a methyl group in 2-position for imidazole led to increase in PCE for PDMII IL. With electrolyte based on PDMII, one of the highest PCE of 0.66% was achieved in this thesis (the electrolyte composition was 0.18 M LiI, 0.05 M I_2 , 0.60 M PDMII in MPN). The iodide counterion of IL proved to be the most promising one, due to the optimal values of J_{SC} , V_{OC} and fill factor. DSCs with $[\text{BF}_4]^-$ containing ILs had shown significantly enhanced values of J_{SC} , however, the

dramatic decreases in V_{OC} and ff overtook the benefits in photocurrent. Studies with Li^+ salt concentrations were performed. Higher amounts of Li^+ ions were beneficial for both $LiPF_6$ and LiI , but overall DSCs with LiI in the electrolyte had better PCE. Moreover, the concentration influence of iodine in the electrolyte was investigated (0.00, 0.01, 0.05, 0.10 and 0.20 M I_2). For ILs like DMII and EMII, 0.10 M I_2 resulted in higher J_{SC} and PCE values compared to other iodine concentrations. For IL with longer alkyl side chain (HMII), the DSCs performances were significantly decreased. For DMII, EMII and PDMII ILs a reduced transport resistance in the semiconductor of the photoanode was observed at lower iodine concentrations. Higher I_2 concentrations resulted in a decrease in diffusion resistance in the electrolyte and in the platinum counter electrode resistance. The electron lifetime and diffusion length decreased from 0.00 to 0.20 M I_2 . To summarize our findings, PMII, PDMII, BMII revealed themselves as the most promising ILs in the presence of 0.05 M I_2 . DMII had shown the best PCE values in combination with 0.10 M I_2 . The LiI concentration of 0.18 M was chosen as the most optimal for all ILs tested in this study.

Moreover, an alternative iron(II) NHC dye was proposed, and a synthetic path was developed. One of the steps required a C-N bond formation between compounds IV-3 and IV-2, which proved to be a challenge. A Buchwald-Hartwig amination was investigated between compound IV-3 and the model substrate 2,6-dibromopyridine (instead of IV-2). It was demonstrated that the desired product can in principle be formed *via* a Buchwald-Hartwig amination. Moreover, it was shown that the reaction requires the presence of a catalyst. Despite extensive studies, major drawbacks with insufficient conversion and selectivity as well as challenges with the actual isolation were not overcome. For a successful preparation of target compound IV-5, further revisions of the synthetic route and reaction optimization are still required.

Iron(II)-based DSCs are a promising alternative to ruthenium dyes due to their sustainability and abundance. Fe dyes are still suffering from low efficiencies compared to Ru. Thus, there is a need to establish new designs for iron-based sensitizers. However, each dye requires an individual electrolyte optimization to achieve the best possible performance.

References

1. <https://www.nationalgeographic.com/environment/article/fossil-fuels> (accessed 17.04.2021).
2. J. P. McBride, R. E. Moore, J. P. Witherspoon and R. E. Blanco, *Science*, 1978, **202**, 1045-1050.
3. <https://www.nrdc.org/stories/fossil-fuels-dirty-facts>, (accessed 17.04.2021).
4. <https://www.catf.us/resource/fossil-fumes-public-health-analysis/>, (accessed 17.04.2021).
5. <https://ourworldindata.org/air-pollution>, (accessed 17.04.2021).
6. <https://ourworldindata.org/fossil-fuels>, (accessed 17.04.2021).
7. <https://climate.nasa.gov/effects/> (accessed 17.04.2021).
8. N. L. Panwar, S. C. Kaushik and S. Kothari, *Renew. Sustain. Energy Rev.*, 2011, **15**, 1513-1524.
9. I. Dincer, *Energy Sources*, 2001, **23**, 83-92.
10. S. Bilgen, K. Kaygusuz and A. Sari, *Energy Sources*, 2004, **26**, 1119-1129.
11. <https://www.admin.ch/gov/de/start/dokumentation/medienmitteilungen.msg-id-80301.html>, (accessed 17.04.2021).
12. <https://www.nationalgeographic.com/environment/article/hydropower>, (accessed 17.04.2021).
13. M. Magni, P. Biagini, A. Colombo, C. Dragonetti, D. Roberto and A. Valore, *Coord. Chem. Rev.*, 2016, **322**, 69-93.
14. C. Battaglia, A. Cuevas and S. De Wolf, *Energy Envir. Sci.*, 2016, **9**, 1552.
15. J. R. Dufloy, J. R. Peeters, D. Altamirano, E. Bracquene and W. Dewulf, *CIRP Annals*, 2018, **67**, 29-32.
16. J. A. Luceño-Sánchez, A. M. Díez-Pascual and R. Peña Capilla, *Int. J. Mol. Sci.*, 2019, **20**, 976.
17. N.-G. Park, *Mater. Today*, 2015, **18**, 65-72.
18. G. Grancini, C. Roldan-Carmona, I. Zimmermann, E. Mosconi, X. Lee, D. Martineau, S. Narbey, F. Oswald, F. De Angelis, M. Graetzel and M. K. Nazeeruddin, *Nature Commun.*, 2017, **8**, 15684.
19. B. O'Regan and M. Grätzel, *Nature*, 1991, **353**, 737-740.
20. K. Kalyanasundaram, *Dye Sensitized Solar Cells*, EPFL Press, Lausanne, Switzerland, 2010.
21. M. L. Parisi, S. Maranghi and R. Basosi, *Renew. Sust. Energ. Rev.*, 2014, **39**, 124.
22. K. Sharma, V. Sharma and S. S. Sharma, *Nanoscale. Res. Lett.*, 2018, **13**, 381.
23. <https://gcell.com/dye-sensitized-solar-cells/advantages-of-dscc/flexible-solar-cells>, (accessed 26.07.2019).
24. C. S. Ponseca, Jr., P. Chabera, J. Uhlig, P. Persson and V. Sundstrom, *Chem Rev*, 2017, **117**, 10940-11024.
25. M. Gratzel, *Inorg Chem*, 2005, **44**, 6841-6851.
26. A. B. Kashyout, M. Soliman, M. El Gamal and M. Fathy, *Mater. Chem. Phys.*, 2005, **90**, 230-233.
27. J. B. Chu, S. M. Huang, D. W. Zhang, Z. Q. Bian, X. D. Li, Z. Sun and X. J. Yin, *Appl. Phys. A*, 2009, **95**, 849-855.
28. J. Tian and G. Cao, *Coord. Chem. Rev.*, 2016, **320-321**, 193-215.
29. <https://www.chemicalsafetyfacts.org/titanium-dioxide/> (accessed 06.04.2021).
30. S. Sharma, S. Bulkesh, S. K. Ghoshal and D. Mohan, *Renew. Sustain. Energy Rev.*, 2017, **70**, 529-537.
31. <http://tdma.info/what-is-titanium-dioxide/>, (accessed 06.04.2021).
32. F. A. Grant, *Rev. Mod. Phys.*, 1959, **31**, 646-674.
33. <https://www.asu.edu/courses/phs208/patternsbb/PiN/rdg/color/color.shtml>, (accessed 06.04.2021).
34. C. Dette, M. A. Perez-Osorio, C. S. Kley, P. Punke, C. E. Patrick, P. Jacobson, F. Giustino, S. J. Jung and K. Kern, *Nano Lett.*, 2014, **14**, 6533-6538.
35. N. G. Park, J. van de Lagemaat and A. J. Frank, *J. Phys. Chem. B*, 2000, **104**, 8989-8994.
36. M. A. M. Al-Alwani, A. B. Mohamad, N. A. Ludin, A. A. H. Kadhum and K. Sopian, *Renew. Sustain. Energy Rev.*, 2016, **65**, 183-213.

References

37. D. Chen, F. Huang, Y.-B. Cheng and R. A. Caruso, *Adv. Mater.*, 2009, **21**, 2206-2210.
38. A. Furube, R. Kato and K. Hara, *Surf. Sci. Rep.*, 2014, **69**, 389-441.
39. H. Nemeč, J. Rochford, O. Taratula, E. Galoppini, P. Kuzel, T. Polivka, A. Yartsev and V. Sundstrom, *Phys Rev Lett*, 2010, **104**, 197401.
40. A. Omar and H. Abdullah, *Renew. Sustain. Energy Rev.*, 2014, **31**, 149-157.
41. A. Hagfeldt, G. Boschloo, L. Sun, L. Kloo and H. Pettersson, *Chem. Rev.*, 2010, **110**, 6595-6663.
42. L. Zhang and J. M. Cole, *ACS Appl. Mater. Interfaces*, 2015, **7**, 3427-3455.
43. K. Kalyanasundaram, *Coord. Chem. Rev.*, 1998, **177**, 347-414.
44. E. Galoppini, *Coord. Chem. Rev.*, 2004, **248**, 1283-1297.
45. T.-F. Lu, W. Li, J. Chen, J. Tang, F.-Q. Bai and H.-X. Zhang, *Electrochim. Acta*, 2018, **283**, 1798-1805.
46. K. Kakiage, Y. Aoyama, T. Yano, K. Oya, T. Kyomen and M. Hanaya, *Chem. Commun.*, 2015, **51**, 6315-6317.
47. K. Kakiage, H. Osada, Y. Aoyama, T. Yano, K. Oya, S. Iwamoto, J. I. Fujisawa and M. Hanaya, *Sci. Rep.*, 2016, **6**, 35888.
48. T. P. Brewster, S. J. Konezny, S. W. Sheehan, L. A. Martini, C. A. Schmuttenmaer, V. S. Batista and R. H. Crabtree, *Inorg. Chem.*, 2013, **52**, 6752-6764.
49. A. J. Huckaba, F. Giordano, L. E. McNamara, K. M. Dreux, N. I. Hammer, G. S. Tschumper, S. M. Zakeeruddin, M. Grätzel, M. K. Nazeeruddin and J. H. Delcamp, *Adv. Energy Mater.*, 2015, **5**.
50. Y. Ren, N. Flores-Díaz, D. Zhang, Y. Cao, J. D. Decoppet, G. C. Fish, J. E. Moser, S. M. Zakeeruddin, P. Wang, A. Hagfeldt and M. Grätzel, *Adv. Funct. Mater.*, 2020, **30**.
51. A. J. Huckaba, A. Yella, L. E. McNamara, A. E. Steen, J. S. Murphy, C. A. Carpenter, G. D. Punecky, N. I. Hammer, M. K. Nazeeruddin, M. Grätzel and J. H. Delcamp, *Chemistry*, 2016, **22**, 15536-15542.
52. A. Peddapuram, H. Cheema, R. E. Adams, R. H. Schmehl and J. H. Delcamp, *J. Phys. Chem. C*, 2017, **121**, 8770-8780.
53. H. Cheema, J. Watson, A. Peddapuram and J. H. Delcamp, *Chem. Commun.*, 2020, **56**, 1741-1744.
54. P. Brogdon, H. Cheema and J. H. Delcamp, *Chem. Sus. Chem.*, 2018, **11**, 86-103.
55. G. Reginato, M. Calamante, L. Zani, A. Mordini and D. Franchi, *Pure Appl. Chem.*, 2018, **90**, 363-376.
56. P. P. Kumavat, P. Sonar and D. S. Dalal, *Renew. Sustain. Energy Rev.*, 2017, **78**, 1262-1287.
57. Y.-C. Chen and J. T. Lin, *Sustain. Energ. Fuels*, 2017, **1**, 969-985.
58. K. Kakiage, Y. Aoyama, T. Yano, K. Oya, J. Fujisawa and M. Hanaya, *Chem. Commun.*, 2015, **51**, 15894-15897.
59. K. Kakiage, Y. Aoyama, T. Yano, T. Otsuka, T. Kyomen, M. Unno and M. Hanaya, *Chem. Commun.*, 2014, **50**, 6379-6381.
60. J. H. Yum, T. W. Holcombe, Y. Kim, K. Rakstys, T. Moehl, J. Teuscher, J. H. Delcamp, M. K. Nazeeruddin and M. Grätzel, *Sci. Rep.*, 2013, **3**, 2446.
61. S. Mathew, A. Yella, P. Gao, R. Humphry-Baker, B. F. Curchod, N. Ashari-Astani, I. Tavernelli, U. Rothlisberger, M. K. Nazeeruddin and M. Grätzel, *Nature Chem.*, 2014, **6**, 242-247.
62. F. J. Malzner, M. Willgert, E. C. Constable and C. E. Housecroft, *J. Mater. Chem. A*, 2017, **5**, 13717-13729.
63. S. Aghazada and M. Nazeeruddin, *Inorganics*, 2018, **6**, 52.
64. J. M. Kroon, N. J. Bakker, H. J. P. Smit, P. Liska, K. R. Thampi, P. Wang, S. M. Zakeeruddin, M. Grätzel, A. Hinsch, S. Hore, U. Würfel, R. Sastrawan, J. R. Durrant, E. Palomares, H. Pettersson, T. Gruszecki, J. Walter, K. Skupien and G. E. Tulloch, *Prog. Photovolt: Res. Appl.*, 2007, **15**, 1.
65. Y. Chiba, A. Islam, Y. Watanabe, R. Komiya, N. Koide and L. Han, *Jap. J. Appl. Phys.*, 2006, **45**, L638.

References

66. M. K. Nazeeruddin, P. Péchy, T. Renouard, S. M. Zakeeruddin, R. Humphry-Baker, P. Comte, P. Liska, L. Cevey, E. Costa, V. Shklover, L. Spiccia, G. B. Deacon, C. A. Bignozzi and M. Grätzel, *J. Am. Chem. Soc.*, 2001, **123**, 1613.
67. T. Moehl, H. N. Tsao, K.-L. Wu, H.-C. Hsu, Y. Chi, E. Ronca, F. De Angelis, M. K. Nazeeruddin and M. Grätzel, *Chem. Mater.*, 2013, **25**, 4497-4502.
68. M. K. Nazeeruddin, A. Kay, I. Rodicio, R. Humphry-Baker, E. Mueller, P. Liska, N. Vlachopoulos and M. Graetzel, *J. Am. Chem. Soc.*, 2002, **115**, 6382-6390.
69. M. K. Nazeeruddin, F. De Angelis, S. Fantacci, A. Selloni, G. Viscardi, P. Liska, S. Ito, B. Takeru and M. Gratzel, *J. Am. Chem. Soc.*, 2005, **127**, 16835-16847.
70. K. Katsumata, H. Matsui, T. Yamaguchi and N. Tanabe, *Inorganica Chim. Acta*, 2017, **463**, 118-125.
71. B. Bozic-Weber, E. C. Constable and C. E. Housecroft, *Coord. Chem. Rev.*, 2013, **257**, 3089.
72. N. Armaroli, *Chem. Soc. Rev.*, 2001, **30**, 113-124.
73. N. Alonso-Vante, J.-F. Nierengarten and J.-P. Sauvage, *J. Chem. Soc., Dalton Trans.*, 1994, DOI: 10.1039/DT9940001649.
74. S. Sakaki, T. Kuroki and T. Hamada, *J. Chem. Soc., Dalton Trans.*, 2002, DOI: 10.1039/B109518H, 840-842.
75. N. Robertson, *Chem. Sus. Chem.*, 2008, **1**, 977-979.
76. T. Bessho, E. C. Constable, M. Graetzel, A. Hernandez Redondo, C. E. Housecroft, W. Kylberg, M. K. Nazeeruddin, M. Neuburger and S. Schaffner, *Chem. Commun.*, 2008, DOI: 10.1039/B808491B, 3717-3719.
77. M. Sandroni, M. Kayanuma, A. Planchat, N. Szuwarski, E. Blart, Y. Pellegrin, C. Daniel, M. Boujtita and F. Odobel, *Dalton Trans.*, 2013, **42**, 10818-10827.
78. B. Bozic-Weber, V. Chaurin, E. C. Constable, C. E. Housecroft, M. Meuwly, M. Neuburger, J. A. Rudd, E. Schonhofer and L. Siegfried, *Dalton Trans.*, 2012, **41**, 14157-14169.
79. B. Bozic-Weber, S. Y. Brauchli, E. C. Constable, S. O. Furer, C. E. Housecroft, F. J. Malzner, I. A. Wright and J. A. Zampese, *Dalton Trans.*, 2013, **42**, 12293-12308.
80. S. Ferrere and B. A. Gregg, *J. Am. Chem. Soc.*, 1998, **120**, 843.
81. O. S. Wenger, *Chem. Eur. J.*, 2019, **25**, 6043.
82. Y. Liu, T. Harlang, S. E. Canton, P. Chábera, K. Suárez-Alcántara, A. Fleckhaus, D. A. Vithanage, E. Göransson, A. Corani, R. Lomoth, V. Sundström and K. Wärnmark, *Chem. Commun.*, 2013, **49**, 6412.
83. T. Duchanois, T. Etienne, C. Cebrián, L. Liu, A. Monari, M. Beley, X. Assfeld, S. Haacke and P. C. Gros, *Eur. J. Inorg. Chem.*, 2015, **2015**, 2469.
84. G. Boschloo and A. Hagfeldt, *Acc. Chem. Res.*, 2009, **42**, 1819-1826.
85. J. N. Clifford, E. Palomares, M. K. Nazeeruddin, M. Grätzel and J. R. Durrant, *J. Phys. Chem. C* 2007, **111**, 6561-6567.
86. S. Pelet, J.-E. Moser and M. Grätzel, *J. Phys. Chem. B*, 2000, **104**, 1791-1795.
87. F. Bella, A. Sacco, D. Pugliese, M. Laurenti and S. Bianco, *J. Power Sources*, 2014, **264**, 333-343.
88. P. Wang, B. Wenger, R. Humphry-Baker, J. E. Moser, J. Teuscher, W. Kantelehner, J. Mezger, E. V. Stoyanov, S. M. Zakeeruddin and M. Grätzel, *J. Am. Chem. Soc.*, 2005, **127**, 6850.
89. Z. Lan, J. Wu, D. Wang, S. Hao, J. Lin and Y. Huang, *Solar Energy*, 2006, **80**, 1483-1488.
90. A. B. Martinson, T. W. Hamann, M. J. Pellin and J. T. Hupp, *Chemistry*, 2008, **14**, 4458-4467.
91. S. Yanagida, Y. Yu and K. Manseki, *Acc. Chem. Res.*, 2009, **42**, 1827-1838.
92. H. Ellis, R. Jiang, S. Ye, A. Hagfeldt and G. Boschloo, *Phys. Chem. Chem. Phys.*, 2016, **18**, 8419-8427.
93. A. Yella, H. W. Lee, H. N. Tsao, C. Yi, A. K. Chandiran, M. K. Nazeeruddin, E. W. Diau, C. Y. Yeh, S. M. Zakeeruddin and M. Gratzel, *Science*, 2011, **334**, 629-634.
94. W. Xiang, F. Huang, Y.-B. Cheng, U. Bach and L. Spiccia, *Energy Environ. Sci.*, 2013, **6**, 121-127.
95. S. O. Furer, B. Bozic-Weber, T. Schefer, C. Wobill, E. C. Constable, C. E. Housecroft and M. Willgert, *J. Mater. Chem. A*, 2016, **4**, 12995.
96. M. Freitag, J. Teuscher, Y. Saygili, X. Zhang, F. Giordano, P. Liska, J. Hua, S. M. Zakeeruddin, J.-E. Moser, M. Grätzel and A. Hagfeldt, *Nat. Photonics*, 2017, **11**, 372.

References

97. S. Hattori, Y. Wada, S. Yanagida and S. Fukuzumi, *J. Am. Chem. Soc.*, 2005, **127**, 9648-9654.
98. M. Karpacheva, F. J. Malzner, C. Wobill, A. Büttner, E. C. Constable and C. E. Housecroft, *Dyes Pigm.*, 2018, **156**, 410-416.
99. S. C. Pradhan, A. Hagfeldt and S. Soman, *J. Mater. Chem. A*, 2018, **6**, 22204-22214.
100. M. Freitag, F. Giordano, W. Yang, M. Pazoki, Y. Hao, B. Zietz, M. Grätzel, A. Hagfeldt and G. Boschloo, *J. Phys. Chem. C*, 2016, **120**, 9595-9603.
101. M. Brugnati, S. Caramori, S. Cazzanti, L. Marchini, R. Argazzi and C. A. Bignozzi, *Int. J. Photoenergy*, 2007, **2007**, 1-10.
102. A. Hagfeldt and M. Grätzel, *Acc. Chem. Res.*, 2000, **33**, 269.
103. A. Fukui, R. Komiya, R. Yamanaka, A. Islam and L. Han, *Solar Energy Mater. Solar Cells*, 2006, **90**, 649.
104. H. Kusama, H. Orita and H. Sugihara, *Langmuir*, 2008, **24**, 4411.
105. J. Shi, B. Peng, J. Pei, S. Peng and J. Chen, *J. Power Sources*, 2009, **193**, 878.
106. Z. Zhang, S. M. Zakeeruddin, B. C. O'Regan, R. Humphry-Baker and M. Grätzel, *J. Phys. Chem. B*, 2005, **109**, 21818.
107. J. R. Jennings and Q. Wang, *J. Phys. Chem. C*, 2010, **114**, 1715-1724.
108. J. Wu, Z. Lan, J. Lin, M. Huang, Y. Huang, L. Fan and G. Luo, *Chem. Rev.*, 2015, **115**, 2136.
109. S. O. Furer, L. Y. N. Luu, B. Bozic-Weber, E. C. Constable and C. E. Housecroft, *Dyes Pigm.*, 2016, **132**, 72-78.
110. P. Wang, S. M. Zakeeruddin, J. E. Moser, R. Humphry-Baker and M. Grätzel, *J. Am. Chem. Soc.*, 2004, **126**, 7164.
111. Y. Bai, Y. Cao, J. Zhang, M. Wang, R. Li, P. Wang, S. M. Zakeeruddin and M. Grätzel, *Nat. Mater.*, 2008, **7**, 626.
112. Z. Fei, F. D. Bobbink, E. Păunescu, R. Scopelliti and P. J. Dyson, *Inorg. Chem.*, 2015, **54**, 10504.
113. W. J. Lee, E. Ramasamy, D. Y. Lee and J. S. Song, *Sol. Energy Mater. Sol. Cells*, 2008, **92**, 814-818.
114. E. Ramasamy, W. J. Lee, D. Y. Lee and J. S. Song, *Appl. Phys. Lett.*, 2007, **90**.
115. J. Ma, S. Qingfeng, Z. Fengbao and W. Mingxing, *Mater. Res. Bull.*, 2018, **100**, 213-219.
116. T. Yohannes and O. Inganäs, *Sol. Energy Mater. Sol. Cells*, 1998, **51**, 193-202.
117. P. Balraju, M. Kumar, M. S. Roy and G. D. Sharma, *Synth. Met.*, 2009, **159**, 1325-1331.
118. P. Sudhagar, S. Nagarajan, Y. G. Lee, D. Song, T. Son, W. Cho, M. Heo, K. Lee, J. Won and Y. S. Kang, *ACS Appl. Mater. Interfaces*, 2011, **3**, 1838-1843.
119. S. Campagna, F. Puntoriero, F. Nastasi, G. Bergamini and V. Balzani, in *Photochemistry and Photophysics of Coordination Compounds I*, Springer, Berlin, Heidelberg, 2007, DOI: 10.1007/128_2007_133, ch. Chapter 133, pp. 117-214.
120. S. Kaufhold and K. Wärnmark, *Catalysts*, 2020, **10**.
121. J. K. McCusker, *Science*, 2019, **363**, 484-488.
122. L. L. Jamula, A. M. Brown, D. Guo and J. K. McCusker, *Inorg. Chem.*, 2014, **53**, 15-17.
123. S. Mukherjee, D. N. Bowman and E. Jakubikova, *Inorg. Chem.*, 2015, **54**, 560-569.
124. L. A. Fredin, M. Papai, E. Rozsalyi, G. Vanko, K. Warnmark, V. Sundstrom and P. Persson, *J. Phys. Chem. Lett.*, 2014, **5**, 2066-2071.
125. T. C. Harlang, Y. Liu, O. Gordivska, L. A. Fredin, C. S. Ponceca, Jr., P. Huang, P. Chabera, K. S. Kjaer, H. Mateos, J. Uhlig, R. Lomoth, R. Wallenberg, S. Styring, P. Persson, V. Sundstrom and K. Warnmark, *Nature Chem.*, 2015, **7**, 883-889.
126. L. A. Fredin, K. Warnmark, V. Sundstrom and P. Persson, *Chem. Sus. Chem.*, 2016, **9**, 667-675.
127. M. Pastore, T. Duchanois, L. Liu, A. Monari, X. Assfeld, S. Haacke and P. C. Gros, *Phys. Chem. Chem. Phys.*, 2016, **18**, 28069.
128. <https://g2voptics.com/solar-simulation/>, (accessed 25.03.2021).
129. H. J. Snaith, *Nature Photon.*, 2012, **6**, 337-340.
130. H. J. Snaith, *Energy Environ. Sci.*, 2012, **5**, 6513-6520.
131. C. Dragonetti, M. Magni, A. Colombo, F. Melchiorre, P. Biagini and D. Roberto, *ACS Appl. Energy Mater.*, 2018, **1**, 751.

References

132. H. Radamson and L. Thylén, in *Monolithic Nanoscale Photonics–Electronics Integration in Silicon and Other Group IV Elements*, eds. H. Radamson and L. Thylén, Academic Press, 2015, DOI: 10.1016/B978-0-12-419975-0.00002-7, ch. Chapter 2, pp. 63-85.
133. K. Ramalingam and C. Indulkar, in *Distributed Generation Systems*, eds. G. B. Gharehpetian and S. Mohammad Mousavi Agah, Butterworth-Heinemann, 2017, DOI: 10.1016/B978-0-12-804208-3.00003-0, ch. Chapter 3, pp. 69-147.
134. J. Halme, P. Vahermaa, K. Miettunen and P. Lund, *Adv. Mater.*, 2010, **22**, E210.
135. W. J. Yang, Z. Q. Ma, X. Tang, C. B. Feng, W. G. Zhao and P. P. Shi, *Sol. Energy*, 2008, **82**, 106-110.
136. D. N. Congreve, J. Lee, N. J. Thompson, E. Hontz, S. R. Yost, P. D. Reusswig, M. E. Bahlke, S. Reineke, T. Van Voorhis and M. A. Baldo, *Science*, 2013, **340**, 334-337.
137. W. Ananda, presented in part at the 2017 15th International Conference on Quality in Research (QiR) : International Symposium on Electrical and Computer Engineering, 2017.
138. M. Pazoki, U. B. Cappel, E. M. J. Johansson, A. Hagfeldt and G. Boschloo, *Energy Environ. Sci.*, 2017, **10**, 672-709.
139. J. Ferber and J. Luther, *Sol. Energy Mater. Sol. Cells*, 1998, **54**, 265-275.
140. M. Liberatore, F. Decker, L. Burtone, V. Zardetto, T. M. Brown, A. Reale and A. Di Carlo, *J. Appl. Electrochem.*, 2009, **39**, 2291-2295.
141. F. Fabregat-Santiago, J. Bisquert, E. Palomares, L. Otero, D. Kuang, S. M. Zakeeruddin and M. Grätzel, *J. Phys. Chem. C*, 2007, **111**, 6550-6560.
142. F. Fabregat-Santiago, E. M. Barea, S. Giménez and J. Bisquert, in *Molecular Devices for Solar Energy Conversion and Storage*, Springer: Singapore, 2018, DOI: 10.1007/978-981-10-5924-7_10, ch. Chapter 10, pp. 353-384.
143. P. Bhatt, K. Pandey, P. Yadav, B. Tripathi and M. Kumar, *Int. J. Photoenergy*, 2016, **2016**, 1-9.
144. P. Ho, L. Q. Bao, K.-S. Ahn, R. Cheruku and J. H. Kim, *Synth. Met.*, 2016, **217**, 314.
145. Q. Wang, S. Ito, M. Gratzel, F. Fabregat-Santiago, I. Mora-Sero, J. Bisquert, T. Bessho and H. Imai, *J. Phys. Chem. B*, 2006, **110**, 25210-25221.
146. F. Fabregat-Santiago, J. Bisquert, G. Garcia-Belmonte, G. Boschloo and A. Hagfeldt, *Sol. Energy Mater. Sol. Cells*, 2005, **87**, 117-131.
147. A. Sacco, *Renew. Sustain. Energy Rev.*, 2017, **79**, 814-829.
148. L. Wei-Qing, L. Zhong-Guan, K. Dong-Xing, H. Lin-Hua and D. Song-Yuan, *Electrochim Acta*, 2013, **88**, 395-403.
149. J. Bisquert, *Phys. Chem. Chem. Phys.*, 2011, **13**, 4679-4685.
150. F. Fabregat-Santiago, G. Garcia-Belmonte, I. Mora-Sero and J. Bisquert, *Phys. Chem. Chem. Phys.*, 2011, **13**, 9083-9118.
151. J. Bisquert, *Phys. Chem. Chem. Phys.*, 2003, **5**, 5360-5364.
152. L. Han, N. Koide, Y. Chiba, A. Islam and T. Mitate, *Comptes Rendus Chim.*, 2006, **9**, 645-651.
153. Y. M. Klein, M. Willgert, A. Prescimone, E. C. Constable and C. E. Housecroft, *Dalton Trans.*, 2016, **45**, 4659-4672.
154. S. Sarker, H. W. Seo and D. M. Kim, *Chem. Phys. Lett.*, 2013, **585**, 193-197.
155. L. Wei, Y. Yang, R. Fan, P. Wang, L. Li, J. Yu, B. Yang and W. Cao, *RSC Adv.*, 2013, **3**, 25908-25916.
156. M. E. Yeoh and K. Y. Chan, *J. Phys. Conf. Ser.*, 2019, 012042.
157. T. H. Nguyen, H. M. Tran and T. P. T. Nguyen, *ECS Trans.*, 2013, **50**, 49-58.
158. J. Bisquert, F. Fabregat-Santiago, I. Mora-Seró, G. Garcia-Belmonte and S. Giménez, *J. Phys. Chem. C*, 2009, **113**, 17278-17290.
159. H. Iftikhar, G. G. Sonai, S. G. Hashmi, A. F. Nogueira and P. D. Lund, *Materials*, 2019, **12**.
160. C. Dragonetti, M. Magni, A. Colombo, F. Fagnani, D. Roberto, F. Melchiorre, P. Biagini and S. Fantacci, *Dalton Trans.*, 2019, **48**, 9703.
161. F. Malzner, C. Housecroft and E. Constable, *Inorganics*, 2018, **6**.
162. B. Bozic-Weber, S. Y. Brauchli, E. C. Constable, S. O. Furer, C. E. Housecroft and I. A. Wright, *Phys. Chem. Chem. Phys.*, 2013, **15**, 4500-4504.
163. S. Nakade, T. Kanzaki, W. Kubo, T. Kitamura, Y. Wada and S. Yanagida, *J. Phys. Chem. B*, 2005, **109**, 3480-3487.

References

164. T. Stergiopoulos, E. Rozi, C. S. Karagianni and P. Falaras, *Nanoscale Res. Lett.*, 2011, **6**, 307.
165. P. Balraju, P. Suresh, M. Kumar, M. S. Roy and G. D. Sharma, *J. Photochem. Photobiol. A*, 2009, **206**, 53-63.
166. M. Dürr, A. Yasuda and G. Nelles, *Appl. Phys. Lett.*, 2006, **89**.
167. C. A. Kelly, F. Farzad, D. W. Thompson, J. M. Stipkala and G. J. Meyer, *Langmuir*, 1999, **15**, 7047-7054.
168. M. H. Ghatee, M. Zare, F. Moosavi and A. R. Zolghadr, *J. Chem. Eng. Data*, 2010, **55**, 3084-3088.
169. M. Gorlov and L. Kloo, *Dalton Trans.*, 2008, DOI: 10.1039/b716419j, 2655-2666.
170. M. Fevre, J. Pinaud, Y. Gnanou, J. Vignolle and D. Taton, *Chem. Soc. Rev.*, 2013, **42**, 2142-2172.
171. Y. Rong, X. Li, G. Liu, H. Wang, Z. Ku, M. Xu, L. Liu, M. Hu, Y. Yang, M. Zhang, T. Liu and H. Han, *J. Power Sources*, 2013, **235**, 243-250.
172. Z. Yu, M. Gorlov, J. Nissfolk, G. Boschloo and L. Kloo, *J. Phys. Chem. C*, 2010, **114**, 10612-10620.
173. M. Becker, M. S. Bertrams, E. C. Constable and C. E. Housecroft, *Materials*, 2020, **13**, 1547.
174. C. Zhang, J. Dai, Z. Huo, X. Pan, L. Hu, F. Kong, Y. Huang, Y. Sui, X. Fang, K. Wang and S. Dai, *Electrochim Acta*, 2008, **53**, 5503-5508.
175. H. Greijer Agrell, J. Lindgren and A. Hagfeldt, *J. Photochem. Photobiol. A: Chem*, 2004, **164**, 23-27.
176. Q. Wang, J. E. Moser and M. Gratzel, *J. Phys. Chem. B*, 2005, **109**, 14945-14953.
177. J. Bisquert, I. Mora-Sero and F. Fabregat-Santiago, *Chem. ElectroChem.*, 2014, **1**, 289-296.
178. A. D. Awtrey and R. E. Connick, *J. Am. Chem. Soc.*, 2002, **73**, 1842-1843.
179. W. Kubo, S. Kambe, S. Nakade, T. Kitamura, K. Hanabusa, Y. Wada and S. Yanagida, *J. Phys. Chem. B*, 2003, **107**, 4374-4381.
180. A. Sacco, A. Lamberti, M. Gerosa, C. Bisio, G. Gatti, F. Carniato, N. Shahzad, A. Chiodoni, E. Tresso and L. Marchese, *Solar Energy*, 2015, **111**, 125-134.
181. J. Bisquert, *J. Phys. Chem. B*, 2002, **106**, 325-333.
182. C. J. Rohbogner, S. H. Wunderlich, G. C. Clososki and P. Knochel, *Eur. J. Org. Chem.*, 2009, **2009**, 1781-1795.
183. P. A. Forero-Cortés and A. M. Haydl, *Org. Process Res. Dev.*, 2019, **23**, 1478-1483.
184. T. P. Brewster, J. D. Blakemore, N. D. Schley, C. D. Incarvito, N. Hazari, G. W. Brudvig and R. H. Crabtree, *Organometallics*, 2011, **30**, 965-973.
185. M. S. S. Jamil, S. Alkaabi and A. K. Brisdon, *Dalton Trans.*, 2019, **48**, 9317-9327.
186. M. Nirmala and P. Viswanathamurthi, *J. Chem. Sci.*, 2016, **128**, 1725-1735.
187. I. G. Smith, J. C. Zgrabik, A. C. Gutauskas, D. L. Gray and G. J. Domski, *Inorg. Chem. Commun.*, 2017, **81**, 27-32.
188. S. K. Gupta, D. Ghorai and J. Choudhury, *Organometallics*, 2014, **33**, 3215-3218.
189. R. Dorel, C. P. Grugel and A. M. Haydl, *Angew. Chem. Int. Ed. Engl.*, 2019, **58**, 17118-17129.
190. N. Kataoka, Q. Shelby, J. P. Stambuli and J. F. Hartwig, *J. Org. Chem.*, 2002, **67**, 5553-5566.
191. K. Kubota, T. Seo, K. Koide, Y. Hasegawa and H. Ito, *Nat. Commun.*, 2019, **10**, 111.
192. J. P. Wolfe and S. L. Buchwald, *J. Org. Chem.*, 2000, **65**, 1144-1157.
193. G. Anderegg, *Inorganica Chim. Acta*, 1986, **111**, 25-30.
194. P. Paoletti, *Pure Appl. Chem.*, 1984, **56**, 491-522.
195. J. Wang, M. Uttamchandani, J. Li, M. Hu and S. Q. Yao, *Chem. Commun.*, 2006, DOI: 10.1039/B609446E, 3783-3785.
196. P. Guo, Q. Chen, T. Liu, L. Xu, Q. Yang and X. Qian, *ACS Med. Chem. Lett.*, 2013, **4**, 527-531.
197. B. Straub, M. Bessel and F. Rominger, *Synthesis*, 2010, **2010**, 1459-1466.
198. S. S. Zalesskiy and V. P. Ananikov, *Organometallics*, 2012, **31**, 2302-2309.
199. D. S. Raghuvanshi, A. K. Gupta and K. N. Singh, *Org. Lett.*, 2012, **14**, 4326-4329.
200. B. Sreedhar, G. Venkanna, K. Shiva Kumar and V. Balasubrahmanyam, *Synthesis*, 2008, **2008**, 795-799.
201. J. P. Collman and M. Zhong, *Org. Lett.*, 2000, **2**, 1233-1236.
202. B. Blank, S. Michlik and R. Kempe, *Chemistry*, 2009, **15**, 3790-3799.

References

203. G. Hanan and J. Wang, *Synlett*, 2005, **2005**, 1251-1254.
204. E. C. Constable, M. Neuburger, D. R. Smith and M. Zehnder, *Inorganica Chim. Acta*, 1998, **275-276**, 359-365.
205. V. Spampinato, N. Tuccitto, S. Quici, V. Calabrese, G. Marletta, A. Torrisi and A. Licciardello, *Langmuir*, 2010, **26**, 8400-8406.
206. A. Mehrani and A. Morsali, *J. Mol. Struct.*, 2014, **1074**, 596-601.
207. J. B. Huang, X. F. Bai, L. Li, Z. J. Zheng, Z. Xu, Y. M. Cui, J. Cao and L. W. Xu, *Chemistry*, 2017, **23**, 4055-4059.
208. A. Fermi, G. Bergamini, M. Roy, M. Gingras and P. Ceroni, *J. Am. Chem. Soc.*, 2014, **136**, 6395-6400.
209. J. Palion-Gazda, B. Machura, T. Klemens, A. Szlapa-Kula, S. Krompiec, M. Siwy, H. Janeczek, E. Schab-Balcerzak, J. Grzelak and S. Maćkowski, *Dyes Pigm.*, 2019, **166**, 283-300.
210. W. R. Bowman, M. O. Cloonan, A. J. Fletcher and T. Stein, *Org. Biomol. Chem.*, 2005, **3**, 1460-1467.
211. J. P. James, G. B. Quistad and J. E. Casida, *J. Agric. Food Chem.*, 2002, **43**, 2530-2535.

CURRICULUM VITAE

Mariia Becker (Karpacheva)
From Moscow, Russia
ORCID ID 0000-0003-4833-1418

Department of Chemistry, University of Basel, BPR
1096, Mattenstrasse 24a, 4058 Basel, Switzerland
E-mail: mariia.karpacheva@unibas.ch

WORK EXPERIENCE

June 2017 – May 2021

University of Basel, Basel, *Switzerland*.

Research and teaching assistant (Doctoral candidate).

Supervisors: Prof. Dr. Catherine E. Housecroft and Prof. Dr. Edwin C. Constable.

Subject of research: Dye-sensitized solar cells based on Earth-sustainable metal complexes.

Oct. 2015 – Dec. 2016

Ludwig-Maximilians University, Munich, *Germany*.

Research and teaching assistant.

Supervisor: Prof. Dr. Paul Knochel.

Subject of research: Selective functionalization of pyridines using organometallic reagents.

July 2014 – Dec. 2014

CINaM (Nanoscience Interdisciplinary Centre) of the CNRS (National Centre for Scientific Research), Marseille, *France*.

Master Thesis research project.

Supervisor: Prof. Dr. Marc Gingras (CINaM).

Subject of research: Synthesis of carbo- and heterohelicenes and their π -complexation studies.

EDUCATION

June 2017 – May 2021

University of Basel, Basel, *Switzerland*.

PhD student under supervision of Prof. Dr. Catherine E. Housecroft and Prof. Dr. Edwin C. Constable.

Sept. 2010 – June 2015:

High education (Master degree).

Russian D. Mendeleev University of Chemical Technology, Moscow, *Russia*.

PUBLICATIONS

- M. Becker, C. E. Housecroft, E. C. Constable, *Materials*, **2021**, *14*, 11, 3053.
- M. Becker, M.-S. Bertrams, E. C. Constable, C. E. Housecroft, *Materials*. **2020**, *13*, 7, 1547.
- G. Risi, M. Becker, C. E. Housecroft, E. C. Constable, *Molecules*. **2020**, *25*, 1528.
- M. Karpacheva, V. Wyss, C. E. Housecroft, E. C. Constable, *Materials*. **2019**, *12*, 24, 4181 (cover).
- Y. M. Klein, A. Perscimone, M. Karpacheva, E. C. Constable, C. E. Housecroft, *Crystals*. **2019**, *9*, 110.
- Y. M. Klein, A. Perscimone, M. Karpacheva, E. C. Constable, C. E. Housecroft, *Polymers*. **2018**, *10*, 1369.
- M. Karpacheva, C. E. Housecroft, E. C. Constable, *Beilstein J. Nanotechnol.* **2018**, *9*, 3069.
- M. Karpacheva, F.J. Malzner, C. Wobill, A. Büttner, E. C. Constable, C. E. Housecroft, *Dyes and Pigm.* **2018**, *156*, 410.
- S. Fernandez, M. A. Ganiek, M. Karpacheva, F. C. Hanusch, S. Reuter, T. Bein, F. Auras, P. Knochel, *Org. Lett.* **2016**, *18*, 3158.